



MICCAI 2008 Workshop Proceedings

Computational Biomechanics for Medicine III

Karol Miller, Poul M.F. Nielsen

<http://www.mech.uwa.edu.au/CBM2008>



Preface:

A novel partnership between surgeons and machines, made possible by advances in computing and engineering technology, could overcome many of the limitations of traditional surgery. By extending surgeons' ability to plan and carry out surgical interventions more accurately and with less trauma, Computer-Integrated Surgery (CIS) systems could help to improve clinical outcomes and the efficiency of health care delivery. CIS systems could have a similar impact on surgery to that long since realized in Computer-Integrated Manufacturing (CIM). Mathematical modeling and computer simulation have proved tremendously successful in engineering. Computational mechanics has enabled technological developments in virtually every area of our lives. One of the greatest challenges for mechanists is to extend the success of computational mechanics to fields outside traditional engineering, in particular to biology, the biomedical sciences, and medicine.

Computational Biomechanics for Medicine Workshop series was established in 2006 with the first meeting held in Copenhagen. The third workshop was held in conjunction with the Medical Image Computing and Computer Assisted Intervention Conference (MICCAI 2008) in New York on 10 September 2008. It provided an opportunity for specialists in computational sciences to present and exchange opinions on the possibilities of applying their techniques to computer-integrated medicine.

Computational Biomechanics for Medicine III was organized into two streams: Computational Biomechanics of Soft Tissues, and Computational Biomechanics of Tissues of Musculoskeletal System. The application of advanced computational methods to the following areas was discussed:

- Medical image analysis;
- Image-guided surgery;
- Surgical simulation;
- Surgical intervention planning;
- Disease prognosis and diagnosis;
- Injury mechanism analysis;
- Implant and prostheses design;
- Medical robotics.

After rigorous review of full (eight-to-twelve page) manuscripts we accepted 15 papers, collected in this volume. They were split equally between podium and poster presentations. The proceedings also include abstracts of two invited lectures by world-leading researchers Professor Chwee Teck Lim from national University of Singapore and Dr. David Lloyd from The University of Western Australia.

Information about Computational Biomechanics for Medicine Workshops, including Proceedings of previous meetings is available at <http://cbm.mech.uwa.edu.au/> .

We would like to thank the MICCAI 2008 organizers for help with administering the Workshop, invited lecturers for deep insights into their research fields, the authors for submitting high quality work, and the reviewers for helping with paper selection.

Karol Miller
Poul M.F. Nielsen

Contents:

Invited Lectures

1. Molecular and Cellular Biomechanics-based Insights into the Pathophysiology of Human Diseases
Chwee Teck Lim 2
2. Computation Biomechanics: Neuromuscular skeletal modelling to estimate tissue loading in the lower limbs
David Lloyd 3

Part 1. Computational Biomechanics Of Soft Tissues

3. Cardiac motion estimation using multi-scale feature points
Becciu A; van Assen H; Florack L; Janssen B; ter Haar Romeny B 5
4. Fast image-based model of mitral valve closure for surgical planning
Hammer P; Vasilyev N; Perrin D; del Nido P; Howe R 15
5. Multimodal Registration of White Matter Brain Data via Optimal Mass Transport
Rehman, Tauseef; Haber, Eldad; Pohl, Kilian; Haker, Steven; Halle, Mike; Talos, Florin; Wald, Lawrence; Kikinis, Ron; Tannenbaum, Allen 27
6. Cardiac Motion Recovery by Coupling an Electromechanical Model and Cine-MRI Data: First Steps
Billet F; Sermesant M; Delingette H; Ayache N 36
7. Inverse Nonlinear Finite Element Methods for Surgery Simulation and Image Guidance
Pratt P 48
8. Nonlinear Elastic Registration with Unbiased Regularization in Three Dimensions
Yanovsky I; Le Guyader C; Leow A; Thompson P; Vese L 56
9. Coupling Finite Element and Mesh-free Methods for Modelling Brain Deformation in Response to Tumour Growth
Berger, Jamie; Horton, Asley; Joldes, Grand; Wittek, Adam; Miller, Karol 68

10.	Simulation of Active Cardiac Dynamics with Orthotropic Hyperelastic Material Model <i>Wong, Ken C.L.; Wang, Linwei; Zhang, Heye; Liu, Huafeng; Shi, Pengcheng</i>	83
11.	Realistic And Efficient Brain-Skull Interaction Model For Brain Shift Computation <i>Joldes, Grand Roman; Wittek, Adam; Miller, Karol; Morriss, Leith</i>	95
12.	Integration of Geometrical Boundary Conditions on Soft Tissue Characterization under large deformation <i>Ahn B; Kim J</i>	106
13.	Finite Element Modeling of the Pulse Wave propagation in the aorta for simulation of the Pulse Wave Imaging (PWI) method <i>Jonathan Vappou; Ioannis Zervantonakis; Jianwen Luo; Elisa Konofagou</i>	118
14.	Comparison of Displacement-Based and Force-Based Mapped Meshing <i>Vincent A. Magnotta; Wen Li; Nicole M. Grosland</i>	128

Part 2. Computational Biomechanics Of Tissues Of Musculoskeletal System

15.	Assessment of Peri-Articular Implant Fitting Based on Statistical Finite Element Modeling <i>Bonaretti S; Reimers N; Reyes M; Nikitsin A; Joensson A; Nolte L</i>	138
16.	Orientation definition of anisotropy is important to finite element simulation of bone material properties <i>Yang H; Guo T; Ma X</i>	148
17.	A Mix-resolution Bone-related Statistical Deformable Model (mBr-SDM) for Soft Tissue Prediction in Orthognathic Surgery Planning <i>He Q; Ip H; Xia J</i>	159

Invited Lectures

Molecular and Cellular Biomechanics-based Insights into the Pathophysiology of Human Diseases

Chwee Teck Lim

Singapore–MIT Alliance; SMART Center, Singapore;
NUS Life Sciences Institute, National University of Singapore;
Division of Bioengineering, National University of Singapore;
E-mail: ctlim@nus.edu.sg

Abstract

The human body, as a physical entity, is constantly subjected to stresses and strains throughout life. As such, the health and function of the organs, tissues and even cells can be affected by these physical interactions and their associated mechanical properties. For example, any deviations in the structural and mechanical properties of a living cell can not only affect its physiological functions, but can also lead to diseases such as malaria and cancer. As such, cell and molecular biomechanics can play an important role in the study of human diseases.

During the onset of a disease, a cell may experience alterations in both the composition and organization of its cellular structural features. Changes in the structural and mechanical properties of the cell, such as deformability and cell adhesiveness, may arise as these properties are reflective of the compositional and structural changes in the cell. Using cell and molecular biomechanics approaches, we can now study and quantify minute mechanical influences acting on individual cells and biomolecules. In fact, knowing the effect of tiny forces, as small as a few piconewtons, acting on a living cell can reveal ways by which diseased cells differ from healthy ones. It can also help us better understand and establish possible connections between the mechanics of living cells and the onset and progression of human disease so as to assist in developing effective diagnostics for disease detection.

Here, we will highlight studies on human diseases such as malaria and cancer, using nanotechnological and biophysical techniques such as atomic force microscopy, optical tweezers, microfluidics as well as micropipette aspiration assay. It is hoped that from these studies, new and efficient methods of detection and diagnosis may be developed since malaria and cancer are examples of diseases that exhibit changes in the mechanical properties during disease progression. For example, the extent to which a cell is able to deform may serve as a possible additional useful biomechanical marker in the detection of a disease that exhibit mechanical property changes. This may subsequently lead to new, effective and efficient methods of detection which are currently needed for diseases where early detection is extremely crucial for their control and prevention. In addition, these studies can also help clinicians in developing appropriate assays to quantitatively evaluate the efficacy of drugs and agents being developed to control or treat some of these diseases.

Computational Biomechanics: Neuromuscular skeletal modelling to estimate tissue loading in the lower limbs

David Lloyd

Faculty of Life and Physical Sciences, The University of Western Australia
Email: dlloyd@cyllene.uwa.edu.au

Abstract

Musculoskeletal tissue injury and disease are commonly experienced by many people around the world. In many sports anterior cruciate ligament (ACL) rupture is a frequent and debilitating injury. Patellofemoral pain (PFP) is one of the most often reported knee disorders treated in sports medicine clinics, and is a common outcome following knee replacement surgery for osteoarthritis. Osteoarthritis is one of the most common musculoskeletal diseases in the world, with the knee and hip the most often affected joints.

To design patient specific orthopaedic interventions, rehabilitation programs, or injury prevention programs one must estimate a person's individual tissue loads during activities of daily living to understand, treat and/or prevent these injuries and disorders. For example, many acute injuries such ACL ruptures occur during sporting movements that involve running and sudden changes of direction. The progression of some joint disorders is also heavily influenced by tissue loading during walking or running, such as PFP and tibiofemoral OA. Normal knee joint architecture, such as bone and cartilage size and quality, are most dependent on the loading experienced in walking. New tissue engineering work, such as autologous chondrocytes implants, seek to re-grow functional hyaline cartilage, but need an appropriate mechanical environment in which to mature.

Loading is crucial to understanding, treating or preventing all these conditions. However, it must be appreciated that for similar or even identical tasks people use different muscle activation and movement patterns depending on the type of control, experience, gender, and/or underlying pathologies. This strongly influences tissue loading. Therefore, to examine tissue loading associated with various injuries or disorders, people from different cohorts must be assessed performing specific tasks, accounting for their anatomy, movement and muscle activation patterns.

Subject specific computational biomechanics, specifically, neuromusculoskeletal computer modelling techniques, model the anatomy and the actions of muscles as controlled by the nervous system. This presentation will explore the development and application of our subject-specific neuromusculoskeletal modelling methods to assess the loads, stresses and strain of tissues in the lower extremities. Our current research has shown that is possible to estimate articular loading of the knee that reflects the loading measured in the total knee prostheses. This work also suggests that it is important to include activation patterns that people use during walking.

Current new directions in these methods will be explored, including making the models more subject-specific, scaling muscle-tendon parameters to the individual and validation studies to show the accuracy of such methods. The forces produced by these models can also be used as inputs to finite element models so that tissue stress and strain can be estimated.

Part 1.

Computational Biomechanics Of Soft Tissues

Cardiac motion estimation using multi-scale feature points

Alessandro Becciu, Hans C. van Assen, Luc Florack, Bart J. Janssen and Bart M. ter Haar Romeny

July 25, 2008

Eindhoven University of Technology, Eindhoven, The Netherlands

Abstract

Heart illnesses influence the functioning of the cardiac muscle and are the major causes of death in the world. Optic flow methods are essential tools to assess and quantify the contraction of the cardiac walls, but are hampered by the aperture problem. Harmonic phase (HARP) techniques measure the phase in magnetic resonance (MR) tagged images. Due to the regular geometry, patterns generated by a combination of HARPs and sine HARPs represent a suitable framework to extract landmark features. In this paper we introduce a new aperture-problem free method to study the cardiac motion by tracking multi-scale features such as maxima, minima, saddles and corners, on HARP and sine HARP tagged images.

1 Introduction

Cardiovascular diseases may seriously influence the heart function, altering its regular wall deformation and increasing the risk of heart failure. In 2004 heart diseases were responsible of more than 850.000 deaths only in the US; they formed the major cause of death for the US population and generated healthcare costs of hundreds of billions of dollars [21]. In this context, there is a necessity to assess the detailed motion of cardiac tissue, using this as an indicator for the progress of disease and/or for the response to therapy and perhaps even as precursors of cardiac symptoms. Optic flow is one of the traditional techniques in carrying out motion analysis. Optic flow measures the apparent velocity pattern of moving structures in an image sequence. In computer vision literature, several optic flow approaches have been described, ranging from gradient based techniques to feature based methods. Differential techniques compute the velocity from spatiotemporal image intensity derivatives or filtered versions of the image, using low-pass or band-pass filters. In most of these techniques it is assumed that brightness does not change by small displacements and the motion is estimated by solving the so-called Optic Flow Constraint Equation (OFCE):

$$L_x u + L_y v + L_t = 0 \quad (1)$$

where $L(x, y, t) : \mathbb{R}^3 \rightarrow \mathbb{R}$ is an image sequence, L_x, L_y, L_t are the spatiotemporal derivatives, $u(x, y, t), v(x, y, t) : \mathbb{R}^3 \rightarrow \mathbb{R}$ are unknown velocity vectors and x, y and t are the spatial and temporal coordinates respectively. Since there is one equation and two unknowns (u and v), a unique solution cannot be found. This has been referred as the "aperture problem". In order to find a plausible solution for equation (1), Horn and Schunck [13] combined the gradient constraint with a global smoothness term, finding the solution by minimizing an energy function. Lucas and Kanade [16] proposed a local differential technique, for which the flow field is constant in a small spatial neighborhood. The results obtained by the early methods were impressively improved by Brox et al. and Bruhn et al. [5, 6], who investigated a continuous, rotationally invariant energy functional and giving a multi-grid approach to the variational optical flow methods. One of the first applications of optical flow methods to tagged MRI was introduced by Dougherty et al. [7]. Florack et al. [10, 9] developed a robust differential technique in a multi-scale framework, whose application to cardiac MR images was presented by Niessen et al [18, 17] and Suinesiaputra et al. [24]. Van Assen et al. and Florack et al. [1, 11] developed a method based on multiple independent MR tagging acquisitions, removing altogether the aperture problem, by generating as many equations as unknowns.

Standard OFCE methods are underconstrained, and need additional assumptions. In this paper we investigate cardiac motion by exploiting point features in Gaussian scale-space. These features are interesting candidates for motion analysis: for those points the aperture problem does not arise and they are detected in a robust framework, which is inspired by findings of the multi-scale structure of the visual system. In the experiments maxima, minima, saddles and corners are chosen as feature points and the approach has been tested on an artificial and real sequence. Outcomes of the proposed technique emphasize the reliability of the vector field.

In sections 2 and subsection 2.1 a preprocessing approach and the multi-scale framework used in the experiments is presented. In 2.2 the topological number will be introduced as a convenient technique for extracting multi-scale features. In 2.3, 2.4 and 2.5, we present the corner detection method, the calculation of a sparse velocity vector field, the dense flow field extension and the angular error measure. Finally in section 3 and 4 we describe the experiment, the results and discuss the future directions.

2 Method

The experiments were carried out on a sequence of tagged MR images of a mouse heart's left ventricle. In 1988 Zerhouni et al. [27] introduced a tagging method for noninvasive assessment of myocardial motion. The method introduces structure, represented as dark stripes (figure 1 top), on the image aiming to improve the visualization of the intramyocardial motion. The approach was later improved by Axel et al. and Fischer et al [2, 8], who explored magnetic resonance imaging using spatial modulation of magnetization (SPAMM) and (CSPAMM) respectively. The images, however, suffer from tag fading, making the frames not suitable for optic flow methods based on conservation of brightness. In the harmonic phase (HARP) method [19, 22], MR images are filtered in the spectral domain and this technique overcomes the fading problem by taking into account the spatial phase information from the inverse transform of the filtered images. In our experiments the HARP technique was employed. Two tagged image series with mutually perpendicular tag lines were acquired (Figure 1 Top) and the first harmonic peak was filtered out using a band-pass filter in the Fourier domain (Figure 1 middle). Once applied the inverse Fourier transform, in the filtered images the phase varies periodically from 0 to 2π creating a saw tooth pattern (Figure 1 fourth from the top, left and middle picture). The combination of frames with horizontal and vertical stripes was used to create a grid pattern, which allowed the extraction of corners (Figure 1 fourth from the top, right picture). A sine function was applied to the phase images so as to avoid spatial discontinuities in the input due to the saw tooth pattern. A combination of sine HARP frames was later employed to produce a grid, from which the features points (maxima, minima and saddles) were retrieved (Figure 1 Bottom).

2.1 Scale Space

Scale is one of the most important concepts in human vision. When we look at a scene, we instantaneously view its contents at multiple scale levels. The Gaussian scale-space representation $L(x, y, s) \in \mathbb{R}^2 \times \mathbb{R}^+$ of a raw 2-dimensional image $f(x, y) \in \mathbb{R}^2$ is defined by the convolution of $f(x, y)$ with a Gaussian kernel $\phi(x, y, s) \in \mathbb{R}^2 \times \mathbb{R}^+$.

$$L(x, y, s) = (f * \phi)(x, y, s) \quad (2)$$

where $\phi(x, y, s) = \frac{1}{4\pi s} \exp(-\frac{x^2+y^2}{4s})$. In equation (2) x and y are the spatial coordinates, whereas $s \in \mathbb{R}^+$ denotes the variance of the Gaussian kernel (scale). Equation (2) provides a blurred version of the image, where the strength of blurring depends on the choice of scale. For an extensive review on scale space see [9, 14, 25, 15].

2.2 Topological Number

Singularities (critical points) induced by the MR tagging pattern are interesting candidates for structural descriptions. Detection and classification of critical points can be performed in an efficient way by the computation of the so-called topological number [25, 23, 20].

We examine a point P in image L and its neighborhood N_P . Suppose that N_P does not have any other critical points with exception of the point P itself, and suppose ∂N_P is the boundary of N_P , which is a $D-1$ dimensional oriented closed hypersurface. Since there are no critical points at ∂N_P , the normalized gradient of the image L on ∂N_P is defined component-wise as: $\xi_i = \frac{L_i}{\sqrt{L_j L_j}}$ with $L_i = \partial_i L$ and $i = 1, \dots, D$ (summation convention applies. Here we have $D = 2$). For a non-singular point we may define the $D-1$ dimensional form

$$\Phi = \xi_{i_1} d\xi_{i_2} \wedge \dots \wedge d\xi_{i_D} \epsilon^{i_1 \dots i_D} \quad (3)$$

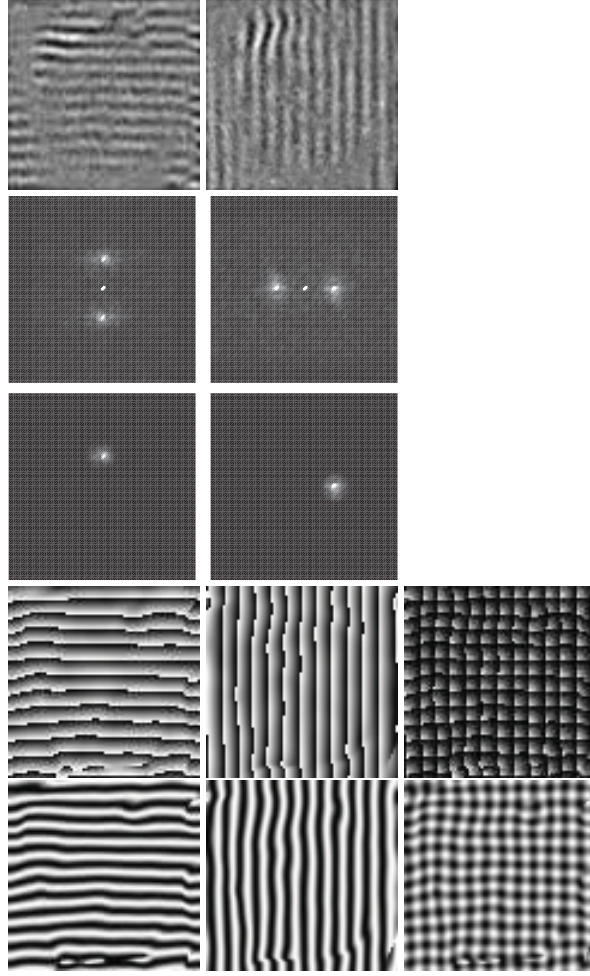


Figure 1: Top: cardiac mouse MR tagged images with horizontal and vertical tags. Second from the top: Fourier transform of cardiac mouse MR tagged images with horizontal and vertical tags. Middle: filtered harmonic peak by using a band-pass filter. Fourth from the top: harmonic phase (HARP), the phase varies periodically from 0 to 2π creating a saw tooth pattern. Grid obtained by combining the vertical with the horizontal tags of the HARP images. Bottom: sine HARP images and grid obtained by combining the vertical with the horizontal stripes.

where the symbol " \wedge " represents the wedge product and $\epsilon^{i_1 \dots i_D}$ is the permutation tensor of order D such that: $\epsilon^{i_1 \dots i_l \dots i_k \dots i_D} = -\epsilon^{i_1 \dots i_l \dots i_k \dots i_D} \forall l \neq k$ and $\epsilon^{1^2 \dots D} = 1$. Making the substitution of ξ_i in Φ we obtain:

$$\Phi = \frac{L_{i_1} dL_{i_2} \wedge \dots \wedge dL_{i_D} \epsilon^{i_1 \dots i_D}}{(L_j L_j)^{D/2}} \quad (4)$$

The topological number can then be defined as

$$v_{\partial N_P} = \frac{1}{A_D} \oint_{x \in \partial N_P} \Phi(x) \quad (5)$$

where A_D represents the area enclosed by ∂N_P .

In two-dimensional images the topological point is referred as the *winding number* and represents the integrated change of angle of the gradient when traversing a closed curve in a plane. In two dimensions,

equation (3) and (5) can be represented in a convenient way using the complex numbers. Given the complex couple of coordinates $z = x + iy$ and the complex conjugate $\bar{z} = x - iy$, the gradient vector field of the image $L(z, \bar{z})$ can be expressed as $W = (L_x + iL_y)/2 \equiv \partial_{\bar{z}}L(z, \bar{z})$. Hence, expression (3) can be written as

$$\Phi = \xi_x d\xi_y - \xi_y d\xi_x = \frac{L_x dL_y - L_y dL_x}{L_x L_x + L_y L_y} = \text{Im} \frac{(L_x - iL_y) d(L_x + iL_y)}{L_x L_x + L_y L_y} = \text{Im} \left(\frac{dW}{W} \right) = \text{Im}(d \ln W) \quad (6)$$

where $\ln W = \ln |W| + i \arg W$. Φ can, therefore, be read as the angle change of the gradient field.

The winding number is always an integer times 2π and classifies singularities of a scalar image at any dimension. For regular points the winding number is zero, for extrema the winding number is $+2\pi$, whereas for saddle points is -2π . Figure 2 shows gradient vector fields and winding number path for maxima, minima, saddle, and regular points respectively.

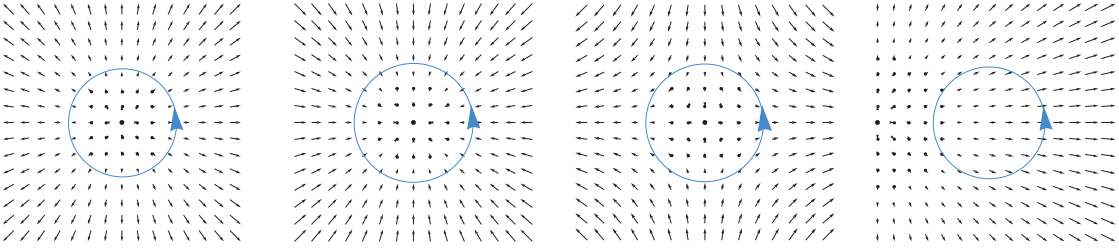


Figure 2: Gradient vector fields and winding number path for maxima, minima, saddle, and regular points respectively.

Algorithm 1 Winding number

- 1: Define the complex gradient as $L_x + iL_y$, where the derivatives are taken in scale-space.
 - 2: For every pixel, extract the complex gradient with respect to the 8 neighbor pixels.
 - 3: Extract the winding number
 - 4: Check the sign of the winding number. Consider only winding numbers greater or smaller than 0.
 - 5: If the sign of the winding number is positive, there is an extrema, else a saddle point.
 - 6: In case of extrema, check the sign of the second order derivatives of the image at those points. In case the sign is negative, there is a maximum, else a minimum.
-

2.3 Corner Detection

From differential geometry, image descriptors can easily be represented by a coordinate system, known as gauge coordinate system, which is dependent on the local structure of the image. One component $\vec{v} = \left\{ \frac{\partial L}{\partial x}, \frac{\partial L}{\partial y} \right\}$ is everywhere perpendicular to the isophote (line with constant intensity) and points in the direction of the gradient vector, the other component $\vec{\mu}$ is tangential to the isophote such that $\vec{\mu} = \left\{ \frac{\partial L}{\partial y}, -\frac{\partial L}{\partial x} \right\}$.

In computer vision a corner is defined as a point with high isophote curvature and high intensity gradient. The curvature gives a measure of local deviation from the tangent line and in gauge coordinates is described as: $k = -\frac{L_{\mu\mu}}{L_v}$. Hence, a corner detector is defined as: $\Theta^n = -\frac{L_{\mu\mu}}{L_v} L_v^n$. In case of $n = 3$, Θ provides the so-called (volume preserving) affine invariant corner detector [25, 4, 12].

$$\Theta^3 = -\frac{L_{\mu\mu}}{L_v} L_v^3 = -2L_x L_{xy} L_y + L_{xx} L_y^2 + L_x^2 L_{yy} \quad (7)$$

In the experiments the maxima of the corner response were used as feature points.

2.4 Sparse Velocities of Feature Points and Dense Flow Field

In our experiments given a sequence of frames, we assume that the singularity (feature) points move along with the moving tissue (this is true by construction of the tagging pattern, provided the feature points correctly correspond to the tag crossings and to the corners of the tag crossings). In general, given a point in a sequence of frames defined as $L(x(t), y(t), t)$, where t indicates the time, the critical points are defined implicitly by a vanishing spatial gradient:

$$\nabla L(x(t), y(t), t) = 0 \quad (8)$$

In order to track the feature points, we derive equation (8) with respect to time and apply the chain rule for implicit functions, yielding:

$$\frac{d}{dt} [\nabla L(x(t), y(t), t)] = \begin{bmatrix} L_{xx}u + L_{xy}v + L_{xt} \\ L_{xy}u + L_{yy}v + L_{yt} \end{bmatrix} = 0 \quad (9)$$

where $\frac{d}{dt}$ is the total time derivative, and where we have dropped space-time arguments on the r.h.s. for simplicity. Equation (9) holds only on location of critical points and can be also written as:

$$\begin{bmatrix} u \\ v \end{bmatrix} = -H^{-1} \frac{d\nabla L}{dt} \quad (10)$$

where H denotes the Hessian matrix of $L(x(t), y(t), t)$.

The velocities computed by equation (10) represent the flow field at a sparse set of positions. In order to retrieve a dense velocity field, the sparse velocities have been interpolated using homogeneous diffusion interpolation. Given a spatial domain $\Omega \rightarrow \mathbb{R}^2$, the scalar functions $u(x, y)$ and $v(x, y)$ are the horizontal and vertical components of a velocity vector $V : \Omega \rightarrow \mathbb{R}^2$. We know the velocity vectors just at certain positions and we call these vectors $\tilde{V} = \{\tilde{u}, \tilde{v}\}$ such that $\tilde{V} : \Omega_s \rightarrow \mathbb{R}^2$, where Ω_s is a finite subset of Ω . We are interested in retrieving a dense set of vectors $V \forall x, y \in \Omega$. In order to do so, we minimize the energy function

$$E(u, v) = \int_{\Omega} (\|\nabla u(x, y)\|^2 + \|\nabla v(x, y)\|^2) dx dy \quad (11)$$

under the constraint $V = \tilde{V} \forall x, y \in \Omega_s$. The minimization of equation (11) is carried out by employing Euler-Lagrange equations and the resulting expression can be solved with numerical schemes.

Algorithm 2 Computation velocities

- 1: Calculate set of velocities by solving (10) only for maxima, minima, saddle points and corners.
 - 2: Determine the velocity of other points by minimizing (11).
 - 3: Interpolate separately the x and the y components of the velocity vectors.
-

2.5 Angular Error

The interpolated flow vector at certain positions in the image can deviate from the true flow vector at that position in direction and in length. In our assessment we are interested in the movement from one frame to the next. Therefore, we set the time component of the flow vector to 1, yielding a 3-dimensional vector $V = \{u, v, 1\}$. The computed vector field has been compared with a ground truth extracted by an artificial

sequence described in section 3 and the assessment has been performed using the so-called average angular error (AAE) introduced by Barron et al. [3]

$$\text{Angular Error} = \arccos\left(\frac{V_t}{\sqrt{u_t^2 + v_t^2 + 1}} \cdot \frac{V_e}{\sqrt{u_e^2 + v_e^2 + 1}}\right) \quad (12)$$

where V_t is the true vector with spatial component u_t, v_t and time component 1, whereas V_e is the estimated velocity vector and u_e, v_e and 1 are its spatial and time components respectively.

3 Results

The proposed optic flow method was applied on a real sequence of 7 MR images (Figure 2), representing a mouse heart in phase of contraction. The images presented a resolution of 80 by 80 pixels and contained tags of 8 pixels wide; this width has been used to choose a physically reasonable range of spatial scales at which the features and the velocity field were calculated. The spatial scale is defined as $\sigma = \sqrt{2s}$ and the experiments were performed from spatial scale $\sigma = 1$ until scale $\sigma = 8$ at time scale 1. In order to assess the extracted vector field, an artificial sequence of 11 frames obtained by combination of translations (with rate of 1 pixel per frame) in different directions was created, using the first frame of HARP and Sine HARP and grid images (Figure 1, Fourth from the top (right) and Bottom (right)). A comparison between the extracted vector field and the ground truth is shown in figure 3. In Table 1 are displayed the performance of the proposed method, by the employment of different multi-scale features. In order to avoid outliers due to boundary conditions, the computation of the flow field was performed from frame 5 to frame 8 and the assessment was carried out on flow field regions 10 pixels distant from the boundaries. Finally, the error has been expressed in terms of "Average Angular Error" (AAE) and its standard deviation. The proposed method achieved the best performance by employing all the feature points (AAE = 2×10^{-2} degrees and Std = 3×10^{-2} degrees).

Feature	M1	M2	S	C	M1 M2	M1 S	M1 C	M2 S	M2 C	S C	M1 M2 S	M1 M2 C	M1 S C	M2 S C	M1 M2 S C
AAE	1.31°	1.44°	0.28°	1.27°	0.26°	0.09°	0.25°	0.1°	0.58°	0.09°	0.03°	0.12°	0.03°	0.05°	0.02°
Std	0.90°	1.02°	0.31°	0.93°	0.27°	0.13°	0.26°	0.13°	0.55°	0.12°	0.04°	0.05°	0.04°	0.07°	0.03°

Table 1: Performance of the proposed optic flow method with different multi-scale feature points. M1:Maxima, M2:Minima, S: Saddle, C: Corners. In the experiments the Average Angular Error (AAE) and its standard deviation have been employed as error measurement. The error measure is expressed in degrees. The scales used in the experiment were: spatial scale $\sigma = \{1, 1.25992, 1.5874, 2., 2.51984, 3.1748, 4., 5.03968, 6.3496, 8.\}$, time scale 1

4 Discussion

In this paper we propose a new method to track cardiac motion from a combination of HARP and Sine HARP images by following the movement of multi-scale singularity points. Qualitative and quantitative analysis of the results emphasize the reliability of the vector field, in particular, we found that the accuracy of the flow field is dependent on the number of the employed features. The best performance has been achieved by using all features simultaneously AAE = 2×10^{-2} degrees. For a more reliable results, however, in the forthcoming experiments we will assess the approach by using more complex test image sequences and compare it with constant brightness based methods. Furthermore, it is interesting to point out, that constant

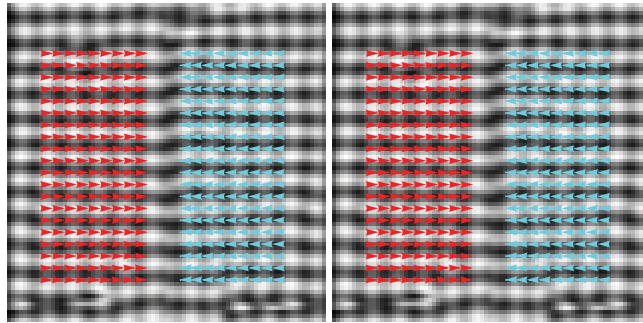


Figure 3: Comparison of vector fields in the artificial sequence. Extracted vector field (left) and ground truth (right).

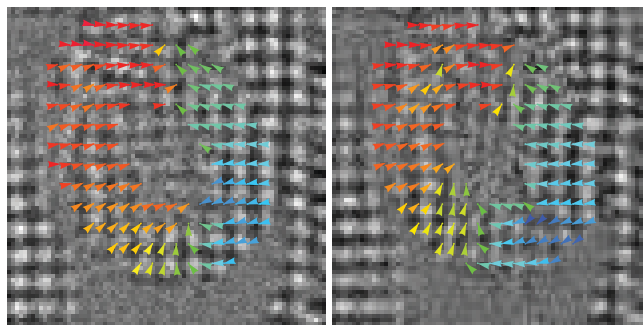


Figure 4: Flow field of MR images sequence, representing a mouse heart in phase of contraction. The sequence consisted of 7 frames and the filtered velocity field of the third and fifth frame has been displayed in the picture. The direction of the velocity vectors is color-encoded, the colors provide information about the coherency of the flow field in certain regions.

brightness methods are sensitive to the tag fading; the MR images have to be filtered in the Fourier domain in order to extract the velocity field. In this process the tag fading and noise are eliminated, but also information about the movement of the tags. Feature based optic flow methods are not dependent on constant brightness and less sensitive to tag fading, which makes our approach suitable for clinical practice. Future tests will include the evaluation of our method directly on MR images. In the experiments the velocity field of our approach has been extracted at fixed scales. In real data, due to deformation of the cardiac walls, the structure changes scale over time, thus, the final results obtained in the assessment may not be optimal. Therefore, it may be interesting to repeat the same experiments by using a scale selection method. The behavior of the cardiac muscle is characterized by twistings and contractions, therefore, interpolation with a term, that takes into account the rotation and the expansion of the vector field may improve the results.

Finally, the retrieved motion field may find also an application in validating mathematical models describing heart deformation. Ubbink et al. [26], for instance, compared 3 simulations of the cardiac muscle, illustrating how the orientation of modeled myofibers plays an important role in the computation of the final strain. A validation of these methods might be carried out by comparing the simulated strain with a ground truth strain calculated from the extracted optic flow field using real data.

References

- [1] H.C. Van Assen, L.M.J. Florack, A. Suinesiaputra, J.J.M. Westenberg, and B.M. ter Haar Romeny. Purely evidence based multiscale cardiac tracking using optic flow. In *MICCAI 2007 workshop on Computational Biomechanics for Medicine II*, pages 84 – 93. Springer-Verlag, 2007.
- [2] L. Axel and L. Dougherty. Mr imaging of motion with spatial modulation of magnetization. *Radiology*, 171(3):841–845, 1989.
- [3] J.L. Barron, D.J. Fleet, and S. Beauchemin. Performance of optical flow techniques. *International Journal of Computer Vision (IJCV1994)*, 12(1):43–77, 1994.
- [4] J. Blom. Affine invariant corner detection, 1991. Dissertation for the Dutch PhD degree, Utrecht University, Utrecht, The Netherlands.
- [5] B. Brox, A. Bruhn, N. Papenberg, and J. Weickert. High accuracy optical flow estimation based on a theory for warping. In *Proceedings of the 8th European Conference on Computer Vision*, volume 3024, pages 25–36. SV, 2004.
- [6] A. Bruhn, J. Weickert, T. Kohlberger, and C. Schnoerr. A muti-grid platform for real-time motion computation with discontinuity-preserving variational methods. *International Journal of Computer Vision*, 70(3):257–277, 2006.
- [7] L. Dougherty, J.C. Asmuth, A.S. Blom, L. Axel, and R. Kumar. Validation of an optical flow method for tag displacement estimation. *IEEE Transactions on Medical Imaging*, 18(4):359–363, 1999.
- [8] S. E. Fischer, G.C. McKinnon, S.E. Maier, and P. Boesiger. Improved myocardial tagging contrast. *Magnetic Resonance in Medicine*, 30(2):191–200, 1993.
- [9] L. Florack. *Image Structure*, volume 75 of *Computational Imaging and Vision*. Kluwer Academic Publishers, Utrecht, The Netherlands, first edition, 1997.
- [10] L. Florack, W. Niessen, and M. Nielsen. The intrinsic structure of optic flow incorporating measurement duality. *International Journal of Computer Vision*, 27(3):263–286, 1998.
- [11] L.M.J. Florack and H.C. Van Assen. Dense multiscale motion extraction from cardiac cine mr tagging using harp technology. In *Proc. Mathematical Methods in Biomedical Image Analysis. Workshop of the ICCV*, 2007.
- [12] L.M.J. Florack, B.M. ter Haar Romeny, and M.A. Viergever. Scale and the differential structure of images. *Image and Vision Computing*, 10(6):376–388, 1992.
- [13] B.K.P Horn and B.G. Shunck. Determining optical flow. *Artificial Intelligence*, 17:185–203, 1981.
- [14] J.J. Koenderink. The structure of images. *Biol. Cybern*, 50:363–370, 1984.
- [15] T. Lindeberg. *Scale-Space Theory in Computer Vision*. The Springer Intern. Series in Engineering and Computer Science. Kluwer Academic Publishers, Dodrecht, The Netherlands, first edition, 1994.
- [16] B. Lucas and T. Kanade. An iterative image registration technique with application to stereo vision. In *Proc. DARPA, Image Process*, volume 21, pages 85–117, 1981.

- [17] W.J. Niessen, J.S. Duncan, L.M.J. Florack M. Nielsen, B.M. ter Haar Romeny, and M.A. Viergever. A multiscale approach to image sequence analysis. *Computer Vision and Image Understanding*, 65(2):259–268, 1997.
- [18] W.J. Niessen, J.S. Duncan, B.M. ter Haar Romeny, and M.A. Viergever. Spatiotemporal analysis of left ventricular motion. In *Medical Imaging 95, San Diego, SPIE*, pages 192–203, 1995.
- [19] N.F. Osman, W.S. McVeigh, and J.L. Prince. Cardiac motion tracking using cine harmonic phase (harp) magnetic resonance imaging. *Magnetic Resonance in Medicine*, 42(6):1048–1060, 1999.
- [20] B. Platel. Exploring the deep structure of images, February 2007. Dissertation for the Dutch PhD degree, Eindhoven University of Technology, Eindhoven, The Netherlands.
- [21] W Rosamond, K Flegal, K Furie, A Go, K Greenlund, N Haase, S M Hailpern, M Ho, V Howard, B Kissela, S Kittner, D Lloyd-Jones, M McDermott, J Meigs, C Moy, G Nichol, C O'Donnell, V Roger, P Sorlie, J Steinberger, T Thom, M Wilson, and Hong, Y; American Heart Association Statistics Committee and Stroke Statistics Subcommittee. Heart Disease and Stroke Statistics 2008 Update. A Report From the American Heart Association Statistics Committee and Stroke Statistics Subcommittee. *Circulation*, 117:e2–e122, 2008.
- [22] S. Sampath, J.A. Derbyshire, E. Atalar, N.F. Osman, and J.L. Prince. Realtime imaging of twodimensional cardiac strain using a harmonic phase magnetic resonance imaging (harpMRI) pulse sequence. *Magnetic Resonance in Medicine*, 50(1):154–163, 2003.
- [23] J. Staal, S. Kalitzin, B. M. ter Haar Romeny, and M. Viergever. Detection of critical structures in scale space. In *Lecture Notes In Computer Science*, volume 1682 archive Proceedings of the Second International Conference on Scale-Space Theories in Computer Vision, pages 105–116, 1999.
- [24] A. Suinesiaputra, L.M.J. Florack, J.J.M. Westenberg, B.M. ter Haar Romeny, J.H.C. Reiber, and B.P.F. Lelieveldt. Optic flow computation from cardiac mr tagging using a multiscale differential method a comparative study with velocity encoded mri. In *Proceedings of the Sixth International Conference on Medical Image Computing and Computer-Assisted Intervention MICCAI 2003*, pages 483–490. LNCS, Berlin, Springer-Verlag, November 2003.
- [25] B. M. ter Haar Romeny. *Front-End Vision and Multi-Scale Image Analysis: Multiscale Computer Vision Theory and Applications, written in Mathematica*. Computational Imaging and Vision. Kluwer Academic Publishers, Eindhoven, The Netherlands, first edition, 2003.
- [26] S.W.J. Ubbink, P.H.M. Bovendeerd, T. Delhaas, T. Arts, and F.N. van de Vosse. Towards model-based analysis of cardiac mr tagging data: relation between left ventricular shear strain and myofiber orientation. *Medical Image Analysis*, 10:632–641, 2006.
- [27] E.A. Zerhouni, D.M. Parish, W.J. Rogers, A. Yang, and E.P. Sapiro. Human heart: tagging with mr imaginga method for noninvasive assessment of myocardial motion. *Radiology*, 169(1):59–63, 1988.

Fast Image-based Model of Mitral Valve Closure for Surgical Planning

Peter E. Hammer^{1,2}, Nikolay V. Vasilyev², Douglas P. Perrin², Pedro J. del Nido² and Robert D. Howe³

July 29, 2008

¹Department of Biomedical Engineering, Tufts University, Medford, MA, USA

²Department of Cardiac Surgery, Children's Hospital, Boston, MA, USA

³Harvard School of Engineering and Applied Sciences, Cambridge, MA, USA

Abstract

Surgical repair of the mitral valve results in better outcomes than valve replacement, yet diseased valves are often replaced due to the technical difficulty of the repair process. A surgical planning system based on patient-specific medical images that allows surgeons to simulate and compare potential repair strategies could greatly improve surgical outcomes. The system must simulate valve closure quickly and handle the complex boundary conditions imposed by the chords that tether the valve leaflets. We have developed a process for generating a triangulated mesh of the valve surface from volumetric image data of the opened valve. The closed position of the mesh is then computed using a mass-spring model of dynamics. In the mass-spring model, triangle sides are treated as linear springs supporting only tension. Chords are also treated as linear springs, and self-collisions are detected and handled inelastically. The equations of motion are solved using implicit numerical integration. The simulated closed state is compared with an image of the same valve taken in the closed state to assess accuracy of the model. The model exhibits rapid valve closure and is able to predict the closed state of the valve with reasonable accuracy

1 Introduction

The mitral valve is the most complex of the four heart valves and is the one most often associated with disease [21]. It consists of two leaflets that open and close as the heart beats to ensure one-way flow of blood into the left ventricle. The leaflets are restrained by fibrous chords during closure. See Figure 1. Mitral regurgitation (MR) occurs when the valve fails to close adequately during ventricular contraction and blood leaks backward through the incompetent valve. It can be caused by ischemic heart disease, dilated cardiomyopathy, rheumatic valve disease, or infection [5]. MR can lead to heart failure if left untreated, and the only effective treatment is surgery. The two primary surgical treatment options are repair of the native mitral valve tissue and replacement with a prosthetic valve. Repair has been shown to result in better function and long-term survival than replacement [9,15,20], so surgical repair of the mitral valve is preferable to valve replacement for the majority of patients who require treatment for MR [7]. However, replacement is often performed instead of repair due the technical difficulty of valve repair [18].

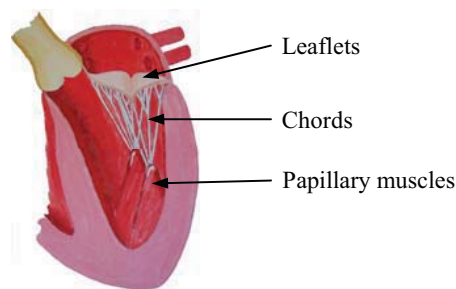


Figure 1 Cross section of the left heart with mitral valve shown in the closed position. Mitral valve structures are identified by arrows.

Valve repair typically requires use of cardiopulmonary bypass, a procedure which involves arresting the heart and emptying it of blood. The surgeon must try to imagine how the valve leaflets, and/or the chords that tether them, must be modified to make the valve close effectively after the heart is refilled with blood and pumping has been restored. Practice and experience are crucial for the development of the skills necessary to reliably repair mitral valves. Studies show that experienced surgeons at large clinical centers have a much better record of successful repairs, and valve replacement is often chosen instead of repair at low volume centers [8].

Surgical simulation has the potential to enable less experienced surgeons to effectively repair valves. This would allow many patients to undergo valve repair who would otherwise have undergone valve replacement. We propose that computer simulations of mitral valve closure can be used to help the surgeon plan effective repair strategies on a patient-specific basis. Under the proposed scheme, the geometry of a particular patient's valve would be extracted from medical images acquired prior to the date of surgery. The surgeon could then modify a computer model of that valve to reflect a particular surgical repair strategy and would use computer simulation to predict the closed state of the valve, indicating the effectiveness of that particular repair strategy. In this way, many potential repair strategies could be simulated and compared prior to the actual surgery, informing the surgeon to help choose the best strategy for a particular patient.

An important component of the proposed surgical simulation system is the computational model of the mitral valve. The proposed surgical simulation environment places two important requirements on the computational model. First, valve anatomy must be modeled in sufficient detail to allow predictive modeling on a patient-specific basis. Second, the model must be able to compute the closed state relatively quickly. A surgeon may want to simulate ten or more surgical strategies for a given patient, so the time to simulate one valve closure must be on the order of minutes.

Several groups have developed finite element models of the mitral valve to study its function [6,11,23]. While these studies modeled important aspects of the complex behavior of the valve, their methods are not well-suited for the surgical simulation environment. They were based on averaged valve data, rather than subject-specific images, assuming symmetry of the leaflets through their midline and neglecting the branching structure of the chords. Another finite element study modeled the valve structures asymmetrically and obtained boundary conditions dynamically using implanted sonomicrometry crystals in an animal model [12]. Unfortunately their sonomicrometry method cannot be used clinically. All of these finite element models have execution times that are too slow for this surgical planning application.

In developing the computational model, several assumptions were made. First we assumed that a static loading state of peak systolic pressure was sufficient to assess valve competency in the model. A justification of this assumption is that the technique used at the end of surgery to test the repaired valve is to load the valve by injecting saline under static pressure [5]. This assumption allows us to ignore the complex interaction between blood flow and the valve structures during ventricular filling and ejection.

The second assumption concerns the role of tissue deformation in determining the shape of the closed valve. The valve leaflets undergo both conformational changes and deformation (tissue strain) in going from the open to the closed, loaded state. While the constitutive properties of valve leaflets and chords are known to be complex and to play a role in maintaining relatively low and uniform stress concentrations across the valve leaflets, we hypothesize that the conformational changes largely dictate whether the valve closes completely and that modeling the conformational changes along with a simple model of tissue properties will enable us to accurately predict the closed state given a particular valve geometry.

To meet these requirements, we have developed a computational model based on a mass-spring system, a method used in computer graphics to simulate the dynamics of fabric [16]. Mitral valve geometry is read directly from computed tomography (CT) data. This data is used to generate a triangular mesh. The mesh is treated as a system of masses connected by springs, and dynamics equations are used to evolve the closed state of the valve. The closed state predicted by the model is compared directly with images of the actual valve taken in the closed state.

2 Methods

2.1 Imaging

The mitral valves of two explanted porcine hearts were statically loaded with air via tubing inserted through the aorta, past the aortic valve, and into the left ventricle. The aorta was then cinched tightly

around the tubing. To prevent air leakage through the coronary arteries, they were sutured closed. In order to supply air at low pressure with high accuracy, a circuit consisting of low-pressure regulators and electronic pressure sensors was constructed. The hearts were imaged in two different states using a micro-CT system (microCAT, Siemens, Munich, Germany): (1) with the mitral valve in the open position (no applied pressure), and (2) with the mitral valve in the closed position under typical porcine peak systolic pressure of 100 mmHg. Images were acquired at 100 μm isotropic voxel size. The volumetric CT image of the hearts were cropped to include only the mitral valve leaflets and chords. The resulting image of the valve was segmented, and an isosurface was fit to the data in Matlab (Mathworks, Natick, MA). The surface consists of an unstructured triangular mesh of points covering all surfaces of the leaflets and chords. The set of triangles comprising the atrial surface of the leaflets was isolated, and all chords that attach to either the free edge or the belly of the leaflets were approximated with line segments.

2.2 Mass-spring Model

Model Structure

The dataset consisting of the triangulated mesh of the open valve leaflets along with the line segments representing the chords was used as the basis for a mass-spring model. All edges of triangles were treated as translational springs supporting only tension, and the mass of each triangular element (assuming finite thickness and known mass density) is treated as being lumped at the nodes. An example of a simple mass-spring mesh is shown in Figure 2. Spring constants for the springs comprising the valve leaflets were chosen using the following equation for approximating elastic membrane behavior with spring meshes [22]:

$$k_c = \frac{E_2 \sum_i \text{area}(T_i)}{|c|^2} \quad (1)$$

where k_c is the spring constant for a given triangle side, E_2 is the two-dimensional Young's modulus for the leaflet tissue, the summation term represents the area of all triangles sharing side c , and the denominator is the squared length of side c . The two-dimensional Young's modulus is the product of Young's modulus and leaflet thickness. We assume uniform leaflet thickness of 1mm.

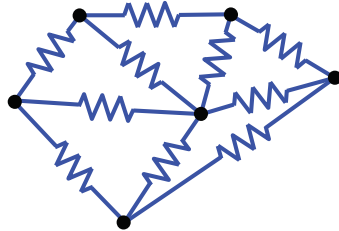


Figure 2 Example of a simple mass-spring mesh. All triangle sides are treated as translational springs, and mass is lumped at the nodes.

The stress-strain relationship for mitral valve leaflet tissue is known to be nonlinear, with a highly extensible pre-transitional region followed by a linear post-transitional region of much higher stiffness. See Figure 3. We approximated this relationship using a bilinear fit, with pre- and post-transitional stiffness of 100 and 6000 kPa and transition point of 25% strain [14]. Chord segments were also treated as

springs supporting only tension, and spring constants were computed as 1-d Young's moduli based on chord length, cross-sectional area and Young's modulus for the chords [11]. Nodal mass was computed as the product of the nodal area (one third of the sum of the areas of triangles sharing that node), leaflet thickness and mass density.

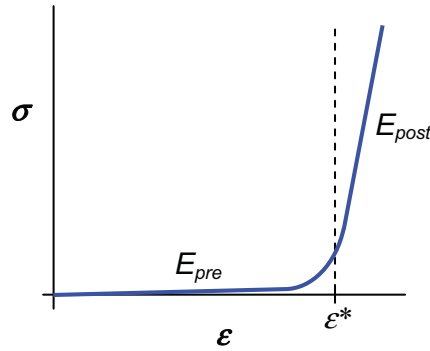


Figure 3 Example of typical stress-strain curve observed in mitral valve leaflets. Young's modulus of the pre-transitional region, E_{pre} , is the slope of the stress-strain curve at low strains, and Young's modulus of the post-transitional region, E_{post} , is the slope at high strains. The transition point is denoted as ϵ^* .

Model Dynamics

The dynamics of the mass-spring system can be expressed in state-space form as:

$$\begin{pmatrix} \ddot{\vec{x}} \\ \ddot{\vec{v}} \end{pmatrix} = \begin{pmatrix} \vec{v} \\ M^{-1} \vec{f} \end{pmatrix} \quad (2)$$

where x and v are vectors of nodal positions and velocities, respectively, M^{-1} is the inverse mass matrix (a diagonal matrix with the reciprocal of nodal mass on the main diagonal), and f is the vector of net nodal force due to springs and external forces. Implicit numerical integration is used because it allows larger integration step sizes and correspondingly faster simulations [1]. In order to use implicit integration, we discretized (2) using a second-order backward-difference formula as:

$$\frac{1}{h} \begin{pmatrix} \frac{3}{2} \vec{x}^{n+1} - 2\vec{x}^n + \frac{1}{2} \vec{x}^{n-1} \\ \frac{3}{2} \vec{v}^{n+1} - 2\vec{v}^n + \frac{1}{2} \vec{v}^{n-1} \end{pmatrix} = \begin{pmatrix} \vec{v}^{n+1} \\ M^{-1} \vec{f}^{n+1} \end{pmatrix} \quad (3)$$

where h is the integration time step. The net nodal force at step $n+1$ depends on the nodal positions at step $n+1$ making the set of equations nonlinear. It can be linearized by replacing f at step $n+1$ with a first-order Taylor series approximation:

$$\vec{f}^{n+1} = \vec{f}^n + \frac{\partial \vec{f}}{\partial \vec{x}} (\vec{x}^{n+1} - \vec{x}^n) + \frac{\partial \vec{f}}{\partial \vec{v}} (\vec{v}^{n+1} - \vec{v}^n) \quad (4)$$

Following a method used in a study simulating the behavior of cloth [3], (3) and (4) can be combined and expressed as the linear system:

$$\left(I - \frac{2}{3}hM^{-1}\frac{\partial \vec{f}}{\partial \vec{v}} - \frac{4}{9}h^2M^{-1}\frac{\partial \vec{f}}{\partial \vec{x}} \right) (\vec{x}^{n+1} - \vec{x}^n) = \frac{1}{3}(\vec{x}^n - \vec{x}^{n-1}) + \frac{h}{9}(8\vec{v}^n - 2\vec{v}^{n-1}) + \frac{4}{9}h^2M^{-1} \left(\vec{f}^n - \frac{\partial \vec{f}}{\partial \vec{v}} \vec{v}^n \right) - \frac{2}{9}hM^{-1}\frac{\partial \vec{f}}{\partial \vec{v}} (\vec{x}^n - \vec{x}^{n-1}) \quad (5)$$

The Jacobian matrix expressing the partial derivative of the net force vector with respect to velocity is an $N \times N$ block matrix where N is the number of nodes in the system, and each block is 3×3 , representing the three spatial coordinates. The forces due to springs as well as those due to applied pressure do not depend explicitly on nodal velocity, so their contributions are zero. Only the viscous damping term depends on nodal velocity, and its partial derivative yields $-bI$ where b is the damping coefficient and I is the $3N \times 3N$ identity matrix.

The Jacobian matrix expressing the partial derivative of the net force vector with respect to position is the same size as the Jacobian described above. In this case, the forces due to viscous damping and those due to applied pressure do not depend explicitly on position, so their contributions are zero. The forces due to the translational springs depend directly on nodal position, and their contribution to the Jacobian was evaluated analytically. For the translational spring between nodes i and j , elements of the Jacobian are computed as:

$$\frac{\partial \vec{f}_i}{\partial \vec{x}_i} = \frac{\partial \vec{f}_j}{\partial \vec{x}_j} = J \quad (6)$$

and

$$\frac{\partial \vec{f}_i}{\partial \vec{x}_j} = \frac{\partial \vec{f}_j}{\partial \vec{x}_i} = -J \quad (7)$$

where

$$J = \begin{pmatrix} l(r - s_x^2) - r^{3/2} & -l s_x s_y & -l s_x s_z \\ -l s_x s_y & l(r - s_y^2) - r^{3/2} & -l s_y s_z \\ -l s_x s_z & -l s_y s_z & l(r - s_z^2) - r^{3/2} \end{pmatrix} \quad (8)$$

In this equation, l is the undeformed length of the spring between nodes i and j , $\{s_x \ s_y \ s_z\}^T$ is the vector from node i to node j , and $r = \{s_x \ s_y \ s_z\} * \{s_x \ s_y \ s_z\}^T$.

Solution Method

Equation (5) is a linear system where the first term on the left side is a sparse $3N \times 3N$ matrix and the second term is a $3N \times 1$ vector of unknowns. All of the terms on the right side are $3N \times 1$ vectors which are known. It can be solved by inverting the sparse matrix. We used an iterative technique based on the method of conjugate gradients [2].

Points lying on the annulus as well as the locations where chords attach to the heart wall are treated as fixed (zero-displacement). However, both of these sets of points move considerably as the valve closes – both during physiological valve closure and during the passive loading that we use to image the closed valve. The closed shape of the valve leaflets is strongly dependent upon the locations of the annulus and chord attachment points, so it is important that we use their positions in the closed state for our simulations. To do so, we took a CT scan of the valve in the closed, loaded state then generated a mesh and identified the annulus and chord attachment points on the mesh. The annulus points were registered to those from the mesh of the open valve using the iterative closest point algorithm [24]. Points lying on the annulus of the open mesh were then linearly warped onto the annulus from the closed image, and the

points of attachments of the chords were moved directly to their positions measured in the image of the closed valve. All of the nodes in the mesh will be disturbed by the jump in positions of the annulus and chord attachments. To calculate their equilibrium state, the spring network was solved using a quasistatic approach. This was done by assembling the global stiffness matrix and solving it subject to zero-displacement boundary conditions on the free edge of the leaflet and prescribed-displacement boundary conditions on the annulus and chord attachment points [13]. Then, during dynamic simulations, the constraint on the free edge of the leaflet is relaxed while annulus and chord attachment points are constrained to remain fixed.

Zero-displacement boundary conditions are implemented during simulations through use of the inverse-mass matrix appearing in (5). A particle i acted upon by springs but not subject to any displacement constraints will contribute the 3×3 diagonal matrix given by $(1/m_i)I$ to the main diagonal of the $3N \times 3N$ inverse-mass matrix. However, we could prevent the velocity of the particle from changing by making the inverse-mass equal to zero, *i.e.*, giving it an infinite mass. An infinite mass cannot be accelerated, so it effectively ignores all forces exerted on it. The zero displacement boundary conditions at the mitral valve annulus and at nodes where chords terminate in the heart wall are handled this way. Self-collisions of the leaflet were identified using a simple method based on proximity of vertices. Detected collisions were handled by inserting forces to render the collisions inelastic.

Model Parameters and Implementation

Some of the model parameters, such as constitutive properties of the tissues and applied transleaflet pressure, affect the closed shape of the valve at equilibrium. These parameters are assigned physically realistic values and are listed in Table 1. The remaining model parameters affect model dynamics and/or stability but not the closed shape of the valve, and those are assigned in order to minimize execution time and instability. The model was implemented in the Matlab programming language.

Table 1. Model parameters.

Parameter	Value
E_{pre} , leaflets	100 kPa
E_{post} , leaflets	6,000 kPa
E , chords	40,000 kPa
ϵ^*	25%
transleaflet pressure	13 kPa (100 mmHg)

3 Results

Images from several stages of the simulation process for two different data sets are shown in Figure 4. The left pair of panels shows CT images of the mitral valve (oblique view from the top) in the opened position. The next pair of panels shows the initial states of the mass-spring model of the valve from the same view. The chords are depicted by line segments. The next pair shows the meshes in the initial state

but after the annulus and chord attachments have been moved to their positions for the closed state. The right pair of panels shows the meshes in the final closed and loaded state. The model shown in the top row contains 381 nodes, 631 triangles, and 1013 translational springs. The model shown in the bottom row contains 276 nodes, 419 triangles, and 700 springs. The valve model closed completely in approximately 5 minutes on a computer with 2.33 GHz dual core CPU.

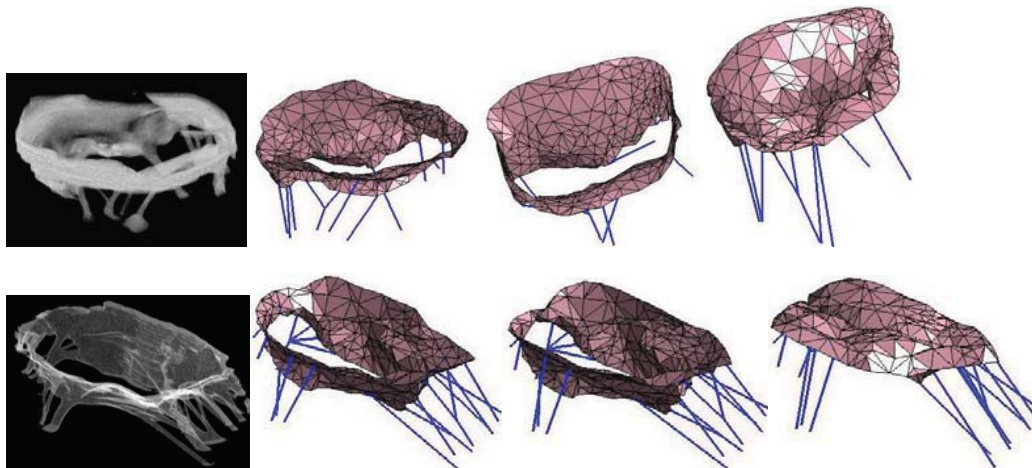


Figure 4 Four stages of the modeling and simulation process are shown above for two different datasets (top and bottom rows). Panels, from left to right, show (1) CT scan of open mitral valve, (2) mesh of open valve, (3) mesh of open valve with annulus and chord attachment points moved to their positions from image of closed valve, and (4) mesh following simulation of valve closure.

To quantitatively compare the closed state predicted by the model to the closed state generated from the image of the closed valve, the two surfaces were co-registered, again using the iterative closest point method based on vertices lying on the valve annuli. The error in the closed state predicted by the model is estimated by computing the magnitude of the distance between points on the closed image and their nearest points on the closed model. This distance is mapped to color and is plotted in Figure 5, with the error map on the left and right corresponding to the data sets in the top and bottom rows of Figure 4. The mean error across the surface was 1.7 mm for the error map on the left and 1.1 mm for the error map on the right. Maximum error was about 4 mm for both error maps.

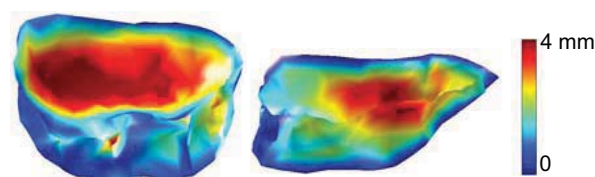


Figure 5 Error between the closed state of the valve simulated by the model and the mesh produced directly from the image of closed valve. Image on the left/right corresponds to the valve shown in top/bottom row of Figure 4. Error, in millimeters, is mapped to color.

The sensitivity of model results to changes in several important model parameters was evaluated. We define sensitivity, S , as:

$$S = \left. \frac{\partial Y}{\partial X} \right|_{X_0} \quad (9)$$

where Y is the measure of model accuracy, X is a parameter being tested, and X_0 is the value of that parameter used for our simulations and listed in Table 1. For Y , we use the mean error across the model surface. We approximate (9) as $\Delta Y / \Delta X$ by increasing parameter X by 10%, repeating a simulation, and computing the resulting change in Y . Sensitivity to the constitutive properties of the leaflets is shown in Table 2.

Table 2. Sensitivity to parameters.

Parameter	Sensitivity
E_{pre}	-0.00349 mm/kPa
E_{post}	2.13×10^{-7} mm/kPa
ϵ^*	-0.0221 mm/%

4 Discussion

The goal of this study was to develop a simplified model of mitral valve mechanics specifically for use in surgical planning. There are three main requirements for the model. First, the model must represent the geometry of the valve structures in sufficient detail to allow patient-specific simulation. Second, the model must be able to simulate valve closure quickly and robustly. The third requirement concerns accuracy. Each of these requirements will be discussed below.

To produce models capable of conveying patient-specific anatomical detail, we produced dense meshes directly from images. Our imaging method provided high resolution and contrast and enabled us to acquire images under carefully controlled loading conditions. Micro-CT scans cannot be used to acquire images in the clinical setting because of the small bore diameter, and a patient's heart cannot be statically loaded for imaging. However, flat-panel volume CT can be used to image a human heart *in vivo* with similar resolution to our data [10]. Cardiac gating allows images to be captured at any point in the cardiac cycle, obviating the need for static loading.

Our mitral valve models were able to simulate one closing cycle in approximately 5 minutes, and significant speed gains can likely be made by implementing some of the bottleneck sections of the program in the C programming language. Further gains could be made by taking advantage of multiple CPU's or by using the GPU [19]. Simulations proved to be very robust. They were stable for all meshes that were tested, and stability was not affected by the quality of triangles in the mesh.

In choosing mass-spring modeling over finite element approaches, we have deliberately traded off some accuracy in the interest of speed and robustness. Finite element methods are based on continuum mechanics and can rigorously handle the anisotropy and nonlinearity that are known to characterize valve biomechanics [17]. Furthermore, they provide detailed analysis of stresses throughout the structures under load. However, our accuracy goals are more modest. At present, the surgeon hopes simply to create a mitral valve repair geometry that closes completely at peak load; our model is presented as a tool that could better inform surgeons as they try to understand the relationship between the geometry of the opened valve and its closed state. Analysis of stress concentrations throughout the leaflets is beyond the capability of the type of model presented here.

The model is able to predict many features of the closed state accurately and estimates the actual position of the closed leaflets with mean errors of 1.7 mm or less. By quantifying and plotting the error in the closed state predicted by the model, we can clearly see in which regions the model succeeds or fails to capture the actual behavior. For both mitral valves that we modeled, the maximum error of approximately 4 mm occurred in the middle of the leaflets. Two factors probably contribute to this error. First, by representing the mitral valve leaflets as isotropic, we neglect its strong orthotropic behavior, which is likely to play a role in determining leaflet shape. Second, for chords that attach to the free edge of a leaflet, we attach them at a single point on the edge, while, in reality, the chord inserts into the leaflet over a long overlapping region and imparts high stiffness to that leaflet in the direction of the chord.

The limited sensitivity analysis that we performed demonstrates that the accuracy of the model in predicting the closed state of the leaflets is not highly sensitive to the choice of leaflet properties. For example, a 1 kPa increase in the pre-transitional Young's modulus for the leaflets results in a decrease in model error of less than 1/100th of a millimeter. It is desirable for our model to be relatively insensitive to leaflet properties because it indicates that we could have used any physiological values for leaflet properties (which are known to exhibit a large variance [14]) without significantly affecting our results.

It is important to note that closure of the valve leaflets is not the only metric of valve function, and hence quality of potential repair. One might also consider stress levels in the leaflets, a metric important for long-term durability of the valve. However, accurate simulation of the closed state is a good first-order criterion for valve function.

5 Conclusions

Our method of simulating closure of the mitral valve meets the requirements of surgical planning for valve repair. Simulations are fast and robust, and patient-specific models can be derived directly from images. Results are in reasonable agreement with images of the loaded valve. The relationship among the full set of model parameters need to be better understood, and the effect of changing the mesh density on speed and accuracy needs further investigation.

References

- [1] Baraff, D. and Witkin, A. "Large steps in cloth simulation," *Computer Graphics*, 43-54 (1998).
- [2] Barrett, R., Berry, M., Chan, T.F., Demmel, J., Donato, J., Dongarra, J., Eijkhout, V., Pozo, R., Romine, C., Van der Vorst, H. [Templates for the Solution of Linear Systems: Building Blocks for Iterative Methods, 2nd Edition], SIAM, Philadelphia, PA (1994).
- [3] Choi, K.J. and Ko, H.S. "Stable but responsive cloth," *ACM Trans Graphics*, 21(3), 604-611 (2002).
- [4] Clark R. "Stress-strain characteristics of fresh and frozen human aortic and mitral leaflets and chordae tendinae. Implications for clinical use," *J Thorac Cardiovasc Surg*; 66:202-208 (1973).
- [5] Cohen LM. [Cardiac surgery in the adult, 3rd edition.] McGraw Hill (2007).
- [6] Einstein, D.R., Kunzelman, K.S., Reinhall, P.G., Nicosia, M.A., Cochran, R.P. "Non-linear fluid-coupled computational model of the mitral valve," *J Heart Valve Dis*, 14, 376-385 (2005).
- [7] Fedak PWM, McCarthy PM, Bonow RO. "Evolving concepts and technologies in mitral valve repair," *Circulation*; 117: 963-974 (2008).
- [8] Gammie, J.S., O'Brien, S.M., Griffith, B.P., Ferguson, T.B., Peterson, E.D. "Influence of hospital procedural volume on care process and mortality for patients undergoing elective surgery for mitral regurgitation," *Circ*, 115, 881-887 (2007).
- [9] Goldman, M.E., Mora, F., Guarino, T., Fuster, V., Mindich, B.P. "Mitral valvuloplasty is superior to valve replacement for preservation of left ventricular function: an intraoperative two-dimensional echocardiographic study," *J Am Coll Cardiol*, 10, 568-575 (1987).
- [10] Gupta, R., Grasruck, M., Suess, C., Bartling, S.H., Schmidt, B., Stierstorfer, K., Popescu, S., Brady, T., Flohr, T. "Ultra-high resolution flat-panel volume CT: fundamental principles, design architecture, and system characterization," *Eur Radiol*, 16, 1191-1205 (2006).
- [11] Kunzelman, K.S., Cochran, R.P., Chuong, C., Ring, W.S., Verrier, E.D., Eberhart, R.D. "Finite element analysis of the mitral valve," *J Heart Valve Dis*, 2, 326-340 (1993).
- [12] Lim, K.H., Yeo, J.H., Duran, C.M. "Three-dimensional asymmetrical modeling of the mitral valve: a finite element study with dynamic boundaries," *J Heart Valve Dis*, 14, 386-392 (2005).
- [13] Logan D. [A first course in the finite element method, third edition]. Brooks/Cole, Pacific Grove, CA 2002, p. 38 (2002).
- [14] May-Newman K and Yin FCP. "Biaxial mechanical behavior of excised porcine mitral valve leaflets," *Am J Physiol*, 269: H1319-H1327 (1995).
- [15] Moss, R.R., Humphries, K.H., Gao, M., Thompson, C.R., Abel, J.G., Fradet, G., Munt, B.I. "Outcome of mitral valve repair or replacement: a comparison by propensity score analysis," *Circ*, 108 suppl II, II90-II97 (2003).
- [16] Ng, H.N. and Grimsdale, R.L. "Computer Graphics Techniques for Modeling Cloth," *IEEE Computer Graphics and Applications*, 16(5), 28-41 (1996).

- [17] Sacks, M.S., Enomoto, Y., Graybill, J.R., Merryman, W.D., Zeeshan, A., Yoganathan, A.P., Levy, R.J., Gorman, R.C., Gorman, J.H. "In-vivo dynamic deformation of the mitral valve anterior leaflet," *AnnThorac Surg*, 82, 1369-1378 (2006).
- [18] Savage EB, Ferguson TB Jr, DiSesa VJ. "Use of mitral valve repair: analysis of contemporary United States experience reported to the Society of Thoracic Surgeons National Cardiac Database," *Ann Thorac Surg*, 75: 820-825 (2003).
- [19] Taylor ZA Cheng M, Ourselin S. "Real-time nonlinear finite element analysis for surgical simulation using graphics processing units," *MICCAI*; 10(Pt 1):701-708 (2007).
- [20] Tischler, M.D., Cooper, K.A., Rowen, M., LeWinter, M.M. "Mitral valve replacement versus mitral valve repair: a Doppler and quantitative stress echocardiographic study," *Circulation*, 89, 132–137 (1994).
- [21] Turi ZG. "Mitral valve disease," *Circulation*; 109(6):e38-41 (2004).
- [22] Van Gelder A. "Approximate simulation of elastic membranes by triangulated spring meshes," *Journal of Graphics Tools*; 3(2):21-42 (1998).
- [23] Votta, E., Maisano, F., Bolling, S.F., Alfieri, O., Montevicchi, F.M., Redaelli, A. "The Geofrom disease-specific annuloplasty system: A finite element study," *Ann Thorac Surg*, 84, 92–102 (2007).
- [24] Zhang, Z.Y. "Iterative point matching for registration of free-form curves and surfaces," *IJCV*;13(2):119-152 (1994).

Multimodal Registration of White Matter Brain Data via Optimal Mass Transport

Tauseef ur Rehman¹, Eldad Haber², Kilian M. Pohl³, Steven Haker³, Mike Halle³, Florin Talos³, Lawrence L. Wald⁴, Ron Kikinis³ and Allen Tannenbaum¹

June 3, 2008

¹Schools of Electrical & Computer and Biomedical Engg., Georgia Institute of Technology, Atlanta, GA.

²Department of Mathematics and Computer Science, Emory University, Atlanta, GA.

³Surgical Planning Laboratory, Department of Radiology, Brigham & Women's Hospital, Harvard Medical School, Boston, MA.

⁴Martinos Center, Department of Radiology, Massachusetts General Hospital, Harvard Medical School, Charlestown, MA.

tauseef, tannenba@ece.gatech.edu, haber@mathcs.emory.edu, pohl@csail.mit.edu, kikinis@bwh.harvard.edu

Abstract

The elastic registration of medical scans from different acquisition sequences is becoming an important topic for many research labs that would like to continue the post-processing of medical scans acquired via the new generation of high-field-strength scanners. In this note, we present a parameter-free registration algorithm that is well suited for this scenario as it requires no tuning to specific acquisition sequences. The algorithm encompasses a new numerical scheme for computing elastic registration maps based on the minimizing flow approach to optimal mass transport. The approach utilizes all of the gray-scale data in both images, and the optimal mapping from image A to image B is the inverse of the optimal mapping from B to A . Further, no landmarks need to be specified, and the minimizer of the distance functional involved is unique. We apply the algorithm to register the white matter folds of two different scans and use the results to parcellate the cortex of the target image. To the best of our knowledge, this is the first time that the optimal mass transport function has been applied to register large 3D multimodal data sets.

1 Introduction

Registration is an important pre-processing step for many automatic approaches that extract cortical structures from Magnetic Resonance Images (MRI) [9, 22, 11]. Common approaches for aligning the atlas of the segmenter to the patient MRI are based on the B-spline representation [11, 19] and continuum and fluid mechanics, [7, 15, 6, 21]. The accuracy of these approaches generally depends on how well they are tuned to the sequence of patient scan. Tuning these algorithms often requires expertise about the underlying algorithm. Clinicians scanning with new acquisition sequences are therefore often concerned on how to post-process these scans. In this paper, we propose a parameter-free algorithm for the registration of MRIs.

We model the registration of images as an optimal mass transport problem. Introduced by Monge and Kantorovich [13], the solution to the problem is an optimal mapping \hat{u} (in some sense) between two densities $\mu_0 > 0$ and $\mu_1 > 0$. If we now define d as the dimension of the image domain, $\det(\cdot)$ as the determinant, u as a mapping from $\Omega \rightarrow \Omega$ with Ω a subdomain of \mathbb{R}^d , and represent by $\rho(\cdot, \cdot) : \Omega \times \Omega \rightarrow \mathbb{R}^+$ a distance function between two points in Ω , then the problem can be formalized as

$$\hat{u} \triangleq \min_{u \in \mathcal{U}} \frac{1}{2} \int_{\Omega^d} \mu_0(x) \rho(u(x), x) dx, \quad (1.1)$$

where $\mathcal{U} = \{u : \Omega \rightarrow \Omega \mid c(u) = \det(\nabla u) \mu_1(u) - \mu_0 = 0\}$.

We refer to the constraint $c(u) = 0$ as the *mass preserving* (MP) property.

For the remainder of this note, we take $\rho(\cdot, \cdot)$ to be the squared distance function $\rho(u(x), x) \triangleq \|u(x) - x\|^2$. Even for the simple L^2 -norm, (1.1) defines a highly non-linear optimization problem. While there exists a large body of literature which deals with the analysis of the problem, such as [1, 8], only a smaller number of papers discuss efficient *numerical* solutions for the problem. Benamou and Brenier [5] estimate \hat{u} by relating Equation (1.1) to the minimization of a certain kinetic energy functional with a space-time transport partial differential equation (PDE) constraint. Their approach not only estimates the optimal mapping but also provides the transportation path between the densities. A computationally faster solution to (1.1) was proposed by Angenent et al. [3]. Their algorithm directly estimates \hat{u} by first computing a transformation u_0 that fulfills the MP property. Afterwards, the algorithm improves u_0 by concatenating the mapping with the transformation,

$$\hat{s} \triangleq \min_{s \in \mathcal{S}} \frac{1}{2} \int_{\Omega^d} \mu_0(x) (u_0(s^{-1}(x)) - x)^2 dx, \quad (1.2)$$

where $\mathcal{S} = \{s : \Omega \rightarrow \Omega \mid \tilde{c}(s) = \det(\nabla s) \mu_0(s) - \mu_0 = 0\}$.

We refer to the second equation in (1.2) as the \tilde{c} constraint. This means that $s \in \mathcal{S}$ is an MP mapping from μ_0 to itself. The authors in [3] show that \hat{s} can be estimated via a steepest descent flow. To register 2D MRIs, they implement the method using forward Euler equation scheme for time stepping and a simple finite difference discretization of the spatial derivatives. The approach, however, does not enforce the MP constraint at each step of the numerical algorithm, so that the final solution generally does not fulfill the MP property. In addition, steepest descent is very slow in estimating the solution to Equation (1.2). For these reasons it would be very challenging to efficiently register 3D medical images with this approach. To overcome this hurdle, this paper describes a faster numerical solution to Equation (1.2) that enforces the MP constraint.

Unlike [3], we solve the optimization problem via an approach where we choose a direction other than steepest descent and show that it converges faster (see Section 2). Furthermore, we derive a numerical approach that uses a consistent conservative discretization method and enforces the MP constraint at each update of the solution (Section 3). In Section 4, we test the robustness of our approach by registering the white matter folds of two MRIs. The first MRI scan is part of a publicly available atlas [14] with detailed anatomical information about the scan. The second scan was acquired using a very different scanning protocol. Our approach accurately aligns the two scans. We then use the aligned atlas to outline the cortical folds in the new scan.

We end this section with the comment that our approach most closely relates to those registration approaches based on fluid mechanics. The optimal warping map of the L^2 Monge-Kantorovich equation may be regarded as the velocity vector field which minimizes a standard energy integral subject an Euler continuity equation constraint [5]. In particular, in the fluid mechanics framework, this means that the optimal Monge-Kantorovich solution is given as a *potential flow*.

2 Obtaining the descent direction

We now quickly review the derivation presented in [12] but within a variational framework. Assuming that the MP constraint condition is valid, we take a perturbation in s which stays on the MP constrained manifold. This leads to

$$\begin{aligned} 0 &= c(s + \delta s) - c(s) = \det(\nabla(s + \delta s))\mu_0(s + \delta s) - \det(\nabla s)\mu_0(s) \\ &= \det(\nabla s) (\nabla \cdot (\delta s(s^{-1}))(s))\mu_0(s) + \det(\nabla s) \nabla \mu_0(s) \cdot \delta s. \end{aligned}$$

This expression can be simplified as long as the constraint is valid. Since $\det(\nabla u) > 0$ we can divide, and rearranging we have

$$\begin{aligned} 0 &= (\mu_0 \nabla \cdot (\delta s(s^{-1}))) (s) + \nabla \mu_0(s) \cdot \delta s \\ &= \mu_0 \nabla \cdot (\delta s(s^{-1})) + \nabla \mu_0 \cdot \delta s(s^{-1}) = \nabla \cdot (\mu_0 \delta s(s^{-1})). \end{aligned}$$

Defining $\delta \zeta = \mu_0 \delta s(s^{-1})$, we see that $\nabla \cdot \delta \zeta = 0$. Next, looking at $u = u_0(s^{-1})$, we can write $u(s) = u_0$ which implies that,

$$(\nabla u(s))\delta s + \delta u(s) = 0 \Rightarrow \delta u = -(\nabla u)\delta s(s^{-1}).$$

Using the definition of $\delta \zeta$ we obtain that as long as the constraint is valid and that $u(s) = u_0$ we have

$$\delta u = -\mu_0^{-1}(\nabla u)\delta \zeta, \quad (2.3a)$$

$$0 = \nabla \cdot \delta \zeta. \quad (2.3b)$$

Let M be defined as the objective function in (1.2) then it can be shown that

$$\delta M = \int_{\Omega} u \cdot \delta \zeta dx. \quad (2.4)$$

In the the original paper [12], it is suggested to use the Helmholtz decomposition in order to obtain a descent direction. Here we employ a different approach. First, we note that the divergence constraint can be eliminated by selecting $\delta \zeta = \nabla \times \delta \eta$, and thus to reduce M we need to obtain a direction that yields a negative δM , that is we seek a direction, $\delta \eta$ such that $\delta M = \int_{\Omega} u \cdot \nabla \times \delta \eta dx < 0$. Using the Gauss theorem, we obtain that

$$\int_{\Omega} u \cdot \nabla \times \delta \eta dx = \int_{\Omega} \nabla \times u \cdot \delta \eta dx + \int_{\partial \Omega} (u \cdot (\delta \eta \times \vec{n})) dx$$

and therefore the steepest descent direction is given by

$$\delta\eta = \nabla \times u, \quad \delta\eta \in \Omega; \quad \delta\eta \times \vec{n} = 0, \quad \delta\eta \in \partial\Omega$$

which leads to the update $\delta\zeta = \nabla \times \nabla \times u$, and finally to the steepest descent direction in u $\delta u = -\frac{1}{\mu_0}(\nabla u)\nabla \times \nabla \times u$ or, in symmetric form

$$\mu_0(\nabla u)^{-1}\delta u = -\nabla \times \nabla \times u. \quad (2.5)$$

The operator $-\nabla \times \nabla \times$ is negative and elliptic thus, the equation can be thought of as a parabolic PDE as long as real part of the eigenvalues of ∇u are positive. Using the above decomposition a family of different directions may be obtained. Note that in order to reduce the objective $\int_{\Omega} \nabla \times u \cdot \eta \, dx$ any vector field of the form $\delta\eta = A\nabla \times u$ can be used where A is a symmetric positive definite matrix. For example, a choice that leads to a similar method to the one derived in the original paper [12] in 2D is $A = -\Delta^{-1}$, which leads to the update

$$\mu_0(\nabla u)^{-1}\delta u = \nabla \times \Delta^{-1}\nabla \times u. \quad (2.6)$$

Using the above calculation it is easy to see that the flow (2.6) is valid also in 3D. Moreover, it is easy to verify that given a smooth u the second formulation (2.6) leads to a more stable method that should converge faster compared with the first formulation (2.5), because the operator $\nabla \times \Delta^{-1}\nabla \times$ is compact while the $\nabla \times \nabla \times$ operator is unbounded. In this work, we therefore derive a numerical method for (2.6) rather than for (2.5).

3 Deriving an efficient numerical method

In this section, we derive an efficient numerical method for the solution of the flow. The proposed method has three main components: a conservative discretization of differential operators, a criterion to choose step size, and a method to correct steps that deviate from the mass preservation constraint.

3.1 Conservative discretization

The applications we have in mind derive from medical imaging where images are discretized on a regular grid. We therefore construct our discretization based on a finite volume/difference approach. To derive and analyze our discretization we introduce a new variable $\delta p = \Delta^{-1}\nabla \times u$ and rewrite (2.6) as

$$\begin{pmatrix} \mu_0(\nabla u)^{-1} & \nabla \times \\ 0 & \Delta \end{pmatrix} \begin{pmatrix} \delta u \\ \delta p \end{pmatrix} = \begin{pmatrix} 0 \\ \nabla \times u \end{pmatrix}. \quad (3.7)$$

In order for the discrete system to be well posed we need consistent discretizations for Δ , ∇u and $\nabla \times u$. There are a number of possible discretizations that lead to a well-posed system.

We divide Ω into $n_1 \times \dots \times n_d$ cells, each of size $h_1 \times \dots \times h_d$ where d is the dimension of the problem. We discretize all the components of u at the nodes of each cell to obtain d grid functions $\hat{u}^1, \dots, \hat{u}^d$. Since δp is connected to u by the curl operator, we employ a staggered grid and place δp at cell centers. To approximate ∇u at each node, we use long differences. Thus, in 3D, the discretized (1,1) block in (3.7) is a matrix of the form

$$(\nabla_h \hat{u}) = \frac{1}{h} \begin{pmatrix} \text{diag}(D_1 \hat{u}^1) & \text{diag}(D_2 \hat{u}^1) & \text{diag}(D_3 \hat{u}^1) \\ \text{diag}(D_1 \hat{u}^2) & \text{diag}(D_2 \hat{u}^2) & \text{diag}(D_3 \hat{u}^2) \\ \text{diag}(D_1 \hat{u}^3) & \text{diag}(D_2 \hat{u}^3) & \text{diag}(D_3 \hat{u}^3) \end{pmatrix}, \quad (3.8)$$

where D_j is a matrix of long differences in the j^{th} direction. To obtain a consistent discretization of the Laplacian we use a standard discretization (5 point stencil in 2D and 7 point stencil in 3D) with Dirichlet boundary conditions. Finally, we employ short differences in one direction averaged in the other direction to obtain a cell centered approximation of $\nabla \times u$.

3.2 Computation of a step

The computation of each step requires two parts. Firstly, the solution of (3.7) and secondly, a way to determine if it is an acceptable step. The solution of the system (3.7) is straightforward. Any fast Poisson solver can be used for the task. Here we have used a standard multigrid method with weighted Jacobi smoothing, bilinear prolongation and its adjoint as a restriction.

The validity of the update is determined using the following procedure. Assume that at iteration n we have \hat{u}_n as an approximation to u and that we computed $\delta\hat{u}$. The update is then performed using,

$$\hat{u}_{n+1} = \mathcal{P}(\hat{u}_n + \alpha\delta\hat{u}), \quad (3.9)$$

where \mathcal{P} is an orthogonal projection discussed in Section 3.3 below, that projects $\hat{u}_n + \alpha\delta\hat{u}$ into the mass preserving manifold. The step size α is then chosen such that the objective function is decreased and that the real part of the eigenvalues of $(\nabla_h \hat{u})$ is positive. The whole algorithm is outlined Algorithm 1.

Algorithm 1 Solution of OMT:

$\hat{u} \leftarrow \text{OMTsol}(\mu_0, \mu_1);$

Use μ_0 and μ_1 to compute a mass preserving u_0

while true do

Solve (3.7) for $\delta\hat{u}$

line search: set $\alpha = 1$

while true do

$\hat{u}_{n+1} = \mathcal{P}(\hat{u}_n + \alpha\delta\hat{u})$

if $\|\hat{u}_{n+1} - x\|_{\mu_0} < \|\hat{u}_n - x\|_{\mu_0}$ and $\text{Re}(\lambda(\nabla_h u_{n+1})) > 0$ **then**

Break

end if

$\alpha \leftarrow \alpha/2$

end while

end while

3.3 Orthogonal projection into the mass preserving constraint

Assume that we have computed a mass preserving mapping \hat{u}_n , and that we have updated it to obtain $v_n = \hat{u}_n + \alpha\delta\hat{u}$. It should be noted that an infinitesimal $\delta\hat{u}$ does not guarantee mass preservation. Furthermore, we aim to take large steps in $\delta\hat{u}$, and therefore the MP constraint is likely to be invalid. To correct for this we use orthogonal projections. The goal is to compute a vector field δv such that $c(v + \delta v) = 0$. Obviously, δv is non-unique and therefore we seek a minimum norm solution that is we seek δv such that

$$\min_v \frac{1}{2} \|\delta v\|_{\mu_0}^2 \quad \text{subject to} \quad c(\delta v) = \mu_0(v + \delta v) \det(\nabla(v + \delta v)) - \mu_1 = 0.$$

It is easy to verify that a correction for δv can be obtained by solving the system $\delta v \approx c_v^\top (c_v c_v^\top)^{-1} c(v)$. The system $c_v c_v^\top$ can be thought as an elliptic system of equations. The system is solved using preconditioned conjugate gradient with an incomplete Cholesky preconditioner.

4 Registration of Brain Data

Our goal is the identification of cortical structures by mapping a publicly available atlas[14] to the scan of a patient. In our scenario, the scanning sequence of the atlas is very different from the one of the patient. The MRI of the atlas is a spoiled gradient recalled image acquired on a 1.5-Tesla General Electric Signa System (GE Medical Systems, Milwaukee) with $256 \times 256 \times 124$ voxels and voxel dimension of $0.92 \times 0.92 \times 1.5$ mm. The patient scan is a MPRAGE acquired on a Siemens 3T long bore machine using a 8 channel head coil. The resolution of the scan is $256 \times 256 \times 144$ with voxel dimension $0.54 \times 0.54 \times 1.0$ mm (See Figure 1(b)).

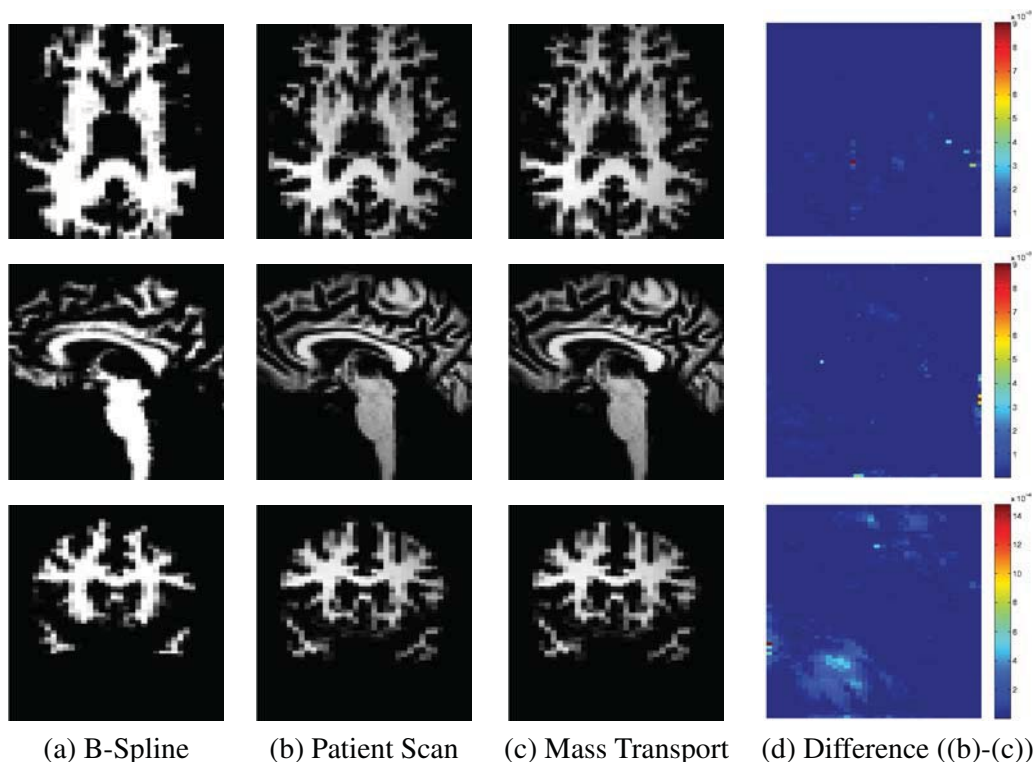


Figure 1: Registration results.

The parcellation of the cortex can be encoded by partitioning the boundary between cortex and white matter into anatomical regions [9]. The label map of cortical structures can then be inferred from this partition by propagating the labeling along the boundary to the entire cortex. The pipeline described below will apply this concept for the parcellation of the cortex to the high resolution scan.

The input of the pipeline consist of the atlas, the high resolution scan as well as a segmentation of the scan into the major tissue classes. In the first step, we coarsely align the atlas to the image data using the B-spline implementation by Rohlfinger[19] with a final spacing of the grid nodes of 2.5 mm. This results in a coarse alignment of the scans. The algorithm has difficulties in mapping the folds of the white matter due to the inherent constraints of the B-spline representation. We then reduce the atlas to the white matter including the parcellation of the cortex along the boundary between gray and white matter (see Figure 1(a)). Afterwards, we refine the alignment of this new atlas to the white matter of the high resolution scan using our Optimal Mass Transport registration approach. Registration using Optimal Mass Transport is a highly flexible approach that is, unlike B-Splines, not constrained to a set of control points. The intensities in the two input datasets are first normalized and rescaled to make sure that both have the same total mass. The

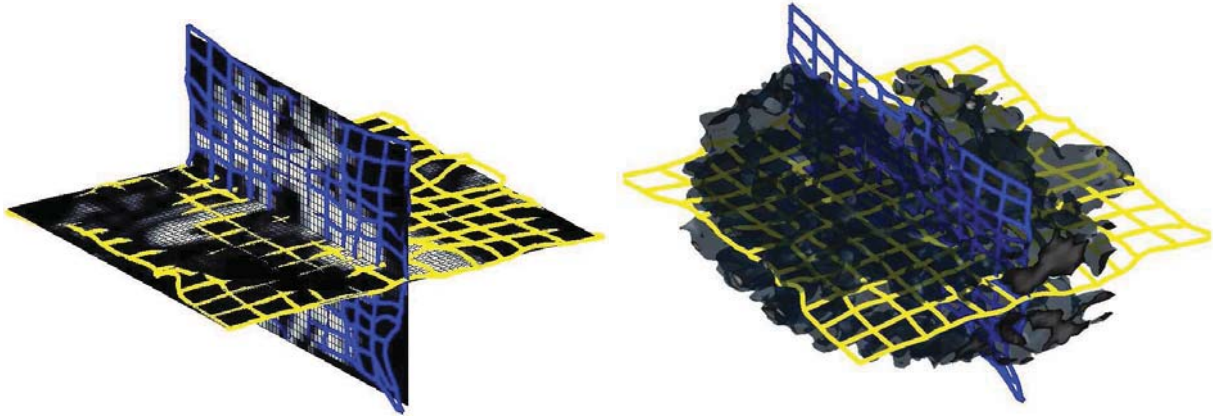


Figure 2: Deformed Grid on white matter Slices (left) and 3D volume (right).

white matter registration with the proposed algorithm took just 12 iterations to converge with 2 iterations of the projection to constraint per iteration. This is a huge improvement over algorithm proposed in [12] where thousands of iterations were required for convergence with roughly the same computational complexity per iteration. The $\nabla \times u$ (convergence metric) was reduced to an order of 10^{-3} indicating an optimal map. Figure 1(c) shows the resampled images with 3D views of the corresponding deformation grid in Figure 2. The difference (Figure 1(d)) between target (Figure 1(b)) and resampled image indicates that our approach accurately aligned the folds. After this local alignment, the folds of the atlas should perfectly align with

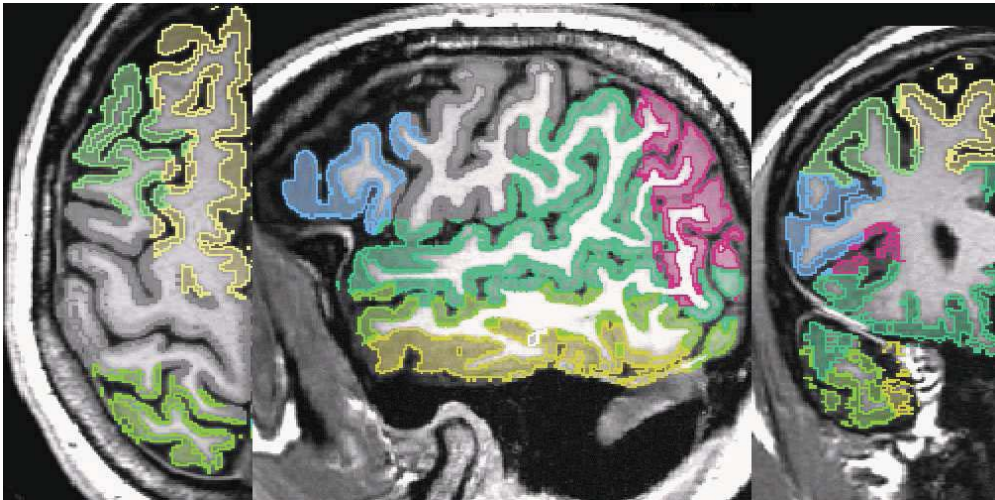


Figure 3: Parcellation results

the ones of the high resolution scan. The parcellation of the folds of the atlas, therefore, also encodes the parcellation of the same region in the high resolution scan. We then complete the cortex parcellation of the high resolution scan by confining the Voronoi diagram of the aligned atlas to the gray matter mask of the high resolution scan. The results in Figure 3 show the corresponding segmentation when applying the deformation map of the B-Spline registration and our approach to the the label map of [14], and propagating the labels to the cortex via the Voronoi diagram.

We are aware of the variety of other methods for registering and segmenting cortical structures. We also note that our segmentation results are by no means perfect. However, to the best of our knowledge, this

is the first time in medical imaging that a parameter-free registration tool has been used for registering the cortical folds of 3D MRIs.

5 Conclusions

The difficulties of aligning cortical folds is reflected by the large body of literature discussing this topic. Registration approaches based on continuum and fluid mechanics are often applied to this problem. However, the accuracy of these approaches generally depends on how well they are tuned to the sequence of patient scan. We view Optimal Mass Transport (OMT) as part of these types of registration approaches. Unlike the current state of the art, OMT is parameter free. It is, therefore, especially suited to align new acquisition sequences, which the other methods have not yet been tuned to.

In this paper we presented an efficient variational methodology for the computation of the optimal L^2 mass transport mapping based on the formulation of [12]. Although, the theory was rigorous in [12], the proposed numerics were problematic. All of these problems have been addressed in our approach. This has led to an efficient robust elastic deformation algorithm which is guaranteed to converge to the optimal solution of the Monge-Kantorovich problem. We applied the approach to register the white matter between two MRI datasets. We then use the results to resample the label map of the source providing us with a parcellation of the cortex of the target image. We note that the approach is applicable to a whole range of registration and image morphing problems where the mass preservation constraint makes sense. Based on deriving this numerical framework, we are quite sure that in the near future we will be able to provide cases in which we show superior performance to other well established tools in the community. Finally, the set-up can be extended directly to optimal transport on a manifold as in [4].

Acknowledgements

This work was supported in part by grants from NSF, AFOSR, ARO, MURI, as well as by a grant from NIH (NAC P41 RR-13218) through Brigham and Women's Hospital. This work is part of the National Alliance for Medical Image Computing (NAMIC), funded by the National Institutes of Health through the NIH Roadmap for Medical Research, Grant U54 EB005149. Information on the National Centers for Biomedical Computing can be obtained from <http://nihroadmap.nih.gov/bioinformatics>. Tannenbaum was also supported by a Marie Curie Grant through the Technion, Israel Institute of Technology.

References

- [1] L. Ambrosio, "Lecture Notes on Optimal Transport Problems," Lectures given at Euro Summer School, July 2000. Available on <http://cvgmt.sns.it/papers/amb00a/>.
- [2] S. Angenent, S. Haker, R. Kikinis, A. Tannenbaum, "Laplace-Beltrami operator and brain surface flattening," *IEEE Trans. on Medical Imaging*, 18:700-711, 1999.
- [3] S. Angenent, S. Haker, and A. Tannenbaum, "Minimizing flows for the Monge-Kantorovich problem," *SIAM J. Math. Anal.*, 35:61-97, 2003.
- [4] A. Dominitz, S. Angenent, and A. Tannenbaum, "On the computation of optimal transport maps using gradient flows and multiresolution analysis," in *Recent Advances in Learning and Control* edited by V. Blondel, S. Boyd, and H. Kimura, Springer-Verlag, New York, 2008.

- [5] J. D. Benamou and Y. Brenier, "A computational fluid mechanics solution to the Monge-Kantorovich mass transfer problem," *SIAM J. Math. Anal.*, 35:61–97, 2003.
- [6] M. Bro-Nielsen and C. Gramkow, "Fast fluid registration of medical images," in *Visualization in Biomedical Imaging* edited by K. Höhne and R. Kikinis, Lecture Notes in Computer Science **1131**, pp. 267-276, Springer-Verlag, New York, 1996.
- [7] G. E. Christensen, R. D. Rabbit, M. Miller, "Deformable templates using large deformation kinetics," *IEEE Trans. on Image Processing* **5** (1996), pp. 1435-1447.
- [8] L. C. Evans, *Partial Differential Equations and Monge-Kantorovich Transfer*. Lecture Notes, 1989.
- [9] B. Fischler *et al.*, "Automatically Parcellating the Human Cerebral Cortex," *Cerebral Cortex*, 14(11):11-22, 2004.
- [10] A. Guimond, A. Roche, N. Ayache, and J. Meunier, "Three-dimensional multimodal brain warping using the demons algorithm and adaptive intensity corrections," *IEEE TMI*, 20(1):58–69, 2001.
- [11] R. A. Heckemann, J. Hajnal, P. Aljabar, D. Rueckert, and A. Hammers, "Automatic anatomical brain MRI segmentation combining label propagation and decision fusion," *NeuroImage*, 33(1):115–126, 2006.
- [12] S. Haker, L. Zhu, A. Tannenbaum, and S. Angenent, "Optimal mass transport for registration and warping," *Int. Jour. Computer Vision*, 60(3):225–240, 2004.
- [13] L. Kantorovich, "On a problem of Monge," *Uspekhi. Mat. Nauk.*, 3:225–226, 1948.
- [14] R. Kikinis *et al.*, "A digital brain atlas for surgical planning, model-driven segmentation, and teaching," *IEEE Trans. on Vis. and Comp. Graph.*, 2(3):232-241, 1996.
- [15] M. Miller, G. Christensen, Y. Amit, U. Grenander, "Mathematical textbook of deformable neuroanatomies," *Proc. Nat. Acad. of Science* **90**, pp. 11944-11948.
- [16] K. Pohl, S. Bouix, R. Kikinis, and W. Grimson, "Anatomical guided segmentation with non-stationary tissue class distributions in an expectation-maximization framework," *IEEE ISBI*, 81–84, 2004.
- [17] J. Nocedal and S. Wright, *Numerical Optimization*, Springer, New York, 1999.
- [18] S. Rachev and L. Rüschendorf, *Mass Transportation Problems*, Volumes I and II, Probability and Its Applications, Springer, New York, 1998.
- [19] T. Rohlfing and C. R. Maurer, Jr., "Nonrigid image registration in shared-memory multiprocessor environments with application to brains, breasts, and bees," *IEEE Trans. on Inf. Techn. in Biomed.*, vol. 7, no. 1, pp. 16–25, 2003.
- [20] Y. Rubner, C. Tomasi, and J. Guibas, "The earth mover's distance as a metric for image retrieval," Technical Report STAN-CS-TN-98-86, Department of Computer Science, Stanford University, September 1998.
- [21] J.-P. Thirion, "Fast non-rigid matching of non-rigid images," *INRIA Technical Report 2547*, Project Epidaure, INRIA, France, 1995.
- [22] A. Toga, *Brain Warping*, Academic Press, San Diego, 1999.

Cardiac Motion Recovery by Coupling an Electromechanical Model and Cine-MRI Data: First Steps

Florence Billet¹, Maxime Sermesant¹, Hervé Delingette¹, and Nicholas Ayache¹

August 4, 2008

¹ INRIA, Asclepios Team, Sophia-Antipolis, France. Corresponding author: Florence.Billet@inria.fr

Abstract

We present a framework for cardiac motion recovery using the adjustment of an electromechanical model of the heart to cine Magnetic Resonance Images (MRI). This approach is based on a constrained minimisation of an energy coupling the model and the data. Our method can be seen as a data assimilation of a dynamic system that allows us to weight appropriately the confidence in the model and the confidence in the data. After a short overview of the electromechanical model of the ventricles, we describe the processing of cine MR images and the methodology for motion recovery. Then, we compare this method to the methodology used in data assimilation. Presented results on motion recovery from given cine-MRI are very promising. In particular, we show that our coupling approach allows us to recover some tangential component of the ventricles motion which cannot be obtained from classical geometrical tracking approaches due to the aperture problem.

1 Introduction

The modelling of the heart's electromechanical activity is an active research area [5, 9, 1, 13, 4]. The simulation of the heart has received growing attention due to the importance of cardiovascular diseases in industrialised nations and to the high complexity of the cardiac function.

In order to help the clinical practice of cardiologists, it is important however that those models not only describe with some degree of realism the cardiac function but also be patient specific. Creating such personalised cardiac models implies that the anatomy of the patient is taken into account but also that the model parameters are tailored such that the simulated cardiac motion matches well with the observed cardiac motion. This represents a great challenge due to the intrinsic physiological complexity of the underlying phenomena which combine tissue mechanics, fluid dynamics, electrophysiology, energetic metabolism and cardiovascular regulation. Also only partial information can be derived from clinical data for a specific patient making the parameter estimation an ill-posed problem.

The objective of this paper is to propose a methodology that aims at creating personalised electromechanical model of the heart from cine MR images. Previous work [6, 10, 8, 12] on the adjustment of a geometrical model of the heart on time series of medical images are mainly based on the concept of deformable models. In such a framework, a surface or volumetric mesh is fitted to the apparent boundaries of the heart by

minimising the sum of two energies: an image term and a regularising or internal term. In such approaches, the model can be considered as a *static system* evolving under the minimization of an energy.

Conversely, electromechanical models of the heart are *dynamic systems* that evolve even in the absence of any image term. Adjusting such dynamic systems to time series of data (a method also known as "data assimilation") is fundamentally different from adjusting a static system since the parameters of the dynamic system are additional degrees of freedom that should be estimated. In the medical imaging community, P.C Shi and his group introduced data assimilation techniques by integrating cardiac models and Kalman filters for state and parameter estimation, see for instance [16] and [18]. However, such techniques, such as extended or unscented Kalman filtering, are often limited by the curse of dimensionality since they involve full covariance matrices whose size are equal to the square of the number of state variables augmented by the number of parameters to estimate. In the case of clinical applications, as cardiac electromechanical models are already complex dynamic systems with changing boundary conditions (cardiac phases), having a computationally efficient estimation method is crucial.

In this paper, we propose an efficient method to estimate the state (*i.e.* the position and velocity) of an electromechanical model from cine MR images which is inspired from the deformable model framework used in medical image analysis. The goal of this paper is to show the formal equivalence between this approach and a filtering method introduced by Moireau et al. [7] used in data assimilation, which is different from Kalman-like filters such as the one used in [18]. The filtering approach proposed in [7] does not involve any matrix inversion (except the mass matrix which is a diagonal constant matrix), so that it allows much faster computations: the motion of a whole cardiac cycle on a mesh with 50 000 tetrahedral elements is estimated in about 10 minutes on a regular PC. This increases largely its potential future clinical application. The theoretical efficiency of this filter for mechanical systems has been demonstrated in [7]. The theoretical equivalence between the deformable model approach proposed here and this filtering approach leads to a better understanding of the trade-off between the electromechanical model and the image data.

We assume in this paper that model parameters are well known, in order to focus only on state estimation. Some preliminary results on parameter estimation are presented in conclusion, but this is not the goal of this paper. The proposed approach is first validated on synthetic time series of images and then applied to clinical cine MR images of a human heart.

2 Electromechanical model

We consider in this paper a fairly reduced electromechanical model since we want the complexity of the model to match the relatively sparse measures available from imaging data. Furthermore, this coarse level of modeling allows us to simulate a whole cardiac cycle on a mesh with 50 000 tetrahedral elements in about 5 minutes on a regular PC. Of course, the heart is a nonlinear material undergoing large strain. Thus, the assumptions of our simplified model are not realistic, but the global behavior of the heart is well represented. Furthermore, the limited computational time makes the estimation of the mechanical state and parameters tractable and allows us to test the behaviour of the model on series of heart beats.

2.1 Anatomy Description

The two ventricles are represented as a tetrahedral volumetric mesh including some anatomical information such as the myocardium geometry, the definition of some clinical anatomical regions (the American Heart Association regions), and the local orientation of fibres. We can build such a mesh from MR images, as explained below in section 3.1. The local fibre orientation can be either created from basic anatomical assumptions (elevation angle across the wall) or extracted from Diffusion Tensor MRI (DT-MRI) [11].

2.2 Simulation of the cardiac electrophysiology

Several electrophysiological models have been proposed in the literature. Due to its efficiency, we use an Eikonal approach for the electrophysiology propagation, with a volumetric implementation of the algorithm described in [15]. The depolarisation time t_d of the electrical wave for a given vertex of the volumetric mesh is computed by solving the anisotropic Eikonal equation $v^2(\nabla t_d^T D \nabla t_d) = 1$, where v is the local conduction velocity parameter and D is the tensor defining the conduction anisotropy. In the fibre coordinates, $D = \text{diag}(1, \rho, \rho)$, where ρ is the conduction anisotropy ratio between longitudinal and transverse directions. An anisotropic multi-front fast marching algorithm was developed in order to solve this model very efficiently.

2.3 Simulation of the myocardium contraction

The biomechanical model presented here is derived from a multi-scale modelling of the myocardium detailed in [2]. The mechanical model is composed of two elements, as shown on Fig. 1.a. The former is a parallel element which represents the passive properties of the tissue. This parallel element is anisotropic linear visco-elastic. The second element is an active contractile element controlled by the electrophysiology. More precisely, when the action potential is higher than a given threshold (i.e. when we reach the depolarisation time t_d), some calcium stored in the sarcoplasmic reticulum inside the cardiac cells is used for the ATP hydrolysis which provides energy to the molecular motors in the sarcomeres, generating the contraction of the fibre. The duration of this depolarisation is the action potential duration (APD). The electrical command u is then set to a constant k_{ATP} which represents the rate of the hydrolysis of the ATP. After contraction, during the repolarisation, calcium moves back into the sarcoplasmic reticulum and this calcium decrease allows the relaxation of the muscle. The electrical command u is then set to another constant $-k_{RS}$ which represents the activity of the sarcoplasmic reticulum.

Thus, the contractile element is controlled by its corresponding command u through the differential equation: $\dot{\sigma}_C + |u|\sigma_C = |u|_+\sigma_0$ where σ_C is the strength of the contraction, and σ_0 the maximum contraction. Then, with its associated command u described above, the strength of the contraction for each tetrahedron element is :

$$\sigma_C(t) = \begin{cases} \sigma_0 (1 - e^{k_{ATP}(t_d-t)}) & \text{during depolarisation} & t_d \leq t < t_r \\ \sigma_C(t_r) e^{k_{RS}(t_r-t)} & \text{during repolarisation} & t_r \leq t < t_d + HP \end{cases} \quad (1)$$

where $t_r = t_d + APD$ is the repolarisation time and HP the heart period. The command u and the intensity of the resulting contraction are represented on Fig. 1.b. Then, the active contractile element creates a stress tensor $\sigma_C \vec{f} \otimes \vec{f}$ where \vec{f} is the 3D fibre orientation and \otimes the dyadic product. For each vertex of each element, this results in a 3D force vector $\vec{f}_C = \frac{1}{4} \int_S (\sigma_C \vec{f} \otimes \vec{f}) \vec{n} dS$ with \vec{n} the surface normal and S the element surface.

Finally, we represent the simplified dynamic law by a stiffness matrix K for the transverse anisotropic elastic part (parallel element), a diagonal mass matrix M , and a damping matrix C for the internal viscosity part, which is the Rayleigh damping matrix $C = \alpha M + \beta K$, the contraction force vector F_C created by the contractile elements, a force vector F_P corresponding to the pressure forces in the ventricles and a force vector F_B corresponding to other boundary conditions. The resulting law of motion is:

$$M\ddot{Y} + C\dot{Y} + KY = F_{PV} + F_C + F_B \quad (2)$$

with $Y = (x_1, y_1, z_1, \dots, x_N, y_N, z_N)^T$ the position vector, N the number of mesh vertices, (x_i, y_i, z_i) the position of the i^{th} vertex, $\dot{Y} = \frac{dY}{dt}$ the velocity, $\ddot{Y} = \frac{d^2Y}{dt^2}$ the acceleration and $F_C = (\vec{f}_{C_1}, \dots, \vec{f}_{C_i}, \dots, \vec{f}_{C_N})$ the assembled contraction force.

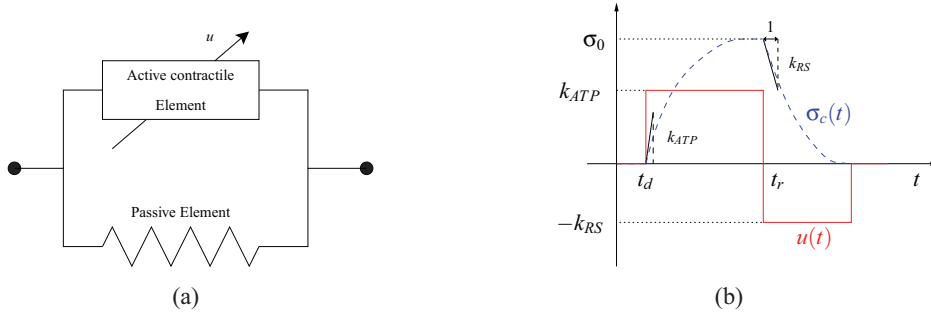


Figure 1: (a) Simplified biomechanical model. (b) Electrical command and intensity of contraction.

Let $X = (Y, \dot{Y})^T$. Then, X is the state vector of the following dynamical system:

$$\begin{cases} \dot{X} &= AX + R(u, \theta) \\ X(0) &= X_0 \end{cases} \quad (3)$$

where X_0 is the initial state vector, θ is the set of parameters of the model such as maximum contractility for example and where A (which depends of some parameters too) and R are defined by:

$$A = \begin{pmatrix} 0_{3N,3N} & I_{3N,3N} \\ -M^{-1}K & -M^{-1}C \end{pmatrix} \quad R = \begin{pmatrix} 0_{3N} \\ F_{PV} + F_C + F_B \end{pmatrix} \quad (4)$$

We simulate the four cardiac phases (filling, isovolumetric contraction, ejection and isovolumetric relaxation) as described in [14]. The arterial pressures were computed using a 3-element Windkessel model described in [17].

3 Mesh Creation and Model Initialisation

3.1 Mesh Creation

4D (3D + t) cine MRI provides time series of high resolution images of the heart that describe in part or in total one (averaged) cardiac cycle. A cine-MRI typically consists in a sequence of 15 to 20 3D images for one cycle. The high intensity contrast between myocardium and ventricular blood pool allows a rough segmentation of the blood pools based on the combination of thresholding and connected component extraction. This segmentation is only used to demonstrate the possibilities of the method, a discussion on the various segmentation methods is out of the scope of this article. Fig. 2.c presents these two connected components for one image of the cardiac cycle. We need to build a computational mesh of the myocardium,

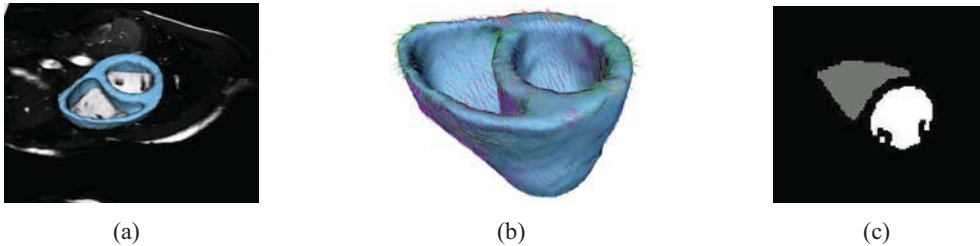


Figure 2: (a) Mid-diastole image. (b) Segmented mesh with synthetic fibre directions. (c) Segmented blood pools of one MR image of the cardiac cycle.

adjusted to the MRI image corresponding to the beginning of our simulation cycle. The first instant of our simulation cycle is the mid-diastole which corresponds to an instant when the ventricles are almost filled, just before the atrial contraction (P wave). We select for this the mid-diastole image, using the volume curves, detailed in the next paragraph. Then, the epicardium and left and right ventricles endocardia were delineated on this image using an interactive tool. These delineations generate three binary masks of the epicardium and the endocardia which are combined to obtain the binary mask of the myocardium used to create the mesh. This is done with isosurface extraction and tetrahedral mesh generation, using the INRIA software GHS3D (<http://www.simulog.fr/mesh/gener2.htm>).

We also need the local fibre orientation for this mesh. We generate synthetic fibre by linearly interpolating the elevation angle between the fibre and the short axis plane, from 80° on the endocardium to -80° on the epicardium. Fig. 2.b represents the obtained anatomical mesh with its synthetic fibre directions.

3.2 Model Initialisation

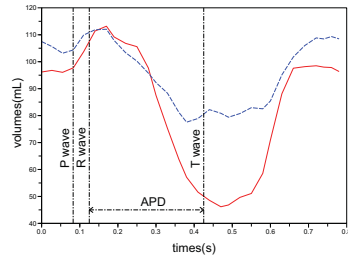


Figure 3: Left (solid line) and right (dashed line) ventricle volumes from MRI.

Electrical Model: As cardiac MRI is ECG-gated, we know the heart rate (here the heart period is 0.8 s) and the acquisition times of the 3D images related to the R-wave instant. This allows a first synchronisation between the image sequence and the simulation cycle. As the electrical information is not fully available, we need to extract additional information from the images. Due to the limited field of view, we only see part of the right ventricle in the MR images. Furthermore, the right ventricle blood pool has a grey level which varies along the cardiac cycle in cine MR images, thus thresholding is not reliable. Finally the trabeculae make the right ventricle segmentation difficult. For all these reasons, we have an important difference in volume between the two ventricles, as shown in Fig. 3. A more advanced segmentation method could overcome most of these difficulties, but this is out of the scope of this article. As our action potential propagation model only needs as inputs the time of the initialisation of the electrical wave and the action potential duration for each element, we extract average values from the volume curves. On these, one can observe the times of the beginning of the atrial contraction (P wave), of the ventricular contraction (R wave), and of the ventricular relaxation (T wave) independently for each ventricle (see Fig. 3). These times were set respectively to 0.0827 s, 0.125 s, 0.425 s. Then, we set the average value of the APD to the difference between the times of the beginning of the ventricular contraction and relaxation. Thus, for each vertex, APD is equal to 300 ms.

Mechanical Model: The passive mechanical parameters used are taken from the literature [16]. For the active component, we can use the volume curves to compute the ejection fraction, which is closely related to these parameters, in order to initialise it. However, due to the possible error on the right ventricle volume, we use only the left ventricle volume curve to calibrate the global contractility (the maximum contractility σ_0 constant for all the volumetric mesh) in order to obtain the same ejection fraction as the one computed from the left ventricle volume curve. For our data, σ_0 was set to 0.073 MPa/mm^2 . The rest position of the mechanical model is defined as the mid-diastole mesh created.

4 Coupling Model and Data: Methodology

In this section, we describe a method for coupling a dynamic system, the electromechanical model of the heart, and motion information from cine MRI. We start by discussing the choice of a metric to compare the simulated and observed motion and then describe formally the problem at hand: having a dynamic system that matches the available observations. Finally we show that motion tracking following a deformable model approach is equivalent to a data assimilation formulation where the error is minimised. This data assimilation formulation is directly inspired from the methodology of [7].

4.1 Metrics for comparing simulated and observed cardiac motion

Our objective is to minimize the discrepancy between the simulated cardiac motion and the actual one. One of the major difficulty is that in cine-MRI (which is the main dynamic modality in clinical routine MRI), only the apparent motion is visible. We see how the boundary moves, but we loose information on the tangential motion, which is important in the heart. We need to provide a metric to compare the model and the data taking this into account.

Since at each image instant the binary segmentation of the right and left blood pools are available it is reasonable to define the metric as the distance of the model endocardial surfaces to the blood pool surfaces as they should ideally match. Thus, for each point Y_i of one endocardium surface of the mesh, we find the nearest point Y_i^c on the corresponding surface extracted in the MR image. Ideally, we want the distance \tilde{d}_i between Y_i and Y_i^c to be zero. This approach is illustrated in Fig. 4 (in green) in which \vec{n}_c is the normal to the blood pool surface at the point Y_i^c .

However, the distance maps must be either precomputed (storage costs) or computed during the estimation (computational costs). Thus, in this paper, we propose to use the reverse metrics: the distance of the blood pool voxels to the mesh vertices as shown in Fig. 4 (in red). In this figure, \vec{N}_i is the normal to the mesh at the point Y_i . Thus, for each point Y_i of one endocardium surface, we find the point Y_i^{img} of the corresponding surface in the image contour for which the nearest point of the heart mesh is Y_i . Ideally, we want the distance d_i between Y_i and Y_i^{img} to be zero.



Figure 4: Distances \tilde{d}_i of the mesh to the blood pool (green) and d_i of the blood pool to the mesh (red).

Data interpolation: Due to limited temporal resolution, only a few MR images are available for a cardiac cycle. The time step used in the estimation is far smaller than the period between two MR images and we need information at each time step. Rather than interpolating the MR images, which would blur the contours, we prefer to interpolate the image forces described in the previous paragraph and computed at the previous and next images at each time step (see [14] for details).

4.2 Deformable Model Approach

This approach is based on segmentation by deformable models in which we minimise the sum of the energy of the dynamic system representing the heart and the energy corresponding to images forces, which are

computed from contour images with distance maps for example. The introduction of the model in the minimised energy allows us to recover some movement which cannot be obtained from classical geometrical tracking approaches. Of course, the image forces have no physiological meaning, but if we couple the model and the data and if we estimate the model parameters (which is the next step of this work), the motion generated by the model should converge to the one observed in the images. Thus, the intensity of image forces should decrease along the estimation and the estimated motion should be more and more physiological.

The definition of image forces are consistent with the metrics chosen in the previous section. Namely, for each mesh point Y_i , we seek the closest point Y_i^{img} along the normal direction \vec{N}_i of the mesh at Y_i . Since the blood pool surfaces are roughly segmented as binary images, we compute Y_i^{img} as the intersection of the normal line at Y_i with the isosurface $I(x,y,z) = 127.5$ for binary masks set to $I = 255$. This intersection can be computed fairly efficiently and with a subvoxel accuracy. More complex image forces involving intensity profiles, image blocks or textures could be used instead as shown in [3]. Here, we minimise the following energy:

$$\tilde{E}_{img}(Y, \dot{Y}, Y^{img}) = \sum_{i=1}^m \gamma_i \|Y_i - Y_i^{img}\|_{\vec{N}_i \vec{N}_i^T}. \quad (5)$$

where \vec{N}_i is the normal of the endocardium surface at the point Y_i , m is the number of points of the endocardium surfaces (the points Y_i are indexed from 1 to m for more simplicity) and γ_i is the confidence in the measure Y_i^{img} . When we differentiate this energy with respect to Y , we obtain:

$$\frac{\partial \tilde{E}_{img}}{\partial Y} = \begin{pmatrix} \vdots \\ 2\gamma_i \vec{N}_i \vec{N}_i^T (Y_i - Y_i^{img}) \\ \vdots \end{pmatrix} = \begin{pmatrix} \vdots \\ 2\gamma_i d(Z, Y_i) \vec{N}_i \\ \vdots \end{pmatrix} \quad (6)$$

Finally, this approach consists in adding the image forces $2\gamma_i d(Z, Y_i) \vec{N}_i$ to the vertex Y_i belonging to endocardium surfaces. This is similar to the pro-active deformable model described in [14].

4.3 Data assimilation approach

We will show in the following that this minimisation of energy can be related to a data assimilation approach. The methodology of this data assimilation is directly inspired from [7]. In this approach, two parts are taken into account: the electromechanical model described by Equation 3 with inputs consisting in the electrical command and different external loads, and the available observations. We assume that the parameters of the model are known, unlike the initial position condition X_0 on which we make an error of ξ_X ($X(0) = X_0 + \xi_X$).

A new dynamical system called *state observer* takes as inputs the electrical command and the image data and returns the *estimated state*, written as \hat{X} which should converge to the *true state* X . In classical data assimilation approach, the *observation* Z (measures) can be directly computed from the true state X , thanks to an *observation operator* H such that $Z = H X$. Then, the observations computed from the estimate state ($\hat{Z} = H \hat{X}$) are compared to the measured observations (Z) and the difference ($\hat{Z} - Z$) called *innovation* is taken into account in the state observer dynamics.

In our case, if we note Z the blood pool surfaces, we no longer have $Z = H X$ since with cine MRI, we cannot track any material points during a cardiac cycle. Instead, we can compare the two surfaces X and Z through a distance map which can be formalized as $H(X, Z) = 0$. The observation operator is taken as the gradient of the square distance between the two surfaces $H(X, Z) = \nabla d^2(Z, X) = 0$

The estimated state \hat{X} does not match perfectly with the observation, and therefore the error between the estimated state and the true state can be quantified with $\nabla d^2(Z, \hat{X}) = 2d(Z, \hat{X})\nabla d(Z, \hat{X})$. Note that $\nabla d^2(Z, \hat{X})$ is a vector of the same size as X and its velocity components and its components which correspond to points that are not on endocardium surfaces are 0. For points on the endocardium, $\nabla d^2(Z, \hat{X}) \equiv 2d_i\nabla d_i$ where $d_i = \|\hat{Y}_i - Y_i^{img}\|$. Furthermore, by definition of a distance map, $\nabla d_i = \vec{N}_i$ where \vec{N}_i is the normal of the heart mesh at point \hat{Y}_i . Then, the built state observer is:

$$\begin{cases} \dot{\hat{X}} &= A\hat{X} + R(u, \theta) + K_d\nabla d^2(Z, \hat{X}) \\ \hat{X}(0) &= X_0 \end{cases} \quad (7)$$

with K_d the gain associated with the data. We can see that with a high gain, the estimated state will rely more on image data information than in the electromechanical model. Conversely, with no gain, the observer does not take into account the data and is equivalent to the electromechanical model. Thus, the choice of the gain K_d depends on the relative confidence in the model and the data.

It is of high interest to analyse the error between the estimated state \hat{X} and the true state X in order to choose the gain. With a proper choice of the gain, the error should converge towards zero. We write the error dynamics by subtracting the model (equation 3) from the observer (equation 7):

$$\begin{cases} \dot{\tilde{X}} &= A\tilde{X} + K_d\nabla d^2(Z, \hat{X}) \\ \tilde{X}(0) &= \xi_X \end{cases} \quad (8)$$

After linearising the data and assuming that the estimated state \hat{X} is close to X :

$$\nabla d^2(Z, X) = \nabla d^2(Z, \hat{X}) + H_d(\hat{X})(X - \hat{X}) \quad (9)$$

where $H_d(\hat{X})$ a matrix $n \times n$ where n is the size of the state vector X . Its components corresponding to points on endocardium surfaces are the 3×3 Hessian matrix of the squared distance d_i and are null otherwise. Since the real state X is supposed to coincide with the position and the movement of the apparent boundaries in the image Z , then $\nabla d^2(Z, X) = 0$. The error dynamics is:

$$\begin{cases} \dot{\tilde{X}} &= (A + K_d H_d)\tilde{X} \\ \tilde{X}(0) &= \xi_X \end{cases} \quad (10)$$

A result of the control theory shows that this error converges to 0 if all eigenvalues of $(A + K_d H_d)$ matrix have negative real parts. This provides a criterion for selecting the gain matrix K_d .

In practice, we choose the gain K_d as in [7]: $K_d = \gamma M^{-1} H_d^T$. Indeed, if we decompose the error dynamics, we have:

$$M\ddot{\tilde{Y}} + C\dot{\tilde{Y}} + (K + \gamma H_d^T H_d)\tilde{Y} = 0 \quad (11)$$

Therefore with this choice of K_d , the stiffness of the error dynamics is increased. It implies an increase of the frequency and the damping of the eigenmodes, and therefore a better convergence toward zero. Here we see the difference between this filtering method and Kalman filtering methods such as the one proposed in [18]. The gain K_d is not the Kalman gain, so that the result of the filter is not the optimal result in a stochastic way, but K_d is chosen in order to ensure the convergence of the error \tilde{X} toward zero. Although we do not ensure an optimal result, we avoid to compute the inverse of a combination of covariance matrices, thus leading to a much faster filter than the Kalman approach.

We use the Houbolt implicit scheme to integrate equation 7. Since the image term is also made implicit, the generalised stiffness matrix that is involved in the linear system of equations should change at each time step since the matrix H_d depends on the position of endocardium vertices Y_i . However, modifying the generalised stiffness matrix at each time step implies that a Cholesky decomposition or a preconditioning must be performed at each iteration which is computationally very expensive. Since the stiffness matrix K is

constant, we chose to estimate the term $\gamma H_d^T H_d \hat{Y}_{t+dt}$ numerically, by first computing the position \hat{Y}_{t+dt} as if there were no image forces and then multiplying it by $\gamma H_d^T H_d$. This proved to be a fairly efficient approach since the preconditioning of the generalised stiffness matrix is only done once. This also gives better results than a semi-implicit scheme where image forces are estimated explicitly.

Finally, one should note that \vec{N}_i is an eigenvector of the Hessian matrix of the distance map d_i with eigenvalue 1. Therefore, when using the gain matrix as $K_d = \gamma M^{-1} H_d^T$, the dynamic law of the state observer is given by :

$$M\ddot{\hat{Y}} + C\dot{\hat{Y}} + K\hat{Y} = F_{PV} + F_C + F_B + \gamma H_d^T \nabla d^2(Z, \hat{X}) = F_{PV} + F_C + F_B + \begin{pmatrix} \vdots \\ 2\gamma d(Z, Y_i) \vec{N}_i \\ \vdots \end{pmatrix} \quad (12)$$

This corresponds exactly to the formulation we obtained with the deformable model approach.

5 Results

5.1 Validation with synthetic data

In order to validate our state estimation method in a quantitative way, we generated synthetic cine-MR images using the electromechanical model with standard values. We took 29 instants of the second simulated cycle and we generated the corresponding segmented 3D images, using rasterisation of the tetrahedra. As we assume here that the model is known, all parameters of the model used in the state estimation are the same than the ones used to generate the synthetic data. Thus the only error is on the initial position. We can then quantify the evolution of the mean position error in this ideal case.

State error analysis: We observed, as expected, that the root mean squared error (RMSE) decreases with time, under the action of the state estimation filter. Here, the gain γ was set to 0.8. Fig. 5.a shows the evolution of the position error along three cardiac cycles. Fig. 5.b shows the intensity of the contraction forces and the intensity of the image forces for one endocardial vertex and along three cardiac cycles. We can see that the image forces decrease rapidly in the first times of the first cycles and that the images forces remain small compared to the intensity of physical forces such as the contraction forces. We can see also that the image forces do not vanish exactly to zero. The decreasing of this RMSE depends on the spatial resolution of the images.

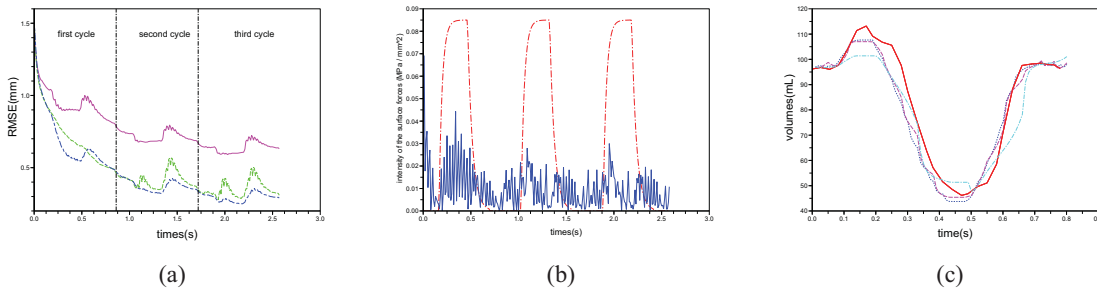


Figure 5: (a) Root mean squared error for three different spatial resolutions. Solid line: 1 mm, dashed line 0.75 mm, dash-dot: 0.5 mm (in all three directions). (b) Intensity of the contraction force (dashed line) and intensity of the image force (solid line) for an endocardial vertex along three cycles. (c) Left ventricle volume curves from the images (solid red), and for three different temporal resolutions: complete sequence (30 images, dash-dot blue), 15 (dash magenta) and 5 (long dash-dot cyan).

Effect of the spatial resolution of the MR images: The voxel sizes used in the synthetic images are respectively 1 mm, 0.75 mm and 0.5 mm in all three directions. The RMSE decreases if we increase the spatial resolution of the images and seems to converge to values which are smaller than the spatial resolution of the images and which should correspond to numerical approximation errors (see Fig. 5.a).

Effect of the temporal resolution of the MR images: For this we used real images (see details in next section). The first one was a complete cine-MRI sequence (30 images), the second and the third ones were subsamples of the cine-MRI sequence (respectively 15 and 5 images). Fig. 5.c shows that the left ventricle volume is better approximated in the case of sequences with 30 or 15 images than in the case of the sequence of 5 images. Nevertheless, as the contractility of the left ventricle was well calibrated, the knowledge of the model allows us to obtain good information on the left ventricle volume curve, and to compute good approximations of the ejection fraction. The left ventricle ejection fractions obtained respectively from the complete segmented sequence, from the estimations with complete MRI sequence, and with 15 and 5 images sequences are respectively: 59.20%, 59.34%, 57.56% and 56.84%.

Cardiac Function Estimation: Finally, in Fig. 6, the physiological curves obtained from the state estimation are compared with the ones given by the reference simulation. These physiological curves correspond to the right and left ventricular pressures (Fig. 6.a), volumes (Fig. 6.b) and flows (Fig. 6.c). In the isovolumic phases, pressures are computed to counterbalance external forces such as contraction forces and image forces in the case of the estimation in order to keep the volume constant. We can see that in these phases, and in the ejection phases in which the pressures depend on flows through the Windkessel model, the pressures are well recovered. We can see also that after a small period due to the initial position error, the volumes and the global evolution of the flow are well recovered. As flows are the derivative of volumes, errors on volumes due to the oscillation of image forces are magnified.

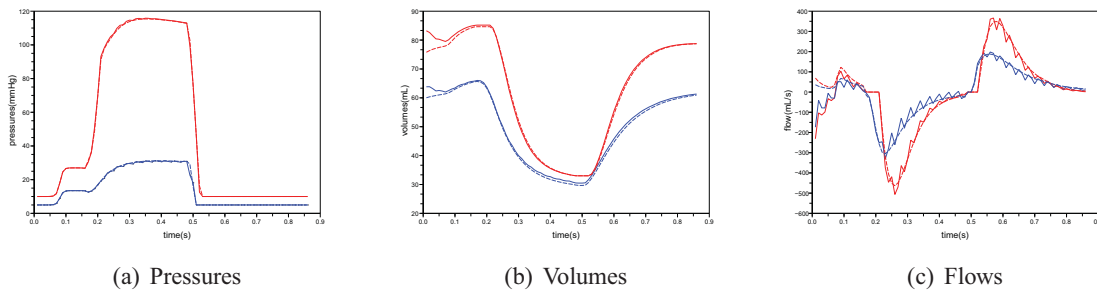


Figure 6: Comparison of: a) Left (red) and right (blue) ventricular pressures(in mmHg). (b) Left (red) and right (blue) ventricular volumes (in mL) (c) Left (red) and right (blue) flows (in mL/s) in the reference simulation (dashed curves) and in the estimation (solid curves) with reference images of voxel size of 0.5 mm in all three directions.

5.2 Results with clinical data

Several estimations were made with different values of the gain γ in order to see the effect of the gain on the state estimation. Fig. 7 shows the MRI segmentation at a time t_i of the cardiac cycle. The superimposed lines represents the endocardium and epicardium surfaces of two heart meshes obtained with different values of γ . The higher value of the gain gives more confidence in the data than in the model, then the image forces are larger in this case as we see in Figs. 7.b and 7.c. We can see that the left ventricle is well tracked in the two cases, while the right ventricle is better tracked in the case of the higher gain. It shows that the contractility parameter in the right ventricle does not equal the one in the left ventricle, which we calibrated with the left

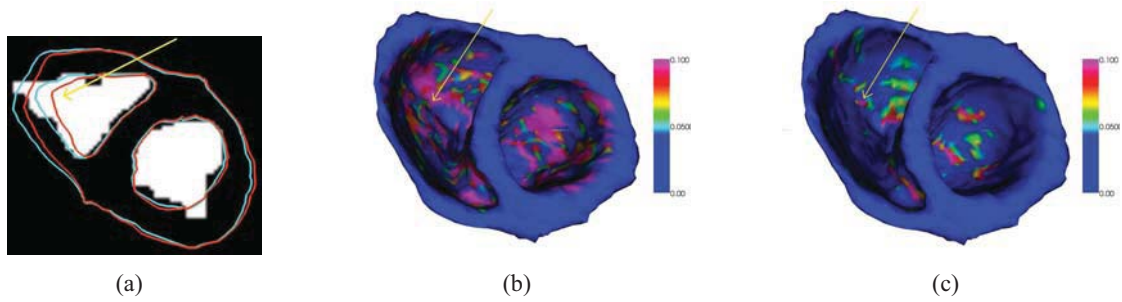


Figure 7: a) Delineation of two estimated heart meshes at a given time t_i during the contraction. These delineation are superimposed to the short axis view of the segmentation. The cyan and red mesh were obtained respectively with a gain γ equal to 0.8 and 0.2. b) and c): 3D view of the estimated heart meshes with a gain of 0.8 (b) and a gain of 0.2 (c) at the same time t_i . Colours correspond to the intensity of the image forces (in $\text{MPa}\cdot\text{mm}^{-2}$).

volume curve obtained from the cine-MRI. Thus, it allows us to detect differences in parameters, which can lead to parameter estimation.

In order to qualitatively evaluate the estimated motion, we used tagged MRI on the same subject to extract the projection of the 3D real cardiac motion in a number of short axis view (Fig. 8.a). The qualitative comparison with the projection of the 3D estimated motion (Fig. 8.b) is promising, as we observe similar motion patterns. The estimated motion is much smoother due to the influence of the model. We are working on a more quantitative comparison with the estimated motion.

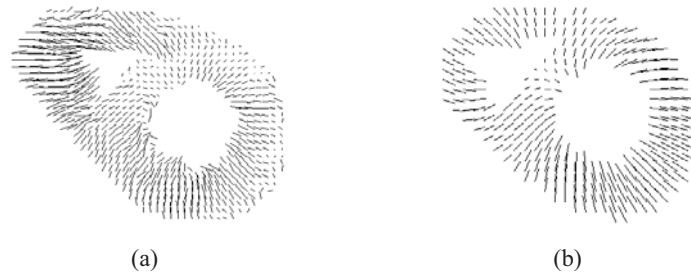


Figure 8: Projection on a short axis view of the 3D end-diastolic motion respectively extracted from tagged MR images (a) and estimated from cine-MRI with the presented method (b). (same subject)

6 Conclusion

Coupling electromechanical models of the heart with clinical data in order to help diagnosis and therapy planning is still very challenging. This article presents the link between deformable models and data assimilation in order to estimate cardiac motion from cine-MRI. The proposed method allows to keep the low computational cost of deformable models while using a rigorous mathematical framework. Motion recovery is demonstrated on synthetic and real data. These promising preliminary results will be extended in order to perform parameter estimation, which is the ultimate goal of the approach.

Acknowledgment

This work is partially funded by the INRIA CardioSense3D action (<http://www-sop.inria.fr/CardioSense3D>). The authors would like to thank CardioSense3D partners and in particular D. Chapelle and P. Moireau (from MACS team at INRIA Rocquencourt) for their collaboration on the data

assimilation method [7], M. Sorine (from SISYPHE team at INRIA Rocquencourt) for his expertise on cardiac modeling [2], and T. Mansi (from ASCLEPIOS team at INRIA Sophia-Antipolis) for the motion extraction from tagged MRI.

References

- [1] J. B. Bassingthwaite. Strategies for the physiome project. *Annals of Biomedical Engineering*, 28:1043–1058, 2000.
- [2] J. Bestel, F. Clément, and M. Sorine. A biomechanical model of muscle contraction. In W. Niessen and M. Viergever, editors, *Medical Image Computing and Computer-Assisted Intervention (MICCAI'01)*, volume 2208 of *LNCS*, pages 1159–1161. Springer-Verlag, Berlin, Germany, 2001.
- [3] H. Delingette. General object reconstruction based on simplex meshes. *International Journal of Computer Vision*, 32(2):111–146, 1999.
- [4] A. Frangi, W. Niessen, and M. Viergever. Three-dimensional modeling for functional analysis of cardiac images: A review. *IEEE Transactions on Medical Imaging*, 1(20):2–25, 2001.
- [5] P.J. Hunter, M.P. Nash, and G.B. Sands. Computational electromechanics of the heart. In *Computational biology of the heart*, pages 345–407. A.V. Panfilov and A.V. Holden Eds, John Wiley & Sons, 1997.
- [6] D. Metaxas and D. Terzopoulos. Constrained deformable superquadrics and nonrigid motion tracking. *IEEE*, pages 337–343, 1991.
- [7] P. Moireau, D. Chapelle, and P. Le Tallec. Joint state and parameter estimation for distributed mechanical systems. *Computer Methods in Applied Mechanics and Engineering*, 197:659–677, 2008.
- [8] J. Montagnat and H. Delingette. 4D deformable models with temporal constraints: application to 4D cardiac image segmentation. *Medical Image Analysis*, 9(1):87–100, February 2005.
- [9] D. Noble and Y. Rudy. Models of cardiac ventricular action potentials: iterative interaction between experiment and simulation. *Phil. Trans. R. Soc. Lond. A*, pages 1127–1142, 2001.
- [10] X. Papademetris, A. J. Sinusas, D. P. Dione, and J. S. Duncan. 3D cardiac deformation from ultrasound images. In *Medical Image Computing and Computer-Assisted Intervention (MICCAI'99)*, volume 1679, pages 420–429. Springer, 1999.
- [11] J-M. Peyrat, M. Sermesant, X. Pennec, H. Delingette, C. Xu, E. McVeigh, and N. Ayache. A computational framework for the statistical analysis of cardiac diffusion tensors: Application to a small database of canine hearts. *IEEE Transactions on Medical Imaging*, 26(11):1500–1514, November 2007.
- [12] Z. Qian, D. N. Metaxas, and L. Axel. A learning framework for the automatic and accurate segmentation of cardiac tagged MRI images. In *Computer Vision for Biomedical Image Applications*, pages 93–102, 2005.
- [13] F. Sachse, G. Seemann, C. Werner, C. Riedel, and O. Dössel. Electro-mechanical modeling of the myocardium: Coupling and feedback mechanisms. In *Computers in Cardiology*, volume 28, pages 161–164, 2001.
- [14] M. Sermesant, H. Delingette, and N. Ayache. An Electromechanical Model of the Heart for Image Analysis and Simulation. *IEEE Transactions in Medical Imaging*, 25(5):612–625, 2006.
- [15] M. Sermesant, E. Konukoglu, H. Delingette, Y. Coudiere, P. Chinchaptanam, K.S. Rhode, R. Razavi, and N. Ayache. An anisotropic multi-front fast marching method for real-time simulation of cardiac electrophysiology. In *Proceedings of Functional Imaging and Modeling of the Heart 2007 (FIMH'07)*, volume 4466 of *LNCS*, pages 160–169, 7-9 June 2007.
- [16] P. Shi and H. Liu. Stochastic finite element framework for simultaneous estimation of cardiac kinematic functions and material parameters. *Medical Image Analysis*, 7(4):445–464, 2003.
- [17] N. Stergiopoulos, B. Westerhof, and N. Westerhof. Total arterial inertance as the fourth element of the windkessel model. *American Journal of Physiology*, 276:H81–8, 1999.
- [18] K. C. L. Wong, H. Zhang, H. Liu, and P. Shi. Physiome model based state-space framework for cardiac kinematics recovery. In *MICCAI (1)*, pages 720–727, 2006.

Inverse Nonlinear Finite Element Methods for Surgery Simulation and Image Guidance

Philip Pratt
p.pratt@imperial.ac.uk

Institute of Biomedical Engineering
Imperial College, London

Abstract

Nonlinear finite element methods are described in which cyclic organ motion is implied from 4D scan data. The equations of motion corresponding to an explicit integration of the total Lagrangian formulation are reversed, such that the sequence of node forces which produces known changes in displacement is recovered. The forces are resolved from the global coordinate system into systems local to each element, and at every simulation time step are expressed as weighted sums of edge vectors. In the presence of large deformations and rotations, this facilitates the combination of external forces, such as tool-tissue interactions, and also positional constraints. Applications in the areas of surgery simulation and minimally invasive robotic interventions are discussed, and the methods are illustrated using CT images of a pneumatically-operated beating heart phantom.

1 Introduction

The future of minimally invasive robotic surgery lies not only in the mechanical evolution of better telemanipulator systems, but also in the development of advanced software tools that facilitate surgical training, patient-specific intraoperative rehearsal, and the seamless integration of preoperative and intraoperative imaging, of various modalities, through augmented reality techniques. The image-constrained biomechanical modelling (ICBM) approach is a key technology which promises to realise the goal of allowing surgeons to alternate between full surgical simulation, endoscopic views enhanced in real-time through the same simulation constrained by imaging data, and completion of the intervention itself. To that end, this paper extends previous work [6] by showing how intrinsic cyclic tissue motion can be inferred from 4D scan data and combined with externally induced motion and other constraints using a *nonlinear* finite element model. Taking known changes in node displacements over time, the finite element model inverted such that the sequence of node forces responsible for the motion can be recovered. These forces are then resolved from the global coordinate system into systems local to each element, thereby expressing them in terms of local geometry. That way, in the presence of large deformations and rotations, external forces and other constraints can be combined when forward simulation is performed.

Accurate modelling of soft tissue deformation represents a significant challenge, since the constitutive behaviour of such tissue is known to be both nonlinear and time-varying, and the assumptions made in linear,

small-strain formulations are not valid, particularly when considering large deformations. Miller *et al.* [5] present the total Lagrangian explicit dynamics (TLED) algorithm, which offers the possibility of accurate simulation at interactive rates. In contrast to the *updated* Lagrangian finite element formulation, the *total* Lagrangian formulation [1, 10] expresses stress and strain measures in terms of the reference configuration, and thus many quantities can be either completely or partially precomputed. Furthermore, an explicit integration scheme coupled with element and node-wise storage enable efficient implementation, particularly when GPU hardware [9] is employed. Several inverse finite element simulations have been described in the literature where deformations are known *a priori*. In particular, Kruggel and Tittgemeyer [4] use an inverse finite element model of linear elasticity to derive a force field given an observed deformation of the brain. Kauer [3] also uses an inverse model to calibrate the properties of a visco-elastic material given experimental pressure data and resulting tissue deformations.

2 Methods

The tetrahedral finite element mesh comprises N nodes, and therefore has at most $3N$ degrees of freedom. In general, the equations of motion are expressed in terms of the $3N$ displacements from the initial mesh configuration, i.e. $\mathbf{U} = [u^0 u^1 \dots u^{3N-1}]^\top$, and following the notation of Bathe [1], are written using the total Lagrangian formulation (in semi-discrete form) as

$$\mathbf{M} \mathbf{t}\ddot{\mathbf{U}} + \mathbf{C} \mathbf{t}\dot{\mathbf{U}} + \mathbf{t}_0\mathbf{F} = \mathbf{t}\mathbf{R} \quad (1)$$

where $\mathbf{t}\dot{\mathbf{U}}$ and $\mathbf{t}\ddot{\mathbf{U}}$ are the velocity and acceleration vectors, respectively, \mathbf{M} is the mass matrix, \mathbf{C} is the damping matrix, $\mathbf{t}_0\mathbf{F}$ is the vector of nodal reaction forces equivalent to the element stresses, and $\mathbf{t}\mathbf{R}$ is the vector of externally applied, time-varying forces. The damping matrix is assumed to be proportional to the mass matrix, i.e. $\mathbf{C} = \alpha\mathbf{M}$, where α is the damping coefficient. The mass matrix is assumed to be constant, and is diagonalised to facilitate explicit integration.

2.1 Nodal Reaction Forces

In the total Lagrangian formulation of the finite element method, quantities are expressed in terms of the reference configuration. Considering an individual element i , the nodal reaction forces are computed as an integral over the element volume, as follows

$$\mathbf{t}_0\mathbf{F}^{(i)} = \int_{0V^{(i)}} \mathbf{t}_0\mathbf{B}_L^\top \mathbf{t}_0\hat{\mathbf{S}} d^0V \quad (2)$$

where $\mathbf{t}_0\mathbf{B}_L$ is the full strain-displacement matrix and $\mathbf{t}_0\hat{\mathbf{S}}$ is the vector of 2nd Piola-Kirchoff stresses. The latter depend on the element deformation and the choice of material constitutive law. For an assemblage of elements, the nodal reaction forces are accumulated in accordance with the mesh's element-node relationships.

2.2 Explicit Central Difference Integration

The motion from which forces are to be inferred is assumed to be cyclic, spanning a period of T seconds. Successor and predecessor functions of time t are defined, using time step duration Δt , as follows.

$$next(t) = \begin{cases} t + \Delta t & \text{if } t < T - \Delta t \\ 0 & \text{otherwise} \end{cases} \quad prev(t) = \begin{cases} t - \Delta t & \text{if } t > 0 \\ T - \Delta t & \text{otherwise} \end{cases} \quad (3)$$

From these definitions, the central finite-difference approximations to the first and second-order time derivatives of the displacement vector yield the following expressions for velocity and acceleration.

$${}^t\dot{\mathbf{U}} \approx \frac{1}{2\Delta t} [{}^{next(t)}\mathbf{U} - {}^{prev(t)}\mathbf{U}] \quad {}^t\ddot{\mathbf{U}} \approx \frac{1}{\Delta t^2} [{}^{next(t)}\mathbf{U} - 2{}^t\mathbf{U} + {}^{prev(t)}\mathbf{U}] \quad (4)$$

Thus, over a single cycle, the fully discretised equations of motion take the form shown in (5). Note that the nodal reaction forces must be calculated at every time step. At the expense of some restriction on time step magnitude, the explicit scheme avoids the iterative solution of the displacements at the next time step, which would otherwise be extremely computationally expensive.

$${}^{next(t)}\mathbf{U} \approx \frac{2}{2 + \alpha\Delta t} \left[\frac{\Delta t^2}{\mathbf{M}} ({}^t\mathbf{R} - {}^t_0\mathbf{F}) + 2{}^t\mathbf{U} - \left(\frac{\alpha\Delta t}{2} - 1\right) {}^{prev(t)}\mathbf{U} \right] \quad (5)$$

Over multiple cycles, this displacement update rule is extended in the conventional manner.

2.3 Recovering Forces from Displacements

By inverting equation (5), one can write the discretised applied force in terms of the displacement, velocity and acceleration vectors, the nodal reaction forces, and other known quantities. By construction, if one were then to solve the equations of motion and apply these forces at the appropriate times, one would recover the original cyclic motion exactly and indefinitely. Note that the recovered forces are expressed in the global coordinate system.

The force recovery process, and therefore also the forward simulation, are initialised by precomputing the spatial derivatives of element shape functions, the element Jacobian determinants, constant strain-displacement matrices ${}^t_0\mathbf{B}_{L0}$, and the diagonalised mass matrix. Furthermore, deformation gradient tensors can be factorised into two parts, depending on global node positions and displacements, respectively, and the former can also be precomputed for efficiency. Subsequently, the following two-stage calculation is performed at each simulation time step.

For each integration point in each element:

- Calculate deformation gradient tensor ${}^t_0\mathbf{X}$
- Calculate strain-displacement matrix ${}^t_0\mathbf{B}_L = {}^t_0\mathbf{B}_{L0} {}^t_0\mathbf{X}^\top$
- Calculate 2nd Piola-Kirchoff stress vector ${}^t_0\hat{\mathbf{S}}$
- Accumulate element nodal reaction forces ${}^t_0\mathbf{F}^{(i)}$ to give node totals ${}^t_0\mathbf{F}$

For each node:

- Invert displacement update step to recover external node force:

$${}^t\mathbf{R} \approx \frac{\mathbf{M}}{\Delta t^2} \left[\left(1 + \frac{\alpha\Delta t}{2}\right) {}^{next(t)}\mathbf{U} - 2{}^t\mathbf{U} + \left(1 - \frac{\alpha\Delta t}{2}\right) {}^{prev(t)}\mathbf{U} \right] + {}^t_0\mathbf{F} \quad (6)$$

For forward simulation, the node-wise update stage is replaced by the following:

- Determine external forces to be applied to each node (e.g. due to virtual tool-tissue interaction)
- Add to the recovered forces and use equation (5) to update displacements
- Apply displacement constraints (e.g. anchor points)

2.4 Local Force Resolution

In order to combine recovered and external forces, the former must be expressed not in the global coordinate system, but for each node in terms of its local surrounding geometry. With the introduction of external forces, the geometry may deviate from the original cyclic motion through potentially large-scale deformations and rotations. By resolving recovered forces locally, they are made to act in the appropriate direction in conjunction with externally induced motion.

The recovered force acting on a particular node in the mesh is assumed to originate from the elements which contain that node. Indeed, an approximation is made whereby the force receives an equal contribution from each such element. For a given element at each point in time, the edge vectors from the node in question to the other three nodes in that element define a local basis in terms of which that element's fraction of the node force can be expressed. This amounts to equating the force to a weighted sum of those edge vectors and solving for the weights. Subsequently, the weights are further computed over the node's other parent elements, ultimately building a set of weights that links all the recovered forces locally to the geometry of the entire mesh.

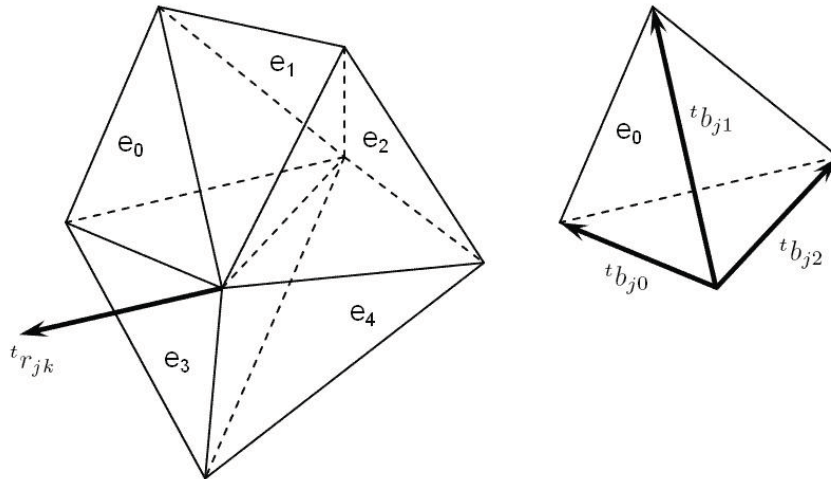


Figure 1: Force resolution using local geometry

Labelled with coordinate indices j , figure 1 (left) depicts at time t a typical node k with its recovered force ${}^t r_{jk}$, and the five surrounding elements e_0, \dots, e_4 to which it belongs. In general, a node will be common to M_k elements. Figure 1 (right) illustrates the first element e_0 , and the three edge vectors ${}^t b_{j0}$, ${}^t b_{j1}$ and ${}^t b_{j2}$ which, with the node itself, define the geometry of the element at that instant. In order to express the required fraction of the force in terms of local mesh geometry, its components in the global coordinate system are equated to weighted combinations of these edge vectors, as shown in (7).

The weights are determined by direct inversion of the left-hand-side matrix. This process is repeated for the element's other three nodes, and subsequently over all nodes in the mesh. In order to ensure that the magnitudes of the recovered forces, expressed as functions of current element edge vectors, remain within reasonable bounds and do not give rise to simulation instability, recovered forces are normalised at each time step to have the same magnitude as those implied from the original motion where no externally applied forces are present.

$$\begin{bmatrix} {}^t b_{00} & {}^t b_{01} & {}^t b_{02} \\ {}^t b_{10} & {}^t b_{11} & {}^t b_{12} \\ {}^t b_{20} & {}^t b_{21} & {}^t b_{22} \end{bmatrix} \begin{bmatrix} {}^t w_0 \\ {}^t w_1 \\ {}^t w_2 \end{bmatrix} = \frac{1}{M_k} \begin{bmatrix} {}^t r_{0k} \\ {}^t r_{1k} \\ {}^t r_{2k} \end{bmatrix} \quad (7)$$

3 Results

The force recovery and resolution techniques are illustrated using data taken from scans of a beating heart phantom, using an isotropic, hyperelastic neo-Hookean tissue model. The Chamberlain Group CABG phantom, illustrated in figure 2 (left), was scanned at 54 bpm with a Philips 64-slice CT scanner, producing 10 uniformly-spaced phases. The first of these was manually segmented and converted into a tetrahedral mesh using the SimBio-Vgrid [2] mesh generator. Figure 2 (right) shows the interaction between the resulting mesh and a virtual tool. The Image Registration Toolkit [7, 8] was used to create a sequence of 3D tensor product cubic B-spline deformations, mapping the initial mesh onto each phase in turn. Cyclic cubic B-splines, defined using 6 uniformly spaced knots, were then used to interpolate mesh node positions over time. The material constitutive law is given as a strain energy density in equation (8), from which [10] the 2nd Piola-Kirchoff stress tensor elements S_{ij} can be derived. Here, C_{ij} is the right Cauchy-Green deformation tensor, I and J are its first and third invariants, respectively, and λ and μ are Lamé constants, defined in terms of Young's modulus E and Poisson's ratio ν .

$$W(I, J) = \frac{1}{2}\mu(I - 3 - 2\ln J) + \frac{1}{2}\lambda(J - 1)^2 \quad (8)$$

$$S_{ij} = \mu(\delta_{ij} - C_{ij}^{-1}) + \lambda J(J - 1)C_{ij}^{-1} \quad (9)$$

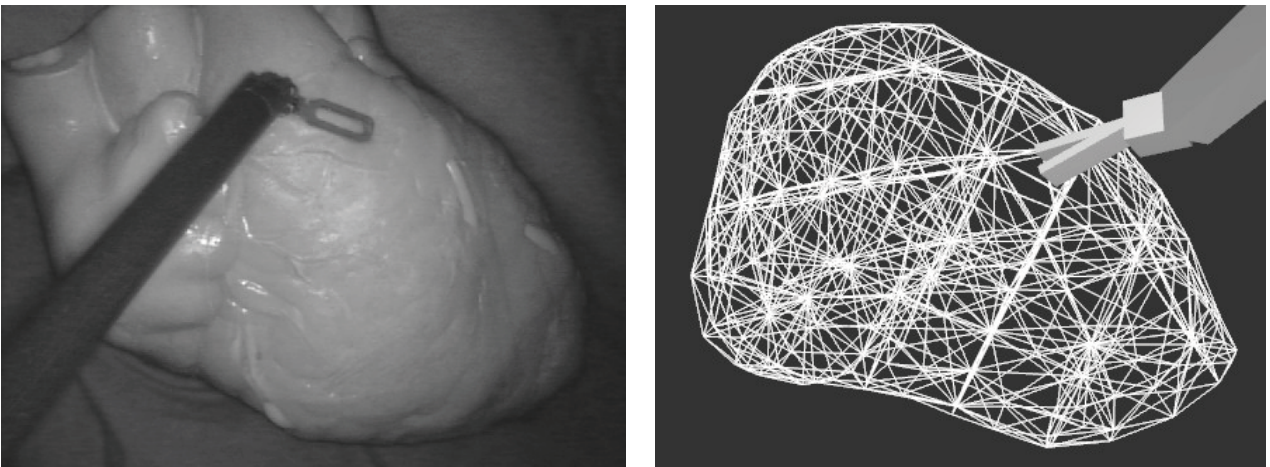


Figure 2: Beating heart phantom and tetrahedral FEM mesh with virtual tool

The following constants were used in all the simulations: Young's modulus $E = 3.0E + 03 \text{ Pa}$; Poisson's ratio $\nu = 0.45$; material density $\rho = 1.0E + 03 \text{ kg/m}^3$; and mass damping coefficient $\alpha = 7.5E + 01$. Thus, $\lambda \approx 9.31E + 03 \text{ Pa}$ and $\mu \approx 1.03E + 03 \text{ Pa}$. The equations of motion were integrated using a time step of $\Delta t = 0.001$ seconds.

Figure 3 shows the motion of a typical surface node as a result of applying recovered forces alone. Unlike the heart phantom itself, several nodes in the base of the mesh are deliberately anchored, and hence it takes a short period of time to converge to an exactly repeatable motion. Figures 4 and 5 show the individual effects of displacement constraints simulating respiratory motion, and externally applied forces simulating tool-tissue interaction, respectively. Finally, figure 6 illustrates how all three motions are combined by the model. The underlying beating motion is apparent throughout the simulation.

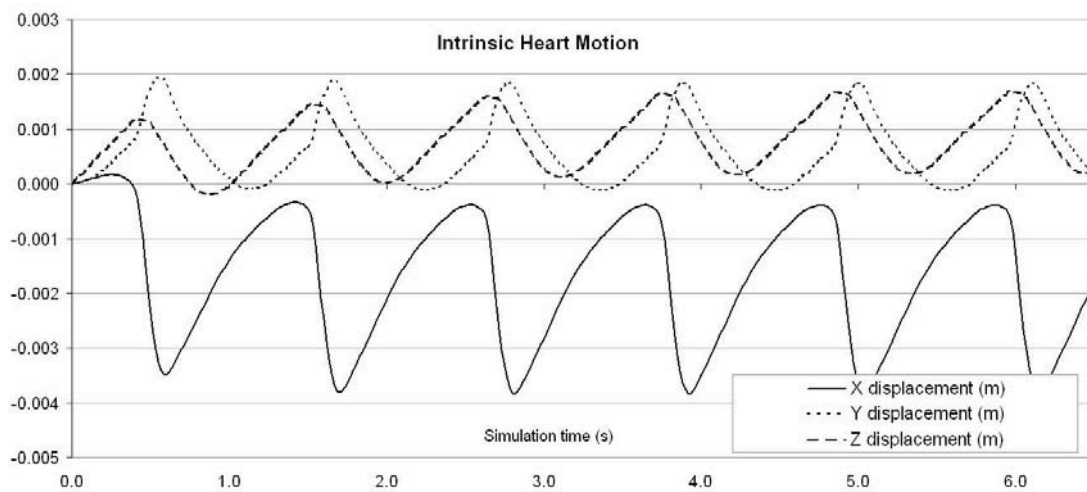


Figure 3: Intrinsic motion

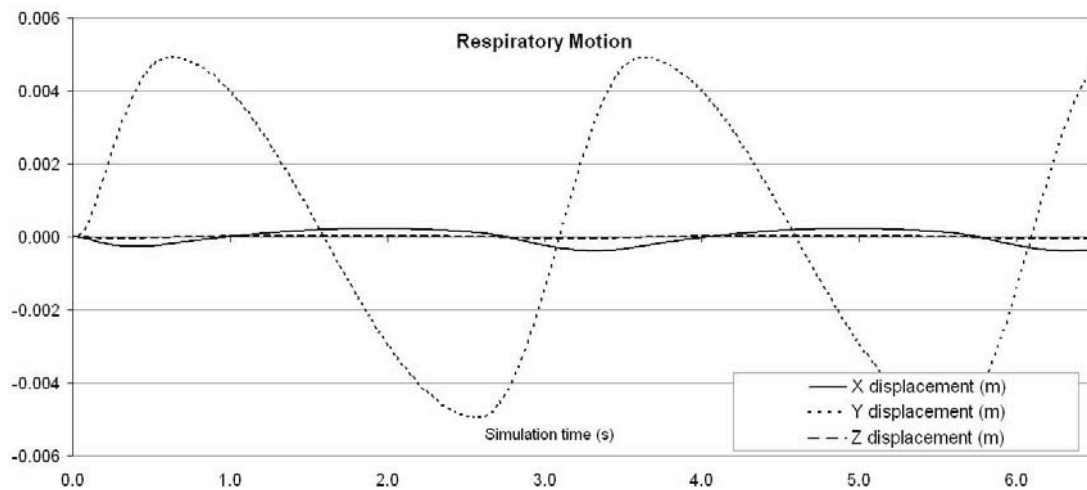


Figure 4: Respiratory motion

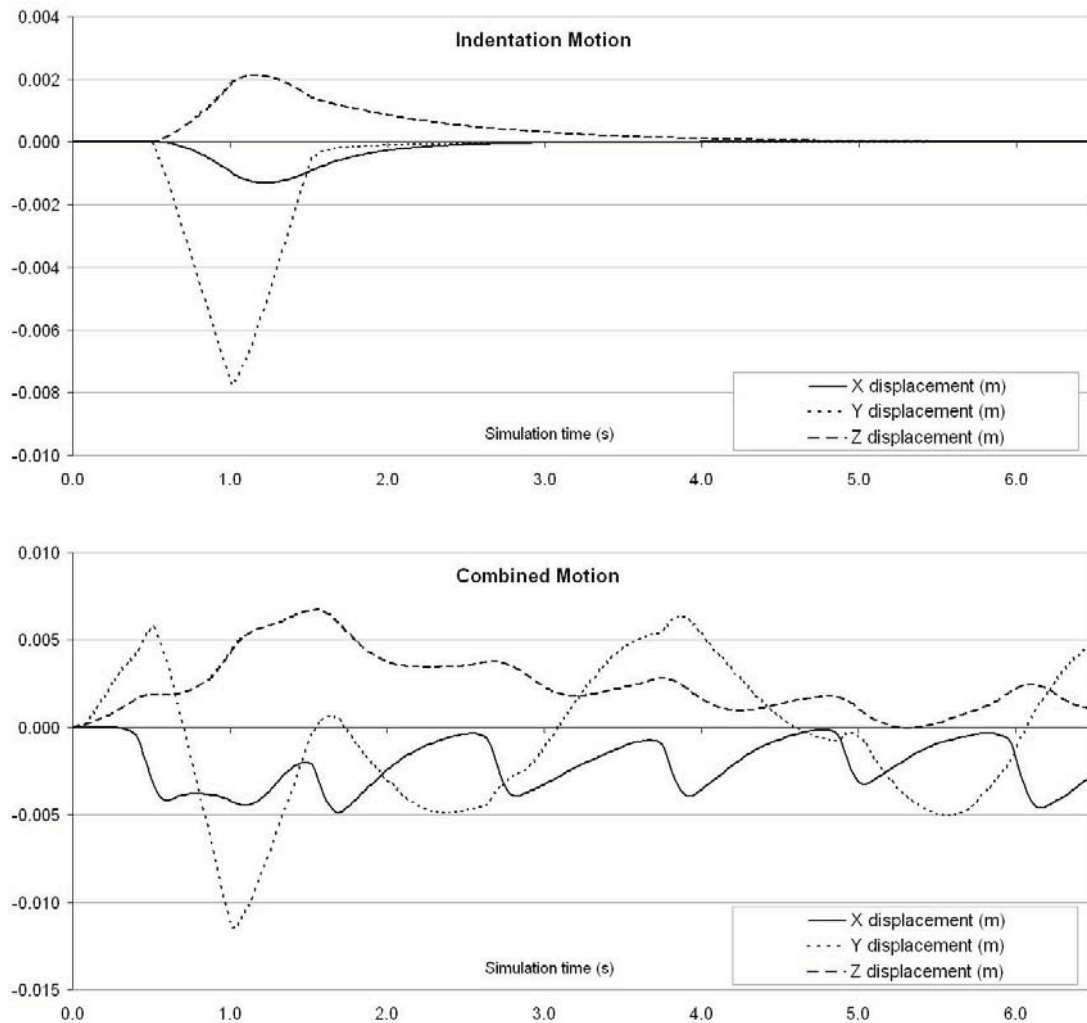


Figure 6: Combined intrinsic, respiratory and indentation motion

4 Conclusion

This paper describes a novel technique for constructing nonlinear finite element simulations with cyclical motion recovered from 4D tomographic scan data, whereby external forces and positional constraints can be combined to produce realistic composite behaviour. The technique has immediate applications in the field of patient-specific surgery simulation, and will also form the basis of an image-constrained biomechanical modelling approach to intraoperative image guidance. Future work includes validation of the technique with real patient data, an efficient GPU implementation, anisotropic weighting during the force recovery procedure, and the introduction of weight interpolation and scaling such that the frequency and intensity of the cyclic motion can be modified.

Acknowledgements

The Image Registration Toolkit was used under licence from IXICO Ltd.. The authors would like to thank staff at St. Mary's and the Royal Brompton hospitals.

References

- [1] Klaus-Jürgen Bathe. *Finite element procedures*. Prentice Hall India, 1st edition, 2007.
- [2] Guntram Berti. Image-based unstructured 3D mesh generation for medical applications. In *European Congress on Computational Methods in Applied Sciences and Engineering - ECCOMAS 2004*. University of Jyväskylä, Department of Mathematical Information Technology, 2004.
- [3] Martin Kauer. *Inverse Finite Element Characterization of Soft Tissues with Aspiration Experiments*. PhD thesis, Swiss Federal Institute of Technology, Zurich, 2001.
- [4] F. Kruggel and M. Tittgemeyer. Inverse Biomechanical Models of the Brain. In *Proceedings of the 2001 Bioengineering Conference*, pages 837–838. The American Society of Mechanical Engineers, New York, 2001.
- [5] Karol Miller, Grand Joldes, Dane Lance, and Adam Wittek. Total lagrangian explicit dynamics finite element algorithm for computing soft tissue deformation. *Communications in Numerical Methods in Engineering*, 23:121–134, 2007.
- [6] Philip Pratt, Fernando Bello, Eddie Edwards, and Daniel Rueckert. Interactive finite element simulation of the beating heart for image-guided robotic cardiac surgery. In *Medicine Meets Virtual Reality 16*, pages 378–383. IOS Press, 2008.
- [7] D. Rueckert, L. I. Sonoda, C. Hayes, D. L. G. Hill, M. O. Leach, and D. J. Hawkes. Non-rigid registration using free-form deformations: Application to breast MR images. *IEEE Transactions on Medical Imaging*, 18(8):712–721, 1999.
- [8] J. A. Schnabel, D. Rueckert, M. Quist, J. M. Blackall, A. D. Castellano-Smith, T. Hartkens, G. P. Penney, W. A. Hall, H. Liu, C. L. Truwit, F. A. Gerritsen, D. L. G. Hill, and D. J. Hawkes. A generic framework for non-rigid registration based on non-uniform multi-level free-form deformations. In *MICCAI 2001*, pages 573–581. Springer, 2001.
- [9] Zeike A. Taylor, Mario Cheng, and Sébastien Ourselin. Real-time nonlinear finite element analysis for surgical simulation using graphics processing units. In *MICCAI 2007, Part I*, pages 701–708. Springer, 2007.
- [10] O. C. Zienkiewicz and R. L. Taylor. *The Finite Element Method, Volume 2: Solid Mechanics*. Butterworth-Heinemann, 5th edition, 2000.

Nonlinear Elastic Registration with Unbiased Regularization in Three Dimensions

Igor Yanovsky¹, Carole Le Guyader², Alex Leow³,
Paul Thompson³ and Luminita Vese¹

August 1, 2008

¹Department of Mathematics, University of California, Los Angeles, CA, USA

²Institute of Mathematical Research of Rennes, France

³Laboratory of Neuro Imaging, UCLA School of Medicine, Los Angeles, CA, USA

Abstract

We propose a new nonlinear image registration model which is based on nonlinear elastic regularization and unbiased registration. The nonlinear elastic and the unbiased regularization terms are simplified using the change of variables by introducing an unknown that approximates the Jacobian matrix of the displacement field. This reduces the minimization to involve linear differential equations. In contrast to recently proposed unbiased fluid registration method, the new model is written in a unified variational form and is minimized using gradient descent. As a result, the new unbiased nonlinear elasticity model is computationally more efficient and easier to implement than the unbiased fluid registration. The unbiased large-deformation nonlinear elasticity method was tested using volumetric serial magnetic resonance images and shown to have some advantages for medical imaging applications.

1 Introduction

Given two images, the source and target, the goal of image registration is to find an optimal diffeomorphic spatial transformation such that the deformed source image is aligned with the target image. In the case of non-parametric registration methods (the class of methods we are interested in), the problem can be phrased as a functional minimization problem whose unknown is the displacement vector field \mathbf{u} . Usually, the devised functional consists of a distance measure (intensity-based, correlation-based, mutual-information based [11] or metric-structure-comparison based [10]) and a regularizer that guarantees smoothness of the displacement vector field. Several regularizers have been investigated (see Part II of [11] for a review). Generally, physical arguments motivate the selection of the regularizer. Among those currently used is the linear elasticity smoother first introduced by Broit [2]. The objects to be registered are considered to be observations of the same elastic body at two different times, before and after being subjected to a deformation as mentioned in [11]. The smoother, in this case, is the linearized elastic potential of the displacement vector field. However, this model is unsuitable for problems involving large-magnitude deformations.

In [5], Christensen *et al.* proposed a viscous fluid model to overcome this issue. Given the force field \mathbf{f} , the deforming image is considered to be embedded in viscous fluid whose motion is governed by Navier-Stokes equations for conservation of momentum:

$$\mu\Delta\mathbf{v}(\mathbf{x},t) + (\nu + \mu)\nabla(\nabla \cdot \mathbf{v}(\mathbf{x},t)) = \mathbf{f}(\mathbf{x},\mathbf{u}(\mathbf{x},t)), \quad (1)$$

$$\mathbf{v}(\mathbf{x},t) = \mathbf{u}_t(\mathbf{x},t) + \nabla\mathbf{u}(\mathbf{x},t) \cdot \mathbf{v}(\mathbf{x},t). \quad (2)$$

Here, equation (2), defining material derivative of the displacement field \mathbf{u} , nonlinearly relates the velocity \mathbf{v} and displacement vector fields. Constants μ and ν are viscosity coefficients of a fluid.

One drawback of this method is the computational cost. Numerically, the image-derived force field $\mathbf{f}(\mathbf{x},\mathbf{u}(\mathbf{x},t))$ is first computed at time t . Fixing the force field \mathbf{f} , linear equation (1) is solved for $\mathbf{v}(\mathbf{x},t)$ numerically using the successive over-relaxation (SOR) scheme. Then, an explicit Euler scheme is used to advance \mathbf{u} in time. Recent works [3, 14, 13] applied Riemannian nonlinear elasticity priors to deformation velocity fields. These alternating frameworks, however, are time-consuming, which motivates the search for faster implementations (see for instance [1] or [7] in which the instantaneous velocity \mathbf{v} is obtained by convolving \mathbf{f} with a Gaussian kernel).

In this paper, we propose an alternative approach to fluid registration. The proposed model is derived from a variational problem which is not in the form of a two-step algorithm and which can produce large-magnitude deformations. For that purpose, a nonlinear elasticity smoother is introduced. As will be seen later, the computation of the Euler-Lagrange equations in this case is cumbersome. We circumvent this issue by introducing a second unknown, a matrix variable V , which approximates the Jacobian matrix of \mathbf{u} . The nonlinear elastic regularizer is now applied to V . The Euler-Lagrange equations are straightforwardly derived and a gradient descent method is used.

Also, allowing large deformations to occur may yield non-diffeomorphic deformation mappings (at least at the discrete level). In [5], Christensen *et al.* proposed a regriding technique that resamples the deforming image and re-initializes the process once the value of the deformation Jacobian drops below a certain threshold. In [8], Haber and Modersitzki introduced an elastic registration model subject to volume-preserving constraints. To ensure that the transformation $\mathbf{g}(\mathbf{x}) = \mathbf{x} - \mathbf{u}(\mathbf{x})$ is volume-preserving (that is, for any domain Ω , $\int_{\Omega} d\mathbf{x} = \int_{\mathbf{g}(\Omega)} d\mathbf{x}$), they proposed the following pointwise constraint: $\det(I - D\mathbf{u}(\mathbf{x})) - 1 = 0$. Pursuing the same direction in [9], the authors introduced a minimization problem under inequality constraints on the Jacobian.

Here we use an information-theoretic approach previously introduced in [16]. In [16], the authors considered

a smooth deformation \mathbf{g} that maps domain Ω bijectively onto itself. Consequently, \mathbf{g} and \mathbf{g}^{-1} are bijective and globally volume-preserving. Probability density functions can thus be associated with the deformation \mathbf{g} and its inverse \mathbf{g}^{-1} . The authors then proposed to quantify the magnitude of the deformation by means of the symmetric Kullback-Leibler distance between the probability density functions associated with the deformation and the identity mapping. This distance, when rewritten using skew-symmetry properties, is viewed as a cost function and is combined with the viscous fluid model for registration, which leads to an unbiased fluid registration model. Unlike the unbiased fluid registration model, the unbiased nonlinear elasticity method, introduced here, allows the functional to be written “in closed form”. The new model also does not require expensive Navier-Stokes solver (or its approximation) at each step as previously mentioned.

2 Method

Let Ω be an open and bounded domain in \mathbb{R}^3 . Without loss of generality, we assume that the volume of Ω is 1, i.e. $|\Omega| = 1$. Let $I_1, I_2 : \Omega \rightarrow \mathbb{R}$ be the two volumetric images to be registered. We seek the transformation $\mathbf{g} : \Omega \rightarrow \Omega$ that maps the source image I_2 into correspondence with the target image I_1 . In this paper, we will restrict this mapping to be differentiable, one-to-one, and onto. We denote the Jacobian matrix of a deformation \mathbf{g} to be $D\mathbf{g}$, with Jacobian denoted by $|D\mathbf{g}(\mathbf{x})| = \det(D\mathbf{g}(\mathbf{x}))$ (thus we will use the notation $|V| := \det(V)$ for any 3×3 matrix V). The displacement field $\mathbf{u}(\mathbf{x})$ from the position \mathbf{x} in the deformed image $I_2 \circ \mathbf{g}(\mathbf{x})$ back to $I_2(\mathbf{x})$ is defined in terms of the deformation $\mathbf{g}(\mathbf{x})$ by the expression $\mathbf{g}(\mathbf{x}) = \mathbf{x} - \mathbf{u}(\mathbf{x})$ at every point $\mathbf{x} \in \Omega$. Thus, we consider the problems of finding \mathbf{g} and \mathbf{u} as equivalent.

In general, nonlinear image registration models may be formulated in a variational framework. The minimization problems often define the energy functional E as a linear combination of an image matching term F and a regularizing term R : $\inf_{\mathbf{u}} \{E(\mathbf{u}) = F(\mathbf{u}) + \lambda_0 R(\mathbf{u})\}$. Here, $\lambda_0 > 0$ is a weighting parameter.

2.1 Registration metrics

In this paper, the matching functional F takes the form of the L^2 norm (the sum of squared intensity differences), $F = F_{L^2}$, and the mutual information, $F = F_{MI}$.

L^2 -norm: The L^2 -norm matching functional is suitable when the images have been acquired through similar sensors (with additive Gaussian noise) and thus are expected to present the same intensity range and distribution. The L^2 distance between the deformed image $I_2 \circ \mathbf{g}(\mathbf{x}) = I_2(\mathbf{x} - \mathbf{u}(\mathbf{x}))$ and target image $I_1(\mathbf{x})$ is defined as

$$F_{L^2}(\mathbf{u}) = \frac{1}{2} \int_{\Omega} (I_2(\mathbf{x} - \mathbf{u}(\mathbf{x})) - I_1(\mathbf{x}))^2 d\mathbf{x}. \quad (3)$$

Mutual Information: Mutual information can be used to align images of different modalities, without requiring knowledge of the relationship of the two registered images [6, 15]. Here, the intensity distributions estimated from $I_1(\mathbf{x})$ and $I_2(\mathbf{x} - \mathbf{u}(\mathbf{x}))$ are denoted by p^{I_1} and $p_{\mathbf{u}}^{I_2}$, respectively, and an estimate of their joint intensity distribution by $p_{\mathbf{u}}^{I_1, I_2}$. We let $i_1 = I_1(\mathbf{x})$, $i_2 = I_2(\mathbf{x} - \mathbf{u}(\mathbf{x}))$ denote intensity values at point $\mathbf{x} \in \Omega$. Given the displacement field \mathbf{u} , the mutual information computed from I_1 and I_2 is provided by

$$MI_{\mathbf{u}}^{I_1, I_2} = \int_{\mathbb{R}^2} p_{\mathbf{u}}^{I_1, I_2}(i_1, i_2) \log[p_{\mathbf{u}}^{I_1, I_2}(i_1, i_2) / (p^{I_1}(i_1) p_{\mathbf{u}}^{I_2}(i_2))] di_1 di_2.$$

We seek to maximize the mutual information between $I_2(\mathbf{x} - \mathbf{u}(\mathbf{x}))$ and $I_1(\mathbf{x})$, or equivalently, minimize the negative of $MI_{\mathbf{u}}^{I_1, I_2}$:

$$F_{MI}(I_1, I_2, \mathbf{u}) = -MI_{\mathbf{u}}^{I_1, I_2}. \quad (4)$$

2.2 Nonlinear Elastic Regularization

The theory of elasticity is based on the notion of strain. Strain is defined as the amount of deformation an object experiences compared to its original size and shape. In three spatial dimensions, the strain tensor, $\mathcal{E} = [\varepsilon_{ij}] \in \mathbb{R}^{3 \times 3}$, $1 \leq i, j \leq 3$, is a symmetric tensor used to quantify the strain of an object undergoing a deformation. The nonlinear strain is defined as

$$\varepsilon_{ij}(\mathbf{u}) = \frac{1}{2}(\partial_j u_i + \partial_i u_j + \sum_{k=1}^3 \partial_i u_k \partial_j u_k),$$

with the nonlinear strain tensor matrix given by

$$\mathcal{E}(\mathbf{u}) = \frac{1}{2}(D\mathbf{u}^t + D\mathbf{u} + D\mathbf{u}^t D\mathbf{u}). \quad (5)$$

Stored energy (Saint Venant-Kirchhoff material) is defined as

$$W(\mathcal{E}) = \frac{\nu}{2}(\text{trace}(\mathcal{E}))^2 + \mu \text{trace}(\mathcal{E}^2),$$

where ν and μ are Lamé elastic material constants. The regularization for nonlinear elasticity becomes

$$R_E(\mathbf{u}) = \int_{\Omega} W(\mathcal{E}(\mathbf{u})) d\mathbf{x}.$$

The regularization term $R_E(\mathbf{u})$ can be minimized with respect to \mathbf{u} . However, since the regularization term is written in terms of partial derivatives of components of \mathbf{u} , the Euler-Lagrange equations become complicated and are computationally expensive to minimize. Instead, following earlier theoretical work [12], we minimize an approximate functional by introducing the matrix variable

$$V \approx D\mathbf{u} \quad (6)$$

and thus consider a new form of nonlinear elasticity regularization functional

$$R_E(\mathbf{u}, V) = \int_{\Omega} W(\widehat{V}) d\mathbf{x} + \frac{\beta}{2} \int_{\Omega} \|V - D\mathbf{u}\|_F^2 d\mathbf{x}, \quad (7)$$

where $\widehat{V} = \frac{1}{2}(V^t + V + V^t V)$, β is a positive constant, and $\|\cdot\|_F$ denotes the Frobenius norm. In the limit, as $\beta \rightarrow +\infty$, we obtain $V \approx D\mathbf{u}$ in the L^2 topology.

2.3 Unbiased Registration Constraint

In [16], the authors proposed an unbiased fluid image registration approach. In this context, *unbiased* means that the Jacobian determinants of the deformations recovered between a pair of images follow a log-normal distribution, with zero mean after log-transformation. The authors argued that this distribution is beneficial when recovering changes in regions of homogeneous intensity, and in ensuring symmetrical results when the order of two images being registered is switched. As derived in [16] using information theory, the unbiased regularization term is given as

$$R_{UB}(\mathbf{u}) = \int_{\Omega} (|D(\mathbf{x} - \mathbf{u}(\mathbf{x}))| - 1) \log |D(\mathbf{x} - \mathbf{u}(\mathbf{x}))| d\mathbf{x}. \quad (8)$$

It is important to note that R_{UB} generates inverse-consistent deformation maps. The inverse-consistent property of the unbiased technique was shown in a validation study of the unbiased fluid registration methods [17]. Also, to see why minimizing equation (8) leads to unbiased deformation in the logarithmic space, we observe that the integrand is always non-negative, and only evaluates to zero when the deformation \mathbf{g} is volume-preserving everywhere ($|D\mathbf{g}| = 1$ everywhere). Thus, by treating it as a cost, we recover zero-change by minimizing this cost when we compare images differing only in noise.

Given equation (6), we have $D\mathbf{g} = I - D\mathbf{u} \approx I - V$, where I is the 3×3 identity matrix. Therefore, as in subsection 2.2, to simplify the discretization, we introduce

$$R_{UB}(V) = \int_{\Omega} (|I - V| - 1) \log |I - V| d\mathbf{x}. \quad (9)$$

Recall that here $|I - V| = \det(I - V)$.

2.4 Unbiased Nonlinear Elasticity Registration

The total energy functional employed in this work, is given as a linear combination of the similarity measure F (which is either F_{L^2} from (3) or F_{MI} from (4)), nonlinear elastic regularization R_E in (7), and unbiased regularization R_{UB} in (9):

$$E(\mathbf{u}, V) = F(\mathbf{u}) + R_E(\mathbf{u}, V) + \lambda R_{UB}(V). \quad (10)$$

The explicit weighting parameter is omitted in front of $R_E(\mathbf{u}, V)$, since this term is weighted by Lamé constants ν and μ . We solve the Euler-Lagrange equations in \mathbf{u} and V using the gradient descent method, parameterizing the descent direction by an artificial time t ,

$$\frac{\partial \mathbf{u}}{\partial t} = -\partial_{\mathbf{u}} E(\mathbf{u}, V) = -\partial_{\mathbf{u}} F(\mathbf{u}) - \partial_{\mathbf{u}} R_E(\mathbf{u}, V), \quad (11)$$

$$\frac{\partial V}{\partial t} = -\partial_V E(\mathbf{u}, V) = -\partial_V R_E(\mathbf{u}, V) - \lambda \partial_V R_{UB}(V), \quad (12)$$

which gives systems of three and nine equations, respectively. Explicit expressions for the gradients and their discretizations are given in Section 3.

Remark: The regularization on the deformation \mathbf{g} proposed in this work can be expressed in a general form

$$R(\mathbf{g}) = \int_{\Omega} R_1(D\mathbf{g}) d\mathbf{x} + \int_{\Omega} R_2(|D\mathbf{g}|) d\mathbf{x},$$

with $|D\mathbf{g}| := \det(D\mathbf{g})$. For the minimization, an auxiliary variable can also be introduced to simplify the numerical calculations, removing the nonlinearity in the derivatives.

3 Implementation

3.1 The Energy Gradients

Computing the first variation of functional F_{L^2} in (3) gives the following gradient: $\partial_{\mathbf{u}} F_{L^2}(\mathbf{u}) = -[I_2(\mathbf{x} - \mathbf{u}(\mathbf{x})) - I_1(\mathbf{x})] \nabla I_2(\mathbf{x} - \mathbf{u}(\mathbf{x}))$.

The gradient of (4) is given by $\partial_{\mathbf{u}} F_{MI}(\mathbf{u}) = (1/|\Omega|)[Q_{\mathbf{u}} * \partial G_{\sigma}/\partial \xi_2](I_1(\mathbf{x}), I_2(\mathbf{x} - \mathbf{u})) \nabla I_2(\mathbf{x} - \mathbf{u})$, where $Q_{\mathbf{u}}(i_1, i_2) = 1 + \log[p_{\mathbf{u}}^{I_1, I_2}(i_1, i_2)/p^{I_1}(i_1)p_{\mathbf{u}}^{I_2}(i_2)]$, and $G_{\sigma}(\xi_1, \xi_2)$ is a two-dimensional Gaussian kernel, with variance σ^2 , which is used to estimate the joint intensity distribution from $I_2(\mathbf{x} - \mathbf{u})$ and $I_1(\mathbf{x})$.

Computing the first variation of functional $R_E(\mathbf{u}, V)$, in equation (7), with respect to \mathbf{u} gives the following components of the gradient $\partial_{\mathbf{u}} R_E(\mathbf{u}, V)$:

$$\partial_{u_k} R_E(\mathbf{u}, V) = \beta(\partial_1 v_{k1} + \partial_2 v_{k2} + \partial_3 v_{k3} - \Delta u_k), \quad k = 1, 2, 3.$$

The first variation of $R_E(\mathbf{u}, V)$ with respect to V , with $V = [v_{ij}]$, gives $\partial_V R_E(\mathbf{u}, V)$:

$$\begin{aligned} \partial_{v_{11}} R_E(\mathbf{u}, V) &= \beta(v_{11} - \partial_1 u_1) + \nu c_1(1 + v_{11}) + \mu(c_2(1 + v_{11}) + c_5 v_{12} + c_6 v_{13}), \\ \partial_{v_{12}} R_E(\mathbf{u}, V) &= \beta(v_{12} - \partial_2 u_1) + \nu c_1 v_{12} + \mu(c_3 v_{12} + c_5(1 + v_{11}) + c_7 v_{13}), \\ \partial_{v_{13}} R_E(\mathbf{u}, V) &= \beta(v_{13} - \partial_3 u_1) + \nu c_1 v_{13} + \mu(c_4 v_{13} + c_6(1 + v_{11}) + c_7 v_{12}), \\ \partial_{v_{21}} R_E(\mathbf{u}, V) &= \beta(v_{21} - \partial_1 u_2) + \nu c_1 v_{21} + \mu(c_2 v_{21} + c_5(1 + v_{22}) + c_6 v_{23}), \\ \partial_{v_{22}} R_E(\mathbf{u}, V) &= \beta(v_{22} - \partial_2 u_2) + \nu c_1(1 + v_{22}) + \mu(c_3(1 + v_{22}) + c_5 v_{21} + c_7 v_{23}), \\ \partial_{v_{23}} R_E(\mathbf{u}, V) &= \beta(v_{23} - \partial_3 u_2) + \nu c_1 v_{23} + \mu(c_4 v_{23} + c_6 v_{21} + c_7(1 + v_{22})), \\ \partial_{v_{31}} R_E(\mathbf{u}, V) &= \beta(v_{31} - \partial_1 u_3) + \nu c_1 v_{31} + \mu(c_2 v_{31} + c_5 v_{32} + c_6(1 + v_{33})), \\ \partial_{v_{32}} R_E(\mathbf{u}, V) &= \beta(v_{32} - \partial_2 u_3) + \nu c_1 v_{32} + \mu(c_3 v_{32} + c_5 v_{31} + c_7(1 + v_{33})), \\ \partial_{v_{33}} R_E(\mathbf{u}, V) &= \beta(v_{33} - \partial_3 u_3) + \nu c_1(1 + v_{33}) + \mu(c_4(1 + v_{33}) + c_6 v_{31} + c_7 v_{32}), \end{aligned}$$

where

$$\begin{aligned} c_1 &= v_{11} + v_{22} + v_{33} + \frac{1}{2}(v_{11}^2 + v_{21}^2 + v_{31}^2 + v_{12}^2 + v_{22}^2 + v_{32}^2 + v_{13}^2 + v_{23}^2 + v_{33}^2), \\ c_2 &= 2v_{11} + v_{11}^2 + v_{21}^2 + v_{31}^2, & c_5 &= v_{21} + v_{12} + v_{11}v_{12} + v_{21}v_{22} + v_{31}v_{32}, \\ c_3 &= 2v_{22} + v_{12}^2 + v_{22}^2 + v_{32}^2, & c_6 &= v_{31} + v_{13} + v_{11}v_{13} + v_{21}v_{23} + v_{31}v_{33}, \\ c_4 &= 2v_{33} + v_{13}^2 + v_{23}^2 + v_{33}^2, & c_7 &= v_{32} + v_{23} + v_{12}v_{13} + v_{22}v_{23} + v_{32}v_{33}. \end{aligned}$$

We can compute the first variation of (9), obtaining $\partial_V R_{UB}(V)$. We first simplify the notation, letting $J = |I - V|$. Also, denote $L(J) = (J - 1) \log J$. Hence, $L'(J) = dL(J)/dJ = 1 + \log J - 1/J$. Thus,

$$\begin{aligned} \partial_{v_{11}} R_{UB}(V) &= -((1 - v_{22})(1 - v_{33}) - v_{32}v_{23})L'(J), \\ \partial_{v_{12}} R_{UB}(V) &= -(v_{23}v_{31} + v_{21}(1 - v_{33}))L'(J), \\ \partial_{v_{13}} R_{UB}(V) &= -(v_{21}v_{32} + (1 - v_{22})v_{31})L'(J), \\ \partial_{v_{21}} R_{UB}(V) &= -(v_{32}v_{13} + v_{12}(1 - v_{33}))L'(J), \\ \partial_{v_{22}} R_{UB}(V) &= -((1 - v_{11})(1 - v_{33}) - v_{13}v_{31})L'(J), \\ \partial_{v_{23}} R_{UB}(V) &= -(v_{12}v_{31} + v_{32}(1 - v_{11}))L'(J), \\ \partial_{v_{31}} R_{UB}(V) &= -(v_{12}v_{23} + v_{13}(1 - v_{22}))L'(J), \\ \partial_{v_{32}} R_{UB}(V) &= -(v_{21}v_{13} + v_{23}(1 - v_{11}))L'(J), \\ \partial_{v_{33}} R_{UB}(V) &= -((1 - v_{11})(1 - v_{22}) - v_{12}v_{21})L'(J). \end{aligned}$$

3.2 Numerical Discretization

Let $\Delta x_1, \Delta x_2, \Delta x_3$ be the spacial steps, Δt be the time step, and $(x_{1i}, x_{2j}, x_{3k}) = (i\Delta x_1, j\Delta x_2, k\Delta x_3)$ be the grid points, for $1 \leq i \leq M, 1 \leq j \leq N, 1 \leq k \leq P$. For a function $\varphi : \Omega \rightarrow \mathbb{R}$, let $\varphi_{i,j,k}^n =$

$\varphi(n\Delta t, i\Delta x_1, j\Delta x_2, k\Delta x_3)$. We define the difference operators based on uniformly-spaced grid as

$$\begin{aligned} D^{x_1}\varphi_{i,j,k}^n &= \frac{\varphi_{i+1,j,k}^n - \varphi_{i-1,j,k}^n}{2\Delta x_1}, & D^{x_1x_1}\varphi_{i,j,k}^n &= \frac{\varphi_{i+1,j,k}^n - 2\varphi_{i,j,k}^n + \varphi_{i-1,j,k}^n}{\Delta x_1^2}, \\ D^{x_2}\varphi_{i,j,k}^n &= \frac{\varphi_{i,j+1,k}^n - \varphi_{i,j-1,k}^n}{2\Delta x_2}, & D^{x_2x_2}\varphi_{i,j,k}^n &= \frac{\varphi_{i,j+1,k}^n - 2\varphi_{i,j,k}^n + \varphi_{i,j-1,k}^n}{\Delta x_2^2}, \\ D^{x_3}\varphi_{i,j,k}^n &= \frac{\varphi_{i,j,k+1}^n - \varphi_{i,j,k-1}^n}{2\Delta x_3}, & D^{x_3x_3}\varphi_{i,j,k}^n &= \frac{\varphi_{i,j,k+1}^n - 2\varphi_{i,j,k}^n + \varphi_{i,j,k-1}^n}{\Delta x_3^2}. \end{aligned}$$

Below, we will use the following notations when it is obvious that the grid point at $(i\Delta x_1, j\Delta x_2, k\Delta x_3)$ is under consideration: $\varphi^n := \varphi_{i,j,k}^n$, $D^{x_l}\varphi^n := D^{x_l}\varphi_{i,j,k}^n$, $D^{x_lx_l}\varphi^n := D^{x_lx_l}\varphi_{i,j,k}^n$, $l = 1, 2, 3$.

To discretize equations (11) and (12), we use finite difference schemes. In order to restrict the maximum displacement change per time step from being large, equation (11) is discretized using explicit scheme with adaptive time-stepping at every point (i, j, k)

$$\begin{aligned} \frac{u_1^{n+1} - u_1^n}{\Delta t} &= -[\partial_{u_1}F(\mathbf{u}^n)] - \beta(D^{x_1}v_{11}^n + D^{x_2}v_{12}^n + D^{x_3}v_{13}^n) + \beta(D^{x_1x_1}u_1^n + D^{x_2x_2}u_1^n + D^{x_3x_3}u_1^n), \\ \frac{u_2^{n+1} - u_2^n}{\Delta t} &= -[\partial_{u_2}F(\mathbf{u}^n)] - \beta(D^{x_1}v_{21}^n + D^{x_2}v_{22}^n + D^{x_3}v_{23}^n) + \beta(D^{x_1x_1}u_2^n + D^{x_2x_2}u_2^n + D^{x_3x_3}u_2^n), \\ \frac{u_3^{n+1} - u_3^n}{\Delta t} &= -[\partial_{u_3}F(\mathbf{u}^n)] - \beta(D^{x_1}v_{31}^n + D^{x_2}v_{32}^n + D^{x_3}v_{33}^n) + \beta(D^{x_1x_1}u_3^n + D^{x_2x_2}u_3^n + D^{x_3x_3}u_3^n), \end{aligned}$$

where $[\partial_{u_l}F(\mathbf{u}^n)]$, $l = 1, 2, 3$, is a discretization of a similarity-based gradient. In our numerical experiments, $\Delta x_1 = \Delta x_2 = \Delta x_3 = 1$, and Δt is chosen so that the maximum displacement per iteration equals 0.1.

Equation (12) is discretized using semi-implicit scheme

$$\begin{aligned} \frac{v_{11}^{n+1} - v_{11}^n}{\Delta t} &= \beta(D^{x_1}u_1^n - v_{11}^{n+1}) - \nu c_1(1 + v_{11}^n) - \mu(c_2(1 + v_{11}^n) + c_5v_{12}^n + c_6v_{13}^n) \\ &\quad + \lambda((1 - v_{22}^n)(1 - v_{33}^n) - v_{32}^nv_{23}^n)L'(J), \\ \frac{v_{12}^{n+1} - v_{12}^n}{\Delta t} &= \beta(D^{x_2}u_1^n - v_{12}^{n+1}) - \nu c_1v_{12}^n - \mu(c_3v_{12}^n + c_5(1 + v_{11}^n) + c_7v_{13}^n) + \lambda(v_{23}^nv_{31}^n + v_{21}^n(1 - v_{33}^n))L'(J), \\ \frac{v_{13}^{n+1} - v_{13}^n}{\Delta t} &= \beta(D^{x_3}u_1^n - v_{13}^{n+1}) - \nu c_1v_{13}^n - \mu(c_4v_{13}^n + c_6(1 + v_{11}^n) + c_7v_{12}^n) + \lambda(v_{21}^nv_{32}^n + (1 - v_{22}^n)v_{31}^n)L'(J), \\ \frac{v_{21}^{n+1} - v_{21}^n}{\Delta t} &= \beta(D^{x_1}u_2^n - v_{21}^{n+1}) - \nu c_1v_{21}^n - \mu(c_2v_{21}^n + c_5(1 + v_{22}^n) + c_6v_{23}^n) + \lambda(v_{32}^nv_{13}^n + v_{12}^n(1 - v_{33}^n))L'(J), \\ \frac{v_{22}^{n+1} - v_{22}^n}{\Delta t} &= \beta(D^{x_2}u_2^n - v_{22}^{n+1}) - \nu c_1(1 + v_{22}^n) - \mu(c_3(1 + v_{22}^n) + c_5v_{21}^n + c_7v_{23}^n) \\ &\quad + \lambda((1 - v_{11}^n)(1 - v_{33}^n) - v_{13}^nv_{31}^n)L'(J), \\ \frac{v_{23}^{n+1} - v_{23}^n}{\Delta t} &= \beta(D^{x_3}u_2^n - v_{23}^{n+1}) - \nu c_1v_{23}^n - \mu(c_4v_{23}^n + c_6v_{21}^n + c_7(1 + v_{22}^n)) + \lambda(v_{12}^nv_{31}^n + v_{32}^n(1 - v_{11}^n))L'(J), \\ \frac{v_{31}^{n+1} - v_{31}^n}{\Delta t} &= \beta(D^{x_1}u_3^n - v_{31}^{n+1}) - \nu c_1v_{31}^n - \mu(c_2v_{31}^n + c_5v_{32}^n + c_6(1 + v_{33}^n)) + \lambda(v_{12}^nv_{23}^n + v_{13}^n(1 - v_{22}^n))L'(J), \\ \frac{v_{32}^{n+1} - v_{32}^n}{\Delta t} &= \beta(D^{x_2}u_3^n - v_{32}^{n+1}) - \nu c_1v_{32}^n - \mu(c_3v_{32}^n + c_5v_{31}^n + c_7(1 + v_{33}^n)) + \lambda(v_{21}^nv_{13}^n + v_{23}^n(1 - v_{11}^n))L'(J), \\ \frac{v_{33}^{n+1} - v_{33}^n}{\Delta t} &= \beta(D^{x_3}u_3^n - v_{33}^{n+1}) - \nu c_1(1 + v_{33}^n) - \mu(c_4(1 + v_{33}^n) + c_6v_{31}^n + c_7v_{32}^n) \\ &\quad + \lambda((1 - v_{11}^n)(1 - v_{22}^n) - v_{12}^nv_{21}^n)L'(J), \end{aligned}$$

where $L'(J)$ is defined as in Section 3.1.

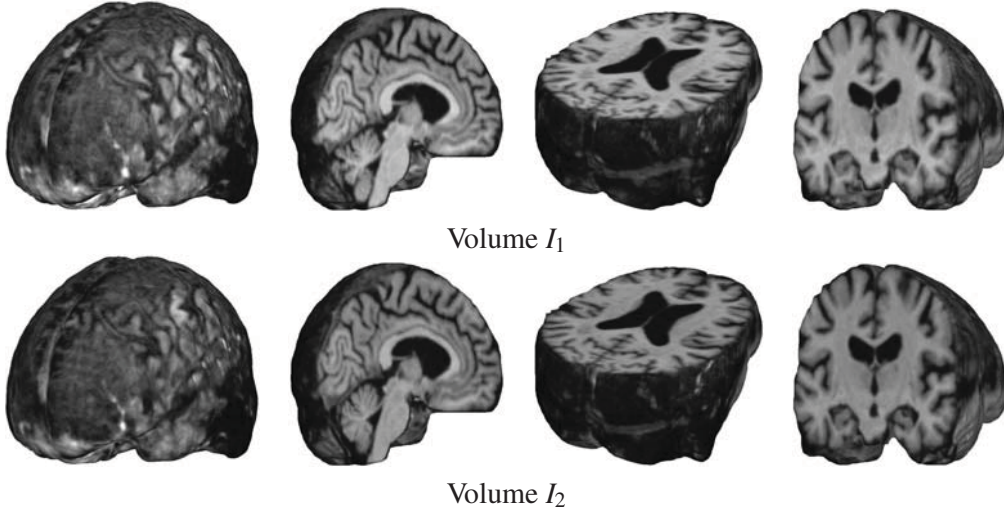


Figure 1: Serial MRI images from the ADNI follow-up dataset (images acquired one year apart) are shown. Volumes I_1 (row 1) and I_2 (row 2) are depicted as a brain volume (column 1) and from sagittal (column 2), axial (column 3), and coronal (column 4) views. Nonrigid registration aligns volume I_2 into correspondence with volume I_1 .

3.3 Algorithm

We are now ready to give the algorithm for the unbiased registration via nonlinear elastic regularization.

Algorithm 1 Unbiased Registration via Nonlinear Elastic Regularization

- 1: Initialize $t = 0$, $\mathbf{u}(\mathbf{x}, 0) = 0$, and $V(\mathbf{x}, 0) = 0$.
 - 2: Calculate $V(\mathbf{x}, t)$ using equation (12), where the equation is discretized using the semi-implicit method described in Section 3.2.
Steps 3-5 describe the procedure for solving equation (11) advancing $\mathbf{u}(\mathbf{x}, t)$ in time using the explicit scheme. Numerical discretization is described in Section 3.2.
 - 3: Calculate the perturbation of the displacement field $\mathbf{R}(\mathbf{x}) = -\partial E_{\mathbf{u}}(\mathbf{u}, V)$.
 - 4: Time step Δt is calculated adaptively so that $\Delta t \cdot \max(\|\mathbf{R}\|_2) = \delta u$, where δu is the maximal displacement allowed in one iteration. Results in this work are obtained with $\delta u = 0.1$.
 - 5: Advance equation (11), i.e. $\partial \mathbf{u}(\mathbf{x}, t) / \partial t = \mathbf{R}(\mathbf{x})$, in time, with time step from step 4, solving for $\mathbf{u}(\mathbf{x}, t)$.
 - 6: If the cost functional in (10) decreases by sufficiently small amount compared to the previous iteration, then stop.
 - 7: Let $t := t + \Delta t$ and go to step 2.
-

4 Results and Discussion

We tested the proposed *unbiased nonlinear elastic* registration model and compared the results to those obtained with the *unbiased fluid registration* method [16], where the unbiased regularization constraint (8) was coupled with the L^2 matching functional (3) and fluid regularization (1), (2). Here, both methods were coupled with the L^2 and mutual information (MI) based similarity measures. In our experiments, we used a pair of serial MRI images ($220 \times 220 \times 220$) from the Alzheimer's Disease Neuroimaging Initiative (ADNI). Since the images were acquired one year apart, from a subject with Alzheimer's disease, real anatomical changes are present, which allows methods to be compared in the presence of true biological changes.

In the tests performed using unbiased nonlinear elasticity coupled with L^2 matching, values of $\beta = 20000$

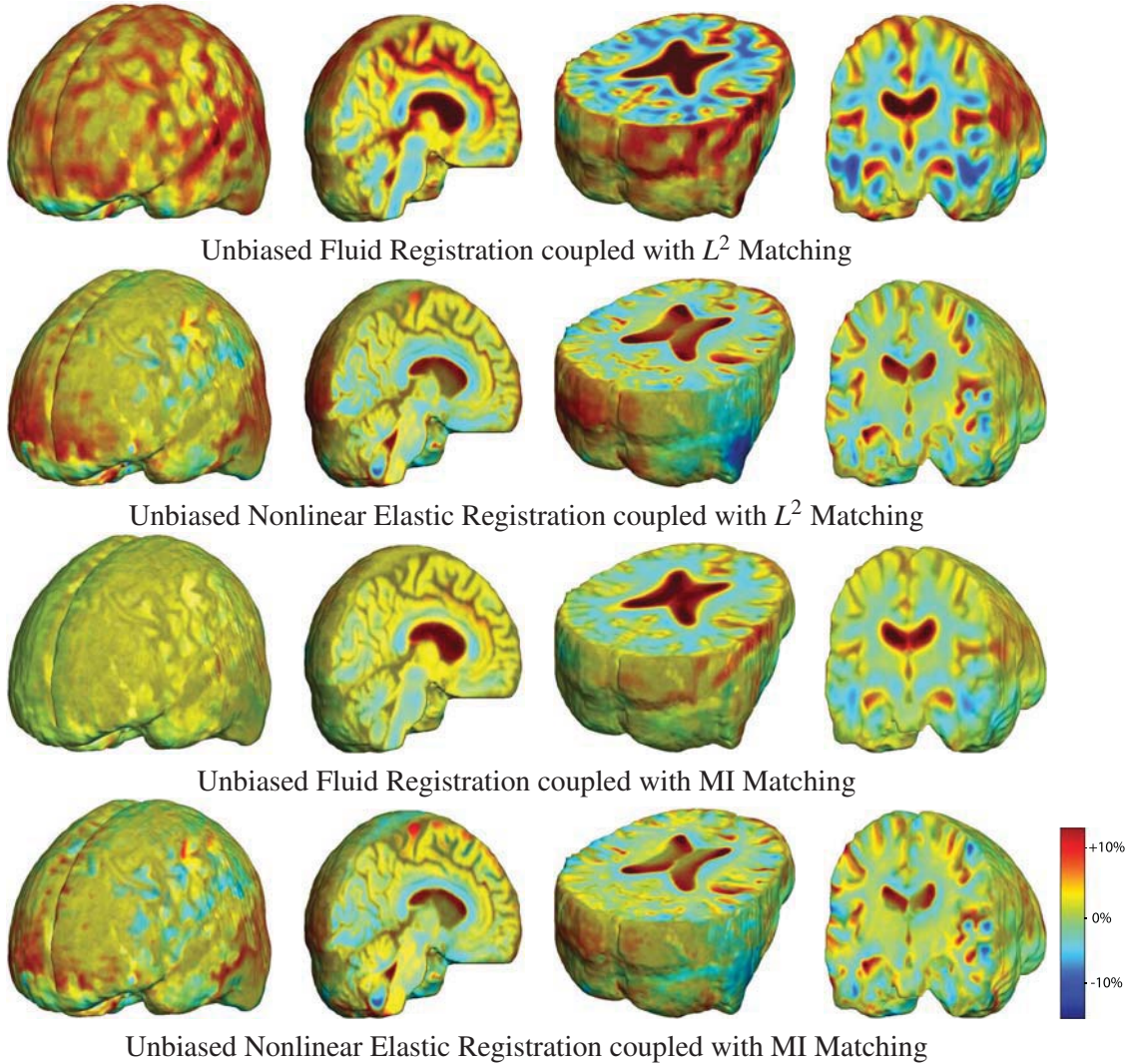


Figure 2: Nonrigid registration was performed on the Serial MRI images from the ADNI Follow-up dataset using unbiased fluid registration and unbiased nonlinear elasticity registration, both coupled with L^2 and MI matching. Jacobian maps are superimposed on the target volume.

in equation (7) and $\lambda = 2000$ in equation (10) were chosen. For MI matching, $\beta = 80$ and $\lambda = 8$ were used. The values of the Lamé coefficients were chosen to be equal, $\mu = \nu$, in all experiments. Bigger values of μ and ν allow for more smoothing. For unbiased fluid registration model, described in [16], $\lambda = 500$ was chosen for L^2 matching, and $\lambda = 5$ for MI matching.

Figure 1 shows the images being registered and Figures 2 shows the resulting Jacobian maps. Results generated using the fluid and nonlinear elasticity based unbiased models are similar, both suggesting a mild volume reduction in gray and white matter and ventricular enlargement that is observed in Alzheimer's disease patients. The advantages of the unbiased nonlinear elasticity model is its more locally plausible reproduction of atrophic changes in the brain and its robustness to original misalignment of brain volumes, which is especially noticeable on the brain surface. The unbiased nonlinear elasticity model coupled with L^2 matching generated very similar results to those obtained with the MI similarity measure, partly because difference images typically contain only noise after registration. Unbiased fluid registration method, however, is more effective in modeling the regional neuroanatomical changes, showing more clearly which parts

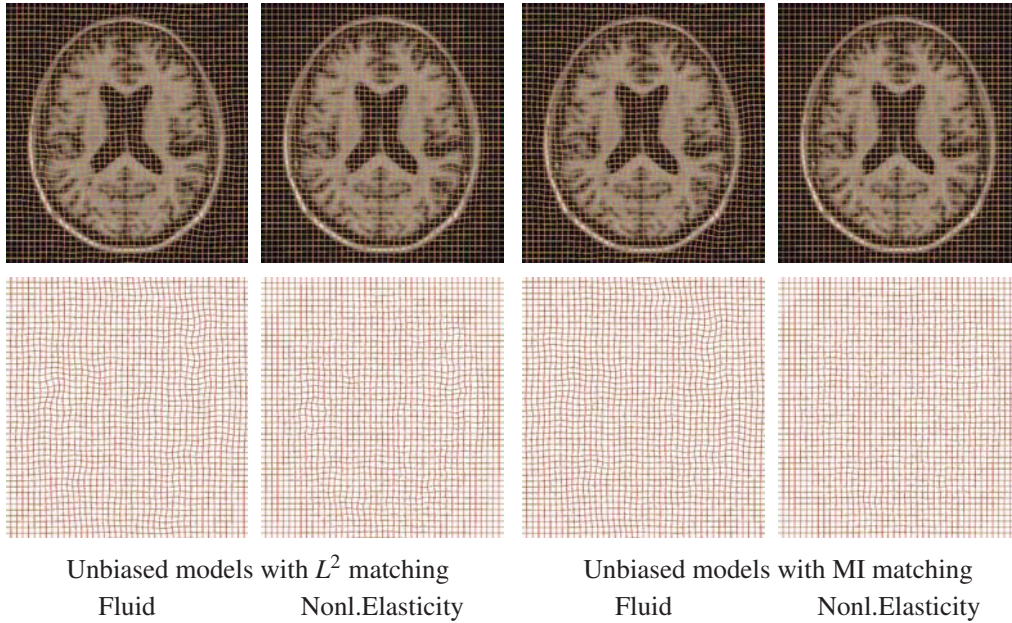


Figure 3: Results obtained using unbiased fluid registration and unbiased nonlinear elasticity registration, both coupled with L^2 and MI matching. The generated grids are superimposed on top of 2D cross-sections of the 3D volumes (row 1) and are shown separately (row 2).

of the volume have undergone largest tissue changes, such as ventricular enlargement as shown in Figure 2.

Figure 3 shows deformed grids generated with unbiased fluid and unbiased nonlinear elastic registration models. Figure 4 shows the energy decrease per iteration for both models. Note that the unbiased fluid registration minimizes the energy defined as $E(\mathbf{u}) = F(\mathbf{u}) + \lambda R_{UB}(\mathbf{u})$.

In Figure 5, we examined the *inverse consistency* of the mappings [4] generated using unbiased nonlinear elastic registration. Here, the deformation was computed in both directions (time 2 to time 1, and time 1 to time 2) using MI matching. The forward and backward Jacobian maps were concatenated (in an ideal situation, this operation should yield the identity), with the products of Jacobians having values close to 1.

The unbiased nonlinear elasticity model does not require expensive Navier-Stokes solver (or its approximation), which is employed at each iteration for fluid flow models. Hence, unbiased nonlinear elasticity model is more efficient than the unbiased fluid step. In our future studies, we will examine the registration accuracy of the different models where ground truth is known, and will compare each model’s power for detecting inter-group differences or statistical effects on rates of atrophy.

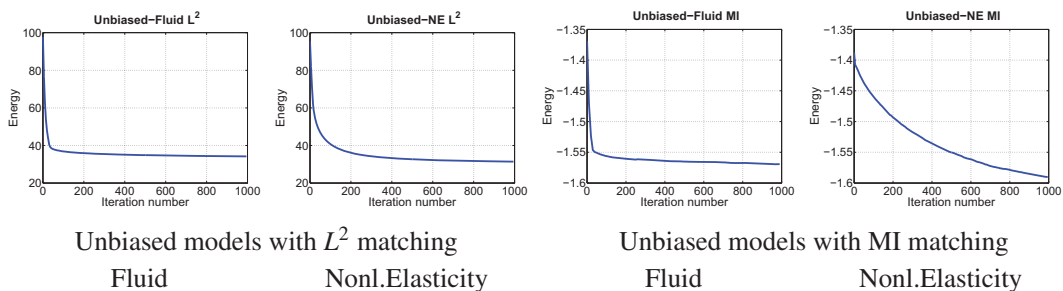


Figure 4: Energy per iteration for the unbiased fluid registration and unbiased nonlinear elasticity registration, both coupled with L^2 and MI matching.

Acknowledgements

This work was funded by the National Institutes of Health through the NIH Roadmap for Medical Research, Grant U54 RR021813.

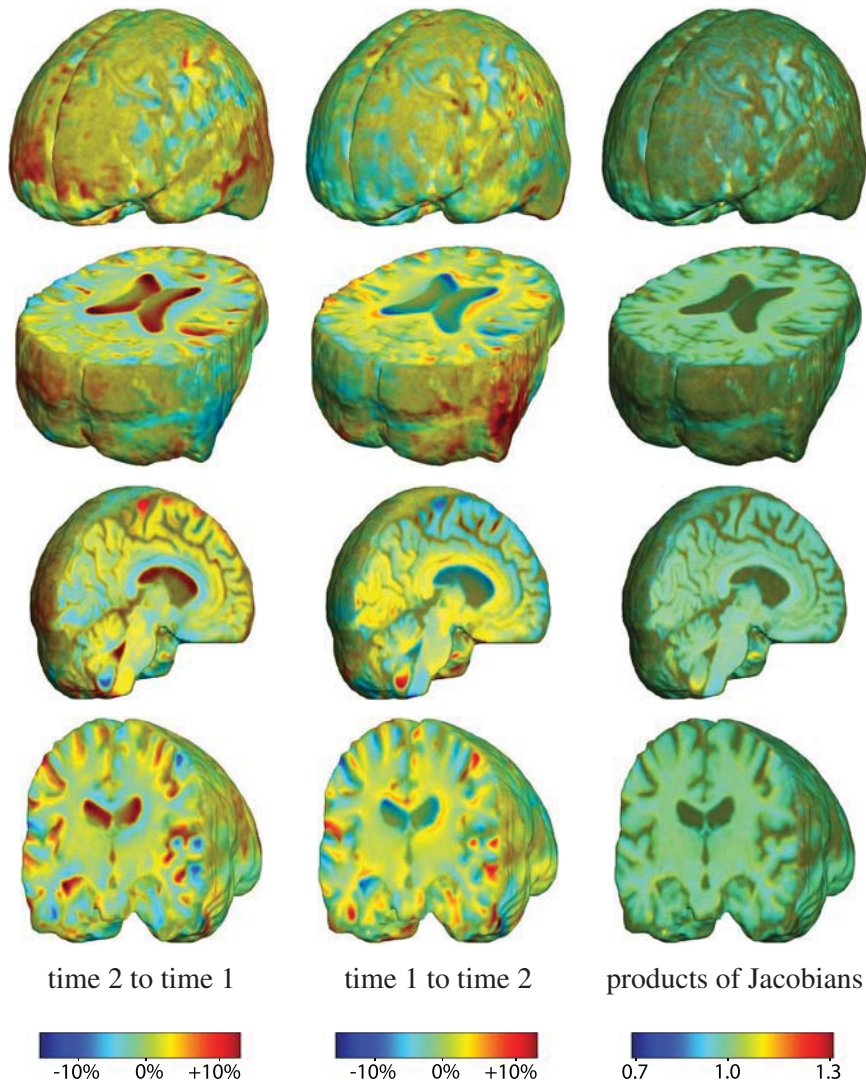


Figure 5: This figure examines the inverse consistency of the unbiased nonlinear elastic registration. Here, the model is coupled with mutual information matching. Jacobian maps of deformations from time 2 to time 1 (column 1) and time 1 to time 2 (column 2) are superimposed on the target volumes. The products of Jacobian maps, shown in column 3, have values close to 1, suggesting inverse consistency.

References

- [1] M. Bro-Nielsen and C. Gramkow. Fast fluid registration of medical images. In *Visualization in Biomedical Computing*, pages 267–276, 1996.
- [2] C. Broit. *Optimal Registration of Deformed Images*. PhD thesis, University of Pennsylvania, 1981.

- [3] C. Brun, N. Lepore, X. Pennec, Y. Chou, O. Lopez, H. Aizenstein, J. Becker, A. Toga, and P. Thompson. Comparison of standard and Riemannian elasticity for tensor-based morphometry in HIV/AIDS. *International Conference on Medical Image Computing and Computer Assisted Intervention*, 2007.
- [4] G. Christensen and H. Johnson. Consistent image registration. *IEEE Transactions on Medical Imaging*, 20(7):568–582, 2001.
- [5] G. Christensen, R. Rabbitt, and M. Miller. Deformable templates using large deformation kinematics. *IEEE Transactions on Image Processing*, 5(10):1435–1447, 1996.
- [6] A. Collignon, F. Maes, D. Delaere, D. Vandermeulen, P. Suetens, and G. Marchal. Automated multi-modality image registration based on information theory. In Y. Bizais, C. Barillot, and R. Di Paola, editors, *Information Processing in Medical Imaging*, volume 3, pages 264–274. Kluwer Academic Publishers, Dordrecht, 1995.
- [7] E. D’Agostino, F. Maes, D. Vandermeulen, and P. Suetens. A viscous fluid model for multimodal non-rigid image registration using mutual information. *Medical Image Analysis*, 7:565–575, 2003.
- [8] E. Haber and J. Modersitzki. Numerical methods for volume preserving image registration. *Inverse problems*, Institute of Physics Publishing, 20(5):1621–1638, 2004.
- [9] E. Haber and J. Modersitzki. Image registration with guaranteed displacement regularity. *International Journal of Computer Vision*, 71(3):361–372, 2007.
- [10] N. Lord, J. Ho, B. Vemuri, and S. Eisenschenk. Simultaneous registration and parcellation of bilateral hippocampal surface pairs for local asymmetry quantification. *IEEE Transactions on Medical Imaging*, 26(4):471–478, 2007.
- [11] J. Modersitzki. *Numerical Methods for Image Registration (Numerical Mathematics and Scientific Computation)*. Oxford University Press, New York, 2004.
- [12] P. Negron-Marrero. A numerical method for detecting singular minimizers of multidimensional problems in nonlinear elasticity. *Numerische Mathematik*, 58(1):135–144, 1990.
- [13] X. Pennec. Left-invariant riemannian elasticity: A distance on shape diffeomorphisms? *International Workshop on Mathematical Foundations of Computational Anatomy*, pages 1–13, 2006.
- [14] X. Pennec, R. Stefanescu, V. Arsigny, P. Fillard, and N. Ayache. Riemannian elasticity: A statistical regularization framework for non-linear registration. In *International Conference on Medical Image Computing and Computer Assisted Intervention*, pages 943–950, 2005.
- [15] P. Viola and W. Wells. Alignment by maximization of mutual information. *International Conference on Computer Vision*, pages 16–23, 1995.
- [16] Igor Yanovsky, Paul Thompson, Stanley Osher, and Alex Leow. Topology preserving log-unbiased nonlinear image registration: Theory and implementation. *IEEE Conference on Computer Vision and Pattern Recognition*, pages 1–8, 2007.
- [17] Igor Yanovsky, Paul Thompson, Stanley Osher, and Alex Leow. Asymmetric and symmetric unbiased image registration: Statistical assessment of performance. *IEEE Computer Society Workshop on Mathematical Methods in Biomedical Image Analysis*, 2008.

Coupling Finite Element and Mesh-free Methods for Modelling Brain Deformation in Response to Tumour Growth

Jamie Berger, Ashley Horton, Grand Joldes, Adam Wittek, Karol Miller

Intelligent Systems for Medicine Lab
The University of Western Australia
35 Stirling Highway
Crawley WA 6009, Australia
Email: kmiller@mech.uwa.edu.au
www.mech.uwa.edu.au/ISML

Abstract

Very little is known about the deformation effects of tumour growth within the brain. Computer simulations have the potential to calculate such deformations. A method for computing localised high deformations within the brain's soft tissue is presented. Such knowledge would be significant towards neuroscience and neurosurgery, particularly for quantifying tumour aggressiveness, therapy planning, as well as surgical planning and simulation. A Finite Element mesh used in the vicinity of a growing tumour is very quickly destroyed and cannot be used reliably unless complicated automatic re-meshing exists. Mesh-free methods are capable of handling much larger deformations, however are known to be less reliable than Finite Element analysis for moderate deformations. A mixed-mesh approach utilises mesh-free regions within localised high-deformation zones, with the remaining model comprised of a Finite Element mesh. In this study, a new algorithm is proposed coupling the Finite Element and Element Free Galerkin methods for use in applications of high localised deformation, such as brain tumour growth. The algorithm is verified against a number of separate Finite Element and mesh-free problems solved via validated/commercial software. Maximum errors of less than 0.85 mm were maintained, corresponding to the working resolution of an MRI scan. A mixed-mesh brain model is analysed with respect to different tumour growth volumes located behind the left ventricle. Significant displacements of up to 9.66 mm surrounding a 4118 mm^3 sized tumour are noted, with 14.5% of the brain mesh suffering deformation greater than 5 mm .

In biomechanics of soft tissues, it is common to encounter extreme deformations that cannot be handled by traditional modelling methods, such as the Finite Element method. An example of this is brain tumour growth. Very little is known within this field and such a model should be useful for medical use, particularly in quantifying tumour aggressiveness, therapy planning, as well as surgical planning and simulation. The three dimensional mechanical response of the brain is highly non-linear, involving extremely complex constitutive models and geometry, which is very time consuming to model using public Finite Element (FE) software (Miller, Taylor, *et al.*, 2005). Furthermore the Finite Element method on its own will be inaccurate and problematic for modelling the brain deformation response to tumour growth, since the mesh surrounding the tumour is easily distorted, consequently destroying elements. Complicated re-meshing can combat this, however it is extremely time consuming. Alternatively a solely mesh-free Element Free Galerkin (EFG) model will be capable of handling larger deformations and topology changes (Li and Liu, 2004). Despite this the method is known to be less reliable than Finite Element analysis for moderate deformations and suffers from Dirichlet boundary difficulties (Fries and Matthies, 2003). A coupled Finite Element / Element Free Galerkin approach is proposed to overcome the shortcomings of each individual method, by placing a mesh-free domain around the tumour affected location, with the remaining brain tissue modelled as a hexahedral mesh.

1. Background Theory

The Finite Element method is a numerical approach for solving systems of partial differential equations, by discretising the domain into small volumes (elements) and estimating the solution in each of the elements via shape functions. The estimated solutions are then substituted into integral differential equations of the weak form with the residuals minimised (Bathe, 1996). The Element Free Galerkin method (Horton, 2006) conducts the same process, without requiring the connectivity of elements. Shape functions are not within elements but small neighbourhoods of nodes, called support domains, each of which is associated to an integration point (Belytschko, Krongauz, *et al.*, 1996). The Moving Least Squares formulation is used to minimise residuals within the EFG method.

2. Coupled Finite Element / Element Free Galerkin Method

Mixed-mesh coupling is achieved by constructing interface support domains in between FE and EFG boundaries, as shown in *Figure 2.1*. Interface support domains are created by allowing the EFG nodal support domains to extend into the FE region, consuming nodes. They follow the same numerical approach as the EFG method. FE nodes that exist within a nodal support domain are considered by both the EFG and FE methods with their nodal forces summed together.

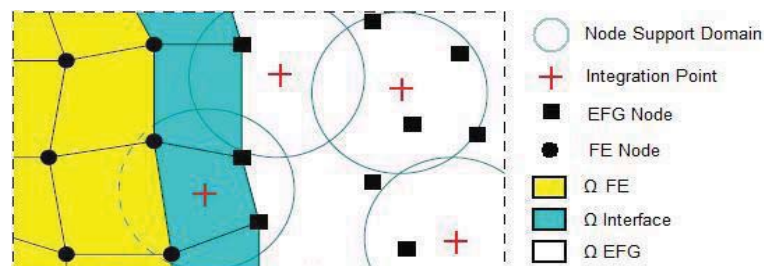


Figure 2.1: Coupled FE/EFG domain with interface region and support domains highlighted.

3. Total Lagrangian Formulation

The Total Lagrangian (TL) formulation is a general convergent method for dealing with materially non-linear effects and large deformations. It is derived from the Principle of Virtual Displacements. The TL formulation references all static and kinematic variables to the initial configuration of the system, which means all derivatives with respect to spacial coordinates can be precomputed. Hence, the number of mathematical operations performed in each time step of the TL algorithm is reduced, and is therefore favourable for surgical simulation (Bathe, 1996, and Miller, Joldes, *et al.*, 2007).

3.1 Explicit Integration

The method of integration for the TL formulation is very important for the performance of the algorithm. Computing the deformation field and internal forces within a soft tissue organ, such as the brain, requires the utilisation of an efficient integration method for integrating static or dynamic equations within the time domain. Both implicit and explicit integration methods are suitable for this problem. The Central Difference Method of explicit integration is chosen over implicit integration as it does not require the solution of simultaneous non-linear equations and performs much faster on materials of very low stiffness, such as the brain (Miller, Joldes, *et al.*, 2007).

The Central Difference Method is derived from Newton's second law as shown,

$$\mathbf{M} \frac{\partial^2 {}^t_0 \mathbf{u}}{\partial t^2} = {}^t \mathbf{R} - {}^t_0 \mathbf{F} \quad (3.1)$$

$$\frac{\partial^2 {}^t_0 \mathbf{u}}{\partial t^2} \approx \frac{1}{\Delta t} ({}^{t-\Delta t} \mathbf{u}_i - 2 {}^t \mathbf{u}_i + {}^{t+\Delta t} \mathbf{u}_i) \quad (3.2)$$

$${}^{t+\Delta t} \mathbf{u}_i = \frac{\Delta t^2}{M} ({}^t R_i^{(n)} - {}^t F_i^{(n)}) + 2 {}^t \mathbf{u}_i - {}^{t-\Delta t} \mathbf{u}_i \quad (3.3)$$

where, \mathbf{M} represents the nodal mass, Δt the simulation time-step, ${}^t F_i^{(n)}$ and ${}^t R_i^{(n)}$ the net force and reaction force on the node. The previous, current, and future nodal displacements are described by ${}^{t-\Delta t} \mathbf{u}_i$, ${}^t \mathbf{u}_i$, and ${}^{t+\Delta t} \mathbf{u}_i$ respectively.

Unfortunately two issues arise with the use of explicit integration. Firstly explicit methods are conditionally stable, requiring time-steps below a critical value (Joldes, 2006). Furthermore explicit methods cannot obtain static solutions unless damping is used. Quasi-static simulations can be conducted such that the load is applied very slowly over a long period of time. The longer the simulation time, the closer the solution is to a static one.

3.2 Total Lagrangian Explicit Dynamics Algorithm

The Total Lagrangian Explicit Dynamics (TLED) algorithm combines the TL formulation with explicit integration. The TLED algorithm has been successfully utilised for non-linear soft tissue deformations in FE and EFG numerical approaches individually (Horton, 2006, and Miller, Joldes, *et al.*, 2007). Both numerical methods have provided reliable and accurate results using the TLED algorithm, thus it is desirable for use in the coupled FE/EFG approach. The following pseudocode describes the TLED algorithm in relation to solving mixed-mesh problems:

Pre-process:

1. Load simulation geometry (FE & EFG nodes), elements, integration points, and boundary conditions.
2. Pre-compute element / integration point spacial derivatives and support domains.
3. Calculate appropriate mass matrix, \mathbf{M} , for allocating mass to every node.
4. Initialise displacements.

Begin Time Loop:

- Loop Over Elements / Support Domains

5. Update FE and EFG displacements from previous time-step.
6. Compute displacement derivatives, $\mathbf{u}_{i,j}$, and deformation gradient, \mathbf{X} :

$$\mathbf{u}_{i,j} = \mathbf{N}'^t \mathbf{u} \quad (\mathbf{N}' - \text{FE/EFG shape function derivatives matrix})$$

$${}^t_0 \mathbf{X} = \mathbf{u}_{i,j} + \mathbf{I} \quad (\mathbf{I} - \text{Identity matrix})$$

7. Compute inverse of Right Cauchy-Green Deformation tensor, C_{ij} , and Second Piola-Kirchhoff

stress vector, \mathbf{S} , at each integration point:

$$C_{ij} = ({}^t_0\mathbf{X}^T {}^t_0\mathbf{X})^{-1}$$

$$S_{ij} = \mu(I - C_{ij}) + \lambda J(J - 1)C_{ij} \quad (\mu, \lambda - \text{Lame` parameters; } J - \text{Jacobian determinant})$$

$${}^t_0\mathbf{S} = \begin{bmatrix} {}^t_0S_{11} & {}^t_0S_{12} & {}^t_0S_{31} \\ {}^t_0S_{12} & {}^t_0S_{22} & {}^t_0S_{23} \\ {}^t_0S_{31} & {}^t_0S_{23} & {}^t_0S_{33} \end{bmatrix}$$

8. Compute elemental/support domain forces, \mathbf{F} , using Gaussian Quadrature:

$${}^t_0\mathbf{F} = \int_{{}^t_0V} {}^t_0\mathbf{X}' {}^t_0\mathbf{S} \mathbf{N}' d^0V$$

9. Combine local reaction forces to obtain net nodal reaction forces at time, t .

10. Explicitly determine displacements, $u^{t+\Delta t}$, using Central Difference formula:

$${}^{t+\Delta t}u_i = \frac{\Delta t^2}{M} ({}^tR_i - {}^tF_i) + 2{}^tu_i - {}^{t-\Delta t}u_i \quad ({}^tR_i - \text{Total nodal reaction force at time, } t)$$

4. Program Implementation

The implementation of the tailor made localised soft tissue deformation simulator is divided into three main sections:

- Preprocessor - Reads in mixed mesh model and constraints, pre-computing all initial configuration stationary properties.
- Analysis Solver - Executes the main time loop performing calculations in accordance with the Total Lagrangian Explicit Dynamics Algorithm.
- Postprocessor - Uses series of visualisation tools to view and identify implications of analysis.

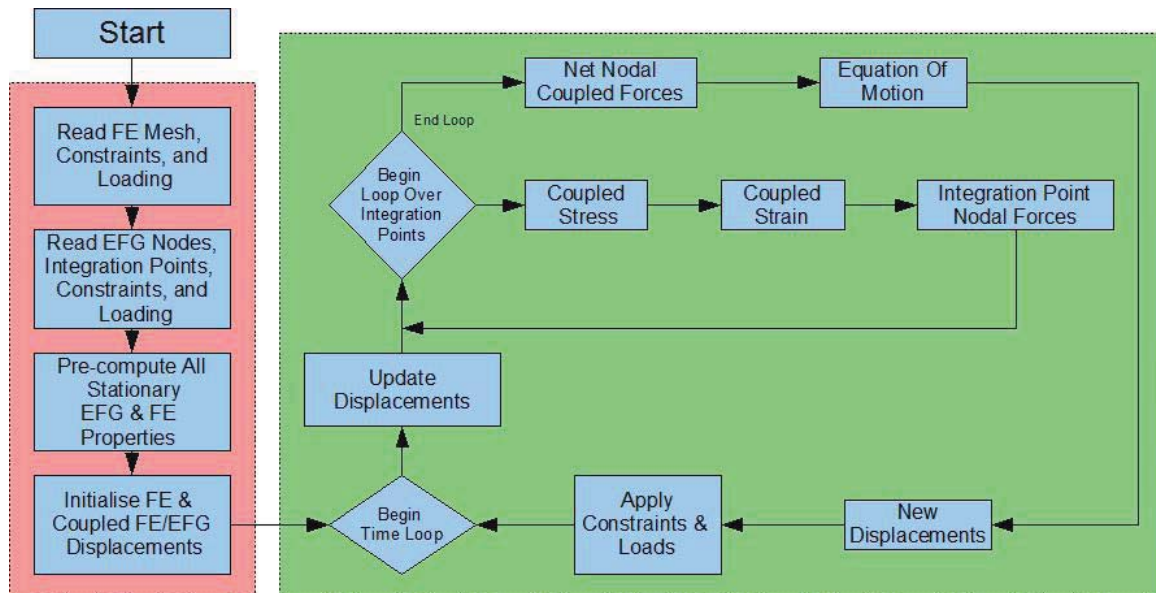


Figure 3.1: Block diagram of the preprocessing phase (red) and analysis solver (green).

The script language, MATLAB, was chosen for the preprocessing and postprocessing stages of the simulator. MATLAB is a very powerful, high level, language, containing many built in functions, which are of particular use for dealing with matrices. This was beneficial for the preprocessing stage, which requires many large matrix operations. Furthermore MATLAB holds significant advantages for the postprocessing phase as it has excellent visualisation tools, allowing for advanced analysis of the results.

Unfortunately MATLAB performs much slower than compiled languages, hence it was not feasible for use in the implementation of the analysis solver. The functional programming language, C, was chosen as it is very fast, with inbuilt optimisation compilation abilities.

4.1 Preprocessor

The implementation of the preprocessor phase can be broken down into a number of smaller subsections. It should be noted that the computational performance of this phase is less important than the analysis solver, since for coarse mixed-meshes, the run time is negligible in comparison.

4.1.1 Simulation Properties

All of the major simulation properties are user defined and must be set prior to running the preprocessor. This includes the maximum displacement, time-step, and the total simulation time. The simulation properties provide enough information to setup the deformation loading curve, for applying incremental displacements at each time-step. The default deformation loading curve is defined in (4.1),

$$d(t) = \left[10 - 15\left(\frac{t}{T}\right) + 6\left(\frac{t}{T}\right)^2 \right] \left(\frac{t}{T}\right)^3, \quad (4.1)$$

where T is the total simulation time.

4.1.2 Mixed-Mesh Reader

The nodes, elements, and boundary conditions of the mixed-mesh are read in from ABAQUS output files. Two ABAQUS output files are required, both containing nodal positions and boundary conditions for each method, with the FE output file containing additional information about element composition. The data format of the information read from the FE and EFG ABAQUS files is displayed in *Table 4.1*. A coupled list of all nodes, $\mathbf{X}_{\text{coupled}}$, is then formed by combining \mathbf{X}_{FE} and \mathbf{X}_{EFG} in that order.

FE ABAQUS Output	FE Nodes	\mathbf{X}_{FE} ($N_{\text{nodes-FE}} \times 3$) matrix of all FE node locations. Each row of the matrix corresponds to the FE node number.
	Elements	\mathbf{E}_{FE} ($N_{\text{elements-FE}} \times 8$) matrix of all FE elements. Each row of the matrix corresponds to the element number, containing eight node numbers forming a hexahedral.
	Constrained FE Nodes	FE_node_fix ($N_{\text{nodes-FE}} \times 3$) binary matrix of all FE nodes, 1 represents if the node is fixed for that dimension.
	Displaced FE Nodes	FE_node_disp ($N_{\text{nodes-FE}} \times 3$) binary matrix of all FE nodes, 1 represents if the node is displaced for that dimension.
EFG ABAQUS / LS-Dyna Output	EFG Nodes	\mathbf{X}_{EFG} ($N_{\text{nodes-EFG}} \times 3$) matrix of all EFG node locations. Each row of the matrix corresponds to the EFG node number.
	Constrained EFG Nodes	EFG_node_fix ($N_{\text{nodes-EFG}} \times 3$) binary matrix of all EFG nodes, 1 represents if the node is fixed for that dimension.
	Displaced EFG Nodes	EFG_node_disp ($N_{\text{nodes-EFG}} \times 3$) binary matrix of all EFG nodes, 1 represents if the node is displaced for that dimension.

Table 4.1: Data format of information read in from the ABAQUS output files.

An integration point grid for the EFG and interface region should also be read in. This is just a matrix holding the three dimensional coordinates of the integration point locations. It is ideal to have a regular grid, such that each integration point can be assigned the same volume.

4.1.3 Material Model

The material model information is to be set, requiring Young's modulus, Poisson's ratio, and the density for each material identified within the mixed-mesh. From this data the lame` material constants can be calculated as follows.

$$\lambda = E \frac{\nu}{(1+\nu)(1-2\nu)} \quad (4.2)$$

$$\mu = E \frac{\nu}{2(1+\nu)} \quad (4.3)$$

The material model is based upon the Neo-Hookeen model (Bathe, 1996).

4.1.4 Support Domains

The construction of nodal support domains for the EFG and interface region is quite simple following on from Horton (2007). The method requires a fixed number, n , of nodes per support domain, which is user defined. Support domains are then constructed by finding the n closest nodes to each integration point. A limit on the number of Finite Element nodes allowed within a single support domain removes the possibility of an entire element being consumed by a support domain, which would have no hourglass control measures. Having a fixed number of nodes per support domain is faster and more robust than typical support domain constructions, which rely on defining a fixed local volume with a varying number of nodes.

4.1.5 Hexahedral Shape Functions

The hexahedral shape functions and derivatives are determined from a series of calculations. The matrix of hexahedral shape function natural derivatives is defined as,

$$\partial \mathbf{h} \mathbf{r}^T = -\frac{1}{8} \begin{bmatrix} 1 & -1 & -1 & 1 & 1 & -1 & -1 & 1 \\ 1 & 1 & -1 & -1 & 1 & 1 & -1 & -1 \\ 1 & 1 & 1 & 1 & -1 & -1 & -1 & -1 \end{bmatrix} \quad (4.4)$$

using the node numbering convention as described in Bathe (1996). Each elemental Jacobian, \mathbf{J} , is then calculated based on the element nodal position vector, $\hat{\mathbf{x}}$.

$$\mathbf{J} = \partial \mathbf{h} \mathbf{r}^T \hat{\mathbf{x}} \quad (4.5)$$

Using the elemental Jacobians, hexahedral shape function derivatives, $\partial \mathbf{h}$, are then computed by,

$$\partial \mathbf{h} = \partial \mathbf{h} \mathbf{r} (\mathbf{J}^{-1})^T \quad (4.6)$$

4.1.6 Moving Least Squares Shape Functions

Calculations of the Moving Least Squares shape functions for each nodal support domain of size n , are derived from Fries and Matthies (2003). Consider a three dimensional space vector of monomial basis functions, \mathbf{p} , of length m .

$$\mathbf{p}(x)^T = [1 \quad x \quad y \quad z \quad xy \quad xz \quad yz \quad x^2 \quad y^2 \quad z^2 \quad xyz \quad \dots \quad x^3 \quad y^3 \quad z^3]$$

The nodal displacement approximation, $\mathbf{u}^h(x)$, is calculated with respect to the coefficient vector, $\mathbf{a}(x)$.

$$\text{i.e. } \mathbf{u}^h(x) = \mathbf{p}^T(x) \mathbf{a}(x) \quad (4.7)$$

The formulation of $\mathbf{a}(x)$ is determined by minimising the weighted residual function, J , where,

$$J = \sum_{i=1}^n W(d_i) (\mathbf{p}^T(x_i) \mathbf{a}(x) - \mathbf{u}(x_i))^2 \quad (4.8)$$

In (4.8) $W(d_i)$ represents a weight function with d_i being the distance between the node, x_i , and integration point, x . Minimising J is done by considering

$$\frac{\partial J}{\partial \mathbf{a}} = 0 \quad (4.9)$$

which leads to the following linear relationship,

$$\mathbf{A}(x)\mathbf{a}(x)=\mathbf{B}(x)\mathbf{U} \quad (4.10)$$

In (4.10) \mathbf{A} is an $m \times m$ matrix known as the moment matrix defined by,

$$\mathbf{A}(x)=\sum_{i=1}^n W(d_i)\mathbf{p}(x_i)\mathbf{p}^T(x_i) \quad (4.11)$$

\mathbf{B} is an $m \times n$ matrix given by,

$$\mathbf{B}(x)=[W(d_1)\mathbf{p}(x_1) \quad W(d_2)\mathbf{p}(x_2) \quad W(d_3)\mathbf{p}(x_3) \quad \dots \quad W(d_n)\mathbf{p}(x_n)] \quad (4.12)$$

and \mathbf{U} is the vector of length n as shown,

$$\mathbf{U}^T=[u_1 \quad u_2 \quad u_3 \quad \dots \quad u_n] \quad (4.13)$$

By finding the inverse of \mathbf{A} equation (4.14) can be solved,

$$\mathbf{a}(x)=\mathbf{A}^{-1}(x)\mathbf{B}(x)\mathbf{U} \quad (4.14)$$

Substituting (4.14) back into (4.7) we get the nodal displacement approximation,

$$\mathbf{u}^h(x)=\Phi_i(x)\mathbf{U} \quad (4.15)$$

where the shape function vector Φ of length n at the i^{th} node in the support domain is given by,

$$\Phi_i(x)=\sum_j^m \mathbf{p}_j(x)(\mathbf{A}^{-1}(x)\mathbf{B}(x))_{j,i} \quad (4.16)$$

The length m of \mathbf{p} is user defined and should be chosen such that shape functions are all interpolated in a similar fashion in each dimension. There is a trade-off between the total number of integration points and the size of m due to the limitations on computational speed. Single point integration is well suited for low order interpolations, hence a lower value of m is chosen, while using a larger number of support domains. More support domains relieve the emphasis on stress calculations at any integration point. It has been found in Horton (2007) that setting $m = 4$ and using 8 nodes per support domain ($n = 8$) is substantial enough for deformation to be transferred between support domains. In addition it has been noted that by using very small support domain sizes, the weighting of each node can be considered equal, without having a negative impact on the accuracy of the solution. This reduces the risk of generating singular matrix \mathbf{A} .

4.1.7 Mass Allocation

Initially a matrix, \mathbf{M}_{FE} , is setup for handling the mass of all nodes within the FE domain. The mass of each node within an element for \mathbf{M}_{FE} is calculated using the determinant of each elemental Jacobian from (4.5) and the material density, ρ .

$$\Delta M_{\text{node}}=\rho \det({}^0J) \quad (4.17)$$

The nodal contributions for all elements are then summed up to give \mathbf{M}_{FE} .

A coupled mass matrix, $\mathbf{M}_{\text{coupled}}$, is then created for allocating masses to all EFG and interface nodes involved in support domains. Each integration point is allocated a volume and consequently a mass based upon the materials density. This mass is equally divided amongst the number of nodes within the support domain,

$$\Delta M_{\text{node}}=\frac{\hat{V}^{(g)}\rho}{n} \quad (4.18)$$

where, n represents the number of nodes per support domain, and $V^{(g)}$ is the volume of the specific integration point, g . The mass of each FE node in \mathbf{M}_{FE} is then added to $\mathbf{M}_{\text{coupled}}$, giving the entire nodal mass of the system. This is a very effective method of distributing mass throughout the EFG/interface region since nodes that appear in more support domains will receive more forces. One concern, however, is that nodes not included in many support domains will have a low mass, which can result in unbalanced forces and high accelerations. This is undesired, often leading to unstable simulations. It can be avoided

by involving each node in at least two or three support domains as suggested in Horton (2007). A further measure is implemented so that any node that manages to escape support domain allocation is removed to prevent massless nodes entering the analysis.

4.2 Analysis Solver

The analysis solver is the most computationally intensive phase of the simulator. It consists of the main time loop described in the Total Lagrangian Explicit Dynamics Algorithm with a few additional considerations. Efficient programming is very important to minimise the number of calculations required in the main time loop, substantially increasing the performance of the algorithm.

4.2.1 Main Time Loop

Both the Finite Element and Element Free Galerkin methods follow the same calculations for the main time loop of the TLED algorithm, making it quite easy to implement the coupling as treating the entire domain as a single method.

Three displacement matrices representing, ${}^{t-\Delta t}{}_0\mathbf{u}$, ${}^t{}_0\mathbf{u}$, ${}^{t+\Delta t}{}_0\mathbf{u}$, and a global nodal force vector, ${}^t\mathbf{F}$, were defined. Pseudocode below presents the implementation of the main time loop.

Begin Time Loop ($t = \Delta t$)

– Update Displacements

$${}^{t-\Delta t}{}_0\mathbf{u} = {}^t{}_0\mathbf{u}$$

$${}^t{}_0\mathbf{u} = {}^{t+\Delta t}{}_0\mathbf{u}$$

– Reset Global Nodal Force Vector

$${}^t\mathbf{F} = 0$$

– Loop Over All Elements & Support Domains

– Compute elemental/support domain displacement derivatives

$$\mathbf{u}_{i,j}^{(k)} = \partial \mathbf{h}_0^t \mathbf{u}$$

$$\mathbf{u}_{i,j}^{(g)} = \Phi^t {}^t{}_0\mathbf{u}$$

– Calculate deformation gradient

$${}^t_0\mathbf{X} = \mathbf{u}_{i,j} + \mathbf{I}_{3 \times 3}$$

– Inverse Right Cauchy-Green deformation tensor

$$\mathbf{C}_{ij} = [{}^t_0\mathbf{X}^T {}^t_0\mathbf{X}]^{-1}$$

– Jacobian Determinant

$$J = \det({}^t_0\mathbf{X})$$

– Second Piola-Kirchoff Stress

$$\mathbf{S}_{ij} = \mu(\mathbf{I} - \mathbf{C}_{ij}) + \lambda J(J - 1)\mathbf{C}_{ij}$$

$${}^t_0\mathbf{S} = \begin{bmatrix} {}^t_0\mathbf{S}_{11} & {}^t_0\mathbf{S}_{12} & {}^t_0\mathbf{S}_{31} \\ {}^t_0\mathbf{S}_{12} & {}^t_0\mathbf{S}_{22} & {}^t_0\mathbf{S}_{23} \\ {}^t_0\mathbf{S}_{31} & {}^t_0\mathbf{S}_{23} & {}^t_0\mathbf{S}_{33} \end{bmatrix}$$

– Integrate to get Elemental/Support domain nodal force

$${}^t\hat{\mathbf{F}}_i^{(k)} = 8J {}^t_0\mathbf{X}_0^t {}^t_0\mathbf{S} \partial \mathbf{h}^{(k)}$$

$${}^t\hat{\mathbf{F}}_i^{(g)} = V^{(g)} {}^t_0\mathbf{X}_0^t {}^t_0\mathbf{S} \Phi^{(g)}$$

– Update Global Force

$${}^t\mathbf{F}_i^{(total)} = {}^t\mathbf{F}_i^{(total)} + {}^t\hat{\mathbf{F}}_i^{(k)} + {}^t\hat{\mathbf{F}}_i^{(g)}$$

– End Loop Over Elements/Support Domains

– Use Central Difference Method to Calculate Displacements

- Loop Over Constrained Nodes
- Loop Over Displaced Nodes

$$\begin{aligned} {}^{t+\Delta t}{}_0\mathbf{u} &= \frac{-\Delta t^2}{M} {}^t\mathbf{F} + 2 {}^t{}_0\mathbf{u} - {}^{t-\Delta t}{}_0\mathbf{u} \\ {}^{t+\Delta t}{}_0\mathbf{u}_i &= 0 \\ {}^{t+\Delta t}{}_0\mathbf{u}_i &= d(\Delta t) \end{aligned}$$

End Time Loop ($t = T$)

4.2.2 Hourglass Control

One of the biggest disadvantages to using single-point integration for hexahedral elements is the requirement for controlling zero energy modes, known as hour-glassing (Hallquist, 2006). In order to control hour-glassing within the Finite Element domain, resistance providing artificial stiffness is implemented, which has a negligible effect on stable global modes. This is an efficient method following on from modifications of Flanagan and Belytschko (1984) perturbation method (Joldes, Wittek, *et al.*, 2007). An additional hourglass control force is added to the total force of the system, based on the hourglass resistance and displacement. Hourglass base matrix is setup as:

$$\mathbf{H}^T = \begin{bmatrix} 1 & -1 & 1 & -1 & 1 & -1 & 1 & -1 \\ 1 & 1 & -1 & -1 & -1 & -1 & 1 & 1 \\ 1 & -1 & -1 & 1 & -1 & 1 & 1 & -1 \\ -1 & 1 & -1 & 1 & 1 & -1 & 1 & -1 \end{bmatrix} \quad (4.19)$$

The k^{th} elemental hourglass control force, ${}^t\mathbf{F}_{hg}^{(k)}$, can then be calculated by the following series of equations:

$$\partial \mathbf{h}_{hg}^{(k)} = \mathbf{H} - \partial \mathbf{h}^{(k)} [x^{(k)}]^T \mathbf{H} \quad (4.20)$$

$$\mathbf{u}_{ijhg} = {}^t u_{i,jhg} = [\partial \mathbf{h}_{hg}^{(k)}]^T {}^t u_i^{(k)} \quad (4.21)$$

$${}^t\mathbf{F}_{hg}^{(k)} = \frac{R_{hg}(\lambda + 2\mu) Vol^{(k)} [\partial \mathbf{h}^{(k)}] \partial \mathbf{h}_{hg}^{(k)} \mathbf{u}_{ijhg}}{8} \quad (4.22)$$

where $\partial \mathbf{h}_{hg}^{(k)}$ is the k^{th} elemental hourglass shape function derivative, \mathbf{u}_{ijhg} represents the elemental hourglass displacement derivatives, and R_{hg} is the hourglass resistance constant. The hourglass force is then added to the elemental force calculated without hourglass control as shown in (4.23).

$${}^t\mathbf{F}^{(k)} = {}^t\mathbf{F}^{(k)} + {}^t\mathbf{F}_{hg}^{(k)} \quad (4.23)$$

A good value for the hourglass resistance, R_{hg} , was found to be $R_{hg} = 0.04/9$.

5. Coupling Considerations

5.1 Mixed-Mesh Generation

One of the main considerations of utilising coupled FE/EFG methods is the generation of mixed-meshes. Meshless methods may have much more freedom with node placement in comparison to hexahedral FE methods, although very regular node placements can lead to singular shape functions within one plane (Horton, 2007). Regular node and integration arrangements for meshless methods have been successful, however this becomes equivalent to a hexahedral mesh, suffering from hour-glassing and furthermore is quite complicated to generate over irregular domains, such as the brain (Li, and Liu, 2004). A way around this is to model the meshless region using a well refined tetrahedral mesh, which helps to maintain a roughly even density, while not conforming to very regular node placements. The tetrahedral element information is omitted, since meshless methods do not require the connectivity of nodes. It is possible to convert sections of a hexahedral mesh into tetrahedrals in commercial meshing software such as Hypermesh, which easily gives rise to the generation of mixed-meshes. Unfortunately this procedure

relies on the existence of a Finite Element mesh, which, depending on the complexity of the shape, may still be quite complicated and time consuming to create.

Another aspect of mixed-mesh generation is the requirement for an integration point domain. As found in Horton (2006), a background grid of integration points for the EFG domain leads to greater accuracy and stability, while still performing efficiently. The background grid can be extended up to the boundary between the EFG and FE region in order to maximise coupling as mentioned in Chapter 5.2.

5.2 Coupling Integration Point Distribution

An investigation into the depth of coupling and its effects on the accuracy of the method was conducted. The level of coupling is indicated by the number of FE nodes involved in interface support domains. This is strongly dependent on the distribution of integration points around the boundaries of each region. The best results occur when the coupling integration point grid is mapped up to the boundary of the FE region. This maximises the number of FE nodes within interface support domain.

To avoid unnecessarily using too many integration points around the coupling region the findings of Horton (2007) should be employed with respect to interface support domains. That is, by using twice as many interface support domains to interface nodes, the Moving Least Squares approximation will still give very accurate results.

5.3 Interface Support Domain Composition

An area of interest in the coupling method is the number of allowable FE nodes to be considered within a single interface support domain. A support domain should not be allowed to contain only Finite Element nodes, as there is the possibility that it has coincided with an entire element, which would not have any hourglass control measures. For this reason a limit on the maximum number of FE nodes within an interface support domain must be defined, based on the number of nodes within a hexahedral element. This condition would then be checked when allocating support domains within the preprocessor.

It was found that by reducing the amount of allowable FE nodes per interface support domain causes the level of coupling to decrease, which produces results with poorer accuracy. Allowing up to 7 FE nodes per interface support domain, one node less than a hexahedral element, maximises the coupling, consequently leading to increased accuracy of solutions.

6. Validation & Results

6.1 Validation

The coupling method was validated by a series of quasi-static deformation tests, using the material properties of healthy brain tissue. Initially the algorithm was trialled and compared against a Finite Element solution using commercial software (ABAQUS) for a homogeneous cylinder undergoing compression, extension, and shear deformations. The mixed-mesh contained an outer FE region with an inner EFG core. The results were further compared against validated Element Free Galerkin software, showing that the coupling method performs slightly better than a solely EFG method and is still very close to the FE solution. Comparisons against a FE solution is preferable over an analytical solution due to the complicated mathematical nature of analytical methods and general loss of accuracy for non-linear problems. The results shown in *Table 6.1* reflect the maximum nodal displacement error in comparison to the FE ABAQUS solution.

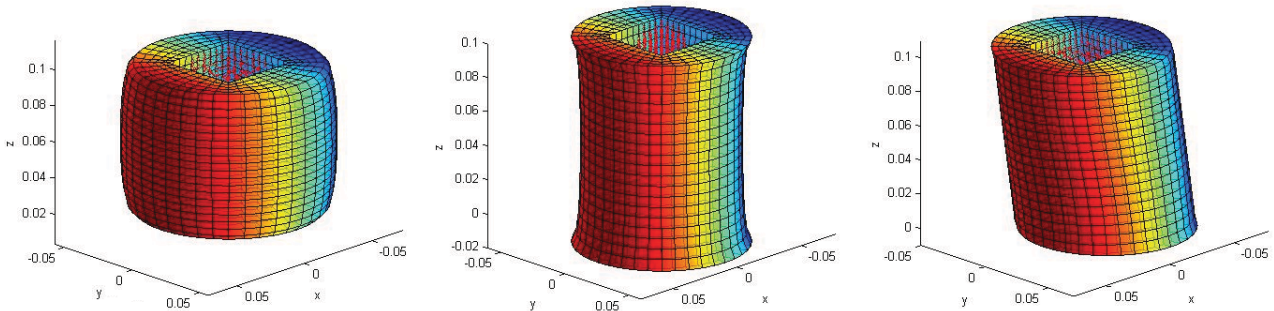


Figure 6.1: Final deformed mixed mesh cylinders. Compression (left), Extension (middle), Shear (right).

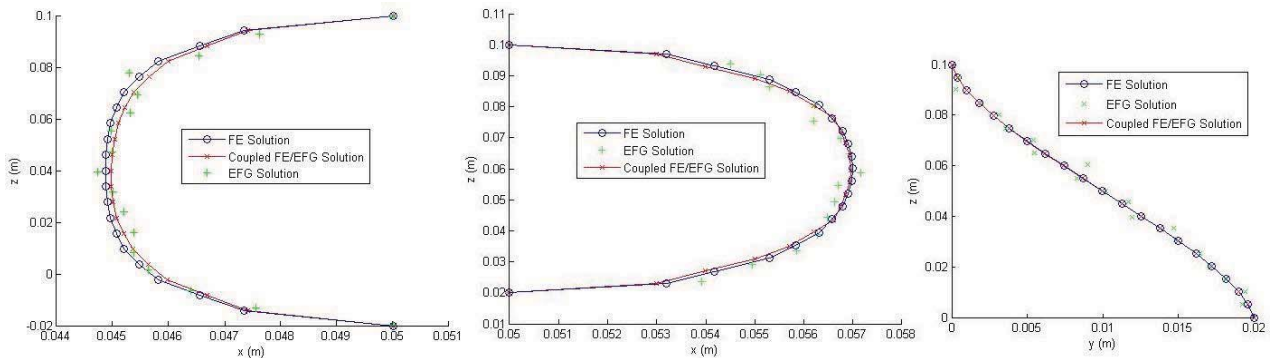


Figure 6.2: Coupled cylinder edge deformation comparisons against FE ABAQUS solution and validated EFG model undergoing extension (left), compression (middle), and shear (right).

The final validation test involved a partially constrained ellipsoid undergoing indentation on the surface. The mixed mesh gave highly accurate results in comparison with a FE mesh simulated in ABAQUS.

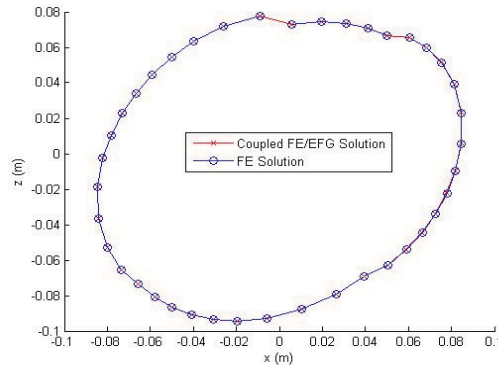


Figure 6.3: Cross-section comparison of deformed boundary for indented ellipsoid.

Deformation Model	Maximum Error (mm)		
	Δx	Δy	Δz
Cylinder Extension	0.1744	0.0055	0.0694
Cylinder Compression	0.1058	0.0177	0.0672
Cylinder Shear	0.0193	0.0273	0.0097
Ellipsoid Indentation	0.1628	0.0734	0.1055

Table 6.1: Maximum displacement errors in coupling method compared against FE ABAQUS solutions.

It is evident from *Table 6.1*, *Figure 6.2*, and *Figure 6.3* that the maximum error in all cases falls within the allowable 0.85 mm tolerance for surgical accuracy (Bourgeois, Magnin, *et al.*, 1999).

An additional investigation has been conducted comparing tumour growth on an ellipsoid using a stand alone FE mesh and a mixed-mesh, containing an EFG region of high density surrounding the proposed area of localised high deformation. The accuracy of the FE results became questionable as tumours grew larger than 523.6 mm³. *Figure 6.4* demonstrates the localised deformation to the FE mesh with a series of increasing tumour growths. The onset of hour-glassing is present during the very early stages of tumour growth, despite control measures in place to prevent this. *Table 6.2* compares the maximum nodal displacements, surrounding the localised high deformation region, using the stand alone FE mesh and the mixed-mesh. It is apparent that initially both methods give quite similar results, however they begin to differ significantly as the distortion to the FE mesh increases. Discrepancies between the two methods are observed for tumour growths greater than 523.6 mm³.

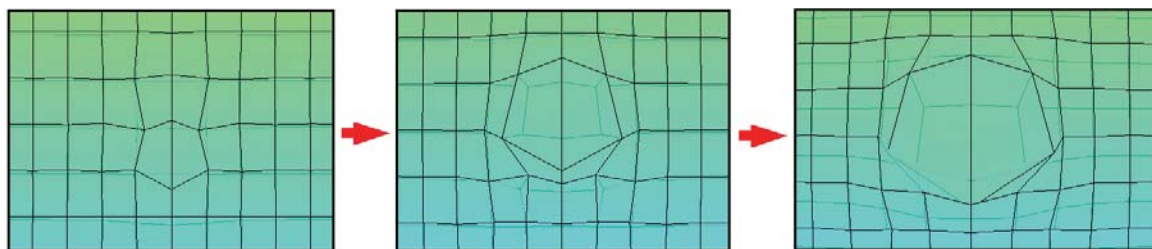


Figure 6.4: Ellipsoid FE mesh tumour progression – 268.1 mm³, 523.6 mm³, and 817.3 mm³ respectively.

Tumour Volume (mm ³)	Maximum Difference (mm)		
	Δx	Δy	Δz
261.8	0.0076	0.0082	0.0061
523.6	0.0188	0.0007	0.0112
817.3	0.0273	0.0133	0.0617

Table 6.2.: Maximum displacement differences for tumour growths.

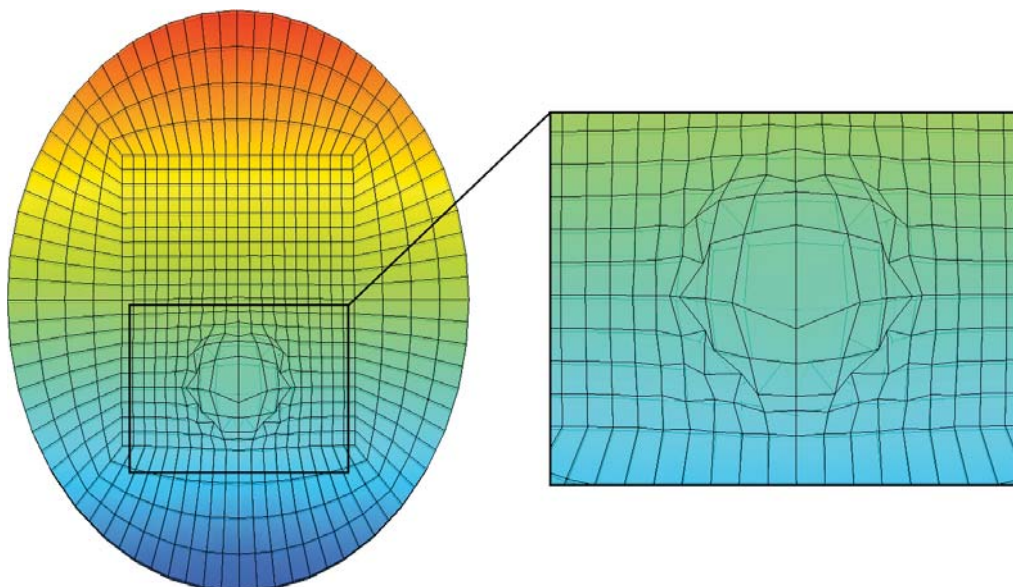


Figure 6.5: Failed 3053.6 mm³ tumour growth on FE ellipsoid mesh.

The FE mesh fails as the tumour reaches a volume of 3053.6 mm^3 . Significant distortion to the FE mesh is present in *Figure 6.5*, with the hexahedral elements compressing up to 70%, well beyond the reliable limits as discussed in Wittek, Dutta-Roy, *et al.* (2008). The mixed-mesh deformation for the same tumour growth volume is shown in *Figure 6.6*.

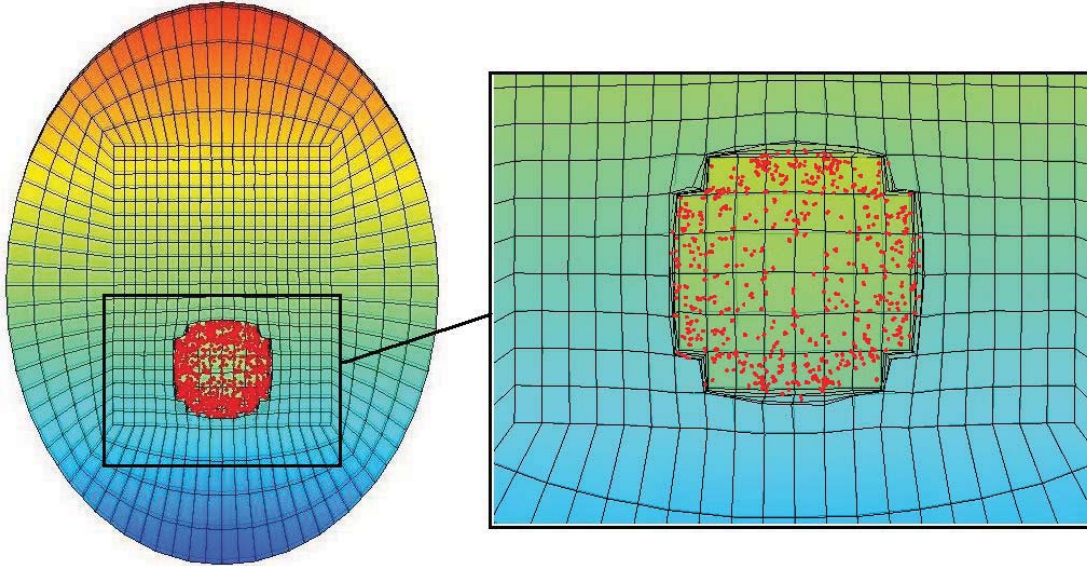


Figure 6.6: Final deformation due to 3053.6 mm^3 tumour using coupled method.

6.2 Tumour Growth Analysis

A mixed-mesh of a brain was created allowing for tumour growth to occur behind the left ventricle, mimicking an MRI scan of a tumour affected brain in Urbach, Binder, *et al.* (2007). An EFG nodal domain of high density surrounds the proposed tumour region allowing for large deformation. The tumour was grown as an ideal sphere, of which the analytical equations are well defined.

For healthy brain tissue and tumour we assume that Young's modulus, E , is 3000 Pa, and Poisson's ratio, ν , is 0.49 (Miller, Chinzei, *et al.*, 2000, Miller, 2002). The ventricles contains cerebro-spinal fluid (CSF), which has very similar material properties to water, hence they are modelled as a soft elastic compressible solid, with $E = 10 \text{ Pa}$ and a low Poisson's ratio, $\nu = 0.1$. A low Poisson's ratio allows to simulate leakage of the cerebro-spinal fluid which may occur under static deformation conditions. (Wittek, Miller, *et al.*, 2006).

A number of different tumour growth sizes were investigated, with deformation volume change in the ventricles, from an initial volume of 57.1 ml , noted in *Table 6.3*.

$V_{\text{Tumour}} (\text{mm}^3)$	113.1	523.6	1436.8	2144.6	4118.8
$\Delta V_{\text{Left-Ventricle}} (\text{ml})$	-0.099	-0.524	-1.224	-1.312	-1.968
$\Delta V_{\text{Right-Ventricle}} (\text{ml})$	-0.075	-0.331	-1.099	-1.143	-1.310
$\Delta V_{\text{Ventricles}} (\text{ml})$	-0.174	-0.855	-2.323	-2.455	-3.278

Table 6.3: Change in left ($\Delta V_{\text{Left-Ventricle}}$), right ($\Delta V_{\text{Right-Ventricle}}$), and total ventricular volume ($\Delta V_{\text{Ventricles}}$) due to tumour volume (V_{tumour}).

Given the location of the tumour, the ventricular deformation and associated volume loss, displayed in *Table 6.3*, is likely to correspond to the leakage of CSF. In reality CSF may leak between the left and

right ventricles, however it is also known to leak out of the ventricles completely, particularly under static deformation (Rando and Fishman, 1992). Furthermore, large tissue deformation is apparent, particularly for the 4118 mm^3 tumour, as shown in *Figure 6.7*, with local displacements of up to 9.66 mm . For this example 14.5% of the brain mesh experienced displacements greater than 5 mm .

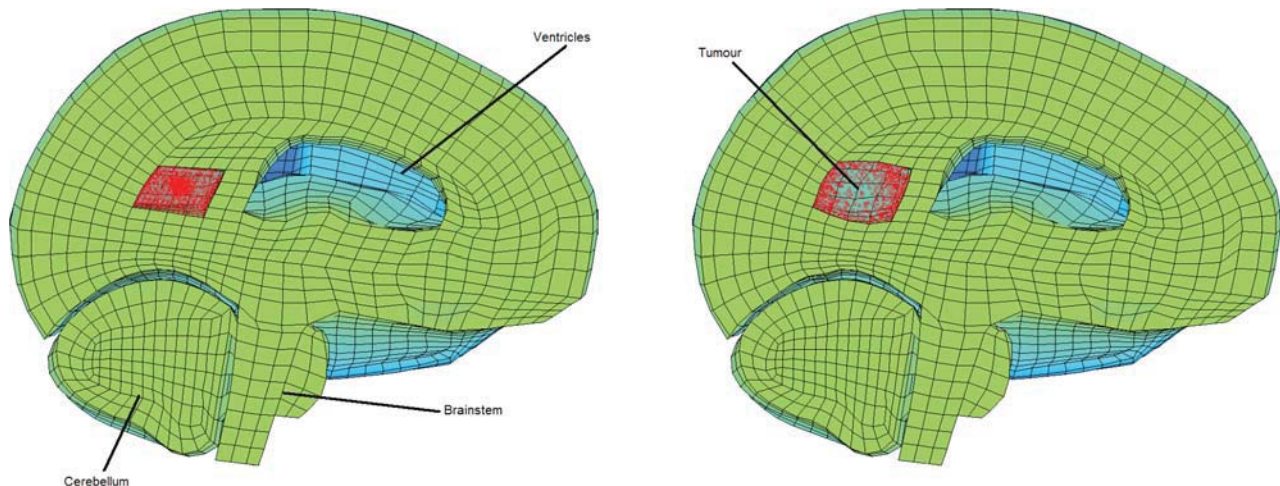


Figure 6.7: Undeformed brain cross-section (left). Deformed brain cross-section due to 4118 mm^3 tumour (right).

This follows on from Clatz, Bondiau, *et al.* (2004), which declared volume variation within the ventricles and large tissue deformation in response to brain tumour growth mass effect. It should be noted that simulated tumour growths larger than 14000 mm^3 on the given mixed-mesh reduced the reliability of the method as the resulting deformation to the Finite Element region became too large. A greater EFG domain would be required surrounding the tumour affected region in order to simulate larger growths accurately.

7. Conclusion

A new coupling method has been proposed to combine the Finite Element and Element Free Galerkin methods for modelling the non-linear soft tissue deformation of the brain in response to tumour growth. The method was verified against FE commercial software and a validated EFG simulator on a number of different mixed meshes. All results were very accurate, easily falling within the 0.85 mm error tolerance, corresponding to the working resolution of an MRI scan. Simple analytical tumour growths were conducted on a comprehensive brain mesh. The tumour's close proximity to the ventricles caused observable volume changes, which may involve leakage of CSF. Furthermore large tissue displacements were noted, with a significant portion of the brain undergoing moderate deformation. In reality this may have a detrimental effect on the cell metabolism and function of the brain, altering the stress distribution and blood flow. Further investigation into realistic tumour growth models and implementation of a brain-skull contact algorithm would increase the reliability of the results. Ultimately this would become beneficial for both clinical prognosis and operation planning as well as for simulated training applications.

References

- Bathe, K. J. (1996). *Finite Element Procedures*. Upper Saddle River, New Jersey, USA, Prentice-Hall Inc.
- Belytschko, T., Krongauz, Y., *et al.* (1996). "Meshless Methods: An Overview and Recent Developments." *Computer Methods in Applied Mechanics and Engineering* 139: 3-47.

Bourgeois, G., Magnin, M., *et al.* (1999). "Accuracy of MRI-guided stereotactic thalamic functional neurosurgery." *NEURORADIOLOGY* 41(9): 636-645.

Clatz, O., Bondiau, P., *et al.* (2004). Brain Tumour Growth Simulation, INRIA.

Flanagan, D. P. and T. Belytschko (1984). "Eigenvalues and Stable Times Steps for the Uniform Strain Hexahedron and Quadrilateral." *Journal of Applied Mechanics* 51: 35-40.

Fries, T. P. and H. G. Matthies (2003). Classification and Overview of Meshfree Methods. Informatikbericht 2003-03. Technical University Braunschweig, Brunswick, Germany, Institute of Scientific Computing.

Hallquist, J. O. (2006). LS-DYNA Theory Manual. California, Livermore Software Technology Corporation.

Horton, 2006. "Mesh Free Methods For Soft Tissue Deformation", Report # ISML/02/2006.

Horton, 2007. "Mesh Free Methods For Soft Tissue Deformation II", Report # ISML/01/2007.

Horton, Wittek, *et al.*, (2007) "Subject-specific biomechanical simulation of brain indentation using a meshless method" MICCAI 2007.

Joldes, G. R., A. Wittek, *et al.* (2007). "An efficient hourglass control implementation for the uniform strain hexahedron using the Total Lagrangian formulation." *Communications in Numerical Methods in Engineering*. Early View.

Li, S. and W. K. Liu (2004). Meshfree Particle Methods. Berkeley, California, Springer.

Miller, K., Chinzei, K., *et al.* (2000). "Mechanical properties of brain tissue in-vivo: experiment and computer simulation." *Journal of Biomechanics* 33(11): 1369-1376.

Miller, K., Joldes, G., *et al.* (2007). "Total Lagrangian Explicit Dynamics Finite Element Algorithm for Computing Soft Tissue Deformation." *Communications in Numerical Methods in Engineering* 23: 121-134.

Miller, K., Taylor, Z., *et al.* (2005). "Towards Computing Brain Deformations for Diagnosis, Prognosis, and Neurosurgical Simulation." *Journal of mechanics in medicine and biology* 5(1): 105.

Rando, T. A. and Fishman, R. (1992). "Spontaneous intracranial hypotension " *Neurology* 42: 481.

Urbach, H., Binder, D., *et al.* (2007). "Correlation of MRI and histopathology in epileptogenic parietal and occipital lobe lesions." *Seizure* 16(1): 608-614.

Wittek, A., Dutta-Roy, T., *et al.*, (2008). "Subject-specific non-linear biomechanical model of needle insertion into brain" *Computer Methods in Biomechanics and Biomedical Engineering* 11: 135-146.

Wittek, A., Miller, K., *et al.* (2006). "Patient-specific model of brain deformation: Application to medical image registration." *Journal of Biomechanics* 40: 919-929.

Simulation of Active Cardiac Dynamics with Orthotropic Hyperelastic Material Model

Ken C. L. Wong¹, Linwei Wang¹, Heye Zhang²,
Huafeng Liu³, and Pengcheng Shi¹

August 3, 2008

¹B. Thomas Golisano College of Computing and Information Sciences,
Rochester Institute of Technology, Rochester, New York, USA
Email: {kenclwong, maomaowlw}@mail.rit.edu, pengcheng.shi@rit.edu

²Bioengineering Institute, University of Auckland, New Zealand
Email: heye.zhang@auckland.ac.nz

³State Key Laboratory of Modern Optical Instrumentation,
Zhejiang University, Hanzhou, China
Email: liuhf@zju.edu.cn

Abstract

Meaningful physical models are important for studying cardiac physiology, such as quantitative assessments of pathology via changes in model parameters, and recovering information from medical images. In order to achieve realistic deformation studies, an anatomically accurate cardiac model under the prolate spheroidal coordinate system has been proposed, which comprises the pole-zero constitutive law characterized by 18 material parameters. Nevertheless, the large number of parameters and the complicated mathematics under the curvilinear coordinate system make it difficult to implement and computationally expensive. In consequence, we propose a cardiac model under the cartesian coordinate system comprising the Costa law, which is tailored for medical image analysis. The Costa law is characterized by a strain energy function with only seven material parameters, but has been reported as the best among the five tested well-known models in a comparative study, including the pole-zero law. In our framework, the penalty method for material incompressibility is used to avoid introduction of extra variables. Furthermore, we introduce a simple but novel boundary condition for enforcing cardiac specific boundary displacements under the cartesian coordinate system. With the active stresses provided by cardiac electromechanical models, and also the blood pressures acting as the natural boundary conditions on the endocardial surfaces, the physiologically plausible active deformation of the heart can be simulated. Experiments have been done on a cubical object to verify the correctness of the implementation, and also on a canine heart architecture to show the physiological plausibility of the cardiac model.

1 Introduction

Physiologically meaningful cardiac models are important for studying cardiac physiology, such as quantitative assessments in pathology study via changes in model parameters, and recovering information from medical images [7]. At the macroscopic level, an active cardiac deformation model comprises an electrical propagation model, an electromechanical coupling model, and also a biomechanical model, among which the biomechanical model plays the crucial role in archiving realistic deformation. In [10] and [13], a cardiac electromechanical model has been introduced for image analysis and simulation. The model utilizes the Mooney-Rivlin material model, which is an isotropic hyperelastic material model usually used to describe the behavior of incompressible rubber like material [5]. With the implementation under the cartesian coordinate system, this framework is relatively easy to implement and computationally efficient. Nevertheless, according to biomechanical literatures [3, 4, 6], as well as nonlinear stress-strain relation and incompressibility, the myocardial tissues are also locally orthotropic in nature because of their fibrous-sheet structures, thus using an isotropic model will effect the physiological meaningfulness of the active cardiac deformation. On the other hand, an anatomically accurate cardiac model was proposed in [9] with more realistic material properties. This model comprises a nonlinear orthotropic pole-zero strain energy function characterized by 18 material parameters, which is implemented under the prolate spheroidal coordinate system so that the heart geometry can be best expressed. In consequence, this model provides physiologically plausible deformation. However, the large number of material parameters increases the difficulties of the derivation of the elasticity tensor. Furthermore, some complicated mathematical terms which only appear in the curvilinear coordinate system, such as the contravariant components, make this framework theoretically very hard to implement and also computationally expensive. Moreover, the transformations between the local (cartesian), global (curvilinear), and element coordinate systems also impose large difficulties in implementation and scalability, especially for image analysis where data are presented in the cartesian coordinate system.

In view of these problems, we introduce a cardiac model targeting for medical image analysis. It comprises an orthotropic hyperelastic material model, and is implemented under the cartesian coordinate system, thus it can be physiologically plausible yet relatively easy to implement. The Costa law is utilized as the biomechanical constitutive law, which consists a nonlinear strain energy function containing only seven material parameters, but is reported as the best among the five tested well-known constitutive laws in a comparative study, including the pole-zero law [2, 11]. The penalty method for material incompressibility is used to avoid introduction of hydrostatic pressures as extra variables. With the active stresses provided by electromechan-

ical models, and also the blood pressures acting as the natural boundary conditions on the endocardial surfaces, the physiologically plausible active deformation of the heart can be simulated. While the Costa Law has been implemented under the prolate spheroidal coordinate system to study the effect of laminar orthotropic myofiber architecture in a canine left ventricle [15], we contribute a simple but novel boundary condition for enforcing cardiac specific boundary displacements under the cartesian coordinate system, implemented using the meshfree methods to benefit medical image analysis [18]. Experiments have been done on a cubical object to verify the correctness of the implementation, and on a canine heart architecture to show the physiological plausibility of the proposed cardiac model.

2 Methodology

The biomechanically accurate material model, the incompressibility of the myocardium, and also the cardiac specific boundary conditions are essential for realistic cardiac deformation. With the cardiac system dynamics connecting these components with the kinematic quantities and active contraction forces, physiologically plausible deformations of the heart can then be achieved.

2.1 Hyperelastic Material Model

Biomechanical experiments showed that material properties of the myocardium are nonlinear and orthotropic, thus the fibrous-sheet structure and also the nonlinear stress-strain relation have to be properly considered [3, 4, 6].

Strain Energy Function

There are different hyperelastic material models describing the nonlinear myocardial stress-strain relation [9, 2, 11]. In an experiment of constitutive parameter optimizations with pig cardiac tissues, the Costa law has been reported as the best among the five well-known nonlinear constitutive laws [2, 11]. Furthermore, compared with the pole-zero law that has 18 parameters [9], the Costa law has only seven parameters, which results in a much smaller degree of freedoms for material parameters recovery from medical images, and thus can largely improve the computational efficiency especially when statistical state-space frameworks are utilized [14, 19]. As our goal is to construct a cardiac model which can facilitate medical image analysis, the Costa law is chosen as our material model, which describes the local orthotropic material property through the strain energy function [2]:

$$\Psi(E_{ff}, E_{fn}, E_{fs}, E_{nf}, E_{nn}, E_{ns}, E_{sf}, E_{sn}, E_{ss}) = \frac{1}{2}a(e^Q - 1) \quad (1)$$

where

$$Q = b_{ff}E_{ff}^2 + 2b_{fn}\left(\frac{1}{2}(E_{fn} + E_{nf})\right)^2 + 2b_{fs}\left(\frac{1}{2}(E_{fs} + E_{sf})\right)^2 + b_{nn}E_{nn}^2 + 2b_{ns}\left(\frac{1}{2}(E_{ns} + E_{sn})\right)^2 + b_{ss}E_{ss}^2 \quad (2)$$

with $E_{\alpha\beta}$ the components of the Green-Lagrange strain tensor \mathbf{E} defined under the local coordinate system (f, n, s ; fiber, normal, sheet). a , b_{ff} , b_{fn} , b_{fs} , b_{nn} , b_{ns} and b_{ss} are the seven constitutive material parameters of the tissue, with the unit of a as Pa and $b_{\alpha\beta}$ have no unit. The local fibrous-sheet structure is represented by the f - n - s coordinate system, which orientation can be different at different locations.

Stress Tensor

With the strain energy function defined, we can derive the second Piola-Kirchhoff (PKII) stress tensor $\mathbf{S} = \partial\Psi/\partial\mathbf{E}$ under the f - n - s basis as [5]:

$$S_{\alpha\beta} = \frac{\partial\Psi}{\partial E_{\alpha\beta}} = \begin{cases} ae^Q b_{\alpha\beta} E_{\alpha\beta}, & \text{if } \alpha = \beta \\ \frac{1}{2} ae^Q b_{\alpha\beta} (E_{\alpha\beta} + E_{\beta\alpha}), & \text{if } \alpha \neq \beta, \text{ with } b_{\alpha\beta} = b_{\beta\alpha} \end{cases} \quad (3)$$

It can be seen that the stress-strain relation is highly nonlinear, and the material stiffness increases with the deformation.

Elasticity Tensor

The problems of finite elasticity are nonlinear and usually have no closed-form solution, thus incremental solution techniques of Newton's type are required. In consequence, the elasticity tensor \mathbb{C} which provides the linearized stress-strain relation at a particular strain state is given as [5]:

$$\mathbb{C} = \frac{\partial\mathbf{S}}{\partial\mathbf{E}} = \frac{\partial^2\Psi}{\partial\mathbf{E}\partial\mathbf{E}} \quad \text{or} \quad C_{\alpha\beta rs} = \frac{\partial^2\Psi}{\partial E_{\alpha\beta} \partial E_{rs}} \quad (4)$$

\mathbb{C} possesses the major symmetries ($C_{\alpha\beta rs} = C_{rs\alpha\beta}$) and the minor symmetries ($C_{\alpha\beta rs} = C_{\beta\alpha rs} = C_{\alpha\beta sr}$), thus it has only 21 independent components.

Defining $[\Delta\mathbf{S}]_{\text{local}} = [\Delta S_{ff}, \Delta S_{nn}, \Delta S_{ss}, \Delta S_{fn}, \Delta S_{fs}, \Delta S_{ns}]^T$ and $[\Delta\mathbf{E}]_{\text{local}} = [\Delta E_{ff}, \Delta E_{nn}, \Delta E_{ss}, 2\Delta E_{fn}, 2\Delta E_{fs}, 2\Delta E_{ns}]^T$, with ΔS_{ij} and ΔE_{ij} the components of the local incremental PKII stress and strain tensors respectively, we have $[\Delta\mathbf{S}]_{\text{local}} = [\mathbb{C}]_{\text{local}} [\Delta\mathbf{E}]_{\text{local}}$, where:

$$[\mathbb{C}]_{\text{local}} = \begin{bmatrix} C_{ffff} & C_{ffnn} & C_{ffss} & C_{fffn} & C_{fffs} & C_{ffns} \\ C_{mfff} & C_{nnnn} & C_{nnss} & C_{nnfn} & C_{nnfs} & C_{nnns} \\ C_{ssff} & C_{ssnn} & C_{ssss} & C_{ssfn} & C_{ssfs} & C_{ssns} \\ C_{fnff} & C_{fnnn} & C_{fnss} & C_{fnfn} & C_{fnfs} & C_{fnns} \\ C_{fsff} & C_{fsnn} & C_{fsss} & C_{fsfn} & C_{fsfs} & C_{fsns} \\ C_{nsff} & C_{nsnn} & C_{nsss} & C_{nsfn} & C_{nsfs} & C_{nsns} \end{bmatrix} \quad (5)$$

This matrix is symmetric because \mathbb{C} possesses the major symmetries. Note that $[\mathbb{C}]_{\text{local}}$ must be multiplied with incremental *engineering* shear strain components ($2\Delta E_{ij}, i \neq j$) to obtain the proper incremental PKII stress tensor components.

To transform $[\mathbb{C}]_{\text{local}}$ into the global coordinate system, we have the relation:

$$[\mathbb{C}]_{\text{global}} = [T][\mathbb{C}]_{\text{local}}[R][T]^{-1}[R]^{-1} \quad (6)$$

with $[T]$ the transformation matrix which is a function of the f - n - s directions, and $[R]$ is a diagonal matrix responsible for the transformation between strain and engineering strain components, with elements $\{1, 1, 1, 2, 2, 2\}$. As both local and global coordinate systems are cartesian in our model, $[T]$ is much simpler compared with those using curvilinear global coordinate system [9].

2.2 Penalty Method for Incompressibility

It has been widely accepted in literatures that the myocardium is nearly incompressible [3, 4, 6]. In order to approximate this condition while not increasing the number of variables, the penalty method is used, which

is based on the idea of modeling the nearly incompressibility by using a large value of bulk modulus [5]. It is standard to use the decoupled representation of the strain-energy function:

$$\Psi(\mathbf{E}) = \Psi_{\text{vol}}(J) + \Psi_{\text{iso}}(\bar{\mathbf{E}}) \quad \text{with} \quad \Psi_{\text{vol}}(J) = \kappa \mathcal{G}(J) \quad (7)$$

where $J = (\det \mathbf{C})^{1/2}$ defining the volume ratio, with \mathbf{C} the right Cauchy-Green tensor, and $\bar{\mathbf{E}} = 0.5(J^{-2/3}\mathbf{C} - \mathbf{I})$. Ψ_{vol} describes the volumetric elastic response, and Ψ_{iso} describes the isochoric elastic response of the hyperelastic material which has the same form of (1) with \mathbf{E} replaced by $\bar{\mathbf{E}}$.

The volumetric contribution Ψ_{vol} is characterized by a penalty parameter $\kappa > 0$, which is an adjustable numerical parameter chosen through numerical experiments. The function \mathcal{G} is known as the penalty function with the form [5]:

$$\mathcal{G}(J) = \frac{1}{2}(J-1)^2 \quad (8)$$

While \mathcal{G} has different forms for different material properties, as the one for the myocardium is unknown, we use the simplest one which can account for the incompressibility.

With (7) and (8), the respective PKII stress tensor can now be defined as:

$$\mathbf{S} = \mathbf{S}_{\text{vol}} + \mathbf{S}_{\text{iso}} = Jp\mathbf{C}^{-1} + \frac{\partial \Psi_{\text{iso}}}{\partial \mathbf{E}}; \quad p = \frac{d\Psi_{\text{vol}}}{dJ} = \kappa(J-1) \quad (9)$$

and the respective decoupled representation of elasticity tensor is given as:

$$\mathbb{C} = \mathbb{C}_{\text{vol}} + \mathbb{C}_{\text{iso}} = \frac{\partial \mathbf{S}_{\text{iso}}}{\partial \mathbf{E}} + \frac{\partial \mathbf{S}_{\text{vol}}}{\partial \mathbf{E}} \quad (10)$$

Although this approach cannot impose total incompressibility, it can avoid the introduction of hydrostatic pressures which may lead to a global system matrix with rank deficiency [5].

2.3 Enforcing Cardiac Specific Displacement Boundary Conditions

Various structures constraining the cardiac deformation, among which the pericardial sac exhibiting high axial stiffness and low transmural shear resistance plays an important role in limiting the movement of the epicardium [9]. It is relatively easy to simulate this boundary condition under the prolate spheroidal coordinate system by limiting the corresponding displacement variables, however, it is not trivial under the cartesian coordinate system. To simulate the axial stiffness, we propose the boundary condition:

$$\mathbf{u} \cdot \mathbf{n} = b \quad (11)$$

where \mathbf{u} and \mathbf{n} are the displacement and normal on the epicardial surface under the cartesian coordinate system. b controls the displacement along the normal direction, which can be a function of deformation, or zero if displacement is forbidden. This boundary condition can be imposed using the generalized Lagrange multiplier or penalty method on the epicardium [1]. Furthermore, the penalty method is used to constrain the circumferential displacement of the epicardial surface, simulating the transmural shear resistance of the pericardial sac. Equation (11) is important for medical image analysis as it provides an efficient yet realistic way to couple the model with information from images, for example, to incorporate the displacement information of the epicardium extracted from the images using the method described in [12] into b . Although (11) is simple, we could not find any relevant literature which specifies this simple but useful relation for simulating the constraint of the pericardial sac under the cartesian coordinate system. The experimental results in section 3.2 will show that this constraint leads to the proper twisting motion of the myocardium.

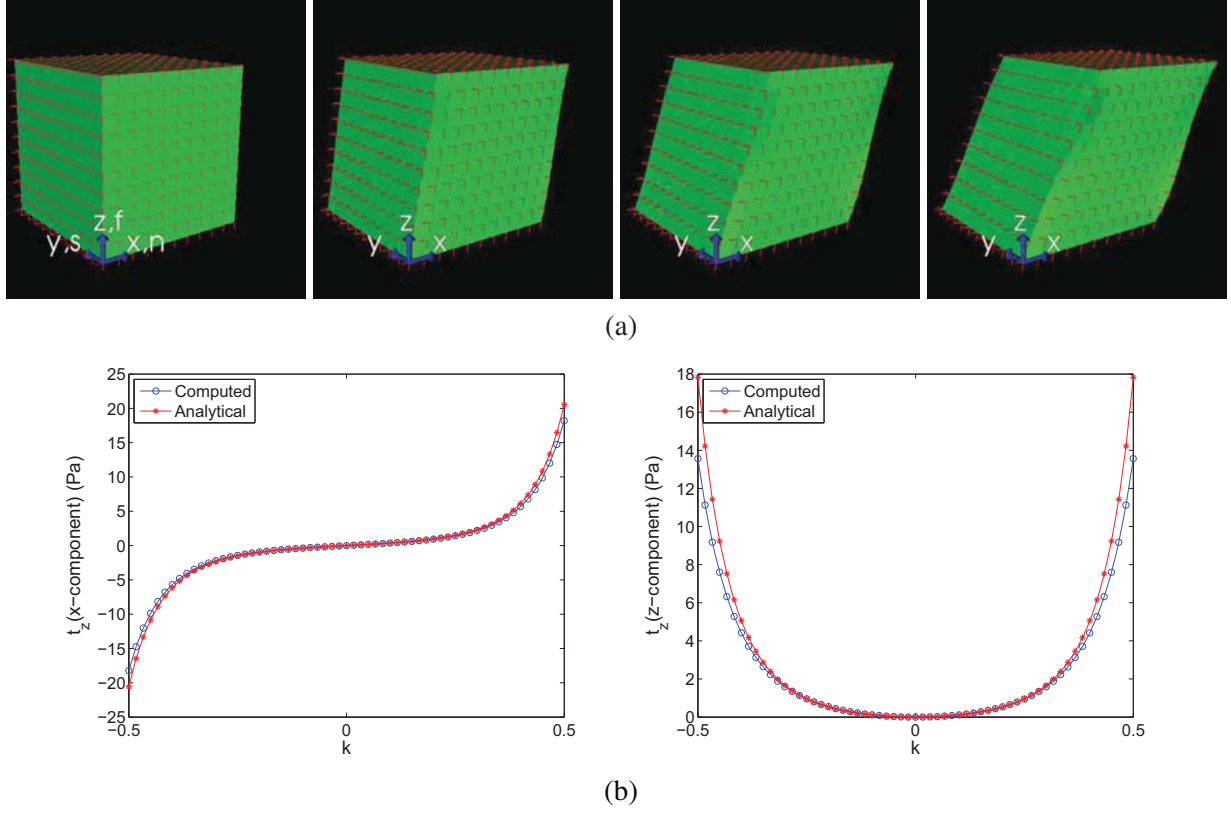


Figure 1: Static shear test on a cubical object. (a) The bottom surface is fixed and displacement is enforced along the x -direction on the top surface. Red lines indicate the fiber-normal-sheet orientations. Left to right: $k = 0, 0.167, 0.334$, and 0.5 . (b) Analytical and computed forces on the positive z -surface (top surface) of the cubical object. Left: the x -component. Right: the z -component.

2.4 Cardiac System Dynamics under Finite Deformation

The cardiac system dynamics acts as the central link between the material properties, external forces, and kinematic quantities. The displacement-based total-Lagrangian (TL) system dynamics of the heart under finite deformation is utilized. Using the meshfree methods for spatial approximation, the matrix representation of the TL system dynamics is given as [18]:

$$\mathbf{M}\ddot{\mathbf{U}} + \mathbf{C}\dot{\mathbf{U}} + \mathbf{K}\Delta\mathbf{U} = \mathbf{R}_c + \mathbf{R}_b - \mathbf{R}_i \quad (12)$$

where \mathbf{M} is the mass matrix, \mathbf{C} is the damping matrix, and \mathbf{K} is the strain incremental stiffness matrix containing the material and deformation properties. The hyperelastic material properties and incompressibility is embedded in \mathbf{K} as it comprises \mathbb{C} in (10). \mathbf{R}_c is the force vector containing the active forces obtained through a electromechanical coupling model. \mathbf{R}_b is the force vector for enforcing boundary conditions, and \mathbf{R}_i is the nodal force vector for finite deformation only and is related to the internal stresses. $\ddot{\mathbf{U}}$, $\dot{\mathbf{U}}$ and $\Delta\mathbf{U}$ are the respective nodal acceleration, velocity and incremental displacement vectors. By using the Newmark method for temporal integration, (12) can be solved for the nodal kinematic quantities, and thus the active cardiac deformation can be obtained.

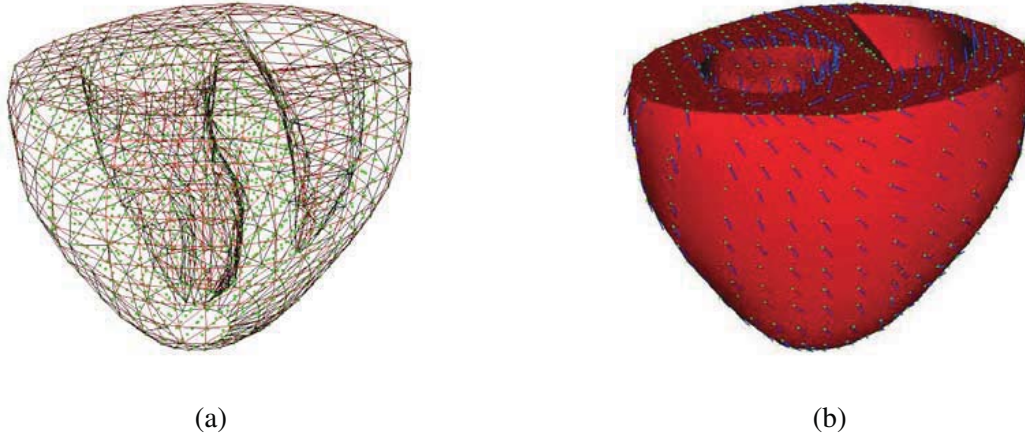


Figure 2: Meshfree representation constructed from the canine heart architecture. (a) A set of nodes (green) bounded by surface elements (red lines) representing the cardiac boundaries. (b) Fiber orientations shown as blue lines on the heart surfaces.

3 Experiments

3.1 Cubical Object

In order to verify the correctness of the implementation, a static passive shear test described in [11] was adopted. A cubical object with lengths 60 mm is utilized, which has the initial fibrous-sheet structure f - n - s pointing towards the z - x - y axes of the cartesian coordinate system. Suppose we have the deformation gradient tensor in the global x - y - z coordinate system as:

$$\mathbf{F} = \begin{bmatrix} 1 & 0 & k \\ 0 & 1 & 0 \\ 0 & 0 & 1 \end{bmatrix}_{x,y,z} \Rightarrow \mathbf{E} = \frac{1}{2} \begin{bmatrix} 0 & 0 & k \\ 0 & 0 & 0 \\ k & 0 & k^2 \end{bmatrix}_{x,y,z} \quad (13)$$

where k ranges between -0.5 and 0.5. Then the analytical force on the surface with normal pointing towards the positive z -direction (positive z -surface) is:

$$t_z = \begin{bmatrix} \frac{1}{2}Aak(b_{ff}k^2 + b_{fn})e^Q \\ 0 \\ A\frac{1}{2}ak^2b_{ff}e^Q \end{bmatrix} \quad (14)$$

with A the area of the surface before deformation, and $Q = 0.25b_{ff}k^4 + 0.5b_{fn}k^2$.

In the experiment, displacement boundary conditions are enforced on both z -surfaces of the cubical object to simulate the deformation in (13) in 60 steps, and the force on the positive z -surface is computed. Figure 1(a) shows the deformed structures. In Figure 1(b), we can see that the computed results are very close to the analytical results, yet the errors increase when the deformation becomes large. This is because for the hyperelastic material, the stress-strain relation is very steep when the strain is large, and thus the linearization error of the elasticity tensor becomes large when the step size is constant. The y -component of the computed force is about 10^{-5} of the x and z -components. These show that our implementation can capture the realistic stress-strain relation of the Costa law.

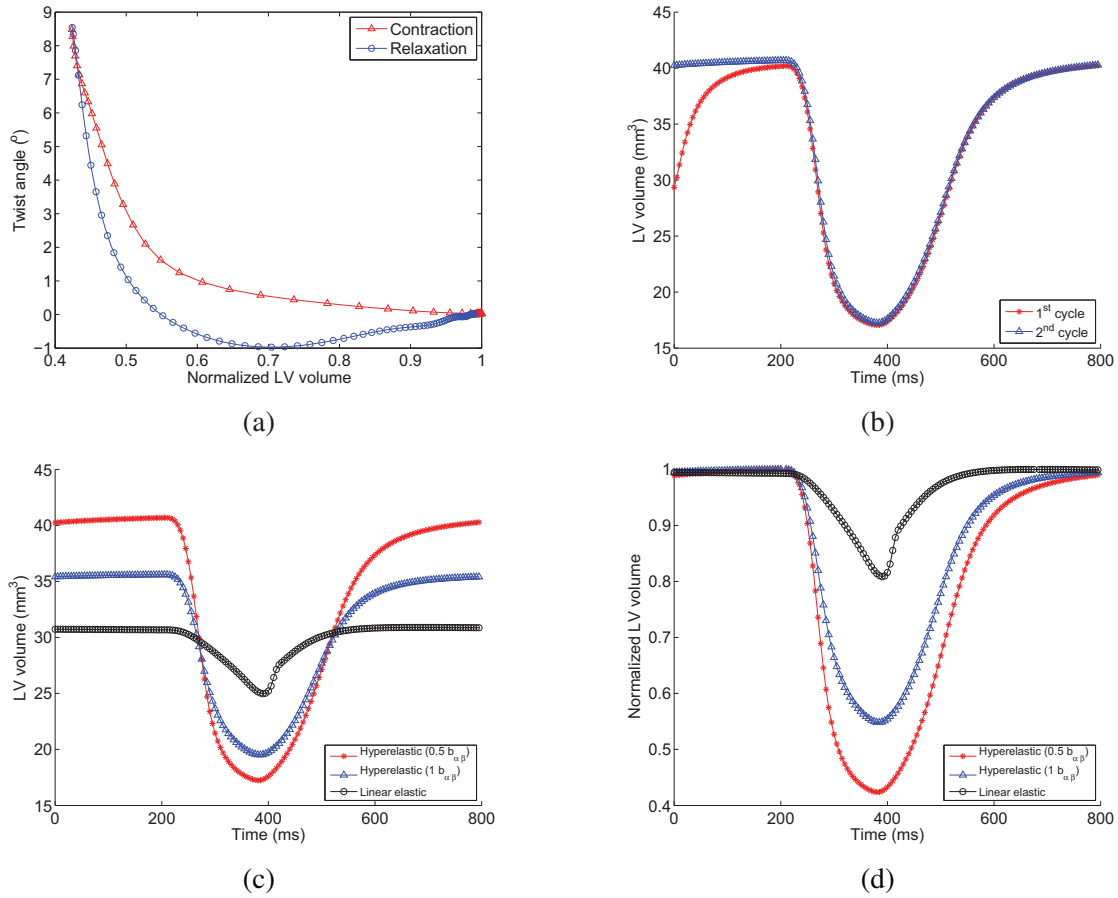


Figure 3: (a) Averaged twist angle versus normalized LV volume. The positive twist angle represents anticlockwise rotation, when viewed along the long axis of LV from the apex. (b) LV volume change versus time of different cardiac cycles for the $0.5 b_{\alpha\beta}$ case. (c) LV volume change versus time of different material parameters. (d) Normalized LV volume change of (c), for easier comparison of the stroke volumes. Stroke volumes of the $0.5 b_{\alpha\beta}$, $1 b_{\alpha\beta}$, and linear elastic cases are 57.6%, 45.2%, and 19.1% respectively.

3.2 Canine Heart Architecture

The canine heart architecture of the University of Auckland was used, which provides both the geometry and fibrous-sheet structure [9]. A meshfree representation was constructed from the canine heart geometry [8], with the fiber orientations shown in Figure 2. Active contraction forces were simulated through the cardiac electromechanical model described in [19], and deformations of one cardiac cycle in 800 ms were computed. As the canine heart architecture was obtained through in-vitro anatomical experiments when the bloods were not inside the ventricles, its geometry should not be treated as the end-of-diastole, and blood pressures were applied to the surfaces of the endocardia of the left and right ventricles (LV and RV) to inflate them. This step built up stresses in the myocardium at the end of diastole, and thus increase the physiological meaningfulness of the simulation. Two consecutive cardiac cycles were run so that the effects of the improper initial conditions, such as the zero velocities, zero accelerations, and zero myocardial stresses, could be alleviated. Figure 3(b) shows the change of the LV volume of the two cardiac cycles, and we can see that the end-of-diastole volume become stable in the second cycle.

Figure 4 shows the deformation of the simulated beating heart, and also a MRI sequence for comparison. The

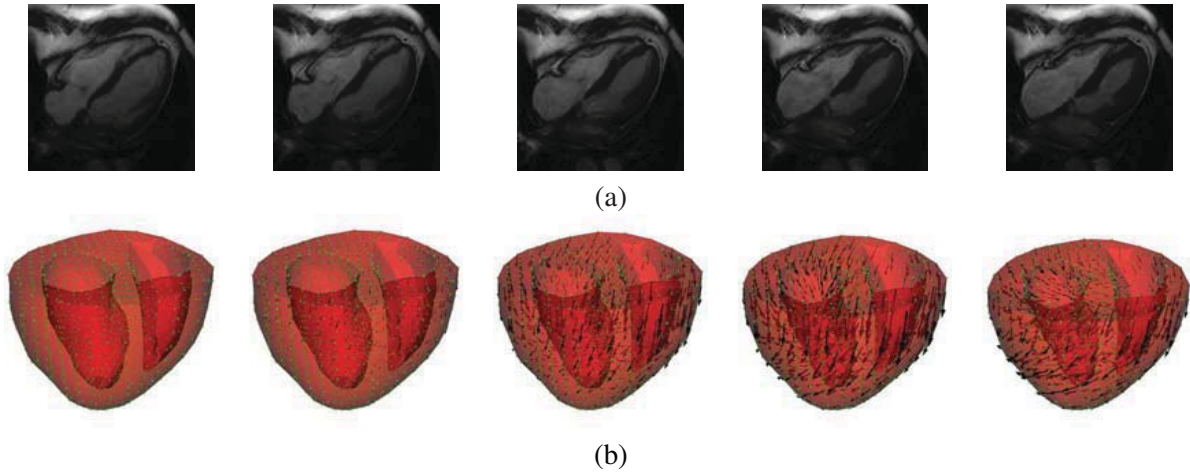


Figure 4: Deformations of cardiac geometries during systole. (a) MRI sequence of a healthy human heart. Left to right: 0 ms, 86 ms, 172 ms, 258 ms, and 344 ms. (b) Simulated cardiac cycle. The green dots represent the material points in the myocardium and the black arrows represent the incremental displacement vectors. Left to right: 220 ms, 240 ms, 260 ms, 280 ms, and 300 ms.

MRI sequence contains 20 frames of a cardiac cycle of a healthy human. Each 3D image frame contains eight image slices, with 10 mm inter-slice spacing, in-plane resolution of 1.56 mm/voxel, and temporal resolution of 43 ms/frame. It can be seen from the MRI that, because of the constraint of the pericardial sac, the motion of the epicardium along the normal direction of the epicardial surface is limited. Furthermore, the apex is almost fixed, and the base moves towards the apex during contraction. All of these deformation patterns can be found in our simulation because we have applied proper displacement boundary conditions to simulate the effects of the structures surrounding the heart, especially those described in section 2.3. If the boundary condition of the pericardial sac is not included, the epicardium will displace towards the septum and results in unrealistic deformation. We can also observe from the displacement vectors of Figure 4(b) that the heart twisted during contraction. Again, because of the boundary conditions described in section 2.3, the amounts and directions of the twist angles are similar to those described in the literatures [4, 9], with the numerical results plotted in Figure 3(a).

The values of the material parameters were adopted from [11] for the initial experiments ($a = 0.171$ kPa, $b_{ff} = 34$, $b_{fn} = 11.1$, $b_{fs} = 12.6$, $b_{nm} = 19.3$, $b_{ns} = 9.01$, $b_{ss} = 13$). Nevertheless, even when very large contraction stresses were applied (around 50 kPa), the stroke volume of LV, which is defined as the difference between the end-diastole volume and the end-systole volume, could not achieve a proper value which should be about 60-70% when normalized by the end-diastole volume. This is because the stiffness of the material exponentially increases with the deformation, and the myocardium becomes too stiff to contract any more. As stated in [2], the material parameters are actually different at different locations of the heart, and some locations are softer so that larger deformation is allowed. As the precise distribution of different material parameters is not available, in order to investigate the effect of the parameters to the stroke volume, we performed another simulation with all the $b_{\alpha\beta}$ halved. Larger stroke volume was obtained, and the temporal changes of the LV volume became more similar to those presented in literatures [4, 6](Figure 3(c) and (d)). Furthermore, in order to verify the importance of using hyperelastic material, a simulation using linear elastic material was performed under exactly the same setting, with Young's moduli along and cross the myofiber as 75 and 25 kPa respectively [4]. It can be seen that the resulted stroke volume is very small, and the change of volume is almost linear compared with the hyperelastic model. This is because the stiffness of the linear elastic material does not change with deformation, while the hyperelastic material is relatively

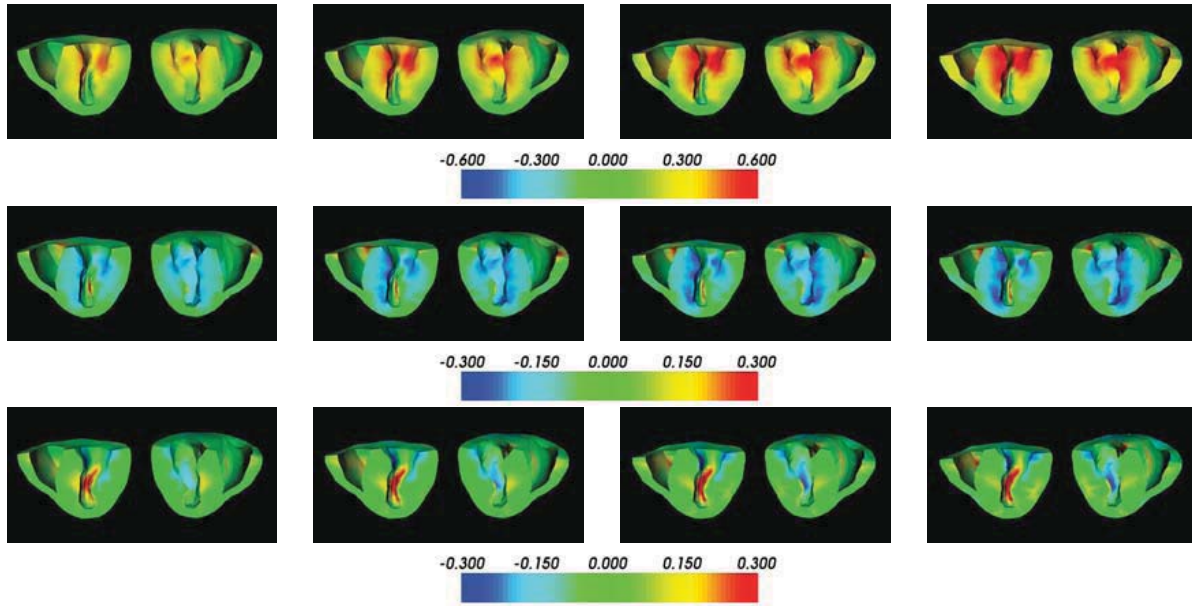


Figure 5: Strain maps of the simulated cardiac cycle. Top to bottom: radial, circumferential, and radial-circumferential strains, defined under a cylindrical coordinate system with the long axis of the LV as the long axis. Left to right: 300 ms, 320 ms, 340 ms, and 360 ms (during systole). Positive values represent extensions and negative values represent contractions.

soft at the beginning and becomes very stiff after deformation.

The strain maps of the simulation with $0.5 b_{\alpha\beta}$ are shown in Figure 5. While the displacements were obtained under the cartesian coordinate system, the strains were represented under the cylindrical coordinate system for the physiological meaningfulness. From Figure 5, we can observe the circumferential contraction and radial extension of the myocardium during systole, which are consistent with the descriptions in cardiological literatures [4, 6].

4 Conclusion and Discussion

In this paper, we have introduced a cardiac model tailored for medical image analysis. The Costa Law which was verified as the best among the five tested well-known hyperelastic material models has been adopted, its relatively few material parameters can facilitate the efficiency of the material property recovery from medical images. The corresponding PKII stress tensor and elasticity tensor have been derived, and the penalty method for incompressibility has been presented. We have also proposed a simple but realistic displacement boundary condition to simulate the constraint of the pericardial sac under the cartesian coordinate system. The correctness of the implementation was verified through an experiment on a cubical object, and the physiological plausibility of our model was verified through experiments on a canine heart architecture.

As we can enforce blood pressures as the natural boundary conditions to inflate LV and RV, our model is capable of incorporating the four cardiac phases of blood filling, isovolumic contraction, blood ejection, and isovolumic relaxation. While the blood filling and the blood ejection phases can be described through physical models such as the Windkessel model [16], the isovolumic phases can only be handled numerically without proper physical meaning [10, 13]. In view of this, we only apply the blood pressure of the blood

filling phase to simulate the inflation of the ventricles, and we are working on using the computational fluid dynamics to provide proper stress boundary conditions for the isovolumic phases, or even other phases. Furthermore, this cardiac model will be used for cardiac information recovery from medical images after completion. As this model is highly nonlinear, following the spirit of [17], the unscented Kalman filter will be utilized for the recovery process.

References

- [1] K. J. Bathe. *Finite Element Procedures*. Prentice Hall, 1996.
- [2] K. D. Costa, J. W. Holmes, and A. D. McCulloch. Modelling cardiac mechanical properties in three dimensions. *Philos. Trans. R. Soc. London*, 359(1783):1233–1250, 2001.
- [3] Y. C. Fung. *Biomechanics: Mechanical Properties of Living Tissues*. Springer-Verlag, 2nd edition, 1993.
- [4] L. Glass, P. Hunter, and A. McCulloch, editors. *Theory of Heart: Biomechanics, Biophysics, and Nonlinear Dynamics of Cardiac Function*. Springer-Verlag, 1991.
- [5] G. A. Holzapfel. *Nonlinear solid mechanics: a continuum approach for engineering*. John Wiley & Sons, Inc., 2000.
- [6] J. D. Humphrey. *Cardiovascular solid mechanics: cells, tissues, and organs*. Springer-Verlag, 2001.
- [7] P. J. Hunter. Modeling human physiology: The IUPS/EMBS physiome projec. *Proceedings of the IEEE*, 94(4):678–691, 2006.
- [8] H. Liu and P. Shi. Meshfree particle method. In *IEEE International Conference on Computer Vision*, pages 289–296, 2003.
- [9] M. Nash. *Mechanics and Material Properties of the Heart using an Anatomically Accurate Mathematical Model*. PhD thesis, University of Auckland, 1998.
- [10] J. Sainte-Marie, D. Chapelle, R. Cimrman, and M. Sorine. Modeling and estimation of the cardiac electromechanical activity. *Computers and Structures*, 84:1743–1759, 2006.
- [11] H. Schmid, M. P. Nash, A. A. Young, and P. J. Hunter. Myocardial material parameter estimation — a comparative study for simple shear. *Journal of Biomechanical Engineering*, 128:742–750, 2006.
- [12] M. Sermesant, H. Delingette, and N. Ayache. An electromechanical model of the heart for image analysis and simulation. *IEEE Transactions on Medical Imaging*, 25(5):612–625, 2006.
- [13] M. Sermesant, P. Moireau, O. Camara, J. Sainte-Marie, R. Andriantsimiavona, R. Cimrman, D. L. G. Hill, D. Chapelle, and R. Razavi. Cardiac function estimation from MRI using a heart model and data assimilation: advances and difficulties. *Medical Image Analysis*, 10:642–656, 2006.
- [14] P. Shi and H. Liu. Stochastic finite element framework for simultaneous estimation of cardiac kinematic functions and material parameters. *Medical Image Analysis*, 7:445–464, 2003.

- [15] T. P. Usyk, R. Mazhari, and A. D. McCulloch. Effect of laminar orthotropic myofiber architecture on regional stress and strain in the canine left ventricle. *Journal of Elasticity*, 61:143–164, 2000.
- [16] J.-J. Wang, A. B. O’Brien, N. G. Shrive, K. H. Parker, and J. V. Tyberg. Time-domain representation of ventricular-arterial coupling as a windkessel and wave system. *Am J Physiol Heart Circ Physiol*, 284:H1358–H1368, 2003.
- [17] L. Wang, H. Zhang, P. Shi, and H. Liu. Imaging of 3D cardiac electrical activity: A model-based recovery framework. In *International Conference on Medical Image Computing and Computer Assisted Intervention*, volume 4190 of *LNCS*, pages 792–799. Springer, 2006.
- [18] K. C. L. Wong, L. Wang, H. Zhang, H. Liu, and P. Shi. Simulation of active cardiac electromechanical dynamics. In *Medical Imaging and Augmented Reality*, volume 5128 of *LNCS*, pages 60–69. Springer, 2008.
- [19] K. C. L. Wong, H. Zhang, H. Liu, and P. Shi. Physiome-model-based state-space framework for cardiac deformation recovery. *Academic Radiology*, 14(11):1341–1349, 2007.

Realistic And Efficient Brain-Skull Interaction Model For Brain Shift Computation

Grand Roman Joldes, Adam Wittek, Karol Miller, Leith Morriss

Intelligent Systems for Medicine Lab.
The University of Western Australia,
35 Stirling Highway
Crawley, WA 6009, AUSTRALIA
grandj@mech.uwa.edu.au

Abstract

In this paper we propose a very efficient contact implementation for modeling the brain-skull interaction. This contact algorithm is specially designed for our Dynamic Relaxation solution method for solving soft-tissue registration problems. It makes possible the use of complex bio-mechanical models which include different nonlinear materials, large deformations and contacts for image registration. The computational examples prove the accuracy and the computational efficiency of our methods. For a model having more than 50000 degrees of freedom, a complete simulation can be done in less than a minute on a standard personal computer.

Keywords: real time computations, brain-skull contacts, image registration

1 Introduction

Brain deformation during surgery – commonly known as brain shift - is the primary motivation for this study. Deformations within the brain due to brain shift are difficult to monitor in real time as high resolution intra-operative MRI still remains a research rather than a clinical tool. These unknown changes in the location and shape of the brain and associated anatomy present the neurosurgeon with challenges and barriers to safe successful surgery. The “accurate localization of target” has been listed as the first principle in modern neurosurgical procedures [1] and this project aims to make accurate localization of targets more achievable.

Surgery related brain deformations occur for a number of reasons – loss of fluid during a craniotomy, brain edema or physiologic changes [2, 3]. Deformations of up to 10 mm are common in nearly all neurosurgical cranial procedures [4] and can be up to 25 mm in some cases [5]. These deformations make surgery difficult as the neurosurgeon is usually unable to track them using high quality intra-operative medical images. The surgeon may see that the surface of the brain collapsed by 10 mm, but they will not be able to predict the deformation within the brain due to this collapse.

The resolution of intra-operative images is much lower than the one of pre-operative images, thus registration of the accurate pre-operative images to the intra-operative state is required for a complete and accurate visualization. A registration method that leads to physically plausible deformation estimates is the computation of the intra-operative brain deformations using a biomechanical model. Such a method treats brain shift as a solid mechanics problem.

The context of neurosurgery provides a number of constraints for a useful computation of brain deformation. Predominately the two most important constraints are short computation time and high accuracy. The computation time must be very short, so that updates to the model – from intra-operative measuring and imaging – can be immediately shown to the surgeon.

If only partial information about the brain surface can be obtained intra-operatively (i.e. only in the area of craniotomy), the deformation problem can not be solved accurately without considering the interaction between the brain and the skull for the remaining of the surface.

This paper is organized as follows: the problem of brain-skull interaction is analyzed in the next section, the resulting contact algorithm implementation is presented in Section 3, simulation results are presented in Section 4 and the last section contains some discussions and conclusions.

2 Problem Formulation

2.1 Registration As A Solid Mechanics Problem

The process of matching images of the same anatomy in differing modalities or resolutions is termed registration [6]. When the anatomy imaged is rigid (e.g. skeletal structure) only rigid registration is required, which is a simple process of mapping points between two coordinate systems. When the anatomy deforms – as is the case for the brain – more advanced non-rigid registration techniques are required.

Non-rigid registration is required for image-guided surgical procedures, where high resolution pre-operative images are warped to the configuration of lower quality intra-operative images. This has traditionally been achieved through applying image distortion or transformation algorithms to warp images ([7-9]). These methods work well when differences between images are not too large, however the plausibility of the solution can not be guaranteed with purely image based warping. When registering the finite deformations it is instead suggested to consider the registration process as a solid mechanics problem, to produce a solution based on the established principles of continuum mechanics.

The use of biomechanical models was proposed by many researchers. When appropriate nonlinear models and solution methods are used, good registration results are obtained even in case of finite deformations [10-12].

2.2 Interaction Modeling For The Brain-Skull Interface

There are three membranes: dura mater, the arachnoid and pia mater between the brain and skull. The subarachnoid space (SAS) contains cerebrospinal fluid (CSF). This complex structure is presented in Fig. 1 (edited from [13]). During craniotomy CSF can leak freely from the subarachnoid space, creating a gap between the brain and the skull [12].

As the Young's modulus of the skull bone is several orders of magnitude greater than that of the brain tissue we can treat the skull as a rigid body. Therefore it is sufficient to model the brain-skull interaction as a contact between a deformable continuum (the brain) and a rigid body (the skull).

Some authors have tried to model the brain-skull interaction as a sliding contact with no separation, in which the nodes on the brain surface can move only tangentially to the skull surface [14]. In such case the brain can not move towards the skull or separate from it. Considering the anatomical structure of the brain-skull interface and based on comparisons between pre-operative and intra-operative MRI images, we consider this is not an appropriate approach.

Other authors have applied displacements over the entire surface of the brain, to match the deformation of the surface to the intra-operative images [15, 16]. Although this is a realistic approach from the modelling point of view, the problem of obtaining the displacements of the entire brain surface intra-operatively remains.

The following assumptions are made in order to simplify the contact problem:

- If the skull is considered rigid and fixed, then deformation of this body is irrelevant. Only consideration of brain deformation is required.
- As lubrication is present, friction is low and sliding of the brain on the skull occurs – frictionless contact conditions are the simplest representation of sliding contact.
- Separation of brain from skull is allowed.
- Only the deformation of the brain is of interest for registration purposes – thus the contact force is not specifically of interest. The brain deformation is formulated as a “displacement – zero traction problem”, as only displacement constraints are prescribed and no surface tractions are applied. This leads to a smaller influence of the material constitutive model on the simulation results [17].

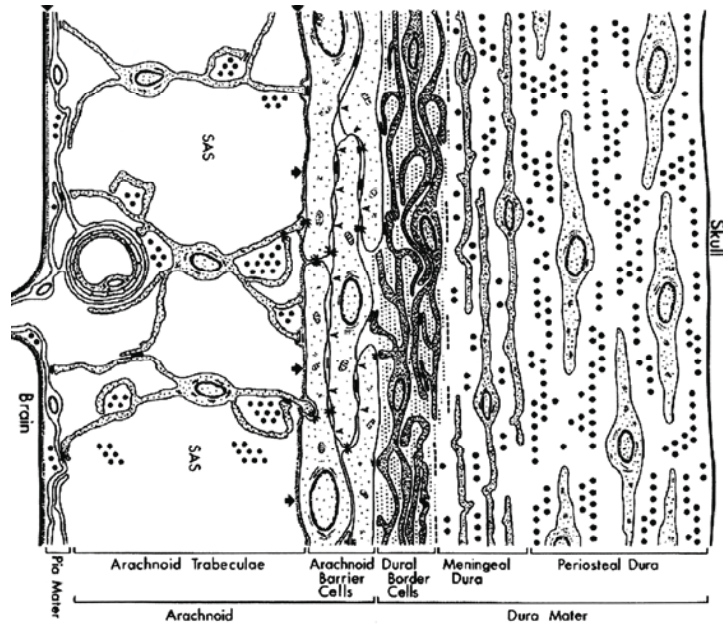


Fig. 1. The structure of the brain-skull interface, adapted from [13]

When selecting the best contact formulation we must also consider the solution method used for solving the finite element problem. We use Dynamic Relaxation [18] for finding the deformed state of our biomechanical model. This is an explicit method in which the position of the brain nodes is updated at every time step.

The simplest contact formulation for the brain-skull interaction, that accounts for the points discussed above, would be a finite sliding, frictionless contact between a deformable object (the brain) and a rigid surface (the skull). This can be implemented as a kinematic constraint type of contact that does not require the computation of any contact forces at the interface. A similar approach was proposed in [19], but no details are given regarding the contact algorithm and the simulations are performed using a commercial software (Abaqus).

There are many interaction (contact) handling algorithms available in commercial software, but there are some problems in using them: a large number of parameters (that influence the contact behaviour and the accuracy of the results) and long computation time. The contact algorithm we present has no configuration parameters (does not require the computing of contact forces) and is very fast, with the speed almost independent of the mesh density for the skull surface.

The main parts of the contact algorithm are: detection of nodes on the brain surface (also called the slave surface) which have penetrated the skull surface (master surface) and the displacement of each slave node that has penetrated the master surface to the closest point on the master surface.

3 Contact Algorithm Implementation

3.1 Detecting Penetration

The surfaces of the anatomical structures of segmented brain images are typically discretized using triangles; therefore we consider the skull surface as a triangular mesh. We will call each triangle surface a “face”, the vertices - “nodes” and the triangle sides - “edges”.

We base our penetration detection algorithm on the closest master node (nearest neighbor) approach [20]. The basic algorithm is as follows:

- For each slave node P:
 - Find the closest master node C (global search)
 - Check the faces and edges surrounding C for penetration (local search)

To improve the computation speed, the global search phase is usually implemented using bucket sort [20]. A good description of this searching algorithm is given in [21]. In our implementation the size of the buckets used for the global search is different in the three directions. For each direction, this size is given by half of the maximum size of all master edge projections on that direction. This ensures that the number of nodes in each bucket is minimal while there are no buckets for which a closest node can not be found.

The next step (local search), for a slave node P, aims at finding the closest node R on the master surface, on the faces or edges surrounding node C (Fig. 2). Once the closest point on the master surface is identified, the penetration is detected by checking the sign of the scalar product $RP \cdot \mathbf{n}$, with \mathbf{n} the inside normal to the master surface in R. For an edge or a node the normal is defined as the sum of the normal vectors of adjacent faces.

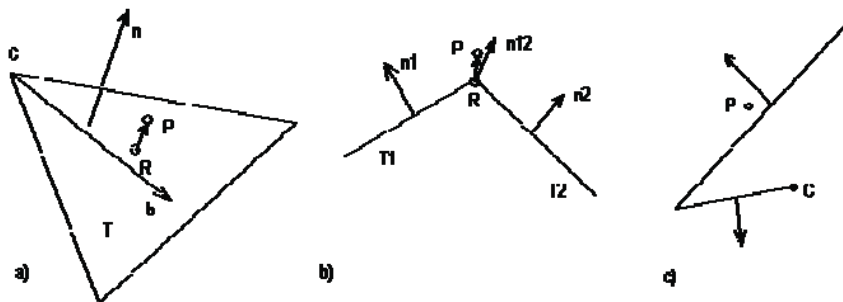


Fig. 2. Local search a) Penetration of a face b) Penetration of an edge c) Penetration of a face that is not connected to the closest node

Consider a triangular face T that contains node C, and the projection R of slave node P on the face (Fig. 2.a). If R is outside the triangle T, the face is discarded, otherwise the distance to the face is $[PR]$. In order to improve the speed of the search, only the faces for which $CP \cdot \mathbf{b} > 0$ are checked, with \mathbf{b} being the bisector of angle C in triangle T.

When P projects outside triangle T, it can project on one of the adjacent triangles or it can project on the common edge between two adjacent triangles, as shown in Fig. 2.b (seen along the common edge). Therefore all the edges containing the closest master node C must also be checked.

Another possibility is that the node does not project inside any of the edges either and the closest node itself is the closest point on the master surface.

In most of the cases, the basic tests presented above are sufficient for identifying the closest point on the master surface. Nevertheless, there are also special cases that must be considered, when the closest point on the master surface is not on the faces and edges adjacent to C . A simple case is presented in Fig. 2.c for a two-dimensional situation. In a tri-dimensional setting the situation is more complex and such cases are more likely to occur even without having such sharp corners.

In commercial software this problem is solved by searching for the closest face or edge on the master surface instead of searching for the closest master node [20]. This search is time consuming even if bucket sort is used. Therefore our proposal for handling these special cases is to make an analysis of the master surface and identify, for each node C , all the faces and edges that are possible to be penetrated by a slave node P in the case C is the closest master node to P . This analysis is done based on geometrical considerations as explained in the next section. The identified faces and edges are kept in a list for each master node C and they are checked in addition to the faces and edges that contain C when the local search is performed.

In some cases the slave node P is too far from the closest master node C to penetrate any face or edge that contains C . If d is the maximum penetration possible in any given time step and

$$CP^2 > d^2 + r^2 \quad (1)$$

then the basic tests are skipped and only the additional tests are done. In the above relation r is the radius of influence of node C , being equal with the maximum length of all master surface edges containing C .

3.2 Finding additional edges and faces that must be checked

Consider an edge AB and a node on the master surface C (Fig. 3.a). We must check if it is possible for a slave node to be closer to C than to A or B but to have penetrated AB . In triangle ABC , the location of nodes that are closer to C than to A and B (\mathbf{R}) is delimited by the lines OP and ON , where O is the center of the circumscribed circle and P and N are the middle of edges AC and BC . In space, \mathbf{R} is delimited by two planes perpendicular on ABC and containing OP and ON respectively. The following tests are made for edge any edge AB that does not contain C and is not part of the same master triangle as C :

- If $[CM] < [AM]$ or ($[CM] > [AM]$ and $[OM] < d$) then AB is added to the list for node C . These conditions are equivalent to the edge AB crossing or being very close (less than d) to \mathbf{R} .

For a node C and a face $T_1T_2T_3$ on the master surface, the location of nodes that are closer to C than to T_1 , T_2 or T_3 (\mathbf{R}) is delimited by 3 planes \mathbf{P}_i which are perpendicular at the midpoint M_i to segments CT_i ($i = 1,2,3$). These planes all contain point O which is the center of the sphere circumscribed to the tetrahedron $CT_1T_2T_3$. G_1 , G_2 , G_3 and \mathbf{R} are the projections of O to the faces of this tetrahedron (Fig. 3.b).

If \mathbf{n} is the normal to the face pointing in the direction of C , we build the points D_1 , D_2 and D_3 by displacing T_1 , T_2 and T_3 in the direction of \mathbf{n} by distance d . We name E_1 , E_2 and E_3 the middle of the edges of the triangle $D_1D_2D_3$ and with O_1 the center of the circumscribed circle for the same triangle. The following tests are made for each master triangle $T_1T_2T_3$ which does not have C as a node:

- It is easy to show that if $[CR] > 2*[T_1R]$ then R can not intersect the interior of the triangle $T_1T_2T_3$, and therefore the face is discarded
- Consider the set of points $S = \{ D_1, D_2, D_3, E_1, E_2, E_3, O_1 \}$. O_1 is included in S only if it is in the interior of triangle $D_1D_2D_3$. If any of these points is on the same side of all three planes P_i as C then the face is added to the list of additional faces to check for node C . From the geometry, these tests are equivalent to:

$$M_i S \cdot M_i C > 0, \quad i = 1, 2, 3 \quad (2)$$

with S being any point from S .

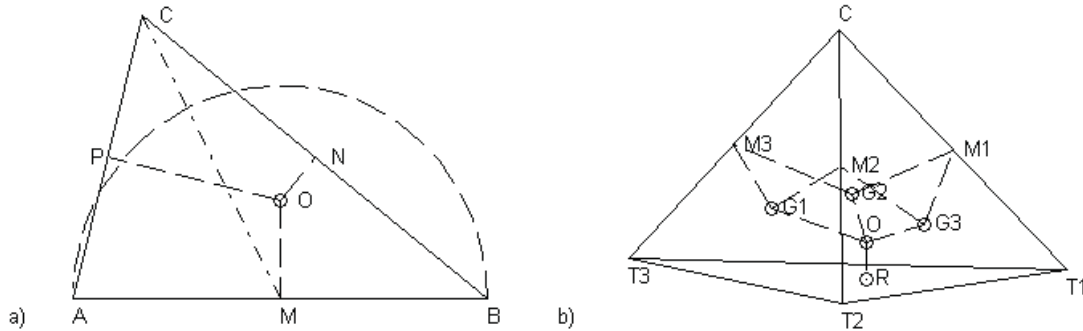


Fig. 3. Detection of additional edges (a) and triangles (b) to check for node C

When the relation between nodes and edges or faces from the master surface is studied, bucket sort is used for decreasing the computation time. The edges are organized in buckets based on their middle point and the size of the buckets in all three directions is equal with half of the maximum edge length. The faces are organized in buckets based on the centers of their circumscribed circles and the size of the buckets is given by the maximum radius of these circles.

3.3 The complete algorithm

The basic contact algorithm is as follows:

1. Preprocessing stage:

- Study master surface and create lists with additional edges and faces to check for each master node;
- Pre-compute all dimensions related to the master surface that are needed in the local search stage (such as normal directions, lengths, bisectors, etc.)
- Distribute master nodes into buckets;

2. At the end of each Dynamic Relaxation step, for each slave node P :

- Identify the bucket containing P and search for the closest master node C in that bucket and all the surrounding buckets;
- Find the closest point on the master surface, R , by searching the master edges and faces that contain C and the additional master edges and faces related to node C
- Check for penetration, using the normal to the master surface in R ;
- If penetration is detected, move the slave node P to the point R

4 Simulation results

In order to assess the performance of the algorithm we performed simulations using our implementation of the contact algorithm (combined with Dynamic Relaxation as a solution method) and the commercial software package LS-Dyna [20] and compared the results.

The same loading conditions and material models were used in both cases. The loading consisted in displacements applied to the nodes from the craniotomy area using a smooth loading curve. Neo-Hookean material models were used for the brain tissue and for the tumor and a linear elastic model was used for the ventricles. In order to obtain the steady state solution, the oscillations were damped away using both mass and stiffness proportional damping in LS-Dyna.

In a first experiment, we displaced an ellipsoid (made of a nonlinear Neo-Hookean material) with the approximate size of a brain inside another ellipsoid simulating the skull. The maximum displacement applied was 40 mm. The average difference in the nodal displacement field between our simulation and the LS-Dyna simulation was less than 0.12 mm (Fig. 4.a).

In another experiment we performed the registration of a patient specific brain shift. LS-Dyna simulations for this case have been done previously and the results were found to agree well with the real deformations [11]. We performed the same simulations using Dynamic Relaxation and our contact algorithm. The average difference in the nodal displacement field was less than 0.2 mm (Fig. 4.b).

For a master surface consisting of 1993 nodes and 3960 triangular faces and a slave surface having 1749 nodes, the computation time dedicated to the contact handling for 1000 time steps is about 3.2 s on a standard 3 GHz Intel® Core™ Duo CPU system.

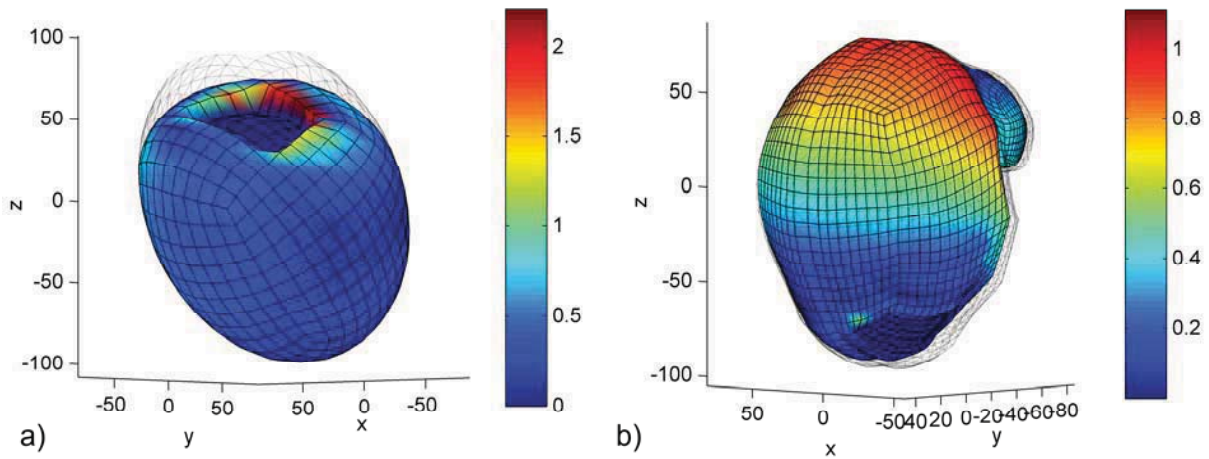


Fig. 4. Displacement differences (in millimeters) between our results and LS-Dyna simulations are presented using color codes. The transparent mesh is the master contact surface.

It is worth noting that if we refine the master surface and increase the number of triangles 4 times (to 15840), the computation time for 1000 time steps increases to 3.8 s. Therefore the computation time is almost independent of the number of triangles on the master surface. This happens because we use bucket sort with the bucket size depending on the dimensions of the triangles belonging to the master surface.

For the brain shift simulation a mesh with 16710 nodes and 15050 elements was used. The computation time for 1000 time steps was about 12 s and less than 3000 time steps are needed to reach the steady state solution. Therefore we need less than one minute for a complete brain shift simulation.

5 Discussion and conclusions

We presented in this paper a very simple and efficient contact algorithm that can be used for simulating the brain-skull interaction in a biomechanical model, when combined with an explicit solution algorithm – Dynamic Relaxation.

The surface representing the skull is considered rigid and therefore it can be analyzed pre-operatively and many quantities needed for handling the contact can be pre-computed. No parameters are needed for defining the contact (contact thickness, stiffness, etc.), as it only imposes kinematic restrictions on the movement of the brain nodes. The brain nodes are prevented from penetrating the skull, but they can slide along or separate from it.

By imposing only kinematic restrictions, no contact forces need to be computed. Although the contact forces can be extracted from the strains occurring in the brain elements, they are not of interest in our application. The absence of any forces applied on the brain surface leads to a smaller influence of the material constitutive model parameters on the simulation results.

The skull surface is considered to be a C0 triangular mesh, as this leads to a fast method for detecting penetration. If quadrilateral elements were present in this mesh, they can easily be split into two triangular elements. Because this surface is not smooth, it can be argued that high frequency vibrations will be introduced in the solution. In commercial codes such vibrations are handled using contact damping or by smoothing the surface (see [20]). Our solution algorithm naturally damps all the high frequency vibrations [18], therefore no additional effort is needed for handling these vibrations.

Combining Dynamic Relaxation with this contact implementation we can perform a brain shift simulation in less than a minute on a normal PC, for a model having over 50000 degrees of freedom. Therefore, we are one step closer to intra-operative brain shift simulation.

Acknowledgements: The first author was an IPRS scholar in Australia during the completion of this research. The financial support of the Australian Research Council (Grant No. DP0343112, DP0664534 and LX0560460) and NIH grant No. 1-RO3-CA126466-01A1 is gratefully acknowledged.

6 Bibliography

1. Nakaji, P. and Speltzer, R.F.: The Marriage of Technique, Technology, and Judgement. *Innovations in Surgical Approach* (2004) 51: p. 177-185
2. Himpens, J., Leman, G., and Cadiere, G.B.: Telesurgical laparoscopic cholecystectomy. *Surgical Endoscopy* (1998) 12: p. 1091
3. Hata, N., et al.: Three-dimensional optical flow method for measurement of volumetric brain deformation from intraoperative MR images. *Journal of Computer Assisted Tomography* (2000) 24: p. 531-538
4. Soza, G., et al.: Determination of the elasticity parameters of brain tissue with combined simulation and registration. *International Journal of Medical Robotics and Computer Assisted Surgery* (2005) 1: p. 87-95
5. Nabavi, A., et al.: Serial intraoperative magnetic resonance imaging of brain shift. *Neurosurgery* (2001) 49: p. 75-85
6. Lavallée, S.: *Registration for Computer Integrated Surgery: Methodology, State of the Art., Computer-Integrated Surgery, 1995*, Cambridge, Massachusetts: MIT Press
7. Beauchemin, S.S. and Barron, J.L.: The computation of optical flow. *ACM Computing Surveys* (1995) 27(3): p. 433-467
8. Viola, P. and Wells III, W.M.: Alignment by maximization of mutual information. *International Journal of Computer Vision* (1997) 24(2): p. 137-154
9. Toga, A. and Mazziotta, J.: *Brain Mapping - the methods*. Academic Press, Sydney (2002)
10. Wittek, A., et al.: Brain shift computation using a fully nonlinear biomechanical model, 8th International Conference on Medical Image Computing and Computer Assisted Surgery MICCAI 2005, 2005, Palm Springs, California, USA
11. Wittek, A., et al.: Patient-Specific Model of Brain Deformation: Application to Medical Image Registration. *Journal of Biomechanics* (2007) 40: p. 919-929
12. Hu, J., et al.: Intraoperative brain shift prediction using a 3D inhomogeneous patient-specific finite element model. *Journal of Neurosurgery* (2007) 106: p. 164-169
13. Haines, D.E., Harkey, H.L., and Al-Mefty, O.: The "subdural" space: A new look at an outdated concept. *Neurosurgery* (1993) 32: p. 111-120
14. Lunn, K.E., et al.: Data-guided brain deformation modeling: evaluation of a 3-d adjoint inversion method in porcine studies. *IEEE transactions on bio-medical engineering* (2006) 53: p. 1893-1900
15. Ferrant, M., et al.: Serial registration of intraoperative MR images of the brain. *Medical Image Analysis* (2002) 6(4): p. 337-359

16. Warfield, S.K., et al.: Real-time registration of volumetric brain MRI by biomechanical simulation of deformation during image guided surgery. *Computing and Visualization in Science* (2002) 5: p. 3-11
17. Wittek, A., Hawkins, T., and Miller, K.: On the unimportance of constitutive models in computing brain deformation for image-guided surgery. *Biomechanics and modeling in mechanobiology* (2008) published online
18. Underwood, P.: Dynamic Relaxation, in *Computational Methods for Transient Analysis*, Editor: T. Belytschko and T.J.R. Hughes (1983) New-Holland: Amsterdam. p. 245-265
19. Skrinjar, O., Nabavi, A., and Duncan, J.: Model-driven brain shift compensation. *Medical Image Analysis* (2002) 6: p. 361-373
20. Hallquist, J.O.: *LS-DYNA Theory Manual*. Livermore Software Technology Corporation, Livermore, California 94551 (2005)
21. Sauve, R.G. and Morandin, G.D.: Simulation of contact in finite deformation problems – algorithm and modelling issues. *International Journal of Mechanics and Materials in Design* (2004) 1: p. 287–316

Integration of Geometrical Boundary Conditions on Soft Tissue Characterization under Large Deformation

Bummo Ahn and Jung Kim

Korea Advanced Institute of Science and Technology

Abstract

Soft tissue characterization with finite element (FE) modeling is important to develop a realistic model for medical simulation, since it is possible to display complex tool-tissue interactions during medical interventions. However, it is difficult to integrate large deformation and geometrical boundary conditions to the FE computations. In this paper, the force responses and surface deformation fields of the tissues against the indentation were measured by a force transducer and three-dimensional optical system. Large indentation experiments on porcine liver were performed to estimate the radius of influence from the indented point up to 8 mm indentation and to measure the force response for 7mm indentation. The radius of influence region was plotted against various indentation depths and indenter shapes, and it could be used to determine the model size for the characterization. The tissue behavior of large deformation considering influence of the boundary conditions was characterized with FE modeling via hyperelastic and linear viscoelastic model.

1 Introduction

Virtual reality (VR)-based medical simulations [1, 2] provide a realistic environment as in the surgical operation for the training of surgeons. The simulations enable novice surgeons to safely acquire competency in complicated surgical skills that are otherwise risky and difficult to learn through surgery on actual patients.

Many medical procedures induce large deformation to soft tissues by instruments, but the force feedback or deformation of the simulation are currently based on linear elastic models with small deformation [3]. Therefore, the tissue behavior considering large deformation should be described by the nonlinear elasticity theory. While several studies were carried out regarding the measurement and modeling of the quantitative responses of the tissues, the researches on that under large deformation were insufficient due to the complex experiment conditions and nonlinear properties of the tissue. It can also be seen that according to the experiments and characterization methods, the measured mechanical properties show a large variation. In addition, currently developed models have limitations due to the complex experimental conditions and nonlinear properties of the tissue. Therefore, for more accurate modeling, especially medical simulation, organ experiments under large deformation have to be performed, and the mechanical models are characterized using the geometrically accurate boundary conditions and experimental results.

In comparison to the earlier studies, this study measured the surface deformation as well as force responses against the indentation to develop more accurate tissue model with considering both quantitative results. This work starts from mechanical experiments measuring the force responses and surface deformation of the tissues against the indentation, with force transducer and three-dimensional optical system. From these results, the maximum radius of influenced extent by the deformation was calculated according to the indentation depths and shapes of indenter tips. The maximum radius could be used to determine the minimal required size of FE model for the simulation. The model was designed and integrated into inverse FEM optimization algorithm to characterize tissue model parameters. The algorithm estimates unknown parameters by minimizing the least-square errors between simulation results of the FE model and force responses obtained from indentation experiments.

2 Soft Tissue Experiments

2.1 Experimental setup

While the previous studies focused only on the force responses of soft tissues, this study measured the surface deformation as well as force responses against the indentation. More accurate tissue model could be developed with considering both quantitative results. The deformation were obtained using the optical three-dimensional deformation analyzer (ARAMIS, GOM co., Germany) and the force responses were measured using one-dimensional indentation device [4] (see Fig. 1).

The deformation analyzer consists of a pair of digital CCD cameras, a light source, a trivet and a controller. The camera resolution is 1280×1024 pixels with the measuring range covering from millimeters to meters. The measuring accuracy, including the noise and vibration effects, is reported as less than $5 \mu\text{m}$. This analyzer is a non-contact measuring system, which is well suited for three-

dimensional deformation and strain distribution measurement under static or dynamic load. The procedures for measuring tissue deformation consist of sample preparation, image acquisition, and image

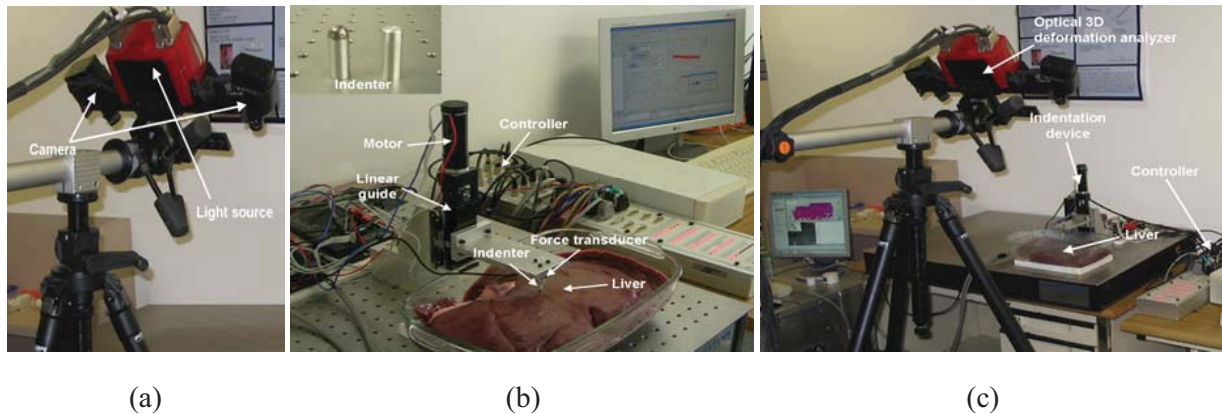


Figure 1. (a) Optical three-dimensional deformation analyzer, (b) Indentation device and indenters (flat and hemisphere tips), and (c) Experimental setup.

processing. Firstly, white and black color dots are sprinkled on the surface of a target tissue to make the reference patterns, shown in Fig. 2. Secondly, for the measurement, synchronized stereo images of the deformed pattern are recorded at different indentation depths. Finally, three-dimensional coordinate, displacement, and plane strain tensor of the tissue surface are calculated automatically using photogrammetric evaluation procedures [5]. Then, the results, three-dimensional visualization, sectional diagram of deformation, and time dependent deformation trajectory, were recorded for further analysis. Using this system, high resolution deformation and deformation trajectory depending on time was measured.

The indentation device is composed of a force transducer (Senstech co., Ltd., Korea), a DC motor (Maxon Precision Motors, Fall River, MA, USA), and two different shaped indenters. The force transducer's resolution is 1 mN and its measurement range is from 1 mN to 9.8 kN. The maximum position error is less than 5 μm , found by calibrating the dynamic motion of the motor. The displacement range is up to 41.5 mm, and the maximum speed is 8 mm/s. The device can induce unit step, sinusoidal, rectangular and saw tooth wave inputs of 10 μm ~ 41.5 mm displacements. Since even small changes in an indenter tip shape can make large differences in the mechanical responses of the tissues, the shape of indenter tips is an important factor [6]. Therefore, the indenters with cylindrical body (10 mm diameter) have flat and hemisphere shaped tips.

2.2 Sample preparation

The liver is a solid organ located in the abdominal cavity and is composed of a mass of lobules held together by fine areolar tissue [7]. It plays a major role in metabolism and has a number of functions in the body, including glycogen storage, decomposition of red blood cells, plasma protein synthesis, and detoxification of harmful substances [8]. We select the porcine liver as a target organ, because of the similarity in structure and functions to the human liver. Moreover, the porcine liver is readily available, relatively inexpensive and generally robust for a surgical model. Fresh livers were obtained from a local abattoir, which were preserved in an icebox and delivered to the laboratory in a few hours after extraction

to avoid dehydration. The indentation zone of the porcine liver was the center area of the median lobe for the consistency of experiments.

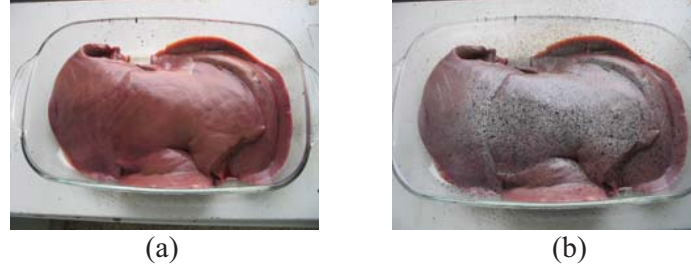


Figure 2. Specimen preparation to measure the surface deformation with sprinkling a random pattern on (a) the original tissue's surface with (b) the white and black color dots.

2.3 Experimental procedure

The following procedure was adopted for measuring the soft tissue behavior by the indentation. After sprinkling dots on the tissue surface, the indenter was brought into contact with the sample surface. Up to 8 mm indentations were induced to measure the surface deformation and the force responses for 5 mm and 7 mm indentations. Then the deformation under the applied indentations is recorded by the CCD cameras, and the three-dimensional coordinates of the entire surface are precisely calculated. In addition, the force responses were measured with force transducer and recorded with the data acquisition system (Ace Kit 1103 PX4 CLP, D-Space Inc., Germany). At the end of the experiments, the indenter was removed from the tissue surface and repositioned to proceed with the next experiment.

2.4 Data analysis

The schematic illustration and organ experiment before and after indentation are shown in Fig. 3. After indenting the tissue, the shape of the tissue surface is deformed. The raw data of the surface deformation obtained from the experiments are shown in Fig. 4. Due to the liver size, it is difficult to measure an entire affected area by the indentation. However, the surface deformations converged to zero according to the distance from the indentation center. The maximum radius of influenced extent by the deformation according to the indentation depths and shapes of the indenters was obtained using this tendency. The total deformation of the tissue surface was calculated by

$$\Delta D_{Total} = \sqrt{\Delta D_X^2 + \Delta D_Y^2 + \Delta D_Z^2} \quad (1)$$

where, ΔD_X , ΔD_Y and ΔD_Z are deformation for the x, y and z directions, respectively. After the deformation is converged at zero, the maximum radius was determined according to the indentation depths (2, 4, 6, and 8 mm) and shape of indenters (flat and hemisphere tip) as shown in Fig. 5. In addition, to obtain the relationship between the maximum radius and indentation depth for the each indenter, the results were fitted with a 1st order exponential function as,

$$R = R_0 - A \cdot \exp(-T/d) \quad (2)$$

where, R and T are the radius of influenced extent by the deformation and indentation depth, respectively. R_0 , A and d are the fitting parameters of the exponential function, which were shown in Table 2.

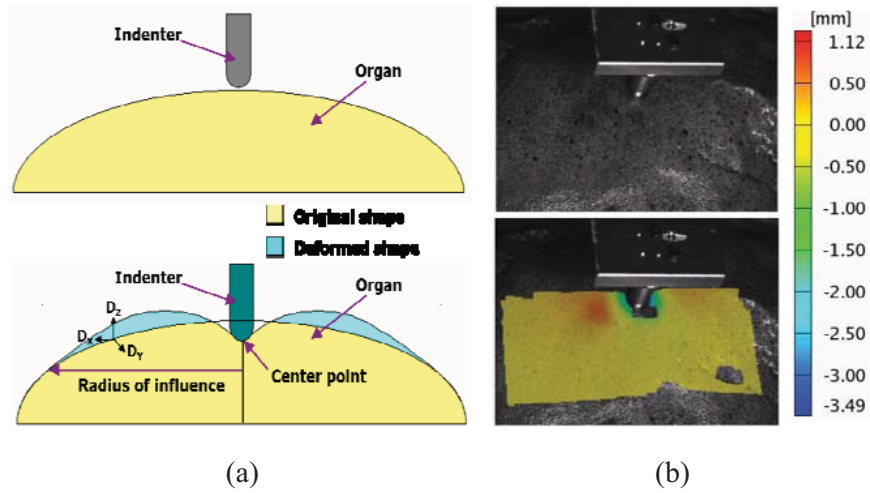


Figure 3. (a) Schematic illustration of the experiment and (b) organ experiment of the tissue before and after indentation.

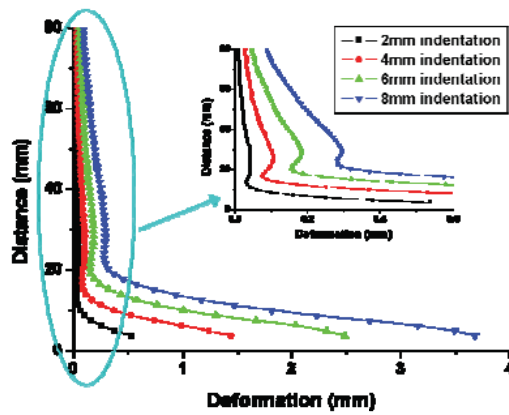


Figure 4. Results of the surface deformation experiments.

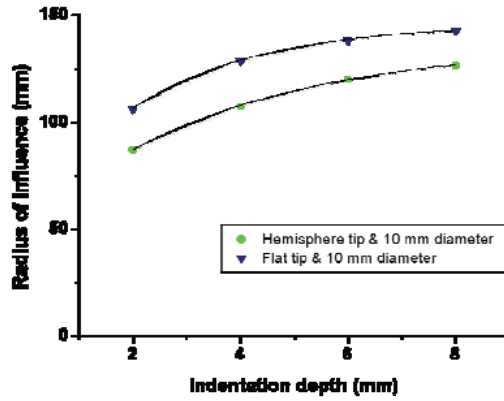


Figure 5. Radius of influenced extent by the deformation for the various indentation depths.

Table 2. Fitting parameters for each indenter.

Shape	Fitting parameters		
	R_0	A	d
Hemisphere tip	136.46	85.33	3.67
Flat tip	145.96	92.19	2.38

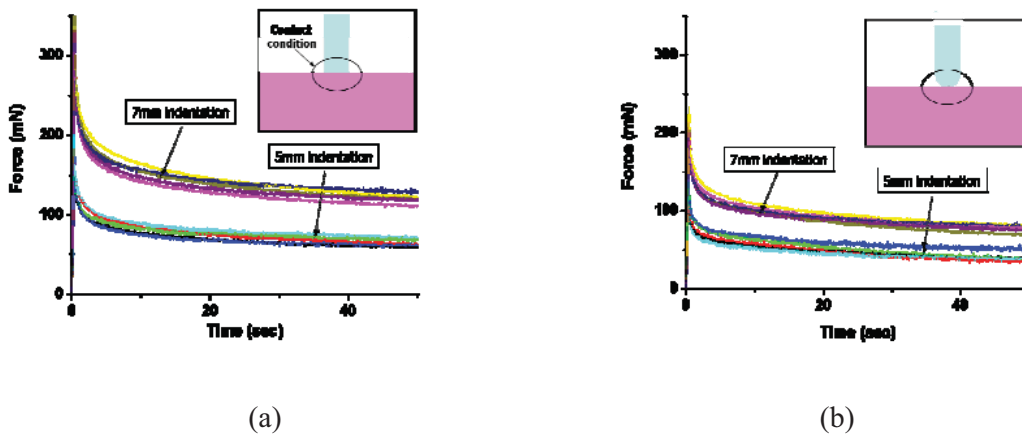


Figure 6. Indentation experimental results and contact conditions (upper and right box) for (a) flat and (b) hemisphere tips.

The force response, typical relaxation behavior, for each indenter is shown in Fig. 6. The magnitudes of the results with respect to the indentation depths and shapes of the indenters are obtained as intended. The results, obtained by the same indentation depth for the both indenters, are different according to the shape of the indenters, because the surface and point contacts between the indenter tip and tissue surface were

occurred by flat and hemisphere tips, respectively. Therefore, the indented tissue volume of the flat tip is larger than that of the hemisphere tip. Consequently, the force response of the flat tip is larger.

3 Soft Tissue Characterization

Many medical procedures induce large deformation to soft tissues by instruments, but the force feedback or deformation of the simulation are currently based on linear elastic models with small deformation [3]. Therefore, the tissue behavior considering large deformation should be described by the nonlinear elasticity theory. In addition, considering the complex boundary and contact conditions between the indenter and tissue, the FE method has been widely used in simulations [9]. The inverse FEM optimization algorithm [10-13], therefore, has been applied for the tissue characterization. The algorithm uses FEM simulation iteratively to find the parameters fitted to the experimental results.

In this study, the quasi-linear viscoelasticity (QLV) framework [14] was used for the modeling of soft tissues. The QLV framework assumes that mechanical behavior can be decoupled into a linear viscoelastic stress-relaxation response and a time-independent elastic response. The 2nd order standard linear solid model as a linear viscoelastic model is expressed as a Prony series expansion in the time domain as follows,

$$G(t) = k_0 + k_1 e^{-t/\tau_1} + k_2 e^{-t/\tau_2} = G_0(1 - \bar{g}_1^P(1 - e^{-t/\tau_1}) + \bar{g}_2^P(1 - e^{-t/\tau_2})), \quad (3)$$

where k_i , τ_i , t , and \bar{g}_i^P are the rigidity modulus, reduced relaxation time constant, given time, and Prony series parameters, respectively, which can be determined by using a nonlinear least square method. From $G(t=0)$, $G(t=\infty)$ conditions, the Prony series parameters are

$$\bar{g}_i^P = k_i / (k_0 + k_1 + k_2) \quad (4)$$

Table 3 lists the liver's computed Prony series parameters, which can be used directly to represent viscoelastic modeling.

Table 3. Prony series parameters from the normalized experimental data.

Shape	Depth (mm)	τ_1 (sec)	τ_2 (sec)	\bar{g}_1^P	\bar{g}_2^P
Flat tip	5	0.776 ± 0.135	14.701 ± 2.104	0.454 ± 0.028	0.197 ± 0.025
	7	1.058 ± 0.082	16.768 ± 1.932	0.411 ± 0.033	0.208 ± 0.021
Hemi. tip	5	0.761 ± 0.114	22.534 ± 2.689	0.436 ± 0.051	0.273 ± 0.047
	7	1.102 ± 0.0625	21.061 ± 2.142	0.388 ± 0.022	0.240 ± 0.029

For the time-independent elastic response, the hyperelastic material model was selected. Ideally, W is defined with only the parameters that are required to make an FE model. The incompressible neo-

Hookean model was selected for use here, which is widely used in soft tissue simulations. The strain energy function of the three dimensional incompressible neo-Hookean model is given by [15]

$$W = C_{10}(I_1 - 3) \quad (5)$$

where C_{10} is mechanical parameter, and I_1 is a principal invariant.

The model was built in Altair Hyperworks 7.0 (Altair, USA) and simulated with ABAQUS/Standard 6.5.1 (SIMULIA, USA). The contact between the indenter and tissues was treated as a rigid / deformable contact with a contact mechanics module, and the non-uniform element density over the model was used to improve the accuracy of the contact region. Although friction between indenter and tissue is important boundary condition, the model was assumed frictionless condition. In addition, the material properties of the model were assumed to be homogeneous, isotropic, and incompressible.

Note that the maximum radius of influenced extent as plotted in Fig. 5 was used to determine the minimal required size of the FE model. If the model size was designed smaller than our results, the estimated mechanical properties would not be accurate, and the computational time could be longer, if the model is bigger. Therefore, it can be a useful guide to design the model size for the FEM simulation.

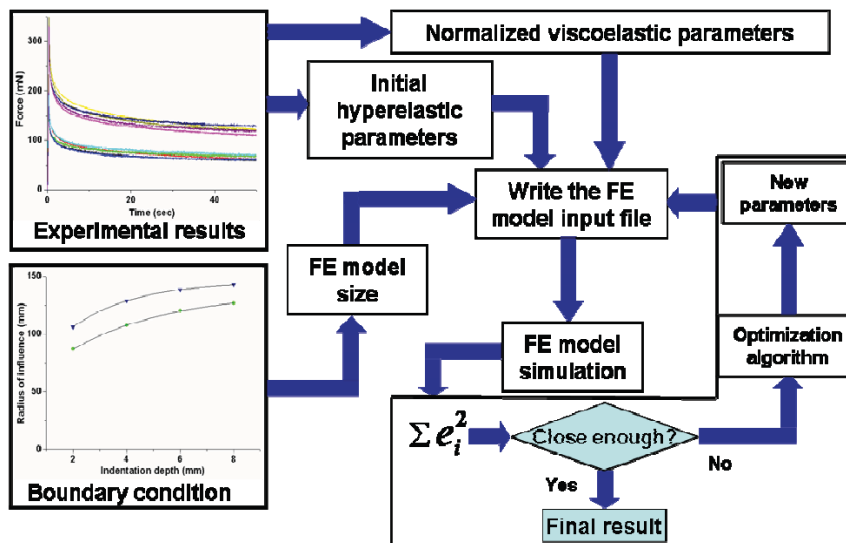


Figure 7. Flow chart for the inverse FEM optimization algorithm.

The initial hyperelastic parameter was inferred using Hertz-Sneddon equations [16, 17] and indentation experimental results. The optimization algorithm, Levenberg-Marquardt algorithm [18], was used to iterate the FE simulation and update the hyperelastic parameter automatically, which are shown in Fig. 7. With this algorithm, the parameter reached convergence after two or three iterations. Table 5 presents the initial and estimated parameters for the neo-Hookean model of each experimental condition. The parameters of 5 mm indentation depth are smaller than that of 7 mm indentation depth. In this result, the liver has layer by layer structure with inner layer stiffer than outer layer. In Fig. 5, the maximum radius of influenced extent for the flat indenter is larger than that of the hemisphere indenter. Therefore, the indented tissue volume of the flat indenter is larger than that of the hemisphere indenter. Figure 8 shows the typical simulation results for the stress and deformation of the developed FE model, which were captured at 50 second after inducing the indentation. It was shown that the stress and deformation

contours of the model's inner structure and the simulation converged. Figure 9 shows the experimental data from the indentation experiments and predicted force data from the FEM simulation. The force responses of the soft tissue model and experimental data are similar according to the coefficient of determinant (R^2) defined by

$$R^2 = 1 - \sqrt{\sum_{i=1}^m ((F_s - F_e)^2 / F_e^2)}, \quad (6)$$

where F_e , F_s , and m are experimental data, simulated data, and total number of data, respectively.

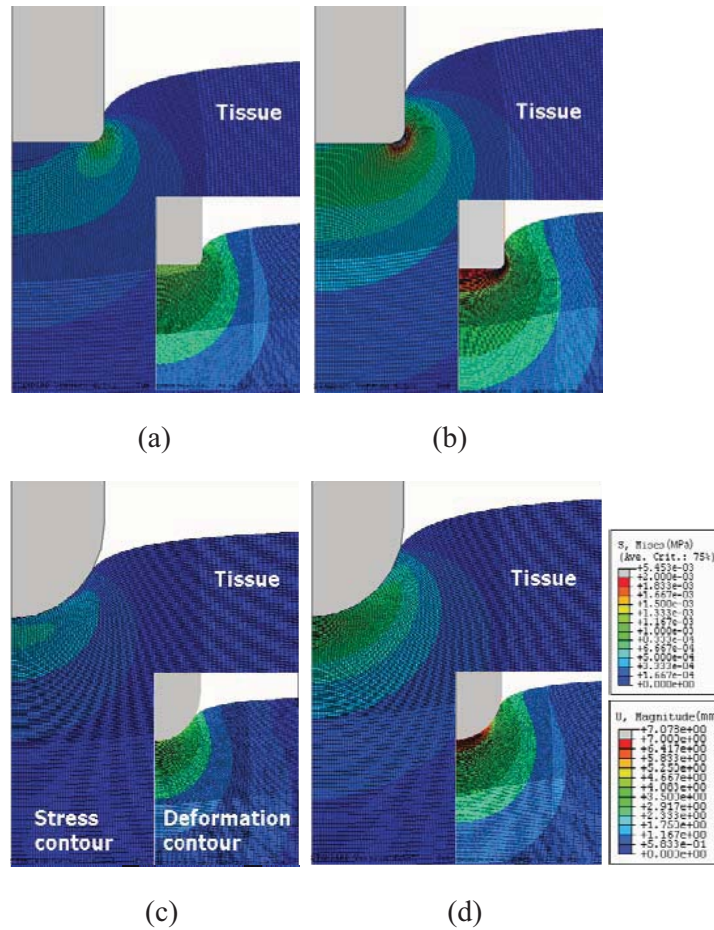


Figure 8. FE simulation results: stress and deformation contours for (a) 5mm indentation and (b) 7mm indentation of flat tip, and (c) 5mm indentation and (d) 7mm indentation of hemisphere tip.

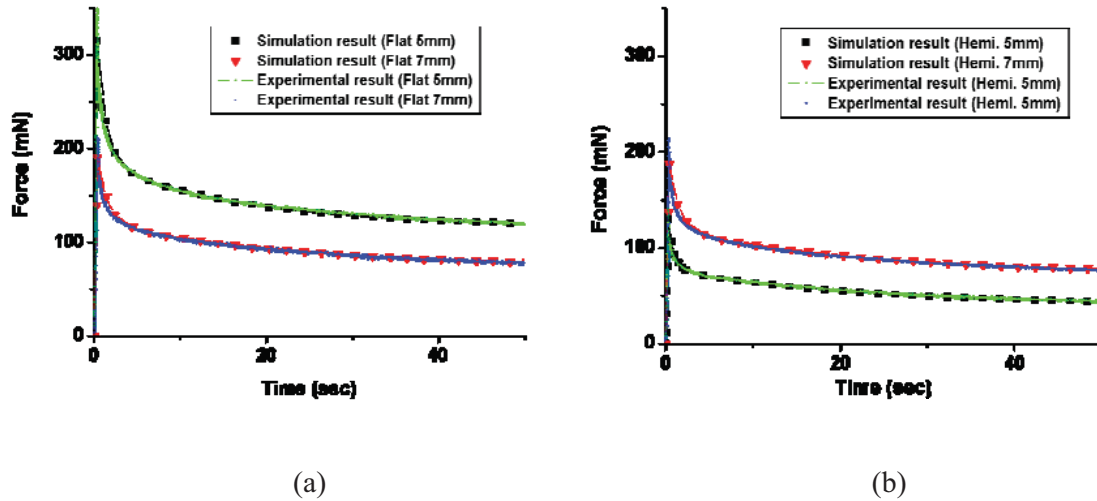


Figure 9. Force responses of the simulation and experiment: (a) flat and (b) hemisphere tips for 5mm and 7mm indentations.

Table 4. Initial and estimated parameters of the neo-Hookean model, and coefficient of determinant.

Shape	Depth (mm)	C_{10} (Pa)		$R^2 \pm S.D.$
		Initial	Estimated \pm S.D.	
Flat tip	5	100.3	181.5 ± 14.7	0.996 ± 0.001
	7	155.2	248.4 ± 8.9	0.995 ± 0.001
Hemi. tip	5	112.7	150.8 ± 15.2	0.994 ± 0.001
	7	174.7	214.1 ± 10.4	0.997 ± 0.002

4 Concluding remarks

Soft tissue characterization considering large deformation with associated boundary conditions has been challenging due to experimental difficulties and computational complexity. In this paper, the tissue deformation was captured by the optical vision system and force responses at the indenter were also measured by a force transducer. The maximum deformation distances with respect to various indentation depths were measured, and these data were fit by the empirical equation. Using the calibrated FE model and the nonlinear optimization algorithm, the nonlinear material properties of the soft tissues were characterized.

The mechanical properties of soft tissues have been measured *in vivo* and *in vitro* for decades. Although *in vitro* testing is capable to provide controllable and stable conditions, the responses could not guarantee the same as live ones. Because the properties of samples may be affected by temperature, hydration, protein oxidation, and loss of blood pressure after removing from a body, the *in vivo* testing is ideal for the soft tissue characterization, especially for medical simulation. The medical simulation requires tissue models simulating live tissue behavior to provide an identical environment as in operating rooms. However, due to the effects on respiration, circulation of blood, and fine motion of the live body, the

measurements of the stable and consistent results of *in vivo* testing are still challenging. Stopping respiration of the subject during the measurement could be reduced the influence of the motion, but the measurement period is limited at most one minute due to the safety of the subject. Moreover, the removing influence of instrumentation and experimental condition from the *in vivo* raw data still needs more work to be used for characterization tasks. Therefore, the data from the harvested tissues (*in vitro*) and live tissues (*in vivo*) should be studied to complement each other until the instrumentation with robustness and sufficient stimulus are developed and validated.

The mechanical properties presented in this study offer two basic uses in medical simulators. First, they can be used directly in the simulator to compute visual deformations and interaction forces that are displayed in real time. Although real-time computations of complex tissue behaviors are challenging, there is some encouraging work [19]. Second, the mathematical models presented here can be used as a standard for the evaluation of new real-time algorithms for computing deformation [20].

Further progress on the soft tissue characterization requires work in three areas. First, it is essential to establish experimental protocols, and devices with the range, robustness and bandwidth required to obtain comprehensive organ data rapidly. Second, mechanical models should be developed, which could efficiently represent organs' topologies, anatomical structures, boundary conditions and mechanical properties. Finally, three-dimensional FE model applied the geometrical information is necessary to obtain more accurate mechanical properties of soft tissues.

Reference

- [1] Basdogan C., Ho C.H., Srinivasan M.A.: Virtual environments for medical training: Graphical and haptic simulation of laparoscopic common bile duct exploration. *IEEE Transactions on Mechatronics* **6** (2001) 269-285.
- [2] Tendick F., Downes M., Goktekin T., Cavusoglu M.C., Feygin D., Wu X., Eyal R., Hegarty M., Way L.W.,: A Virtual Environment Testbed for Training Laparoscopic Surgical Skills. *Teleoperators and Virtual Environments* **9** (2000) 236-255.
- [3] Misra, S., Okamura, A.M., Ramesh, K.T., 2007. Force Feedback is Noticeably Different for Linear versus Nonlinear Elastic Tissue Models. *World Haptics*, 519-524.
- [4] Ahn, B., Kim, J., 2007. Estimation of Soft Tissue's Mechanical Properties with Indentation Experiments and Optimization Algorithm. 3rd Asian Pacific Conference on Biomechanics, Tokyo, Japan.
- [5] Moffitt, F.H., Mikhail, E.M., 1980. *Photogrammetry*. Harper & Row Publishers, New York.
- [6] Mahvash, M., Hayward, V., 2004. High-fidelity haptic synthesis of contact with deformable bodies. *IEEE Computer Graphics and Applications*. 24, 48-55.
- [7] Gray, H., 1974. *Gray's Anatomy*. PA: Running Press, Philadelphia.
- [8] Marieb, E., 1992. *Human Anatomy and Physiology*. Benjamin/Cummings Publishing Co., Redwood City, CA.
- [9] Bathe, K.J., 1996. *Finite element procedures*. Englewood Cliffs, N.J.: Prentice Hall.

- [10] Kauer, M., Vuskovic, V., Dual, J., Szekely, G., Bajka, M., 2002. Inverse Finite Element Characterization of Soft Tissue. *Med. Image Anal.* 6, 275-287.
- [11] Kim, J., Srinivasan, M.A., 2005. Characterization of Viscoelastic Soft Tissue Properties from *In vivo* Animal Experiments and Inverse FE Parameter Estimation. *Lect. Notes Comput. Sci.* 3750, 599-606.
- [12] Nava, A., Mazza, E., Furrer, M., Villiger, P., Reinhart, W.H., 2008. *In vivo* mechanical characterization of human liver. *Med. Image Anal.* 12, 203-216.
- [13] Samur, E., Sedef, M., Basdogan, C., Avtan, L., Duzgun, O., 2007. A robotic indenter for minimally invasive measurement and characterization of soft tissue response. *Med. Image Anal.* 11, 361-373.
- [14] Fung, Y.C., 1993. *Biomechanics, Mechanical Properties of Living Tissues*, second ed. Springer-Verlag, New York.
- [15] Boyce, M.C., Arruda, E.M., 2000. Constitutive models of rubber elasticity: A review. *Rubber Chem. Technol.* 73, 504-523.
- [16] Johnson, K.L., 1985. *Contact mechanics*. Cambridge University Press, New York.
- [17] Ottensmeyer, M.P., Kerdok, A.E., Howe, R.D., Dawson, S.L., 2004. The Effects of Testing Environment on the Viscoelastic Properties of Soft Tissues. *Lect. Notes Comput. Sci.* 3078, 9-18.
- [18] Press, W.H., Teukolsky, S.A., Vetterling, W.T., Flannery, B.P., 1992. *Numerical recipes in C++, the art of scientific computing*, second ed. Cambridge University Press.
- [19] Wu, X., Downes, M.S., Goktekin, T., Tendick, F., 2001. Adaptive Nonlinear Finite Elements for Deformable Body Simulation Using Dynamic Progressive Meshes. *Computer Graphics Forum*, 20, 349-358.
- [20] Kerdok, A.E., Cotin, S.M., Ottensmeyer, M.P., Galea, A., Howe, R.D., Dawson, S.L., 2003. Truth Cube: Establishing Physical Standards for Real Time Soft Tissue Simulation. *Med. Image Anal.* 7, 283-291.

Finite Element Modeling of the Pulse Wave propagation in the aorta for simulation of the Pulse Wave Imaging (PWI) method

Jonathan Vappou, Ioannis Zervantonakis, Jianwen Luo, and Elisa Konofagou

June 2008

Department of Biomedical Engineering, Columbia University, New York, NY, USA

Abstract

A large number of pathological conditions result in significant changes of the mechanical properties of the aortic wall. Using the Pulse Wave Velocity (PWV) as an indicator of aortic stiffness has been proposed for several decades. Pulse Wave Imaging (PWI) is an ultrasonography-based imaging method that has been developed to map and quantify the pulse wave (PW) propagation along the abdominal aortic wall and measure its local properties. We present a finite-element-based approach that aims at improving our understanding of the complex PW patterns observed by PWI and their relationship to the underlying mechanical properties. A Fluid-Structure Interaction (FSI) coupled model was developed based on an idealized axisymmetric aorta geometry. The accuracy of the model as well as its ability to reproduce realistic PW propagation were evaluated by performing a parametric analysis on aortic elasticity, by varying the aortic Young's modulus between 20 kPa and 2000 kPa. The Finite-Element model was able to predict with good accuracy the expected PWV values in different theoretical cases, with an averaged relative difference of 14% in the 20kPa-100kPa, which corresponds to a wide physiologic range for stiffness of the healthy aorta. This study allows to validate the proposed FE model as a tool that is capable of representing quantitatively the pulse wave patterns in the aorta.

1 Introduction

For several decades, the pulse wave velocity (PWV) has been used as a health indicator of the cardiovascular system. This assertion relies on the fact that the PWV is directly linked to the aortic stiffness and that a large number of pathological conditions result in a significant alteration of the aortic mechanical properties. Such alterations can be either global (e.g., chronic hypertension) or localized (e.g., atherosclerosis, aneurysm). Hence, the knowledge of the PWV is potentially helpful for the detection of some cardiovascular diseases, especially at an early stage.

Different non-imaging methods have been proposed to measure the PWV, but they rely on the same principle, i.e., measuring the time delay between pulse profiles at two different locations in the arterial tree [1]. Knowing the distance between those two locations, the averaged PWV can then be calculated (see Figure 1). The most common method consists of measuring the delay in the “foot” of the pressure wave between the carotid and the femoral arteries. Although they are relatively simple, the principal flaw of such methods is their poor accuracy and the fact that they provide a global, averaged measurement of the PWV. They are therefore useless for the identification and localization of focal and/or subtle changes of the mechanical properties. As a consequence, there is a strong interest in proposing a method that would allow the visualization and the measurement of local values of the PWV along the entire aorta. This is especially relevant for abdominal aortic aneurysms (AAA). As it has been widely suggested in the literature, biomechanical aspects are essential in the understanding of the rupture of AAA, and having a method that would be able to characterize the aneurysmal wall would be of great interest for essentially two reasons. The first reason is that the development of the AAA is accompanied by the alteration of the metabolism of the elastic fibers like elastin and collagen [2], resulting in an alteration of the mechanical properties. Such changes in the mechanical properties are suspected to possibly occur prior to changes in the aortic wall geometry, and being able to measure them could help their characterization at an early stage even before their detection by conventional medical imaging, so, at the very early stages. The other reason is related to the choice that a vascular surgeon has to make when deciding whether the AAA has to be repaired or not. The only currently applied criterion is based on its size, i.e., if the AAA exceeds 5.5 cm in diameter, surgical intervention is warranted [3]. However, it has been shown that a significant number of AAA rupture below this critical size whereas also a significant number of them never rupture despite their large size [4]. The rupture of the AAA is a biomechanical issue that can be described in a simple way by the fact that rupture occurs when the stress that the wall undergoes exceeds its strength. Finite-element modeling of the AAA with realistic geometries has been shown to be a useful method to predict the stress distribution along the wall [5,6,7], based though on constitutive relationships derived from *in vitro* experiments. A method that would be capable of measuring *in vivo* mechanical properties of the wall is therefore key in order to accurately understand the mechanical behavior of the AAA.

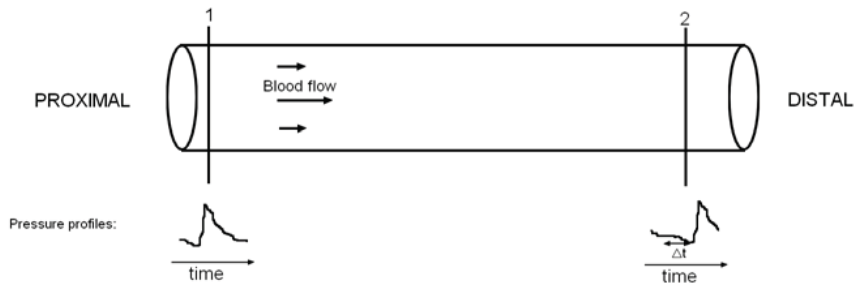


Figure 1: Principle of the foot-to-foot delay method. The foot of the pressure profile is detected at locations (1) and (2) of the aorta. The foot arrives at location (2) after a delay Δt . Knowing this delay and the distance between (1) and (2) allows to estimate the PWV.

Pulse Wave Imaging (PWI) has been proposed as an ultrasonography-based method to estimate the PWV along the abdominal aorta [8, 9]. By using a retrospective electrocardiogram (ECG) gating technique, the radio-frequency (RF) signals over one cardiac cycle are obtained at very high frame rate (8 kHz, with a field-of-view (FOV) of $12 \times 12 \text{ mm}^2$ for mice). The radial velocity of the aortic wall is estimated using an RF-based speckle tracking method along the entire aorta. PWI has been performed on both normal mice and on mouse models of AAA, and distinct PW profiles were obtained [10]. Figure 2 illustrates an example of the propagation of the pulse wave in the normal mouse. Determining the mechanical properties from such varying PW patterns is not straightforward due to the complexity of the problem that involves the intricate wall mechanics with the coupled interaction between the blood flow and the wall. We present a finite-element-based approach that aims at improving our understanding of the PW patterns and their relationship to its underlying mechanical properties. The accuracy of the model as well as its ability to reproduce realistic PW propagation are also evaluated regarding theoretical idealized situations.

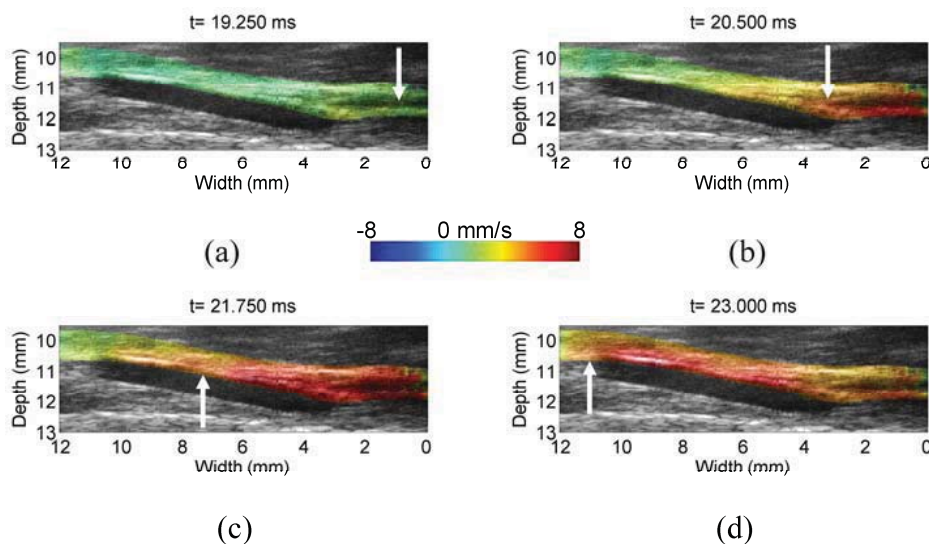


Figure 2: In vivo PWI on normal mouse at different times (a,b,c,d) showing the propagation of the pulse wave along the abdominal aorta. Radial wall velocity is color-encoded and overlaid on the B-mode Image.

2 Methods

2.1 General Description of the Model

The Fluid-Structure Interaction coupled model was developed in a commercial FE package (COMSOL, Burlington, MA, USA). The fluid motion is governed by the Navier-Stokes equation that describes the incompressible blood flow:

$$\rho\left(\frac{\partial v}{\partial t} + v \cdot \nabla v\right) = -\nabla p + \mu \nabla^2 v, \quad (1)$$

where v is the velocity vector, μ the dynamic viscosity, ρ the fluid density and p the pressure. The arterial wall was supposed nearly incompressible and linear elastic. The limitations of such approach will be discussed further in this work. The action of the fluid on the wall was derived from the action of the fluid pressure p . The problem was solved using a two-way FSI coupling, where the fluid and solid motion equations were solved simultaneously and loads and boundary conditions were exchanged after each converged increment. The abdominal aorta was modeled as a 2D axisymmetric domain consisting of a fluid (blood) and a solid (wall) region (Figure 3). The assumption of axisymmetry is commonly used in hemodynamics studies and offers the advantage of reducing significantly the computational cost compared to 3D models. However, this approach allows for the combined study of pulse wave propagation in the longitudinal direction and of the spatial variation of the wall motion in the radial direction.

The dimensions of the FE model were chosen in order to simulate previous experiments performed on mice [10]. The abdominal aorta was 12mm long. The radius of the vessel was 0.5mm and the wall thickness 0.1mm, similar to the values observed in vivo in the ultrasound scans. A structural computational grid was designed by defining 40 elements in the longitudinal direction and 12 in the radial direction. Blood flow was assumed to be Newtonian. The blood density was chosen to $\rho=1050\text{kg/m}^3$ and its viscosity was chosen to $\mu=0.004$ Pa.s. The arterial wall was modeled as elastic, with a Poisson's ratio of $\nu=0.499999$. The values of the the Young's modulus were varied for a parametric analysis as it will be described below.

2.2 Boundary Conditions and Simulation Parameters

A time-dependent pressure profile was imposed as an inflow boundary condition, representing the cardiac output of the murine heart. This was based on non-invasive in vivo pulsed Doppler measurements in normal murine aortas under resting conditions. The pressure profile was calculated from the measured flow data assuming a parabolic velocity profile. The arterial tree on the distal side of the model was represented by a two-element Windkessel model, consisting of a capacitor C and a resistance R in parallel. The value of the capacitance C was accordingly selected to account for the distensibility of the large and small blood vessels, while the value of the resistance R accounts for the large pressure decrease in the small systemic arteries and capillaries. Figure 3 represents the proposed FE model.

In the structural mechanics model, the time-dependent pressure spatial distribution was prescribed as a load p on the arterial wall. A zero longitudinal translation was imposed on all boundaries, while free motion was allowed in the radial direction. These boundary conditions correspond to fixing the ends of the aorta in the longitudinal directions.

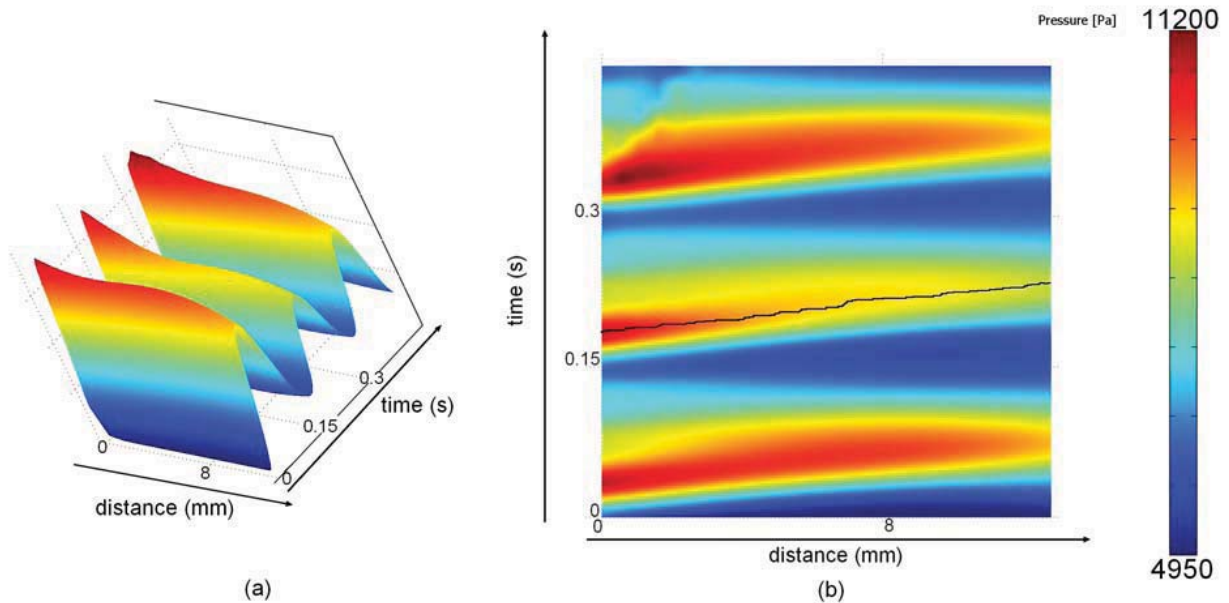
A total of 3 cardiac cycles were simulated. The transient coupled fluid-solid problem was solved with a fixed time step of 0.1ms, which is also similar to the in vivo temporal resolution of 0.125ms.



Figure 3: FEM of the aorta showing also the Boundary conditions for the fluid domain

2.3 Data Analysis

The peak of the pressure wave was tracked in space versus the distance from the inflow boundary (z) and versus time t , allowing to measure, for each discrete value of z , the time at which the peak of the wave arrives. The coordinates (z, t) of the peak were linearly fitted in a region of interest (ROI) from this plot, allowing to calculate the PWV. Figure 4 illustrates that principle. When the wall was implemented as homogeneous, the ROI was simply the entire aorta. In the case of heterogeneous wall, several ROI were chosen for each distinct region in the FE model. This issue will be discussed further in this paper.



4: (a) 3D and (b) 2D representation of the pressure versus time and distance from the inflow boundary. The dark line illustrates the tracking of the peak of the curve. A linear regression of this curve allows to compute the PWV. Here, the input Young's modulus is 50kPa.

2.4 Parametric Analysis

A parametric analysis was performed by varying the values of Young's modulus of the wall from $E=20\text{kPa}$ to $E=2000\text{kPa}$. For each value, the PWV was calculated from the simulations by the method described above. The values of the PWV were compared to the analytical solution of a pulse wave propagating in a cylindrical homogeneous linear elastic tube, given by the modified Moens-Korteweg equation, i.e.:

$$PWV = \sqrt{\frac{Eh}{2\rho R(1-\nu^2)}} \quad , \quad (2)$$

where E is the aortic Young's modulus, ν the Poisson's ratio, h and R the wall thickness and radius, respectively, and ρ its density. Such analysis was performed in order to test the ability of the presented model to predict correctly the PWV in simple cases that have a straightforward easy analytic solution, e.g., the case of an axisymmetric thin-walled tube. The stiffness range was chosen according to extreme values reported in the literature for healthy and diseased aortas. A commonly accepted range for the healthy aorta is $E=50\text{-}100\text{kPa}$ [1].

An analysis was also performed on a heterogeneous aorta. For this case, a stiffer region of $E=500\text{kPa}$ was included in the aorta with $E=100\text{kPa}$. This region was 5mm long. It aims at simulating an alteration of the stiffness that would result, for example, from the existence and formation of an aneurysm, before the shape or the aortic lumen change significantly.

3 Results

The effect of changing the aortic Young's modulus was clearly observed, as represented in figure 5. It was found that an increase in Young's modulus results in an increase in the PWV. The Young's modulus calculated by equation 2 was found in good agreement in the 10kPa-500kPa range. For higher values, the PWV was too high for the temporal resolution and no convenient fit of the peak (z,t) coordinates could be performed ($r^2 < 0.5$). The results found in the 10kPa-500kPa range are shown in figure 6. All results are shown in table 1.

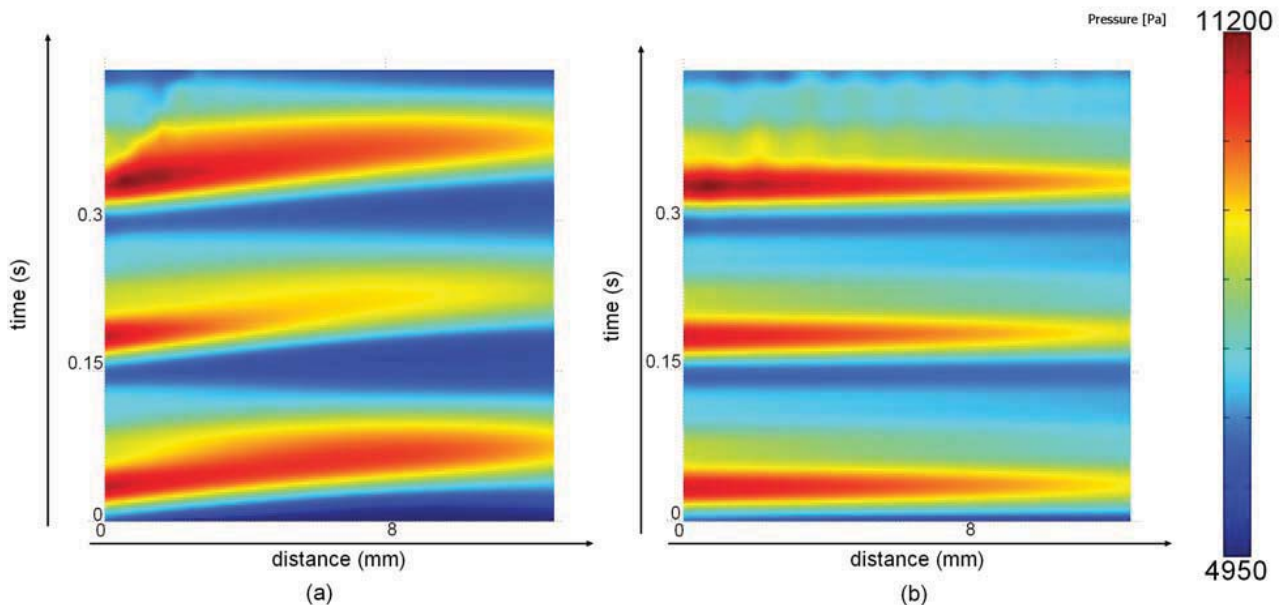


Figure 5: Pressure profiles for (a) $E=50\text{kPa}$ and (b) $E=500\text{kPa}$, illustrating that the PWV increases with the aortic stiffness

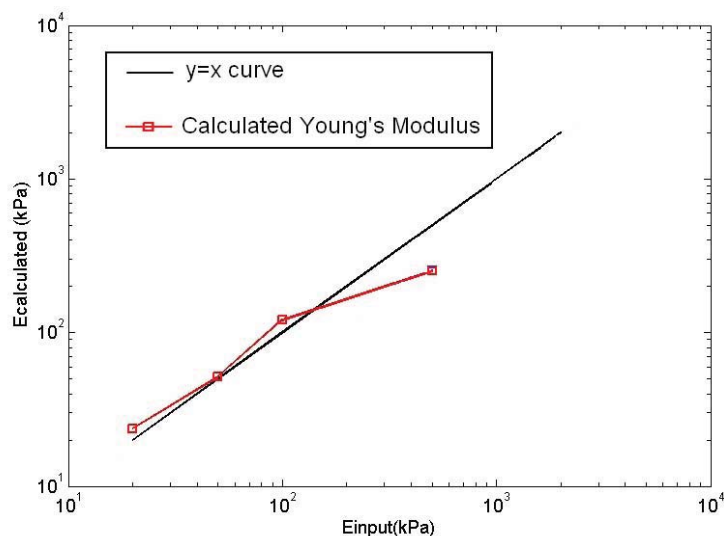


Figure 6: Young's modulus calculated from the PWV versus the assigned Young's modulus

E_{input}	20 kPa	50 kPa	100 kPa	500 kPa	1000 kPa	2000 kPa
r^2 of the PWV linear regression	0.94	0.96	0.91	0.75	0.48	0.43
$E_{calculated}$	24 kPa	51 kPa	121 kPa	255 kPa	-	-
Relative difference	20%	2%	21%	49%	-	-

Physiological Healthy Aortic stiffness

Table 1: Values of Young's modulus obtained by calculating the PWV and using the modified Moens-Korteweg equation. These results show the limits of validity of the method ($E < 500$ kPa)

The stiffer region was clearly detected in the case of the heterogeneous aorta, and a considerable variation of the PWV was found, as illustrated in figure 7. A value of $E = 720$ kPa was found in the stiffer region, which has to be compared to the input value of $E = 500$ kPa.

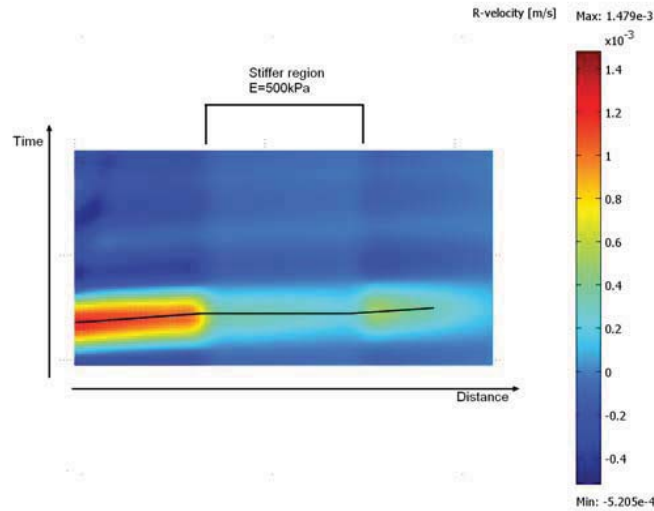


Figure 7: Illustration of the incremental radial displacement of the wall in the case of an aorta ($E=100\text{kPa}$) with a stiffer inclusion ($E=500\text{kPa}$), for one cycle. Approximate slopes are represented, which clearly show that the PWV is higher inside the stiffer region.

4 Discussion and Conclusions

In this study, a FE model of the aorta was developed in order to simulate the propagation of the pulse wave. Such a FE approach will be essential in our understanding of complex PW patterns that appear in sophisticated, real problems that can not be easily solved analytically. The current model is still basic, as it will be discussed below, but it was shown to be capable of quantitatively predicting correct values of the PWV. As a consequence, it was validated for the measurement of the PWV under its underlying physical assumptions. For such validation purposes, a 2D cylindrical geometry was studied since such geometry can easily be solved analytically by means of the Moens-Korteweg equation, allowing therefore a comparison to be established.

The proposed FE model was shown to be able to quantitatively predict the expected aortic Young's modulus in the 20kPa-500kPa range. This method relies on the determination of the PWV by performing a linear regression on the temporal and spatial variations of the peak. As the stiffness increases, so does the PWV and the precision of the linear regression decreases due to the limitations in temporal resolution. The limit value of 500kPa corresponds to a correlation coefficient of $r^2=0.75$ for the linear regression. Such limitations in temporal resolution represent a clear limitation for the PWV method. However, the upper limit of 500kPa is above reported aortic stiffness values. As a result, the method is appropriate for physiologic aortic stiffness values and seems to perform most reliably within the healthy aorta range (20kPa-100kPa).

In this study, only 2D axisymmetric geometries were considered. Although this geometry is a relatively good representation of the abdominal aorta, it can be critical in certain cases where the exact specific geometry needs to be known. Further development consists in developing a similar 3D realistic model based on patient-specific geometries that will be recorded by 3D imaging. Vorp et al. [5] showed the importance of knowing the wall geometry in order to predict correct stress distributions. Although the goal of this model is not to predict stresses, but rather to predict correct PW patterns, it can be expected that the geometry will have a significant influence on the PW propagation properties.

In this study, the arterial wall has been considered as an incompressible, homogeneous, linear Hookean isotropic elastic material. Even though the hypothesis of incompressibility seems to be reasonable for all soft tissues, it has been repeatedly shown that the arterial wall is an anisotropic medium that exhibits complex non-linear viscoelastic properties. Assuming a linear elastic model is especially critical as deformation levels of the wall can range up to 20% during the cardiac cycle [11]. However, despite the complex nature of this material, it remains important to start using a simplified rheological model of the arterial wall. Going further into the complexity of its mechanical description would not make sense, if the simplified model is not quantitatively validated by simple basic simulations. Ongoing work deals with the use of a non-linear stress-strain relationship for the aortic wall in order to improve the realism of its mechanical response.

Compared to other existing FE models of the aorta [5,6,7], this current model might be simplistic in terms of geometry and mechanical properties, as explained above. However, it uses time-dependent boundary conditions obtained from in vivo Doppler flow measurements, and it takes into account the time-dependent coupled interaction between the fluid and the solid domains. This provides it with the capability of studying transient problems such as the propagation of the pulse wave. Preliminary experimental validation of this model is currently the topic of ongoing studies.

References

- [1] W.W. Nichols, M.F. O'Rourke. *McDonald's blood flow in arteries*. Fifth Edition, Hodder Arnold, 2005.
- [2] M. Carmo, L. Colombo, A. Bruno, F. R. M. Corsi, L. Roncoroni, M. S. Cuttin, F. Radice, E. Mussini, P. G. Settembrini, *Alteration of Elastin, Collagen and their Cross-links in Abdominal Aortic Aneurysms*, Eur J Vasc Endovasc Surg 23, 543±549, 2002.
- [3] D. Vorp, *Biomechanics of abdominal aortic aneurysm*, Journal of Biomechanics 40:1887-1902, 2007.
- [4] R.C. Darling, C.R. Messina, D.C. Brewster, L.W. Ottinger, *Autopsy study of unoperated abdominal aortic aneurysms*. Circulation 56:161–164, 1977.
- [5] D.A. Vorp, M.L. Raghavan, M.W. Webster, *Mechanical wall stress in abdominal aortic aneurysm: Influence of diameter and asymmetry*, Journal of Vascular Surgery 27:632-639, 1998.
- [6] C.M. Scotti, A.D. Shkolnik, S.C. Muluk, E.A. Finol, *Fluid-Structure Interaction in abdominal aortic aneurysms: effects of asymmetry and wall thickness*, Biomedical Engineering Online 4:64, 2005.
- [7] I.E. Vignon-Clementel, C.A. Figueroa, K.E. Jansen, C.A. Taylor, *Outflow boundary conditions for three-dimensional finite element modeling of blood flow and pressure in arteries*, Comput. Methods Appl. Mech. Engrg. 195: 3776-3796, 2006.
- [8] M. Pernot, K. Fujikura, S.D. Fung-Kee-Fung, E.E. Konofagou, *ECG-Gated, Mechanical and Electromechanical Wave Imaging of Cardiovascular Tissues In Vivo*, Ultrasound in Medicine and Biology, 33(7): 1075-85, 2007.
- [9] K. Fujikura, J. Luo, V. Gamarnik, M. Pernot, R. Fukumoto, M.D. Tilson, E.E. Konofagou, *A Novel, Non-Invasive Technique for Pulse-Wave Imaging and Characterization of Clinically Significant Vascular Mechanical Properties in vivo*, Ultrasonic Imaging 29:137-154, 2007.

- [10] J. Luo, K. Fujikura, L.S. Tyrie, M.D. Tilson, E.E. Konofagou, *Pulse wave imaging of normal and aneurysmal abdominal aortas in vivo*, IEEE Trans. Med. Imaging, 2008. (in press)
- [11] J.D. Humphrey, *Cardiovascular Solid Mechanics*, Springer-Verlag New York, 2002.

Comparison of Displacement-Based and Force-Based Mapped Meshing

Vincent A. Magnotta^{1,2,4}, Wen Li^{2,1}, and Nicole M. Grosland^{2,3,4}

August 13, 2008

¹Department of Radiology, The University of Iowa, Iowa City, IA, 52242

²Department of Biomedical Engineering, The University of Iowa, Iowa City, IA, 52242

³Department of Orthopaedics and Rehabilitation, The University of Iowa, Iowa City, IA, 52242

⁴Center for Computer Aided Design, The University of Iowa, Iowa City, IA, 52242

Abstract

The finite element (FE) method is a powerful tool for the study of biomechanics. One of the limiting factors in transitioning this tool into the clinic is the time required to generate high quality meshes for analysis. Previously, we developed a mapped meshing technique that utilized force control and a finite element solver to warp a template mesh onto subject specific surfaces. This paper describes a displacement based method that directly warps the template mesh onto subject specific surfaces using distance as the driving measure for the deformable registration. The resulting meshes were evaluated for mesh quality and compared to the force based method. An initial evaluation was performed using a mathematical phantom. The algorithm was then applied to generate meshes for the phalanx bones of the human hand. The algorithm successfully mapped the template bone to all of the bony surfaces, with the exception of the distal phalanx bone. In this one case, significant differences existed between the geometries of the template mesh and the distal phalanx. Further refinement of the algorithm may allow the algorithm to successfully generate meshes even in the presence of large geometric shape differences.

In this paper we present an algorithm for the generation of finite element meshes using a mapped meshing approach. The approach computes the distance between the template mesh and the subject specific surface. The position of the surface nodes of the template mesh are incrementally projected towards the surface of interest. The number of iterations used in this mapping is specified by the user. The interior nodes are then mapped to the new representation using a thin-plate spline transformation.

This algorithm is initially evaluated using a mathematical phantom data set consisting of a cube template mesh and spherical surface. Next, the algorithm is applied to map a template mesh to the phalanx bones of the hand. The results of this mapped meshing technique are compared to those of a finite element force control solution that we have previously reported using the same dataset.

1 Introduction

The finite element (FE) method is a powerful tool, widely used in the field of biomedical engineering. One of the limiting factors in transitioning this tool into the clinic is the time and manual effort required to generate anatomic models. The focus of our work is the coupling of mesh generation to medical imaging data to create a pipeline for the rapid generation of finite element models. The ultimate goal is to develop tools that are able to create high quality hexahedral meshes on a subject-specific basis. Our previous work has included the development of a novel building block approach [1] and a deformable registration algorithm that utilized forces to drive the registration [2]. The building block approach is the core of IA-FEMesh, an interactive meshing tool for the generation of high quality hexahedral meshes [3]. Using this tool, we have been able to generate models of several long bones in the human body relatively quickly (on the order of minutes) as well as more complex structures such as the spine. This tool has reduced the time required for mesh generation by an order of magnitude over traditional meshing tools. Once a mesh of high quality is established, especially for complex geometries, it would be ideal to map it to surface representations of similar size and shape, as opposed to redefine the mesh.

Since Couteau et al. [4] proposed a mesh-matching algorithm for automatic grid-based finite element model generation, a number of researchers have published methods for warping a template mesh onto a structures of interest. Jaume et al. [5] labeled the brain surface using a deformable multi-resolution mesh. Gibson et al. [6] generated a finite element mesh from the surface of an adult head subsequently fit to the surface of a neonatal head. We have previously explored the use of a deformable registration based on the finite element method [2]. In this algorithm, the surface and the template were first aligned using an affine transformation to account for differences in the position, orientation, and scale between the datasets. A hierarchical approach was then used to deform the template mesh onto the subject surface by applying forces to the surface nodes.

Using a mapped meshing approach, a convergence study could be conducted on a bone type of interest (e.g., proximal phalanx bone of the hand) to establish the mesh density appropriate for this structure in only a single subject. Once the template mesh is created for this subject, it can then be mapped onto a subject specific surface. An appropriate mapping is one that can accurately align the mesh to the subject surface while maintaining high quality elements in the resulting mesh. In this work, we present a displacement based mapped meshing solution and compare the results to the force based solution that has been previously reported. The main impetus for this work was to decrease the time required for the

mapped meshing algorithm. Our apriori hypothesis was that the displacement based solution would be faster, but would be more prone to the generation of distorted elements in the resulting mesh.

2 Displacement Based Mapped Meshing

The input to the mapped meshing algorithm is the template mesh and a subject-specific surface. The initial registration defines an affine transformation to bring the template mesh into close correspondence with the target surface; thereby accounting for differences in spatial orientation, size, and position.

Thereafter, the registration algorithm is used to define a nonlinear mapping to locally register the surface nodes of the template mesh onto the bony surface. The registration algorithm implemented is based on the distances between the surface nodes of the template mesh and corresponding points on the target surface, identified by intersecting the normals from the template mesh with the triangulated target surface. Each node is repositioned toward the bony surface along the point normal. Consequently, if the node is positioned outside the target surface the distance is negated. The nodal positions are then updated according to the following equation:

$$x' = x + nd \left(\frac{i}{N} \right)$$

Where x' is the updated nodal position, x is the original nodal position, n is the normal direction, d is the distance between the nodal position and the subject surface, N is the total number of iterations, and i is the increment number ($i = 1 \dots N$). If the current iteration is not the last iteration, the resulting deformed mesh is smoothed using Laplacian smoothing. This was done to maintain a smooth representation of the deforming mesh while eliminating large local changes in the mesh resulting from the projection techniques. This process is repeated for the number of iterations specified by the user. The incremental adjustment of the nodal positions was implemented to allow for greater variation between the template and surface without generating distorted representations of the surface faces.

Once the surface nodes have been mapped using the algorithm described above, the next step is to recompute the distribution of the interior nodes. The internal nodes are repositioned using a thin-plate spline transform [7]. The thin-plate spline (TPS) transform is created via the surface nodes of the original template mesh as the source landmark positions, while the final position of the mapped nodal point positions are used as the target landmarks. The resulting transform defines a smooth mapping for the interior nodal positions from their original position to their new position in the mapped mesh. The user has the ability to specify the density of the points used to define the TPS. The complete displacement controlled mapped meshing algorithm is summarized in Figure 1.

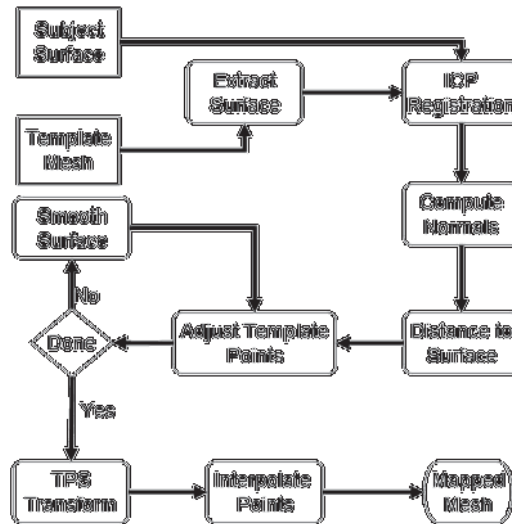


Figure 1. A flow chart for the mapped meshing algorithm based on displacement control.

3 Evaluation of the Displacement Based Mapped Meshing Algorithm

Two data sets were used to evaluate the displacement-based mapped meshing algorithm. The first data set consisted of a cube representing the template mesh and a sphere for the subject surface. The cube had dimensions of 22.5mm x 22.5 mm x22.5 mm and consisted of 1728 elements (12x12x12). The sphere had a diameter of 20mm and contained 19,600 triangles.

The second dataset was used to evaluate the applicability of the method to irregular anatomic structures. Two cadaveric specimens were acquired from the Anatomy Gifts Registry located in Hanover, Maryland. CT datasets were collected at The University of Iowa. The specimens were imaged in the axial plane on a Siemens Sensation 64 CT scanner (Matrix = 512x512, FOV = 172x172 mm, KVP = 120, Current = 94 mA, Exposure = 105 mA) with an in-plane resolution of 0.34 mm and a slice thickness of 0.40 mm. The regions of interests defining the phalanx bones of the index, middle, ring, and little finger were defined by a manual rater using the BRAINS image analysis suite[8]. The resulting regions of interest were converted into a surface representation. The proximal phalanx bone of the index finger from the first specimen was meshed using the building block approach in IA-FEMesh. A mesh convergence study was performed to determine the optimal mesh density for a static FE analysis. The mesh density was increased until minimal change in the internal stress values was observed with 6765 elements. This represented an average element edge length of 1.0mm. This mesh was then used as the template mesh for this study. In order to evaluate the ability of the algorithm to mesh structures of similar shape, the template mesh was mapped to the proximal phalanx bones of the index, middle, ring, and little fingers of the second cadaveric specimen. This experiment was undertaken to simulate the variation in bone size that exists across subjects. To evaluate algorithm's performance when significant variations exist in geometries between the template mesh and subject surface, the template mesh of the proximal phalanx bone was

mapped to the middle and distal phalanx of the index finger. For all of the experiments, the registration algorithm was run for 5 iterations, 1000 iterations of Laplacian smoothing were used after each step, and all of the surface points were used in the TPS based interpolation.

We previously reported on the application of a finite element based mapped meshing algorithm to the same dataset [3]. In this previous work, forces were applied to the template mesh to drive it into correspondence with a subject surface. The two mapped meshing algorithms are compared in this paper using the metrics described below.

4 Evaluation Metrics

In order to evaluate the resulting registration, the quality of the mesh was checked using an in-house program based on the Verdict library [9]. The mesh quality was evaluated in terms of element volume and distortion. The goal was not to introduce any zero-volume or distorted elements to the mesh, as a result of the registration algorithm. An element with an angle between its isoparametric lines either less than 45° or greater than 135° was considered distorted.

5 Software

The algorithm was written in C++ and utilized the Visualization Toolkit (www.vtk.org). The software is available as a command line tool within IA-FEMesh (<http://www.ccad.uiowa.edu/mimx/IA-FEMesh>). IA-FEMesh is an open source software toolkit for rapid anatomic finite element model development. The core of IA-FEMesh employs a multiblock meshing scheme aimed at hexahedral mesh development. An emphasis has been placed on making the tools interactive, in an effort to create a user friendly environment. This tool provides efficient, reliable and valid methods for model development, visualization and mesh quality evaluation.

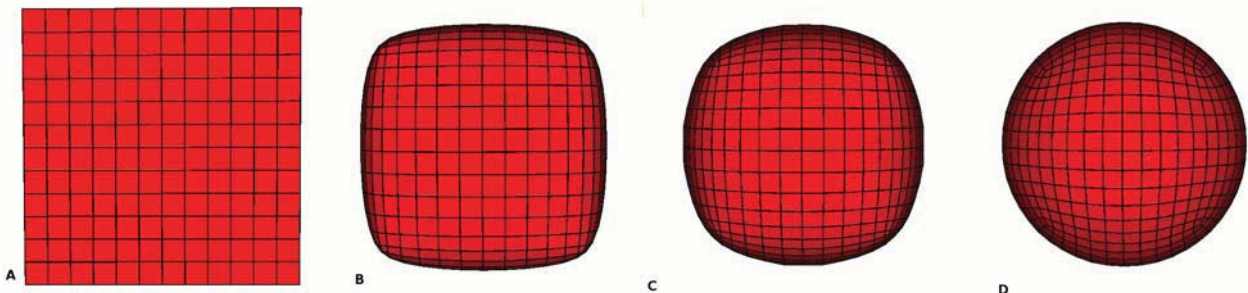


Figure 2. The cube template mesh shown being registered to a sphere. (A) Before registration, (B) after the first iteration, (C) after the second iteration, and (D) after the final iteration.

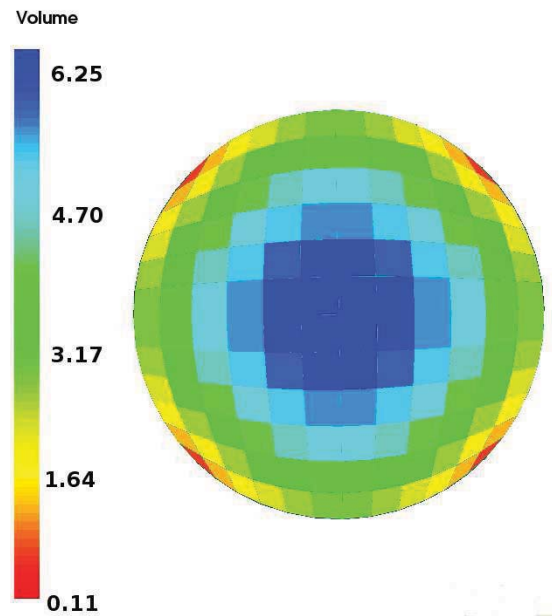


Figure 3. Cross-sectional view of the warped template mesh showing the mesh quality volume metric.

6 Results

Figure 2 demonstrates the iterative nature of the displacement-based registration process as the cube is mapped onto the sphere. As illustrated, the initial configuration is accompanied by mesh definitions following the first, second, and final (fifth) iterations, respectively. The corner points undergo the greatest displacement during the first iteration due to the fact that they initially reside furthest away from the target surface. Figure 3 illustrates the element volumes for the resulting mapped mesh. None of the resulting elements had a negative volume that would preclude this mesh from a finite element analysis. The resulting element volumes ranged from 0.11 to 5.93mm³, as compared to the original element volume of 6.59mm³. The resulting mesh did have 584 distorted elements having an angle smaller than 45 degrees or larger than 135 degrees.

Mapping the template mesh to the bony surfaces using the displacement-based technique was successful in all cases except the distal phalanx bone. Figure 4 illustrates the bony surface and resulting mesh for the proximal and middle phalanx bones of the index finger. There is a slight variation in the geometry between the subject surface and the mapped template for the middle phalanx bone. This is seen in the left proximal aspect of the middle phalanx as shown in Figure 4c. The original template mesh consisted of 340 distorted elements or approximately 5% of the total elements. More distorted element existed in the resulting mapped meshes as compared to the template mesh. The number of distorted elements increased as the variation between the template and target geometry increased. The percentage increase in the number of distorted elements is shown in Table 1. While the percentage increase is fairly large (70-

159%), this still represents a small fraction of the total elements (8.5-13.0%). The resulting distal phalanx mesh resulted in 584 elements with zero, or negative volume.

The FE-based solution that we had published previously [2] showed similar trends as the displacement based mapped meshing algorithm. The number of distorted elements tends to increase as the geometry differences between the surface and template mesh increase. The finite element method resulted in fewer distorted elements. For FE based algorithm, we found a maximum increase of 5.6% for the number of distorted elements in mapping the proximal phalanx bones across the index, middle, ring, and little fingers. The number increased to 10.6% for the middle phalanx of the index finger. This algorithm also generated a mesh with zero or negative element volumes for the distal phalanx bone.

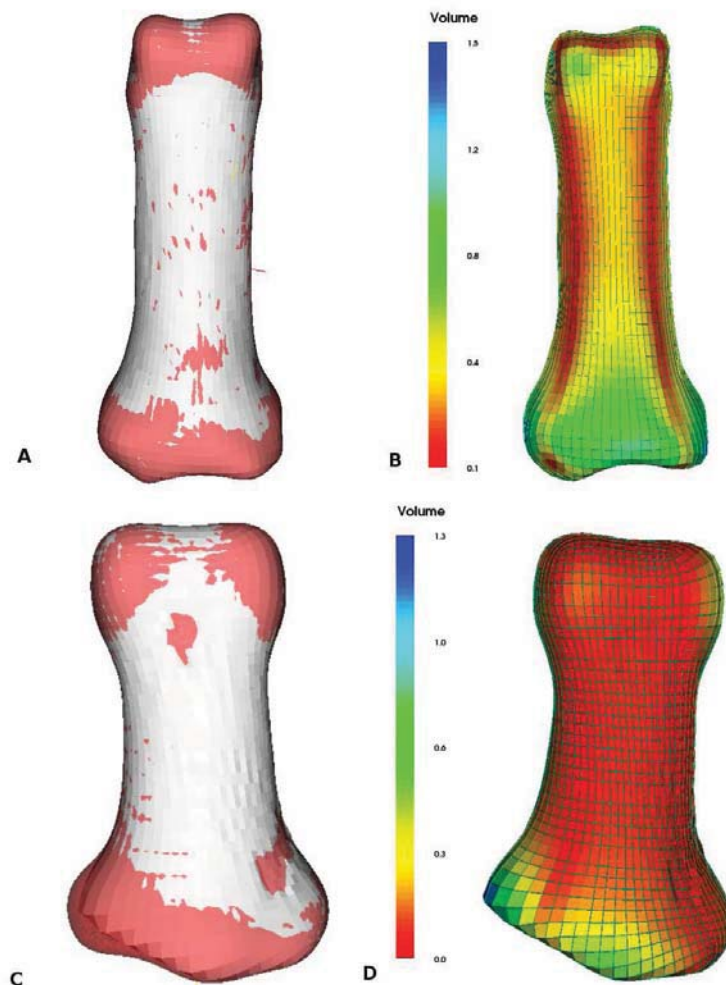


Figure 4. Results showing the warped template mesh. The warped template mesh is shown in white and the subject surface in red for the index finger proximal phalanx (A) and middle phalanx (C). The volume mesh quality metric is shown for proximal phalanx (B) and middle phalanx (D).

Table 1. Results of the mapped mesh algorithm for mapping the template proximal phalanx to other phalanx bones.

Target Surface	Number of distorted elements	Percentage change in distorted elements	Number of zero volume elements
Proximal Index	577	70	0
Proximal Middle	599	76	0
Proximal Ring	621	83	0
Proximal Little	626	84	0
Middle Index	882	159	0
Distal Index	1396	311	584

7 Discussion

The mapped meshing algorithm based on a deformable registration was successfully applied to the phalanx bones of the hand. In this work, we mapped the phalanx bones of the hand to evaluate the effectiveness of the algorithm on a variety of bone sizes. In evaluating the algorithm across different geometries, the algorithm successfully mapped to the middle phalanx bone of the index finger, but generated a mesh that had several hundred zero volume elements in the resulting mesh. We had previously evaluated a FE-based force control mapped mesh algorithm that tended to produce fewer distorted elements and generated only a single zero volume element in the distal phalanx bone. In general, the finite element solution is less sensitive to differences in geometry between the template mesh and the subject surface. Both algorithms would benefit from a higher mesh density within this region. With more nodal points in this region the algorithms would be able to account for more variability between the template mesh and the subject surface.

One advantage of this algorithm was that we were able to utilize a single ICP based algorithm for the all of the surfaces. The FE-based method required the use of an additional algorithm (i.e., Procrustes) to attain initial alignment of the template with the subject surface. Although this alignment was not required, nor used, during the deformation-based approach, future implementations therefore may benefit from an improved initial alignment. Additional consistency in alignment may improve the overall reliability of the method.

An additional advantage of this algorithm was that the resulting mesh could be generated in about half of the time required by the FE based method. Finally, the displacement based mapped meshing eliminated the need for hierarchical mesh refinement that was used in the FE based method to improve performance. The displacement control method presented here did suffer from an increase in the number of distorted elements. It is anticipated that increasing the number of iterations used for registration, along with an improved initial alignment, will help to minimize the mesh distortion.

In summary, the displacement-based solution presented here was able to successfully map a template mesh to a subject surface. In the presence of large geometric shape differences between the template mesh and individual surface, the resulting mesh may contain zero volume elements. It is anticipated that a better initial alignment and increasing the number of iterations will minimize the generation of poor quality elements.

Reference

- [1] Shivanna, K.H., Automating Patient-Specific Diarthrodial Joint Contact Model Development in Biomedical Engineering, The University of Iowa: Iowa City, 2006.
- [2] Grosland NM, Bafna R, and Magnotta VA. Automated hexahedral meshing of human anatomical structures using deformable registration. *Computer Methods in Biomechanics and Biomedical Engineering*. In Press.
- [3] Grosland NM, Shivanna KH, Magnotta VM, Kallemeyn NA, DeVries NA, Tadepalli SC. IA-FEMesh: An open-source, interactive, multiblock approach to musculoskeletal finite element model development. Submitted.
- [4] Couteau, B, Payan Y, Lavalley S, The mesh-matching algorithm: an automatic 3D mesh generator for finite element structures. *Journal of Biomechanics*, 33:1005-1009, 2000.
- [5] Jaume S, Macq B, Warfield SK, Labeling the brain surface using a deformable multiresolution mesh. *MICCAI 2002, LNCS 2488:451-458*, 2002.
- [6] Gibson AP, Riley J, Schweiger M, Hebden JC, Arridge SR, Delpy DT. A method for generating patient-specific finite element meshes for head modeling. *Phys. Med. Biol.* 48:481-495, 2003.
- [7] Brookstein LF. Principal Warp: Thin Plate Splines and the Decomposition of Deformations. *IEEE Transactions on Pattern Analysis and Machine Intelligence* II(6): 567-585, 1989.
- [8] Magnotta, VA, Harris G, Andreasen NC, O'Leary DS, Yuh WT, Heckel D. Structural MR image processing using the BRAINS2 toolbox. *Computerized Medical Imaging and Graphics*, 26(4): 251-264, 2002.
- [9] Pebay PP, Thompson DC, Shepherd JF, Lisle C, Grosland NM, Magnotta VA, New Applications of the Verdict Library for Standardized Mesh Verification, 16th International Meshing Roundtable.

Part 2.

Computational Biomechanics Of Tissues Of Musculoskeletal System

Assessment of Peri-Articular Implant Fitting Based on Statistical Finite Element Modeling

Serena Bonaretti¹, Nils Reimers², Mauricio Reyes¹, Andrei Nikitsin¹, Anders Joensson²,
Lutz-Peter Nolte¹, and Philippe Büchler¹

July 31, 2008

¹MEM Research Center, University of Bern, 3014 Bern, Switzerland
²Stryker Osteosynthesis, Kiel, Germany

Abstract

We present a framework for statistical finite element analysis allowing the statistical evaluation of biomechanical performance of peri-articular implants across a given population. In this paper, we focus on the design of orthopaedic implants that fit a maximum percentage of the target population, both in terms of geometry and biomechanical stability. A statistical shape model of left tibia was built and used to automatically create fractures at the same anatomical site. An automatic implant fitting algorithm was developed as well to optimize implant position to best fit the bone surface. Afterwards finite element analysis is performed to analyze the biomechanical performance of the bone/implant construct. The mechanical behavior of different PCA bone instances is compared for tibia representing the Asian and Caucasian populations.

1 Introduction

Current design processes for orthopedic implants rely on very limited information about the shape of the target bone. Such information may be in the form of a small set of shape parameters (e.g. lengths and angles) derived from the existing literature, which fails to capture the complexity of real anatomical shapes. Alternatively, tests on cadaver bones can be performed. However, extrapolating the findings reached by such tests to the whole target population can lead to implants that may fit some patients, but not others.

For this reason, the current project uses novel population-based design methods to develop market-specific trauma implants. Our technology allows a compact model that represents the range of shape variation encountered in a given population. The model is computed on a large collections of CT scans, using statistical analysis techniques to determine the average bone shape, as well as the shape distribution around this average in the form of principal components of shape variation. Once the model is built, it allows generating as many bone instances as required to accurately represent the population. Finite element calculations are used to evaluate the biomechanical properties of the generated bone instances. By doing so, we are able to reconstruct the statistical distribution of bone biomechanical properties across the population. Initial evaluations focused on bone strength.

2 Statistical Model of the Tibia

Two input datasets composed respectively by 43 Caucasian left tibia CT sets (23 males and 20 females) and 47 Asian left tibia CT sets (28 males and 19 females) were used. The size of each image was 120x130x140 voxels, with an image resolution of 1mm³.

All the input images were pre-processed: after their manual segmentation executed with Amira 4.1.1, they were first rigidly registered and then non-rigidly registered using the methodology presented in [4].

Bone creation was implemented in Matlab 7.0. New shape instances were created using Principal Component Analysis (PCA) [2] applying the following formula:

$$x = \bar{x} + \sum_i \phi_i b_i \quad (1)$$

where x contains the coordinates of the new shape, \bar{x} contains the coordinates of the mean one, ϕ_i is the eigenvector and b_i is the shape parameter: $|b_i| \leq \pm 3\sqrt{\lambda_i}$, with λ_i as eigenvalue. As shown in Figure 1 from the shape statistical model, 13 new instances were created for each ethnic group combining the first mode and second mode that represent about 75% of the total variance. Grey level intensities were created warping the mean intensity distribution on each bone.

Finally these new instances were used to simulate bone fractures, implant fitting and to study biomechanical properties of the bone-implant structure.

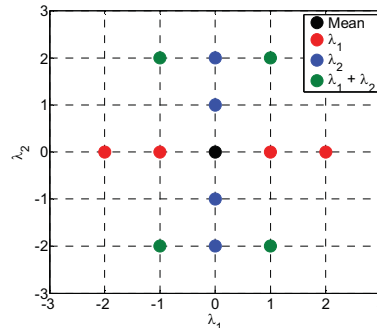


Figure 1 Map of the 13 bones created for each ethnic group through shape PCA. Axes correspond to the first and second mode of variation. Each point represents a bone created using the first (red points) and the second mode (blue points) or combining them (green points). The black point represents the mean bone.

3 Fracture Generation and Propagation

The type of fracture used for the simulation was 41-B1, according to the A.O. group classification [3]. It is a partially articular fracture in which the lateral condyle is split from the rest of the tibia by an almost vertical cut. This kind of fracture shape allowed us to both simulate a situation that is close to reality and to implement calculations with a reduced computational effort. All the implementation was done with Matlab 7.0.

The fracture was created in the same way for Asian and Caucasian image sets. In each group and for the mean bone, the fracture was conceived as an exact vertical cut (below called “reference fracture”). The reference fracture was then propagated to all the instances created through PCA in order to obtain “equivalent” fractures – located at the same anatomical site for all the bones (the fractures created in this way will be called “propagated fractures”).

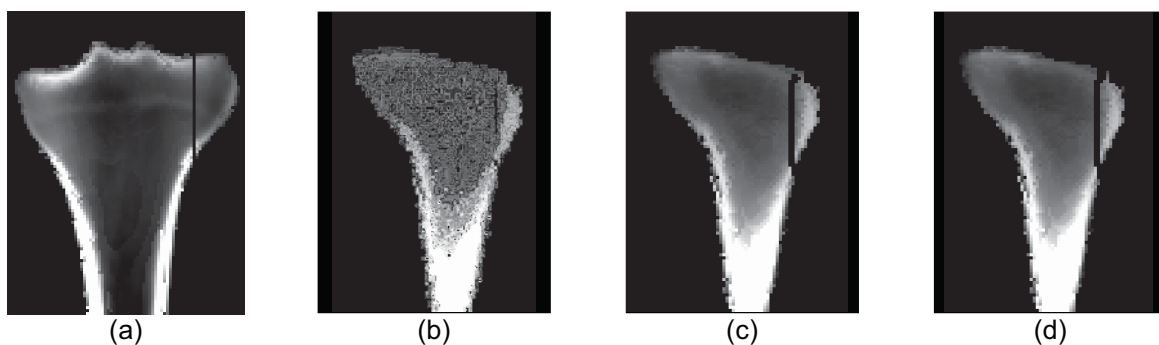


Figure 2 Fracture generation and propagation. (a) Fracture generated as a black sagittal slice in the mean bone. (b) Propagation of the reference fracture to a bone instance using deformation fields. Notice the incomplete fracture. (c) Fracture surface created with Delaunay triangulation; a few voxels are still linked at the edge of the fracture. (d) Elimination of the linking voxels and creation of two completely split bone parts.

The reference fracture was created simply changing to black all the voxels belonging to the same sagittal slice for both Asian and Caucasian (Figure 2a). The creation of the propagated fractures was implemented in an automatic way. The deformation fields obtained after non-rigid registration and used to establish points correspondences for the PCA model, were added to the mean bone fracture coordinates in order to obtain the position of the fracture in the current instance. Differently from the reference fracture, each propagated fracture was not positioned just on one single slice, but it involved modification on more slices (up to 4). Moreover the propagated fractures were not created as a black continuous but as black points spread in few slices (Figure 2b). This is due to the discrete nature of images and deformation fields. In order to perform the following biomechanical analysis the fracture should be continuous, i.e. the bone had to be completely split into two separated parts to create two different meshes. To create a continuous fracture the first approach involved morphological operators (based on connectivity). The obtained results were not satisfactory in terms of fracture thickness. Better results were achieved with an approach that considers the fracture as a continuous surface, created as a Delaunay triangulation, which splits the bone in exactly two parts without any links between them. The black voxels generated through the deformation fields were considered as vertices of the triangles (Figure 3a). Then all the voxels still belonging to the bone that were crossed by a triangle were turned to black and the complete fracture was created, as shown in Figure 2c. However, as it can be seen in Figure 2c, it could happen that at the edges of the fracture there were a few voxels still linking the two parts of the bone. To solve this last issue another triangulation was created with all the black surface voxels as vertices (Figure 3b). This second surface was expanded one voxel outwards, i.e. turning to black all the voxels that were in the same sagittal slice as the surface edge voxels and next to them. With this last operation the fractures were completed and the bones exactly split into two parts (Figure 2d).

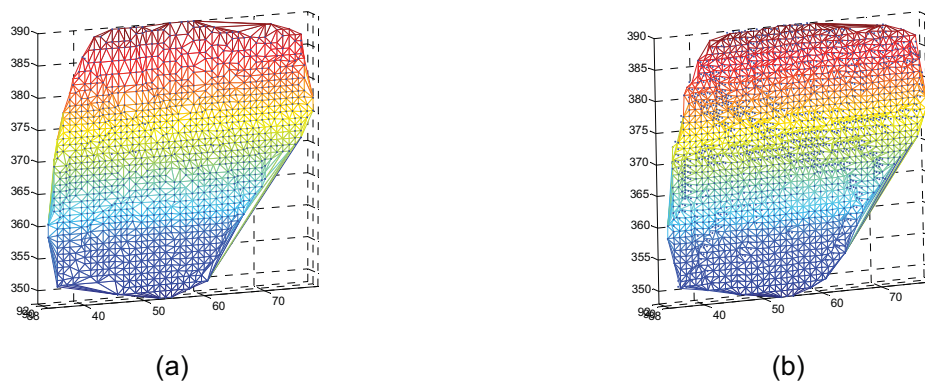


Figure 3 Delaunay triangulations. (a) Triangulation generated with the black voxels obtained through the deformation fields as vertices. (b) Triangulation generated with the surface voxels as vertices.

4 Implant Fitting

The constrained ICP algorithm was used to determine the optimal implant placement on the bone surface. The objective is to minimize the bone/implant distance while taking into account different constraints given by the experience of the implant manufacturer and physical considerations, such as surface collision. The algorithm is based on the optimization of the following functional:

$$\arg \min \sum_i W_i \cdot e_i, \quad (2)$$

where W_i and e_i are the corresponding weight and distance error for point i in the implant mesh model, respectively.

The weights W_i are computed as a linear combination of constraint-specific weights for collision, implant-bone co-linearity and tibia plateau. The last two constraints come from the implant manufacturer and have been established to favour implant fitting:

$$W_i = W_i^C + W_i^{\parallel} + W_i^P. \quad (3)$$

The collision weight W_i^C is computed as follows:

$$W_i^C = \begin{cases} 1 & p_i \notin V_{in} \\ k_i^c \|e_i\| & p_i \in V_{in} \end{cases}. \quad (4)$$

To detect if a point p_i is inside or outside the bone model, the sign of the dot product between the normal vector on the bone surface closest to p_i and the vector formed by p_i and its closest point on the bone surface is computed.

In order to avoid biases due to the number of points inside and outside the volume, the variable k_i^c in Eq. 4 was analytically found to be:

$$k_i^c \geq \frac{(N_{tot} - N_{in})}{\sum_{i \in V_{in}} \|e_i\|}, \quad (5)$$

with N_{tot} the number of points of the implant mesh, N_{in} , the number of points falling inside the bone model, and V_{in} the 3-D space inside the bone model.

We have found that adjusting the weight k_i^c we avoid biases due to the variations on the number of points inside and outside the bone volume, as the iterations proceed.

Similarly as for the collision constraint, weights W_i^{\parallel} and W_i^P are computed as follows:

$$W_i^{\parallel} = \begin{cases} 1 & \alpha \leq \alpha_{th} \\ k^{\parallel} \|\alpha_{th} - \alpha\| & \alpha > \alpha_{th} \end{cases} \quad (6)$$

$$W_i^P = \begin{cases} 1 & p_i \in \Gamma \\ k_i^P \|p_i - z_p\| & p_i \notin \Gamma \end{cases} \quad (7)$$

Where α is the angle between the implant main axis and the bone main axis, α_{th} is a threshold angle chosen by the user to set together with the weighting factor k^{\parallel} , the sensitivity of the parallelism constraint. The scalar value z_p is the z-coordinate of the plateau region interface, and Γ is the 3-D space above the bone plateau.

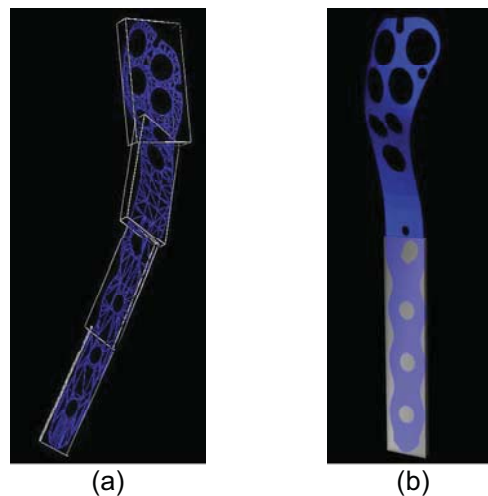


Figure 4 Oriented Bounding Box (OBB) decomposition of the implant shape used to measure deviation of the angle between the main axis of the bone and the lower part of the implant shape. Figure (a) shows a 4-level decomposition and figure (b) shows the main axis of the lower part of the implant obtained after applying a further OBB decomposition of the lower part of the implant.

For the computation of α the main axis of the implant model and the bone are required. This is performed through an Oriented-Bounding-Box (OBB) decomposition of both shapes. Furthermore, for the implant model, only the lower region is used in order to improve the alignment between the bone shaft and the implant. Figure 4a shows a 4-level OBB decomposition of the implant, while Figure 4b shows the aligned bounding-box to the main axis of the implants' lower region.

5 Biomechanical FE Simulations

Finite Element (FE) analysis is a numerical technique to solve partial differential equations over domains of complex shapes. FE techniques find a natural application in biomechanical studies, such as for structural analysis of orthopaedic implants. FE models are useful to assess the design, position and fixation of new implants [1].

A technique to generate FE models representing the target population in terms of shape and mechanical properties is proposed in this study. The statistical models obtained in the former step, average and modes of variation are used to create 3D bone solids representing instances of the population. The obtained bone geometries (both parts of the fractured tibia) are then meshed with a finite number (about 100'000) of 3D tetrahedrons. 10-nodes elements with quadratic shape functions were used to ensure good quality to the results.

The mechanical properties used in the model are inhomogeneous and depend on the bone density distribution. Since calibrated CT scans were used for the construction of the statistical model, instances of the model will maintain a proportional relationship between the bone relative density and the grey level (Hounsfield Units) in the images. It has been shown that the bone's Young's modulus can be obtained directly from the bone density [5]:

$$E = 6.95\rho^{1.49} \quad (8)$$

where E is the Young's modulus in GPa and ρ is the bone relative density (g/cm^3). The Poisson ratio is chosen equal to 0.3 because this parameter is not dependent on bone density.

The implant was also discretized with finite elements. The position of the implant on the bone surface was defined by the fitting algorithm described previously. The implant mechanical properties were $E = 110\,000$ Mpa and a Poisson's ratio of 0.3 corresponding to titanium.

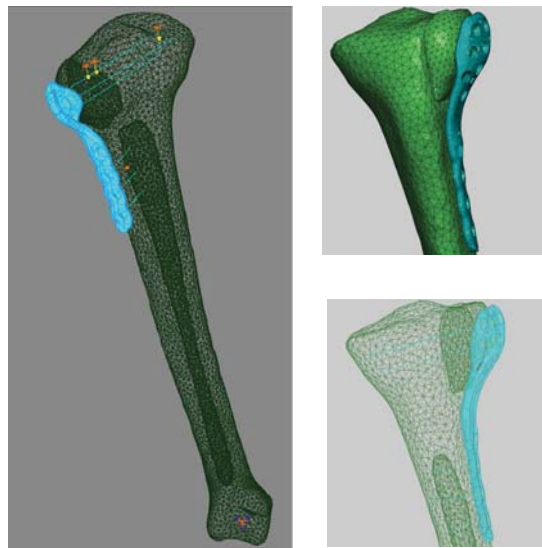


Figure 5 Finite element mesh of the bone (including the fracture) with the implant. Beam elements used to model the screws are shown as blue lines. These elements are “embedded” within the bone elements.

3D beam elements were used to fix the implant to the bone. Six beams were used in total – 3 in the proximal part of the bone and 3 in the distal part. The cross section of the beam was assumed circular with a radius of 3.3 mm, which correspond to the diameter of the fixation screws. The attachment of the beam to the bone was performed using an embedded element technique. The embedded element technique is used to specify that an element or group of elements is embedded in “host” elements. In our situation the beam elements (modeling the screws) are embedded in the bone. If a node of an embedded element lies within a host element, the translational degrees of freedom at the node are eliminated and the node becomes an “embedded node.” The translational degrees of freedom of the embedded node are constrained to the interpolated values of the corresponding degrees of freedom of the host element.

The loading conditions correspond to a 1600 N force (2 times body weight) on the tibia plateau while the distal part of the bone is maintained fixed. A frictionless unilateral contact law was use to account for the

interactions between both bone fragments. In the simulations, locking screws were considered. The locking of the screw on the plate avoids any relative motion between these two parts and also avoids the compression of the plate on the bone; therefore no contact was considered at the bone/plate interface. In total 26 FE models were built. Only small deformations and displacements were expected, therefore a geometrically linear solver was used for the calculations. The commercial finite element package ABAQUS was used for the simulations.

6 Results

The quality of the implant fitting was evaluated on each of the bone generated with the statistical model. Results show that the implant better fits the Caucasian population than the Asian group (Table 1). For the Asian bones, the maximal bone/implant distance was found to be up to 7mm. The difference between the two populations was expected since the implant was first designed to target the Caucasian market.

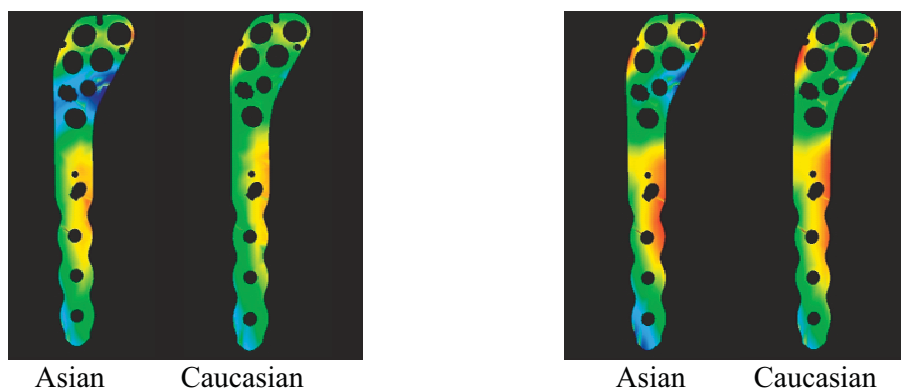


Figure 6 Maximal (right) and average (left) distance map for the Asian and Caucasian bone populations. Red indicated a small distance (0mm) and blue indicates a large bone/implant distance – up to 7mm for the maximal distance in the Asian population.

Once the optimal position for the implant has been found, biomechanical simulations are used to evaluate the mechanical behavior of the implant for the different populations. For the simple fracture considered in this study, stresses in the implant remain far below Yield stress. However, some differences were visible between the two populations (Table 1). The stresses calculated in the plate as well as in the screws are significantly higher ($p < 0.05$) for the Asian than for the Caucasian population. However, no statistical difference was found for the fitting distance in the two populations. Even if the average distance between the bone and the implant was larger for the Asian bones than for the Caucasian bones, the quality of the fit was statistically identical. This result highlights the importance of including biomechanical simulations in the optimization process and that optimization based on the geometrical fitting of the plate is not enough to capture the complexity of the implant biomechanics.

Stresses in the implant also correlate to the bone size in the Asian population. A linear correlation (R^2 higher than 0.6) was found between the length of the bone and the maximum von Mises stress in the plate. Higher stresses were calculated for the short bones than for the long one. On the other hand, no

correlation was found for the Caucasian bones. This observation indicates that probably more care is required to account for implant size scaling in the Asian bones than for the Caucasian bones.

	Caucasian	Asian
Bone-implant distance (mm)	3.7	4.3 (+14%)
Mises stress in the plate (Mpa)	61	69 (+12%)
Max principle stress in the screws (Mpa)	61	80 (+31%)

Table 1 Comparison of the biomechanical and geometrical variables between the Asian and the Caucasian models. The first row shows the average of the maximal bone/implant distance calculated using the image-based method described in sections 2-4, while the other two rows contain the average of the maximal von Mises stress in the plate and maximal principle stress in the screws. Variations are given in %.

7 Discussion

We presented a framework for statistical biomechanical assessment including a combined statistical model of shape and finite element analysis. The application of our methods for modelling bone shape and mechanical behaviour has been shown for the evaluation of a given peri-articular plate.

The statistical model construction and fracture propagation are based on non-rigid registration. This has the advantage that no landmarks or parametric representations need to be defined and the fractures can be placed automatically at the same anatomical site. Future developments will combine shape and intensity information into the statistical model; the model contains information about the correlation between shape and density. This could allow predicting bone density when only shape is known, and this is one of our directions of future work.

The FE analysis shown in this work could be improved by addressing a set of experiment setup issues. For example, bone screws were modeled with simple beams embedded in the bone. Obviously, the screw/bone interactions are more complex than this idealized model. Hence, accuracy of this approximation needs to be evaluated and validated. Further, the bone geometries were meshed independently from each other, resulting in different FE meshes for the different bones. This leads to difficulties in the direct comparison of the stress distribution between the different bone shapes under consideration, as well as discrepancies in the location of the loading forces applied. The alternative is to deform a pre-defined mesh, such as was done by Yeoh et al in 2000 [6]. However, it is extremely difficult to ensure the validity of the mesh for further FEA under arbitrary deformations.

The target application is orthopaedic implant design. Virtual testing of new implants will in the future replace cadaver testing. Furthermore, being able to study the whole range of bone shapes and densities of the target population will lead to better fitting implants, as well as a considerable cost reduction in the design process. In order to assess the appropriateness of an implant, further development should be done

to define the different scenarios of the implant, in terms of positions where the implant is likely to be placed and the force loading conditions.

A complementary application of these techniques will be the patient-specific pre-clinical evaluation of an implant; taking into account the particular skeletal anatomy, bone quality, and implant position to assess the biomechanical performance of the implant on the patient.

Acknowledgements

This research has been supported by the NCCR Co-Me of the Swiss National Science Foundation and the Swiss Innovation Promotion Agency, CTI.

Reference

- [1] Büchler P. and Farron A. *Benefits of an Anatomical Reconstruction of the Humeral Head Using Shoulder Arthroplasty: A Finite Element Analysis*. *Clinical Biomechanics*, 19 (1), 16-23, 2004.
- [2] Cootes T.F., Taylor C.J. *Statistical Models of Appearance for Computer Vision. Technical Report*. University of Manchester, 2004.
- [3] Müller M.E., Allgower M., Schneider R. *Manual of Internal Fixation: Technique Recommended by the A.O. Group*. Springer-Verlag, New-York, 1979.
- [4] Schnabel J.A., Rueckert D., Quist M., Blackall J.M., Castellano Smith A.D., Hartkens T., Penney G.P., Hall W.A., Liu H., Truwit C.L., Gerritsen F.A., Hill D.L.G., and Hawkes D.J. *A Generic Framework for Non-Rigid Registration Based on Non-Uniform Multi-Level Free-Form Deformations*. In Fourth Int. Conf. on Medical Image Computing and Computer-Assisted Intervention (MICCAI 2001), 573-581, Utrecht, NL. 2001.
- [5] Taddei F., Schileo E., Helgason B., Cristofolini L., Viceconti M. *The Material Mapping Strategy Influences the Accuracy of CT-based Finite Element Models of Bones: An Evaluation Against Experimental Measurements*. *Medical Engineering & Physics*, 29 (9), 973-9, 2007.
- [6] Yao, J. and Taylor,R.: *Tetrahedral Mesh Modeling of Density Data for Anatomical Atlases and Intensity-Based Registration*. Proceedings of the Third International Conference on Medical Image Computing and Computer-Assisted Intervention (MICCAI 2000), 531-540, Pittsburgh, PA, USA. 2000.

Orientation definition of anisotropy is important to finite element simulation of bone material properties

Haisheng Yang^{1,2}, Tongtong Guo¹ and Xin Ma^{2,3}

May 21, 2008

¹Harbin Institute of Technology Shenzhen Graduate School

²Shenzhen Institute of Advanced Technology, Chinese Academy of Sciences

³Harbin Institute of Technology

Abstract

The assignment of bone material properties to finite element model is a fundamental step in finite element analysis and has great influence on analysis results. Most work done in this area has adopted isotropic assignment strategy as its simplicity. However, bone material is widely recognized as being anisotropic rather than isotropic. Therefore, this work is aimed to simulate the inhomogeneity and anisotropy of femur by assigning each element of the mesh model the material properties with a numerical integration method and properly defining the principal material orientation, and then compare the biomechanical analysis results of isotropic model with that of anisotropic model under six different loading conditions. Based on the analysis results of the equivalent Von Mises stress and the nodal displacement, four different regions of interest are chosen to achieve this comparison. The results show that significant differences between the two material property assignments exist in the regions where anisotropic material property is sensitive to orientation definition. Thus, orientation definition is important to finite element simulation of bone material properties.

1 Introduction

Finite element (FE) analysis, as a non-invasive method, has been widely used in academic research and clinical applications, such as the theory of bone remodeling [1], the design of prosthesis [2] and the evaluation of fracture risk [3]. Accurate simulation of bone biomechanical behavior depends on not only the accurate model obtained via three-dimensional reconstruction, but also the realistic material properties that consist with different aspects' bone density and anatomical structure.

In early period, the methods used to get bone geometry and mechanical properties were inaccurate and sometimes highly invasive and destructive. It is well known that CT images can provide fairly accurate quantitative information on bone geometry based on high contrast between the bone tissue and the soft tissue around [4]. Moreover, it has been demonstrated that CT numbers are almost linearly correlated with apparent density of biologic tissues [5]. Good experimental relationships have been established between density and mechanical properties of bone tissues [6].

The CT data can be regarded as a three-dimensional scalar field (related to the tissue density) sampled over a regular grid. Once the finite element mesh is generated starting from the same CT data, the mesh and the density distribution are perfectly registered in space. The only problem is how to properly map the density into the finite element mesh. Many approaches were proposed in literature to perform this task [7-10]. However, these algorithms only simulated the inhomogeneity of bone material, and the isotropic material property assignment was adopted without considering the material orientation of bone tissue. Since the bone material is anisotropic [11, 15, 16], the isotropic FE simulation of bone material property cannot reflect the actual structure and mechanical behavior of bone.

In recent studies, more attentions were paid to the orthotropic material property assignment and the comparison between isotropic and orthotropic methods. Peng et al [12] compared isotropic material property assignment with orthotropic assignment on femoral finite element models and demonstrated that the differences were small and bone is weak orthotropic material. Nevertheless, the global coordinate system was defined as the orthotropic orientation over the whole femoral model. This definition can not respect the real anatomical locations in femur, especially in femoral neck. The results, therefore, were distorted. Baca et al [13] overcame above-mentioned shortcomings by manually defining orthotropic orientation based on real anatomical structure that was obtained following a grinding protocol. However, too much manual work needs to be done and the investigator must be quite familiar with anatomical

structure of femur. Besides, this method can only be applicable to cadaveric bone. What's more, the data used for comparison are too little to doubtless support the conclusion. Unfortunately, both studies mistook the unit of shear modulus (GP) for unit (MP) when they quoted the formula of density-modulus relationship in [15] ($G_{12_{max}} = 5.71 \text{ GP}$, $G_{23_{max}} = 7.11 \text{ GP}$, $G_{31_{max}} = 6.58 \text{ GP}$). Moreover, the force (8kN) applied to femoral head was almost ten times to the weight of a normal person. This force may destroy the bone structure or produce abnormal stress and displacement.

This work is aimed to simulate the inhomogeneity and anisotropy of femur by properly defining the principal material orientation automatically, and investigate the differences between isotropic and orthotropic material property assignments through correctly defining the material orientation and exactly using the parameters.

2 Materials and methods

2.1 CT data

The CT dataset of a man's femur is obtained from the public database which is created by VAKHUM project (<http://www.ulb.ac.be/project/vakhum/index.html>). The use of the data is free for academic purposes. The CT data are in standard DICOM formats. The slice thickness is 1mm in the epiphysis and 3mm in the diaphysis.

2.2 Finite element mesh

The finite element mesh of a right femur (Figure 1) generated from the corresponding CT dataset above is also obtained from the VAKHUM project. It is in a Patran Neutral file format. The mesh is made of linear hexahedral elements and is generated using the HEXAR (Cray Research, USA) automatic mesh generator that implements a grid-based meshing algorithm. The model mesh is spatially registered with the CT dataset. The complete finite element mesh consisted of 9,294 nodes and 7,934 elements.

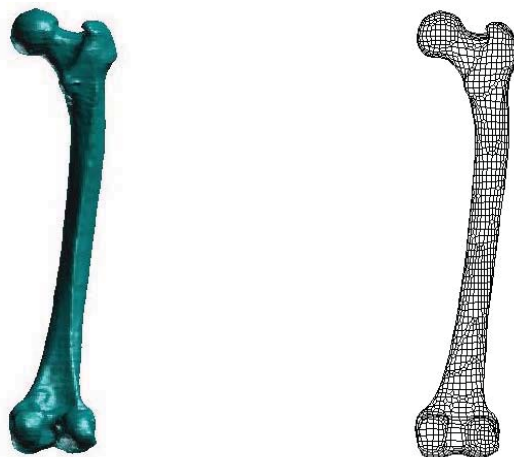


Figure 1 (a) The geometrical model of femur. (b) The finite element mesh of femur.

2.3 The procedure of material property assignment

2.3.1 Calculation of the average CT number

For each element of the mesh, an average HU value is calculated with a numerical integration as follows:

$$\begin{aligned} \overline{HU}_n &= \frac{\int_{V_n} HU(x, y, z) dV}{\int_{V_n} dV} \\ &= \frac{\int_{V'_n} HU(r, s, t) \det J(r, s, t) dV'}{V_n} \end{aligned} \quad (1)$$

where V_n indicates the volume of the element n , (x, y, z) are the coordinates in the CT reference system, (r, s, t) are the local coordinates in the element reference system, and J represents the Jacobian of the transformation. The integrals in Equation 1 are evaluated numerically, and the order of the numerical integration can be chosen by us. The value of $HU(x, y, z)$ in a generic point of the CT domain is determined by a tri-linear interpolation between the eight adjacent grid points' values.

2.3.2 Calibration of the CT dataset

It has been demonstrated that the relationship between CT number and apparent density is linear. The calibration equation is then:

$$\overline{\rho}_n = \alpha + \beta \overline{HU}_n \quad (2)$$

where $\overline{\rho}_n$ is the average density assigned to the element n of the mesh, \overline{HU}_n is the average CT number and α , β are the coefficients provided by calibration.

Generally, a calibration phantom [14] was used to obtain the parameters of the linear regression. In this paper, referenced values are selected for approximate calibration from [7]: Radiographic and apparent density of water (0 HU, 1 g/cm³); Average radiographic density in the cortical region and the apparent density value for cortical bone (1840 HU, 1.73 g/cm³).

2.3.3 Calculation of the elastic constants

Large number of experiments shows that the bone material properties can be expressed as function of apparent density, and various experimental relationships between elastic modulus and apparent density can be found in the literature. In the case of isotropic material property:

- Cortical bone:

$$E = 2065\rho^{3.09}, \nu = 0.3 \quad (3)$$

- Cancellous bone:

$$E = 1094\rho^{1.64}, \nu = 0.3 \quad (4)$$

where E is the average Young's modulus assigned to the element n of the mesh, ρ is its apparent density and ν is the Poisson ratio.

In the case of orthotropic material property:

- Cortical bone:

$$\begin{aligned} E_1 = E_2 &= 2314\rho^{1.57}, E_3 = 2065\rho^{3.09} \\ \nu_{12} &= 0.58, \nu_{13} = \nu_{23} = 0.32 \\ G_{12} &= E_1 / 2(1 + \nu_{12}), G_{13} = G_{23} = 3.3 \end{aligned} \quad (5)$$

- Cancellous bone:

$$\begin{aligned} E_1 = E_2 &= 1157\rho^{1.78}, E_3 = 1094\rho^{1.64} \\ \nu_{12} &= 0.58, \nu_{13} = \nu_{23} = 0.32 \\ G_{12} &= E_1 / 2(1 + \nu_{12}), G_{13} = G_{23} = 0.11 \end{aligned} \quad (6)$$

where E is the Young's modulus (MPa), G the shear modulus (GPa), ν the Poisson's ratio. The coordinate systems of these parameters are defined in next step. In order to get a limited number of material card, a ΔE_3 threshold is chosen in the program. In this work, $\Delta E_3 = 50$ MP.

2.4 The definition of material orientation

As we know, bone structure is customarily recognized as confirming to 'wolff's law' which is essentially the observation that bone changes its external shape and internal architecture in response to stresses acting on it. Thus, the structure of bone (or material orientation) strongly coincides with the principal stress track. Since bone tissue is recognized as orthotropic material, the determination of principal material orientation based on real anatomical bone structure is essential to the real simulation of bone material properties. According to the cortical bone structure in femoral stem and cancellous bone structure in femoral neck, the principal material orientation of cancellous bone is defined by the direction of the trabecular structures and the principal material orientation of cortical bone by the direction of the haversian system.

2.5 Loading conditions

After the generation of finite element models with bone material properties and orthotropic orientation, six loading conditions (Figure 2) are applied to the isotropic models and orthotropic models respectively:

- LC1. Neutral: femoral axis vertical.
- LC2. Maximum adduction: 24° in the frontal plane.
- LC3. Maximum abduction: 3° in the frontal plane.

- LC4. Maximum flexion: - 3° in the sagittal plane.
- LC5. Maximum extension: 18° in the sagittal plane.
- LC6. High stress in neck: 8° in the frontal plane.

The force (500N) is applied on femoral head based on the local reference coordinate system defined in [18] and the distal femur is fully constrained.

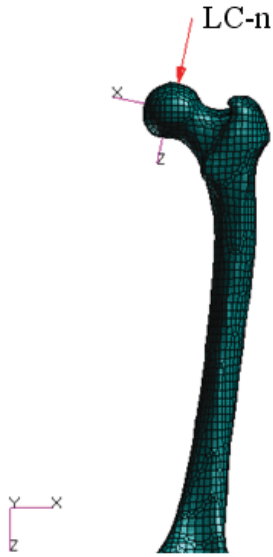


Figure 2 Boundary conditions and local reference coordinate system.

2.6 Comparison of isotropic and orthotropic material property assignments

The objective of this study is to investigate the differences between isotropic and orthotropic material property FE-simulation. Thus, two parameters are defined to show the differences. The first parameter ($\Delta\sigma$) represents the difference of equivalent Von Mises stress in the regions of interest (ROI) between isotropic and orthotropic models. The second parameter (Δu) represents the difference of nodal displacement in ROI:

$$\Delta\sigma^n = \left| \frac{\sigma_i^n - \sigma_o^n}{\sigma_o^n} \right| \quad (7)$$

$$\Delta u^n = \left| \frac{u_i^n - u_o^n}{u_o^n} \right| \quad (8)$$

where $\Delta\sigma^n$ is the difference of stress in ROI n ($n=1,2,3,4$), $\Delta\sigma_i^n$ and $\Delta\sigma_o^n$ represent the parameter $\Delta\sigma^n$ in case of the isotropic material property assignment and the orthotropic material property assignment. Δu^n is the difference of stress in ROI n ($n=1,2,3,4$), Δu_i^n and Δu_o^n represent the parameter Δu^n in case of the isotropic material property assignment and the orthotropic material property assignment.

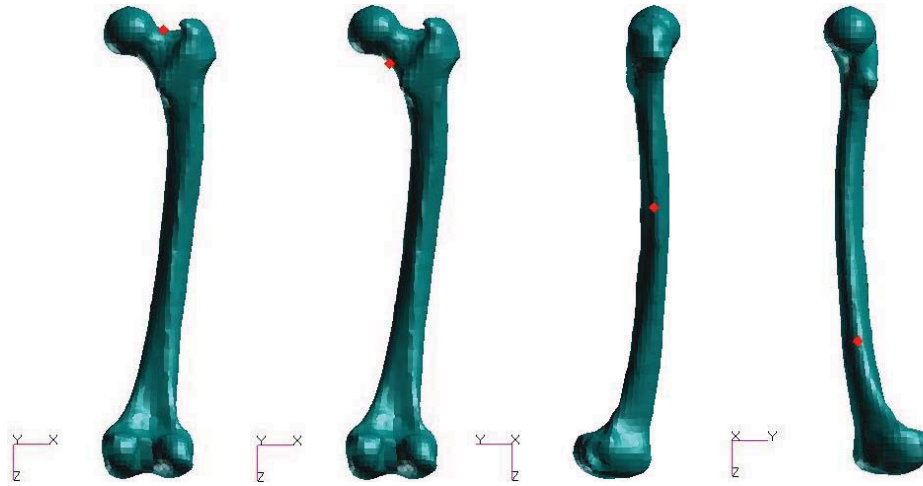


Figure 3 Four regions of interest: ROI1 in superior neck, ROI2 in inferior neck, ROI3 in diaphysis and ROI4 in distal femur.

In order to make the compared results more comprehensive, four different regions of interest (including femoral neck, diaphysis and distal femur) are chosen for comparison instead of only comparing the maximum value of Von Mises stress and nodal displacement (Figure 3).

3 Results

3.1 Inhomogeneous distribution of material properties

This material assignment procedure produces 165 different material definitions. The distribution of all kinds of material properties in femur are shown in Figure 4.

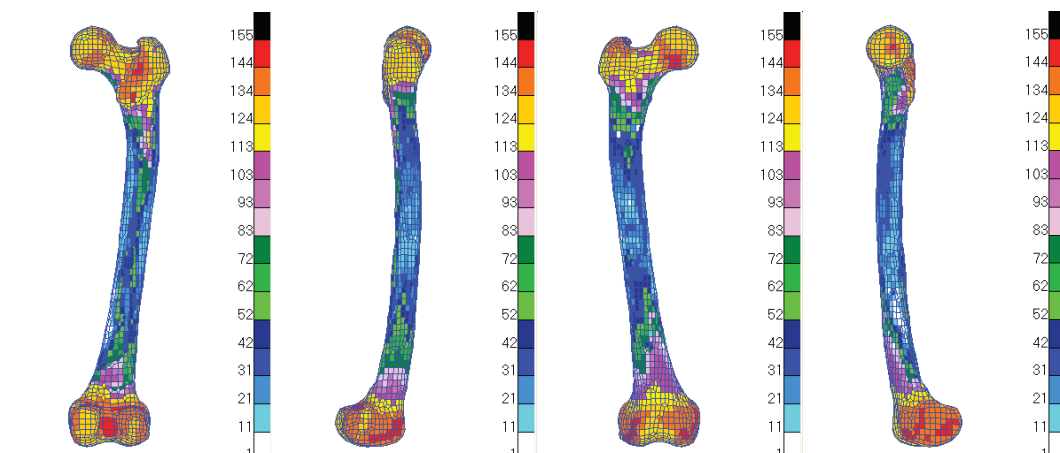


Figure 4 Right femur with different material properties mapped on it: posterior, lateral, anterior and medial views.

The maximum and minimum values for apparent density and elastic modulus are listed in Table 1. The maximum is corresponding to the material property 1 and the minimum to number 165 as a result of the definition in the program.

	Material properties		
	ρ	$E_1(E_2)$	E_3
Maximum	1.787	5755.799	12410.846
Minimum	0.686	591.512	1026.157

Table 1 Density and elastic modulus (The unit for density is g/cm^3 , and for elastic modulus is MP).

3.2 The definition of principal material orientation (orthotropic FE-simulation)

After separating the femoral neck and stem, different principal material orientations are automatically assigned to the two aspects. As is shown in Figure 5: In femoral neck, the principal axis is along the direction of neck which has an angle 120° to z axis; In femoral stem, the principal axis is along the direction of stem which has an approximate angle 12° to z axis. Besides, the other two transverse axes are defined perpendicular to the z axis.

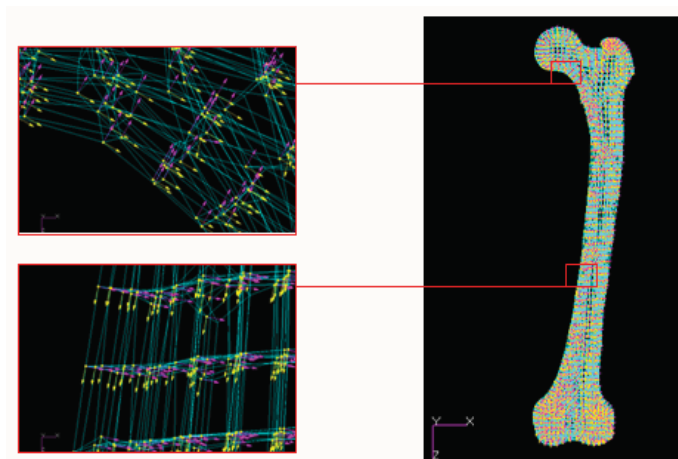


Figure 5 Orthotropic FE model with principal material orientation presented in vector form.

3.3 Differences between isotropic and orthotropic material models

Table 1 shows the relative differences of equivalent Von Mises stress $\Delta\sigma$ in four regions (ROI1-ROI4) under six loading conditions (LC1- LC6). Table 2 shows the relative differences of nodal displacement Δu . Under each loading condition, the change of data from ROI1 to ROI4 is quite similar. For equivalent Von Mises stresses, two material property assignments show marked differences in ROI1: the values of $\Delta\sigma$ are from 16.63% to 18.17%. Significant differences still appear in ROI2: the values of

$\Delta\sigma$ are greater than 9.96% and the maximum reaches 11.67%. On the contrary, the differences of stress between two material property assignments are lower than 0.41% in ROI3 and 1.62% in ROI4.

For nodal displacement, the values of Δu are nearly 5% in ROI1, ROI2 and ROI3 under all the loading conditions except LC2 and LC5. The differences are larger than 8.67% in ROI4 and bigger values of Δu exist here under LC2 and LC5: 17.73% for LC2 and 15.77% for LC5.

Regions of interest	Loading conditions					
	LC1	LC2	LC3	LC4	LC5	LC6
ROI1	18.17	16.63	17.78	18.10	17.14	17.97
ROI2	11.09	9.99	11.63	11.67	11.16	9.96
ROI3	0.29	0.35	0.27	0.41	0.39	0.26
ROI4	0.91	1.62	1.01	1.21	0.57	1.35

Table 1 The relative differences of stress $\Delta\sigma$ in four regions of femur under six loading conditions (%).

Regions of interest	Loading conditions					
	LC1	LC2	LC3	LC4	LC5	LC6
ROI1	4.22	8.43	4.33	4.74	6.55	4.69
ROI2	4.25	9.33	4.41	4.95	7.03	4.90
ROI3	4.07	7.42	3.90	4.06	6.26	3.69
ROI4	8.67	17.73	9.29	11.27	15.77	11.59

Table 2 The relative differences of displacement Δu in four regions of femur under six loading conditions (%).

4 Discussion

The finite element method has been increasingly accepted as a useful tool to study the biomechanical behavior of bone structure. As we know, CT data can offer not only the accurate information on bone geometry but also the density information which has been demonstrated having relationship with bone material properties. Once the finite element mesh has been generated from CT data, how to assign the realistic material properties to finite elements becomes crucial for the FEA. Most work done in this domain only simulates the inhomogeneity and isotropy of bone as its simplicity. Bone, however, is widely recognized as anisotropic material and can be simplified to orthotropic material that has nine independent elastic constants and spatial orientation of the principal axes of orthotropy.

It has been demonstrated that the structure of femur is highly variable, especially to cancellous bone. Thus, a clear and exact definition of the principal axes of orthotropy is impossible. In this study, we only separate the femoral neck and stem. Then, the principal orientations of neck are defined on the basis of the direction of trabecular structure and the principal orientation of stem on the basis of the direction of Haversian system. As the structure of femur (or material orientation) coincides with the track of principal stress, the orientation definition based on pass of stress is reasonable.

In order to thoroughly investigate the differences between the isotropic model and orthotropic model, equivalent Von Mises stresses and nodal displacements from four regions of femur are chosen to achieve this comparison. As shown in Table 1, significant differences appear in ROI1 and ROI2: the maximum of $\Delta\sigma$ reach 18.17% and 11.67% respectively. ROI1 and ROI2 located in femoral neck where the principal material orientations are defined according to the trabecular structure and have great differences with the global coordinate system. Consequently, it is considered that anisotropic material property is sensitive to orientation definition in these regions. The results indicate that large differences of stress just exist in these regions. The differences of stresses are lower in ROI3 and ROI4 where the principal material orientation only has an angle 12° to z axis of the global coordinate.

For nodal displacement, the differences are lower in ROI1, ROI2 and ROI3 (about 5% for Δu). But, nodal displacements for two models show obvious differences in ROI4. According to the analysis results in both models, we find that there are fewer displacements in ROI4. This means significant differences between isotropic and orthotropic models may appear in these regions where absolute displacements are lower. Moreover, largest equivalent Von Mises stress is in the ROI4 where the differences are quite small. Therefore, incorrect results may be obtained if researchers compare the differences with maximum equivalent Von Mises stress and maximum nodal displacement.

In this study, six loading conditions are applied to the models aiming to investigate whether different loads have influence on compared results. As shown in Table 2, the values of Δu under LC2 and LC5 are obviously different from others. Thus, different loading conditions will lead to different comparison results. Besides, the loading conditions have different effects on stress and displacement.

With the comparison of isotropic and orthotropic material property assignments on femoral finite element models, significant differences exist in the regions where anisotropic material property is sensitive to orientation definition. Therefore, it is inaccurate to simplify orthotropy to isotropy during the procedure of material properties FE-simulation and orientation definition is important to the finite element simulation of material property.

How to simulate the real material properties of bone with finite element method is a problem all the while. Although since several years, some studies have been performed to generate an isotropy FE modeling of femur, these models can not reproduce exactly in vivo conditions. In our study, the principal material orientations are defined according to the macroscopical structure that consists with the stress pass. Thus, this method has reproducibility. Future work has to be done to validate the anisotropy model via experiment.

Reference

[1] P.R. Fernandes, J. Folgado, C. Jacobs, V. Pellegrini. A contact model with ingrowth control for bone remodeling around cementless stems. *Journal of Biomechanics*, 35:167-176, 2002.

- [2] P. Kowalczyk. Design optimization of cementless femoral hip prostheses using finite element analysis. *Journal of Biomechanics*, 123:396-402, 2001.
- [3] J. H. Keyak. Improved prediction of proximal femoral fracture load using nonlinear finite element models. *Medical Engineering and Physics*, 23:165-173, 2001.
- [4] M. Viceconti, L. Bellingeri, L. Cristofolini, and A. Toni. A comparative study on different methods of automatic mesh generation of human femurs. *Medical Engineering and Physics*, 20:1-10, 1998.
- [5] J. Y. Rho, M. C. Hobatho, and R. B. Ashman. Relations of mechanical properties to density and CT numbers in human bone. *Medical Engineering and Physics*, 17:347-355, 1995.
- [6] D.C. Wirtz, N. Schiffers, T. Pandorf, K. Radermacher, D. Weichert, and R. Forst. Critical evaluation of known bone material properties to realize anisotropic FE-simulation of the proximal femur. *Journal of Biomechanics*, 33:1325-1330, 2000.
- [7] C. Zannoni, R. Mantovani, and M. Viceconti. Material properties assignment to finite element models of bone structures: a new method. *Medical Engineering and Physics*, 20:735-740, 1998.
- [8] F. Taddei, A. Pancanti, and M. Viceconti. An improved method for the automatic mapping of ct numbers onto finite element models. *Medical Engineering and Physics*, 26:61-69, 2004.
- [9] F. Taddei, E. Schileo, B. Helgason, L. Cristofolini, and M. Viceconti. The material mapping strategy influences the accuracy of CT-based finite element models of bones: an evaluation against experimental measurements. *Medical Engineering and Physics*, 29:973-979, 2007.
- [10] B. Helgason, F. Taddei, H. Palsson, E. Schileo, L. Cristofolini, M. Viceconti, and S. Brynjolfsson. A modified method for assigning material properties to FE models of bones. *Medical Engineering and Physics*, 30:444-453, 2007.
- [11] R. B. Ashman, S. C. Cowin, W. C. Van Buskirk, and J. C. Rice. A continuous wave technique for the measurement of the elastic properties of cortical bone. *Journal of Biomechanics*. 17:349-361, 1984.
- [12] Peng L, Bai J, Zeng X, Zhou Y. Comparison of isotropic and orthotropic material property assignments on femoral finite element models under two loading conditions. *Medical Engineering and Physics*; 28:227-233, 2006.
- [13] Baca V, Horak Z, Mikulenka P, Dzupa V. Comparison of an inhomogeneous orthotropic and isotropic material models used for FE analyses. *Medical Engineering and Physics*, 2008.
- [14] W. A. Kalender. A phantom for standardization and quality control in spinal bone mineral measurements by qct and dxa: design considerations and specifications. *Medical Physics*, 19:583-586, 1992.
- [15] Taylor WR, Roland E, Ploeg H, Hertig D, Klabunde R, Warner MD. Determination of orthotropic bone elastic constants using FEA and modal analysis. *Journal of Biomechanics*, 35:767-773, 2002.
- [16] Wirtz DCH, Pandorf T, Portheime F, Radermacher K, Schiffers N. Concept and development of an orthotropic FE model of the proximal femur. *Journal of Biomechanics*, 36:289-293, 2003.
- [17] Bergmann G, Deuretzbacher G, Heller M, Graichen F, Rohlmann A, Strauss J, Duda G.N. Hip contact forces and gait patterns from routine activities. *Journal of Biomechanics*, 34:859-871, 2001.

A Mix-resolution Bone-related Statistical Deformable Model (mBr-SDM) for Soft Tissue Prediction in Orthognathic Surgery Planning

Qizhen He^{1,2}, Horace H. S. Ip¹ and James Xia³

May 21, 2008

¹Image Computing Group, Department of Computer Science, City University of Hong Kong, Hong Kong, China

²Department of Computer Science and Technology, University of Science & Technology of China, Hefei, China

³Surgical Planning Laboratory, Department of Oral and Maxillofacial Surgery, The Methodist Hospital Research Institute, U.S.A

Abstract

In this paper, we propose a Mix-resolution Bone-related Statistical Deformable Model (mBr-SDM) to improve the predicting accuracy of orthognathic surgery, particularly for the main deformation region. Mix-resolution Br-SDM consists of two separate Br-SDM of different resolutions: a high-resolution Br-SDM which is trained with more samples to capture the detail deforming variations in the main deforming regions of interest, together with a low-resolution Br-SDM which is trained with a smaller number of samples to capture the major variations of the remaining facial points. The experiments have shown that the mix-resolution Br-SDM is able to significantly reduce the predicting error compared with the corresponding Finite Element Model, while giving a low computational cost which is characteristic of the SDM approach.

1 Introduction

Orthognathic surgery aims to correct for abnormalities of the facial anatomies. Computer aided planning of such surgeries has been an area of active research in the past decades because the predicted facial outcome of the surgery helps surgeons to choose the best surgical strategy among the possible surgical plans, as well as to improve the communications between the surgeons and the patients. Conventionally, the appropriate osteotomy line and the necessary displacements of the jaw segment are determined by 2D cephalometry. The advent of high quality medical imaging modalities (such as CT images) has made possible accurate and efficient representation and prediction of the 3D facial changes as a result of surgery, and at the same time, posed many new challenging problems, among them is the prediction of facial soft tissue deformation as a result of craniofacial bone movements. The Mass Spring Models (MSM) has been introduced [1] to model the facial tissue as masses and springs connecting neighboring masses. The model structure is intuitive, and computational cost of predicting tissue deformation is low. The major disadvantage is that the parameters in a MSM, such as the spring constant [4], typically do not bear direct relation to the biomechanical properties of human soft tissues. Later on, Finite Element Models (FEM) [2], as a general discretization procedure of continuum problems is suggested to solve the problem of facial deformation. FEM is accurate [3], but computational and memory intensive which makes it not particularly suitable for real-time surgical planning where interactive response with the user is a key requirement. While the Mass Tensor Model (MTM) [5] provides a model that has the simplicity of MSM as well as the accuracy of FEM, the computational demand for prediction process using high resolution models is still far from real-time responses. Statistical Deformable Model (SDM) which has been developed originally for object segmentation [6] and motion analysis [7] has been introduced for soft tissue prediction by Meller in 2005[8]. With SDM, the system is able to learn the prior knowledge of tissue deformation from a set of training samples, and predict facial changes according to the learned knowledge. This method, while it is efficient, it suffers from the small sample size problem [9] which is typical of many other applications of SDM. This problem is particularly significant in surgical planning applications because typically we do not have many real life instances of medical organ samples. Additionally, in [8], the authors used the pre-operational facial model to predict the post-operational facial changes by assuming that all patients underwent the same standard surgery, and, more important, the approach does not take bone movements into account. Thus it is not particularly applicable to orthognathic surgical planning where different surgical plans would be investigated and evaluated.

To harness the accuracy of FEM and the computational efficiency of SDM as well as taking into account the bone-movement that cause the tissue deformation in the first place, we have introduced a novel statistical deformable model called Bone-related SDM or *Br-SDM* in [10]. In Br-SDM, FEM is first applied to generate a large sample set of soft-tissue deformation instances with respect to different jaw-bone movements, then the generated set of deformation samples are used to train a Statistical Deformable Model (SDM) for subsequent surgical planning, which is eventually used to predict the facial changes for specific jaw movements. The experimental results demonstrate that the Br-SDM has comparable accuracies with FEM (the average predicting difference of the two methods stayed within 10% of the jaw movement) while using only 10% of the computational time and memory of conventional FEM. However, it is also observed that, the predicting differences between Br-SDM and FEM in the main deforming area,

e.g. the region of the chin, has the highest errors compared with the other points on the face by almost 20% to 30% of the jaw movement. One possible cause of this phenomenon may be due to the insufficient sample size for the training of the SDM as well as insufficient resolution of the bone and soft tissue meshes around those facial regions.

To address the above problems, the primary contribution of this paper is that we propose a novel mixed-resolution Br-SDM (mBr-SDM) which consists of a high-resolution SDM, called *sub-SDM*, for the main deforming regions of interest which is trained with more samples to capture the detail deforming variations in the main deforming area, together with a low-resolution SDM, called *main-SDM*, which is trained with a smaller number of samples to capture the variations of the remaining facial points. The experiments have shown that the sub-SDM is able to reduce the predicting error compared with FEM significantly, while the maintaining the low computational cost which is characteristic of our original Br-SDM approach. The resulting SDM is called **Mixed-resolution Br-SDM** because it consists of two separate SDMs each with a different mesh resolution and different training sample size which enables precise prediction of soft tissue deformation as a result of bone movement, particularly for the facial areas where the main deformation occurs.

The rest of this paper is organized as follows. Section 2 briefly summarizes the work described in [10]. Section 3 presents Mixed-resolution Br-SDM, with the experimental results shown in section 4. We conclude our paper in section 5.

2 Formulation of Br-SDM

We have previously proposed a Bone-related SDM or Br-SDM to achieve both accurate and efficient prediction for orthognathic surgery planning. For the detail formulation of the construction of a Br-SDM, we refer to [10]. We give a brief summary of the technique in the following.

Using conventional linear Finite Element Method (FEM), we can generate different facial outlook according to different surgical plans. Then for each output, displacements of the boundary points (defined as those soft-tissue vertices that overlap with the jaw surface, which reflect the jaw movements of the plans) and the displacements of the non-boundary points (which reflect the facial appearance as predicted by FEM) form a sample $X = (\delta_{boundary}, \delta_{non-boundary})^T = (\delta_1, \dots, \delta_m, \delta_{m+1}, \dots, \delta_n)^T$, where δ_i is the displacement of vertex i of on the soft-tissue mesh, with the first m vertices overlapped with the jaw mesh and defined as *boundary points*, and the remaining $n-m$ points which are free to deform and defined as *non-boundary points*.

All these samples are collected and used in the construction of a Statistical Deformable Model (SDM):

$$X = \bar{X} + \Phi b \quad (1)$$

where \bar{X} is the mean of the sample, calculated by $\bar{X} = \frac{1}{N} \sum_{i=1}^N X_i$ with the sample count N , and $\Phi = (p_1, \dots, p_t)$ is the major variation modes with the eigen-vectors p_1, \dots, p_t correspond to the largest t eigen-values of the covariance matrix S calculated by $S = \frac{1}{N} \sum_{i=1}^N dX_i dX_i^T$.

Given a statistical deformable model for bone-related soft tissue prediction, a surgery plan can be expressed in terms of the cutting plane of the jaw model and the displacement of the jawbone pieces. These displacements can be further transformed into $\delta_{boundary}$ to predict $\delta_{non-boundary}$. Then by minimizing

$$D(b) = \left\| \delta_{boundary} - (\bar{\delta}_{boundary} + \Phi_{boundary} b) \right\|^2 \quad (2)$$

where $\bar{\delta}_{boundary}$ and $\Phi_{boundary}$ are the non-boundary part of \bar{X} and Φ respectively, we can choose appropriate variation parameter b to fit $\delta_{boundary}$ into Br-SDM. And then b is used further to calculate $\delta_{non-boundary}$ which represent the facial changes by:

$$\delta_{non-boundary} = \bar{\delta}_{non-boundary} + \Phi_{non-boundary} b \quad (3)$$

where $\bar{\delta}_{non-boundary}$ and $\Phi_{non-boundary}$ are the non-boundary part of \bar{X} and Φ respectively.

3 A Mixed-resolution Br-SDM (mBr-SDM)

3.1 Motivation

We have shown through experiments that while the Br-SDM presented above can achieve a good average accuracy for post-operative prediction of soft tissue deformation which is around 10% of the predicted deformation by FEM [10], we also observed that the predictive errors for certain areas of face are higher than that for the other areas. Specifically, when we visualize the prediction errors of each point on the soft-tissue mesh according to their positions, we find that the major differences lie in the two sides around the chin, as illustrated in Fig.1.

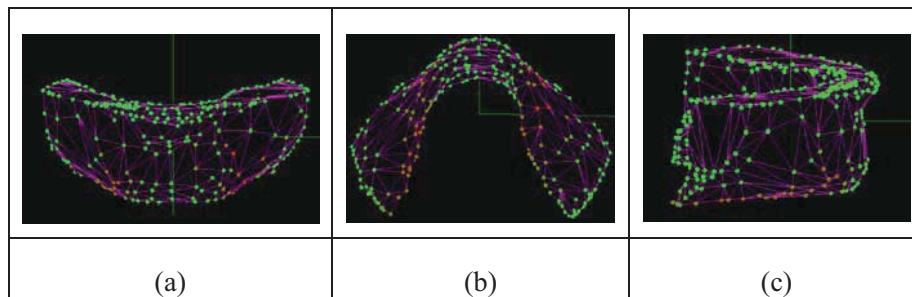


Fig. 1. The differences (colour-coded) in predicted movement of the vertices (comparing with FEM) for the surgical plan of moving jaw-bone forward 5.1mm. (a) the front view, (b) the bottom view and (c) the side view. Green points: points with the least difference (0 mm), red points: points with the largest difference (2.3 mm), the other points: the color is interpolated between red and green according to the difference.

From Fig.1 and fig 2, we can see that points lying on both sides of the chin have the largest differences in terms of predicted movements between Br-SDM and FEM. In Fig.2, we can see that the points within the main deform area suffer from relatively large prediction differences of up to 2.3 mm, while the other points proved to have good accuracy within differences of below 0.5mm. Unfortunately, it is the area, which suffers large prediction differences are the place where we are most interested in, and we need therefore to improve the prediction accuracy compared with FEM.

The reason for large difference may be that points in this area have more deforming variation modes. To capture the large number of fine deformation modes, we need a higher-resolution mesh model and more training samples. But we also need to make sure that the computational requirement does not increase significantly at the same time. To this end, we introduce a mixed-resolution Br-SDM which consists of a high-resolution Statistical Deformable Model (called *sub-SDM*) for the region of particular interests while keeping the original low-resolution SDM (called *main-SDM*) to model the deformations in other areas.

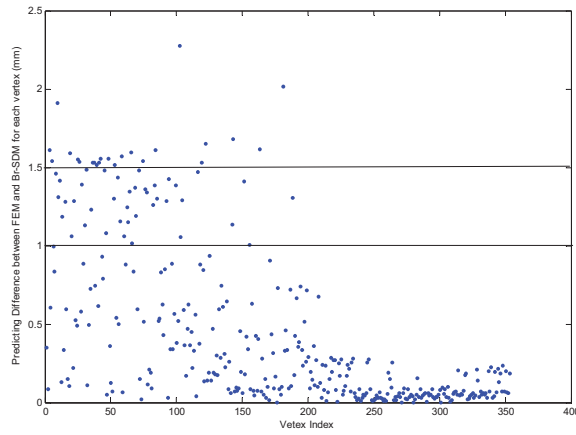


Fig. 2. Differences in the predicted movements between FEM and Br-SDM of each vertex for the surgical plan of moving jaw-bone forward 5.1mm.

3.2 The structure of the Mixed-resolution Br-SDM

The points on the soft-tissue mesh consists of two sets, one of which, we call set A, consists the points within the main deformation area of interest, e.g. the area of the chin as mentioned before (illustrated in Fig.3), and the other set, called set B, consists the other points.

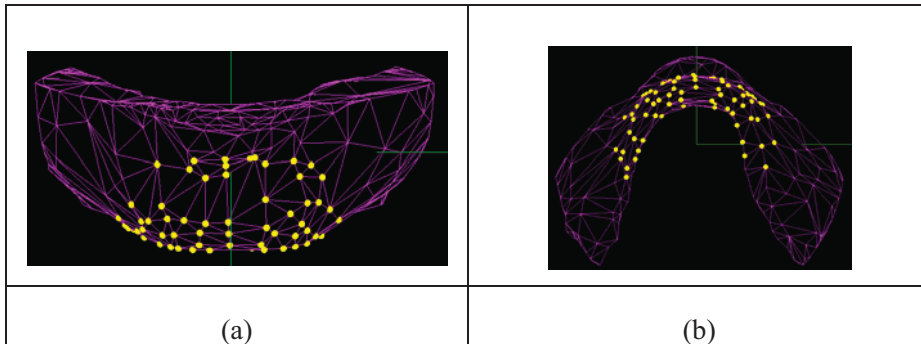


Fig. 3. Points within the main deformation area (marked as yellow). (a) the front view and (b) the bottom view

Consequently, the sample defined in section 2 is divided into two parts, $X_A = \{\delta_{boundary}, \delta_{A-non-boundary}\}$ and $X_B = \{\delta_{boundary}, \delta_{B-non-boundary}\}$, where $\delta_{A-non-boundary}$ are the displacements of the points in set A, and $\delta_{B-non-boundary}$ are the displacements of the points in set B.

Then as described in [10], we use FEM to generate samples, and these samples are transformed into $\{X_A\}$ and $\{X_B\}$ respectively. $\{X_B\}$ is used to train the **main-SDM** :

$$X_B = \bar{X}_B + \Phi_B b \quad (4)$$

with $\bar{X}_B = \{\bar{\delta}_{boundary} \quad \bar{\delta}_{B-non-boundary}\}$ the mean of $\{X_B\}$ and $\Phi_B = \begin{pmatrix} \Phi_{B-boundary} \\ \Phi_{B-non-boundary} \end{pmatrix}$ the variation mode.

As mentioned before, we needs more samples to capture the variation modes within $\{X_A\}$. So introduce and simulate more surgical plans to generate more samples in this critical facial area, and these samples are incorporated into $\{X_A\}$, to train the **sub-SDM** :

$$X_A = \bar{X}_A + \Phi_A b \quad (5)$$

with $\bar{X}_A = \{\bar{\delta}_{boundary} \quad \bar{\delta}_{A-non-boundary}\}$ the mean of $\{X_A\}$ and $\Phi_A = \begin{pmatrix} \Phi_{A-boundary} \\ \Phi_{A-non-boundary} \end{pmatrix}$ the variation mode.

To predict the soft tissue changes of a given surgical plan $\delta_{boundary}$, the displacements of the points in set A $\delta_{A-non-boundary}$ are found using (5), by minimizing

$$D_{X-A}(b_A) = \left\| \delta_{boundary} - (\bar{\delta}_{boundary} + \Phi_{A-boundary} b_A) \right\|^2 \quad (6)$$

and calculating

$$\delta_{A-non-boundary} = \bar{\delta}_{A-non-boundary} + \Phi_{A-non-boundary} b_A \quad (7)$$

where $\Phi_{A-boundary}$ and $\Phi_{A-non-boundary}$ are the first and second parts of Φ_A corresponding to the boundary and non-boundary points respectively, $\bar{\delta}_{boundary}$ and $\bar{\delta}_{A-non-boundary}$ are the first and second parts of \bar{X}_A corresponding to the boundary and non-boundary points respectively, and b_A is the variation parameter estimated in (6) and taken into (7) to compute $\delta_{A-non-boundary}$.

Similarly, the displacements of the points in set B $\delta_{B-non-boundary}$ are found using (4), by minimizing

$$D_{X-B}(b_B) = \left\| \delta_{boundary} - (\bar{\delta}_{boundary} + \Phi_{B-boundary} b_B) \right\|^2 \quad (8)$$

and calculating

$$\delta_{B-non-boundary} = \bar{\delta}_{B-non-boundary} + \Phi_{B-non-boundary} b_B \quad (9)$$

where $\Phi_{B-boundary}$ and $\Phi_{B-non-boundary}$ are the first and second parts of Φ_B corresponding to the boundary and non-boundary points respectively, $\bar{\delta}_{boundary}$ and $\bar{\delta}_{B-non-boundary}$ are the first and second parts of \bar{X}_B corresponding to the boundary and non-boundary points respectively, and b_B is the variation parameter estimated in (8) and taken into (9) to compute $\delta_{B-non-boundary}$.

4 Experiments and Results

4.1 Variations of Prediction accuracy of Br-SDM with different training samples

Fig.5 shows the prediction differences of the selected 82 points of a Br-SDM trained with 244 samples and 334 samples respectively. Compare with Fig.4, which shows the predictions differences of a Br-SDM trained only with 128 samples, we can see that the prediction differences reduce when the number of training samples increases. In case of a Br-SDM trained with 244 samples, the major differences stay below 1.0mm, with the mean 0.64mm; and in case of a Br-SDM trained with 334 samples, the major differences even stay below 0.5mm, however, the deviation is larger, with errors of some points are larger than 1.5mm or even up to 2.5mm. We interpret this observation as the result of over-training.

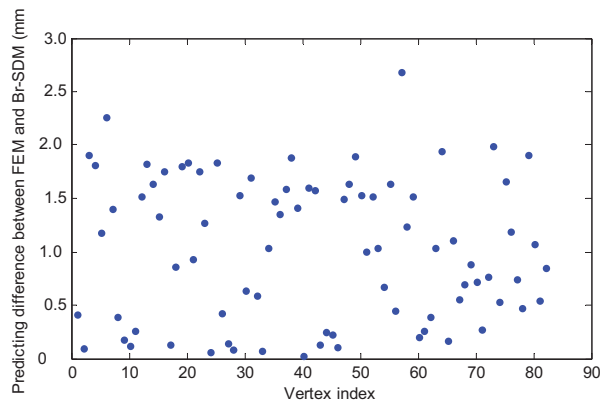


Fig. 4. Prediction differences of the selected 82 points from the original 128 samples (in the case that the jawbone piece is moved forward 5.1mm)

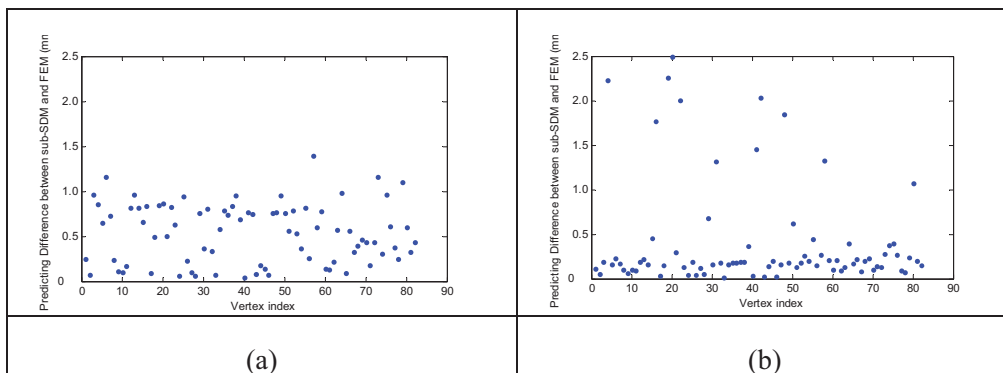


Fig. 5. Predicting differences of the selected 82 points (in the case that the jawbone piece is moved forward 5.1mm). (a) the prediction difference from the SDM trained with 244 samples, (b) the prediction difference for the SDM trained with 334 samples

When we apply the proposed mix-resolution Br-SDM that consists of the sub-SDM of the main deformation area and the main-SDM of the other facial region, we find that the average differences are significantly reduced (table 1).

Table 1. Mean predicting difference for different surgical plans.

Surgical Plan	Mean Difference (Br-SDM)	Mean Difference (mBr-SDM)	Mean Difference (A)
F+3.1mm	0.32mm	0.12mm	0.45mm
F+4.3mm	0.44mm	0.20mm	0.58mm
F+5.1mm	0.51mm	0.32mm	0.64mm

*F+ is for Mandible Advancement. The mean difference is defined as $E = \frac{1}{n} \sum_{i=1}^n e(i)$. It can be seen from Table 1 that the mean differences for mBr-SDM are significantly reduced compared with those for Br-SDM. A denotes the mean difference for the main deforming region calculated by the Mixed-resolution Br-SDM.

4.2 Computational Cost

By incorporating sub-SDM in the mixed-resolutions Br-SDM does not require much additional computational cost. The only additional cost is consumed in the process of training the sub-SDM. Since the sub-SDM typically covers only a small region of the face where the major deformation occurs, it typically consists of a small number of vertices, (82 points in our example), the training of the high-resolution sub-SDM can be completed in our experiment in 1 minute using a PC with Intel Pentium M processor and 2Gbyte RAM with a matlab program.

5 Conclusion

In this paper, we proposed a Mixed-resolution Br-SDM (mBr-SDM) to improve the prediction accuracy of bone-related soft-tissue changes in orthognathic surgical planning while maintaining a low computational cost compared with FEM. Specifically, Mixed-resolution Br-SDM consists of a sub-SDM which serves to capture the detail deformation variations of the points around the main deforming areas of interest, while a low-resolution main-SDM is used to capture the deforming variations of other points of the facial regions. This way, we are able to focus the computations of detail deformation modes using more samples for the regions of interests within a SDM, while keeping the computational costs down compared with FEM.

Acknowledgement

The work described in this paper was supported by grants from the Research Grants Council of Hong Kong, China [Project No. CityU113706 and CityU114007]

Reference

- [1] Erwin Keeve, Sabine Girod, et.al. *Deformable Modeling of Facial Tissue for Craniofacial Surgery Simulation*. Computer Aided Surgery vol.3, pp:228–238 (1998)
- [2] M Bro-Nielsen, HTM Inc, MD Rockville. *Finite Element Modeling in Surgery Simulation*. Proceedings of the IEEE, vol.86(33), pp:490-503 (1998)
- [3] W.Mollema, F.Schutyser et. al. *Predicting soft-tissue deformations for a maxillofacial surgery planning system: From computational strategies to a complete clinical validation*. Medical Image Analysis, vol.11(3), pp:282-301 (2007)
- [4] Roose, L., De Maerteleire, W.,Mollema, W.,Suetens,P. *Validation of different soft tissue simulation methods for breast augmentation*. Proceedings of CARS, pp:485-490 (2005)
- [5] S Cotin, et.al. *A hybrid elastic model allowing real-time cutting, deformations and force-feedback for surgery training and simulation*. The Visual Computer, 16(88):437-452 (2000)
- [6] T.F. Cootes, C.J.Taylor,D.H.Cooper,J.Graham. *Active Shape Models – Their Training and Application*. Computer Vision and Image Understanding, Vol.61(1), pp: 38-59 (1995)
- [7] Charles Kervrann and Fabrice Heitz. *Statistical Deformable Model-Based Segmentation of Image Motion*. IEEE Transactions on Image Processing. Vol.8(4),pp:583-588(1999)
- [8] S Meller, E Nkenke, W Kalender. *Statistical Face Models for the Prediction of Soft-tissue Deformations after Orthognathic Osteotomies*. MICCAI, vol. 3750, pp:443-450 (2005)
- [9] S.J. Raudys, A.K. Jain. *Small Sample Size Effects in Statistical Pattern Recognition: Recommendations for Practitioners*. IEEE Transactions on Pattern Analysis and Machine Intelligence, Vol. 13(3), pp. 252-264 (1991)
- [10] Qizhen He, Jun Feng, Horace H. S. Ip , James Xia and Xianbin Cao. *An Integration of Statistical Deformable Model and Finite Element Method for Bone-related Soft Tissue Prediction in Orthognathic Surgery Planning*. Accepted by: 4th international workshop on Medical Imaging and Augmented Reality. Tokyo, August, 2008.